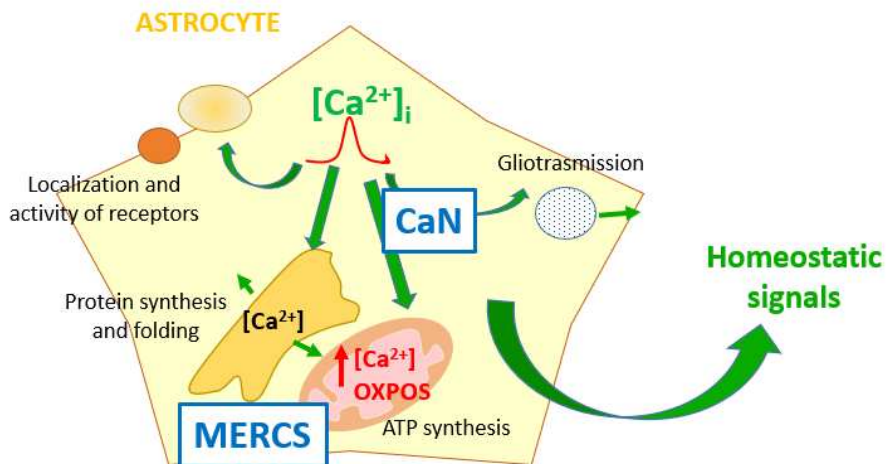# UNIVERSITÀ DEGLI STUDI DEL PIEMONTE ORIENTALE "AMEDEO AVOGADRO"

Department of Pharmaceutical Sciences
Ph.D. in Drig Innovation
XXXVI cycle 2020-2024
(SSD BIO-09)

Ca²⁺ related mechanisms of cellular dysfunction in neurodegeneration

Giulia DEMATTEIS

Supervisor

Prof. Dmitry LIM

PhD program co-ordinator

Prof. Gian Cesare Tron

UNIVERSITÀ DEGLI STUDI DEL PIEMONTE ORIENTALE "AMEDEO AVOGADRO"

Department of Pharmaceutical Sciences
Ph.D. in Drig Innovation
XXXVI cycle 2020-2024
(SSD BIO-09)

Ca2+ related mechanisms of cellular dysfunction in neurodegeneration

Giulia DEMATTEIS

Supervisor

Prof. Dmitry LIM

PhD program co-ordinator

Prof. Gian Cesare Tron

DECLARATION AND AUTHORISATION TO ANTIPLAGIARISM DETECTION

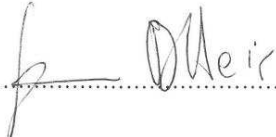The undersigned GiuliaDematteis student of the Drug Innovation

Ph.D course (**XXXVI** Cycle)

declares:

- to be aware that the University has adopted a web-based service to detect plagiarism through a software system called "Turnit.in",
- her Ph.D. thesis was submitted to Turnit.in scan and reasonably it resulted an original document, which correctly cites the literature;

acknowledges:

her Ph.D. thesis can be verified by his/her Ph.D. tutor and/or Ph.D Coordinator in orderto confirm its originality.

Date: 11/11/2023………………………….. Signature: …………………………………………

XY/tcs
Percorso del file

To my mum an my dad

"Aconteceu sem que o mundo agradedcesse,

sem que rosas florescessem"

Contents

Chapter 1

INTRODUCTION

1.1 CALCIUM SIGNALING TOOLKIT

1.1.1 Intracellular [Ca^{2+}] and Ca^{2+} stores

Intracellular [Ca^{2+}] ([Ca^{2+}]$_i$) in the cytosol is kept in the range of 50-150nM.; Cytosolic Calcium increase is mediated by two main phenomena: (i) calcium entry form the extracellular space, and (ii) calcium release form the internal stores, mainly represented by the Endoplasmic Reticulum (ER) [1].

Using genetically encoded, aequorin based probes, targeted to the ER, [Ca^{2+}]$_{ER}$ has been measured, and found to be around 0.1-1 mM ($\sim$10^3-10^4 times higher than in the cytosol) depending on cell type. ER calcium level is constantly monitored by STIM1, calcium sensor protein localized at the endomembrane. Lowering of [Ca^{2+}]$_{ER}$ induces STIM1 polymerization and consequent activation of ORAI or TRPC channels, mediating store operated calcium entry (SOCE) [2] [3]. Upon SOCE activation, Ca^{2+} is rapidly up taken from the cytosol into the ER via sarco-endoplasmic reticulum Ca^{2+} ATPase (SERCA), restoring ER basal calcium levels. SOCE exerts also important signalling functions. In the ER surface inositol-3-phosphate receptors (IP3Rs) and ryanodine receptors (RyRs) are expressed, and upon metabotropic stimulation opening of these receptors drives ER calcium release and cytosolic [Ca^{2+}] increase [1]. Moreover, both these groups of receptors are sensible to calcium itself, determining Ca^{2+} induced Ca^{2+} release, engaging neighbouring receptors in propagation of Ca^{2+} signal in a form of Ca2+ wave.

In mitochondria, at resting conditions [Ca^{2+}] is kept at sub-micromolar levels. However, upon stimulation of Ca2+ release from the ER, [Ca^{2+}]m transients can reach 50-100 µM. Mitochondrial calcium uptake is mediated by mitochondrial calcium uniporter (MCU), a protein complex composed of pore-

forming subunits (MCU and its dominant negative isoform MCUb), the essential MCU regulator (EMRE), which mediates the interaction with the mitochondrial calcium uptake regulatory subunits (MICU1, MICU2 and MICU3), the activity of this channel is directly regulated by the $[Ca^{2+}]$ and the electrochemical gradient across the inner mitochondrial membrane [4] [5]. In resting condition, the $[Ca^{2+}]_{mit}$ is ~ 7µM, but upon stimulation it can arise until 20µM [6]. Indeed, considering mitochondrial ability to uptake and release calcium, and the dynamic localization of this intracellular organelle in the different cellular sub compartments, give rise to the hypothesis of mitochondrial central role in shaping cytosolic calcium responses in a fine and precise manner, in terms of both spatial and time control [7].

Ca^{2+} can be released from mitochondria via mitochondrial Permeability Transition Pore (mPTP) or Sodium- Chloride- Lithium exchanger (NCLX). $[ca^{2+}]_{mit}$ tightly controls also the opening of mPTP, that can both promotes the activation of the apoptotic pathway and also controls the physiological mitochondrial calcium release [8]. Going into details mPTP exists in two different isoforms, with different permeability properties: a low conductance isoform, and a high conductance one. The first one, characterized by a flickering activity of the pore, presents an apparent molecular cutoff < 300 Da, with selectivity for small ions like Ca^{2+}, and its activation is mostly induced by the pH variation due to the mitochondrial membrane depolarization [9]. So, the low conductance isoform cooperates with NCLX during calcium release, promoting the generation of cytosolic calcium signals and preventing mitochondrial calcium overload. For example, it was proved that impairment of mPTP flickering activity inhibit neurotransmitter release and it is correlated with hereditary spastic paraplegia type 7 [10]. On the other hand, the high conductance rate isoform, with a molecular cutoff of approx. 1500 Da, allows

the efflux of a variety of ions and of small molecules, such as the cytochrome c, that is a well-known apoptotic signal [11] [12].

1.2 ASTROCYTES: PHISIOLOGICAL AN PATHOLOGICAL ROLES IN CNS

Astrocytes (from Greek astron=star and Kittaron=cell), together with oligodendrocyte and microglia, constitute neuroglia. The term neuroglia was coined by Virchow in 1856, and is correlated with the idea that those cells have the passive role of filling up space not occupied by neurons [13]. While the term astrocytes was proposed by Michael von Lenhossek in 1891, in association with a star-like shape of astroglial cells, highlighted by Ramón y Cajal that, using a gold chloride stain, accidentally stained intermediate filaments including glial fibrillary acidic protein (GFAP) [14]. Nowadays, via genetically encoded probes we know that astrocytes shape is far from a star like shape, and more like a sponge shape, increasing their ability to contact and cover synapses and blood vessels [24].

Moreover, it's also recognised by the scientific community an active role for neuroglial cells, in the modulation and maintenance of nervous system activity. Indeed, evolution of the nervous system established specialization and division of function:

- Neurons are specialized in firing action potential that propagate to axonal terminals and initiate synaptic transmission and communication.
- Glial cells are involved in maintenance, protection and control of the neural tissue [15].

Astrocytes represent the 20-50% of total glial cells in the central nervous system (CNS), they extend their processes with little overlap between adjacent

cells forming highly organized anatomical domains. Based on their morphology and location, astrocytes can be classified in different categories[1], and in the last years, thanks to transcriptomics approaches a significant heterogeneity among astrocyte's population has emerged[16]. The most relevant and well characterized types of astrocytes are:

- Fibrous astrocytes of white matter which promote myelination of axons (Fig.1.1).
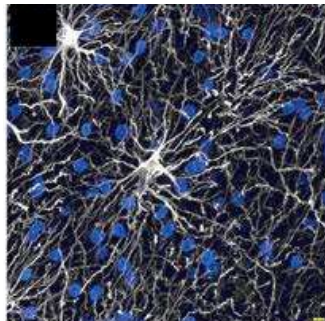

Figure 1.1 Human fibrous astrocytes in white matter [17].

- Protoplasmic astrocytes of grey matter found in the synaptic neuropil. At the ultrastructural level, the protoplasmic astrocytes are much more complex with thousands of fine protrusions, commonly called "peripheral astrocytic processes" or astrocytic leaflets (Fig.1.2).
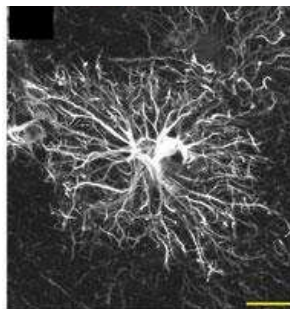
Figure 1.2. Human protoplasmic astrocyte [17].

These astrocytic leaflets enclose synapses and express a large spectrum of receptors for neurotransmitters, cytokines, and growth factors, transporters and ion channels. It has been established that in mouse brain each astrocyte incorporates from 4 to 10 neuronal bodies and makes contacts with more than 20 000 synapses [18]. Moreover, astrocytes project specialized end-foot processes to the intra-parenchymal blood vessels establishing a specialised functional unit called "neuro-vascular unit" [19].

All those anatomical features underline fundamental functions of astroglial cells that have been discovered, until now (Fig.1.3). These functions include:

- structural organization of nervous tissue,
- synaptogenesis and the development of the central nervous system,
- generation and maintenance of the blood-brain barrier and regulation of the local blood flux,
- ion homeostasis in the brain and in metabolic support to neurons,
- clearance of metabolites produced by other cell types, and removal of reactive oxygen species [20].
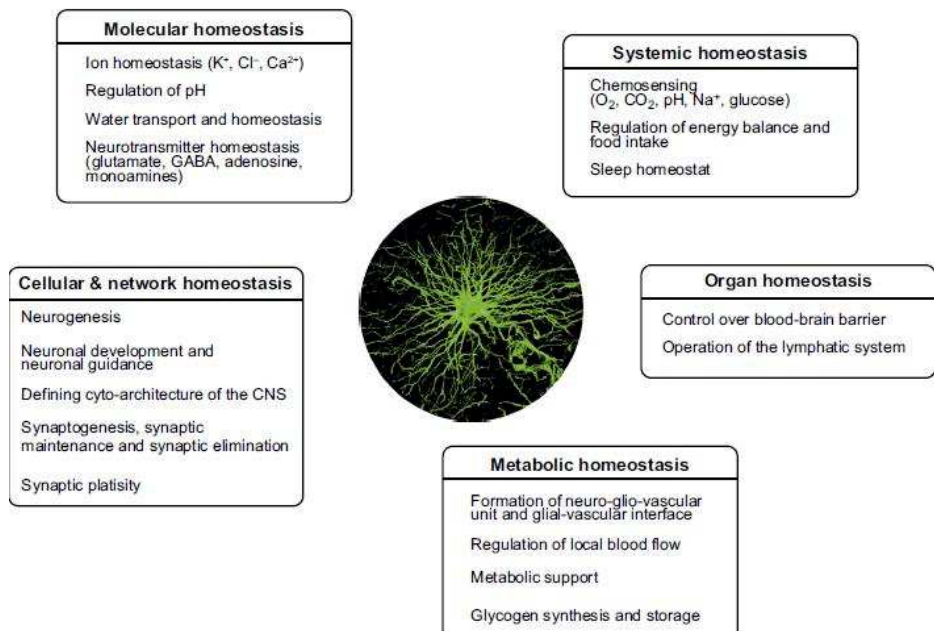
Figure 1.3. Homeostatic functions of astroglia [17].

1.2.1 Multipartite synapse: astrocytes as synaptic cradles

The observation that the astrocyte's leaflets interact with the synapses led to a concept of "multipartite synapse" in which astrocytes may actively participate in the synaptic transmission. This term is referred to an anatomic-functional structure that allows a bidirectional communication between astrocytes and neurons [20] (Fig.1.4).

The main components of multipartite synapses of the CNS are:

- Presynaptic terminal
- Postsynaptic terminal
- Leaflets of the astrocyte
- Extracellular matrix

PRESYNAPTIC NEURON

ASTROCYTE

POSTSYNAPTIC NEURON

NMDAR	mGluR	Glutamate	
AMPAR	CB₁R	D-Serine	
VDCC	IP₃R	eCB	
		IP₃	
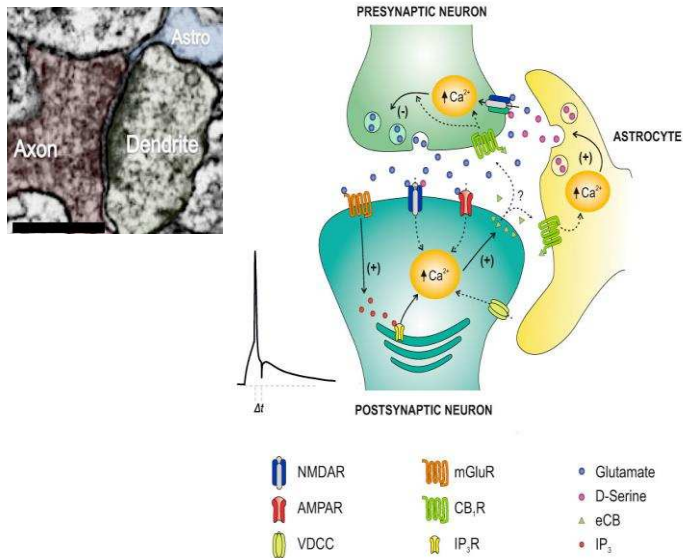
Figure 1.4. The multipartite synapse. Electron microscopy image [19] and schematic representation [21].

A fifth component of the multi-partite synapse is represented by the microglial processes [15].

Astrocytic leaflets, called also "perisynaptic process" cover 60-70% of pre- and post-synaptic terminals. Indeed, astrocytes have the ability to sense and adhere to synapses and coordinate with the neighbouring astrocytes to tile and cover the neuropil. However, astrocytes do not ensheath all synapses, and synapse association of astrocytes is a dynamic process that can be modulated by neuronal activity [22]. For example, during memory formation, astroglial processes undergo rapid and profound changes, determining modification of the neurochemical environment by allowing or denying neurotransmitter spillover, which is a mechanism contributing to memory formation [23].

The perisynaptic compartment has many different functions in the multipartite synapse such as:

1) Synapse formation and elimination

More than 20 years ago Pfiriger and Barres have demonstrated that neuronal primary cultures from rodent form few synapses, and that the number and the strength of synapses are increased by the addition of astrocytes.

Now we know that astrocytes can release specific signals, like thrombospondins (TSPs) and Hevin that promote the interaction between pre- and postsynaptic terminal bridging their own receptors expressed in both regions.

Astrocytes also regulate synapse elimination, this occur by both direct and indirect mechanism. Indeed astrocytes can directly phagocytose excess of synapses, via the functions of astrocytic phagocytic receptors Mertk and Megf10. Moreover astrocytes indirectly regulate synapse elimination via the secretion of transforming growth factor β (TGFβ), which upregulates C1q in neurons, leading to tagging synapses for elimination by microglia [24].

2) Maintenance of extracellular homeostasis

Astrocytes, with their close juxtaposition to synapses, detoxify the local environment by the uptake of K^+, glutamate and other neurotransmitters.

Neuronal propagation of action potential induces a transient release of K^+ into the extracellular space. Prolonged accumulation of K^+ in the extracellular space causes wide-spread depolarization of neurons and glia which results in compromised synaptic transmission and neuronal firing. For this reason, extracellular K^+ must be tightly controlled and removed from the extracellular space immediately after neuronal excitation [25].

At the end of 1980s it has been found that, during neuronal activity, the K^+ release from neurons is paralleled by a rise in intracellular $[K^+]$ in the neighbouring glial cells [26]. The activity–dependent glial K^+ accumulation points to this cellular type as a central point for K^+ buffering during neuron depolarization.

Glutamatergic neurotransmission involves packaging of glutamate into vesicles, exocytotic release triggered by a depolarization signal, which activates voltage- and/or receptor-operated Ca^{2+} channels, and subsequent uptake mainly into astrocytes, in order to avoid excitotoxicity, induced by prolonged exposure of the postsynaptic membrane to high concentrations of glutamate. Inside the astrocytes glutamate is metabolised to glutamine, which may be transferred back to neurons, where it is used to produce new glutamate, or can be utilized as an energy substrate as it can enter the tricarboxylic acid (TCA) cycle after conversion to α-ketoglutarate (α-KG) by the glutamate dehydrogenase [27].

Five transporters for Na^+-coupled glutamate transport have been cloned and they are named EAAT1-5 (Excitatory Amino Acid Transporters 1-5) [28] [29]. Among these, EAAT1 (GLAST) and EAAT2 (GLT-1) are expressed preferentially if not exclusively on the astrocytic plasma membrane [29] providing these cells with an enormous capacity for glutamate uptake.

In the last decade, the ability of astrocytes to release glutamate and other neurotransmitters, such as GABA and D-serine, has been described, unveiling new mechanisms for astrocyte to neuro communication[30]. Schwarz and colleagues demonstrated that stimulation of astrocytes with DHPG, an mGluR1 selective agonist, induced the release of glutamate-containing vesicles via SNARE protein dependent process[31]. The effect of gliotransmission on synaptic activity, depends on the synaptic environment.

Indeed, the same gliotransmitter can have both excitatory and inhibitory effect, depending on the specific environment[32,33].

3) Trophic support to neurons

It has long been known that neurons are unable to supply all their metabolic needs autonomously, and in different experiments it has been shown that neuronal activity shuts down after treatment with astrocyte-specific metabolic inhibitors [27].

Astrocytes with their leaflets, on one hand, communicate with capillaries, and take up until 50% of total glucose of the brain, by GLUT1, and on the other are associated with neurons and synaptic processes. For these structural features, even if neurons can import glucose directly from the extracellular space, astrocytes have been proposed to play an important role in coupling neuronal activity and brain glucose uptake through the astrocyte–neuron lactate shuttle. According to this mechanism, the glutamate uptake into astrocytes following synaptic release causes a stimulation of anaerobic glycolysis and glucose uptake from the circulation via GLUT1. Furthermore lactate, produced by astrocytes via glycolysis is released into the extracellular space and taken up by neurons. Once into neurons, lactate can be used as an energy substrate, in the mitochondrial TCA cycle [19] [34]. However, astrocytes cannot be considered purely glycolytic cells, as it has been thought for long. Instead, they possess a powerful Ox Phos machinery [35].

1.2.2 Astrocytes in neurodegeneration

Neurodegenerative diseases (NDs) are characterized by progressive cognitive decline caused by the dysfunction and death of neuronal cells[23]. In particular,

Alzheimer's disease (AD) is a major cause of dementia in elderly. Aetiology of AD is complex. Minority of cases (early onset, <0.5%) carry mutation in three genes: amyloid precursor protein (APP), presenilin-1 (PS1) and PS2, implicated in production of toxic amyloid-β (Aβ) peptide. In late onset sporadic AD (sAD) (>99.5% of all cases), ~70% of cases are attributable to genetic factors, with APOEε4 allele accounting for ~40% of sAD. Mutations, toxic Aβ, together with other factors, including sedentary lifestyle, low educational level and co-morbidities constitute primary AD-related factors, which initiate a series of molecular and cellular events leading to onset of symptoms and dementia. Thus, AD has a long-lasting pathogenesis, which initiates decades before the onset of symptoms, but cellular alterations occurring at this stage of the pathology are poorly investigated and understood. Unfortunately, multiple attempts to clear Aβ and/or eliminate/revert ongoing neuropathology during the clinical phase revealed unsuccessful highlighting that a crucial challenge for AD research is the one of identifying the early cellular dysfunction determining the prodromal phase of the disease.

Leading AD hypotheses, attempting to explain how primary AD-related insults produce cellular damage, include Ca^{2+} hypothesis, protein clearance hypothesis and bioenergetic deficit hypothesis (Fig.1.5). Deregulated cellular Ca^{2+} signalling may contribute to alteration of cellular proteostasis (disbalance between protein synthesis and degradation including autophagy, lysosomal function and Aβ clearance, and activation of ER-stress/unfolded protein response (UPR)) and bioenergetic deficit (reduced glucose utilization, impaired glycolysis and mitochondrial dysfunction leading to decrease of ATP production and increase of reactive oxygen species (ROS)). Correct ER luminal Ca^{2+} levels are important for proper protein folding and maturation, while ER Ca^{2+} overload may result in enhanced Ca^{2+} transients in the cytosol

and dysregulate cellular Ca^{2+} signalling. Ca^{2+} signals in the mitochondrial matrix are essential for the activity of several enzymes of Krebs cycle and for ATP synthase. Mitochondrial Ca^{2+} mishandling impairs bioenergetic workflow, results in excessive ROS production and may lead to cell death. Altered calcium signalling, protein folding and protein translation, and mitochondrial bioenergetic function have been wildly described in AD neurons, but fine investigations astrocytes cellular dysfunction in AD is still a matter of debate in the literature. Indeed, for decades astrocyte's role in neurodegeneration has been associated with the astrogliosis. In one of our recent publications we described, in an in vitro model of the disease, reduced protein synthesis rate, impaired mitochondrial bioenergetics and altered intracellular calcium signalling, with increased cytosolic calcium response, but impaired mitochondrial calcium uptake. these results indicate that early phase AD related dysfunction is recapitulated in astrocytes and point out astrocytes as possible drivers of the pathology [36].
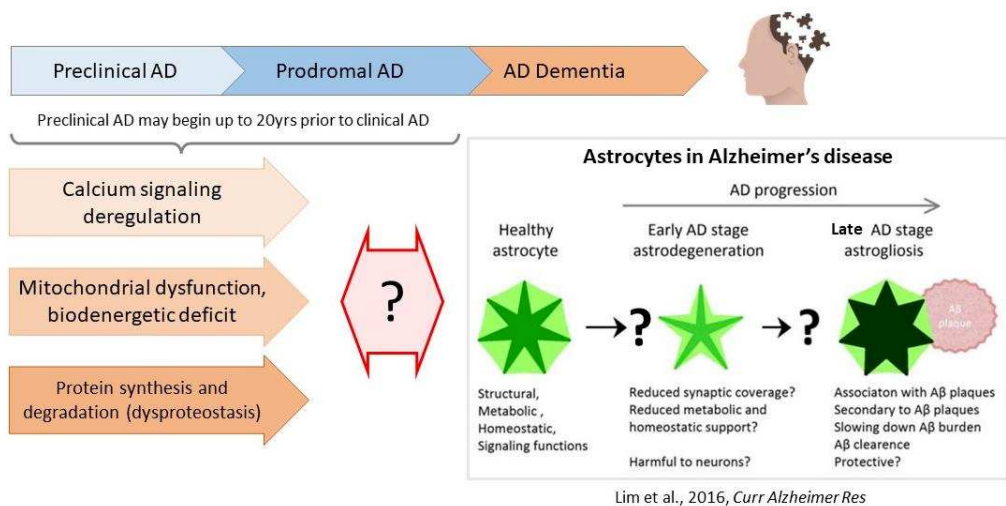

Figure 1. 5 Schematic representation of AD phases and role of astrocytes along AD pathogenesis.

1.3   CALCIUM SIGNALING IN ASTROCYTES

Neurons express, at the plasma membrane, a wide range of inotropic receptors that determine their ability to generate and propagate action potential. Instead, astrocytes, like the others glial cells, express a different pattern of receptors and channels, that define them as electrically not excitable cells due to inability to generate action potentials [37]. Nevertheless, activation and opening of channels and receptors expressed by astroglial cells, determine changes in intracellular ion concentrations, that regulates activity and localization of enzymes, gene expression, cellular metabolism, secretion of gliotransmitters and growth factors driving astrocytic homeostatic responses [1] (Fig.1.6). Ca^{2+} is the ion for which the implication in shaping astroglial function is better described and demonstrated. As an example, it has been reported in different studies, neuronal activity induces astrocytic calcium waves, and synchronized calcium activity has been described in astrocytes of freely moving animals upon whisker or visual stimulation [38] [39] [40] [41]. In astrocytes, metabotropic signalling is crucial for cytosolic calcium response. Indeed, astrocytes express a plethora of metabotropic G coupled receptors, such as mGluR5, P2Y, $GABA_B$, alpha and beta adrenoreceptors, histamine, dopamine cannabinoid receptors [42] [37]. According to brain region localization and astrocytic subtype classification, astrocytes express different sets of metabotropic receptors determining the ability to induce different types of intracellular calcium responses. Indeed, astroglial Calcium signalling presents intra- and inter- brain region specificity, correlated to their morphological diversity (e.g. protoplasmic and fibrous astrocytes) and neuronal circuits specialization [1].

Moreover, it has been described a central role for mitochondria, via calcium uptake and release, in the control cytosolic calcium levels, as an example, in

astrocytes, it was been demonstrated that NCLX is crucial for the modulation of cytoplasmic Ca^{2+} transients required to control different astrocytes functions, such as glutamate release and proliferation [43].
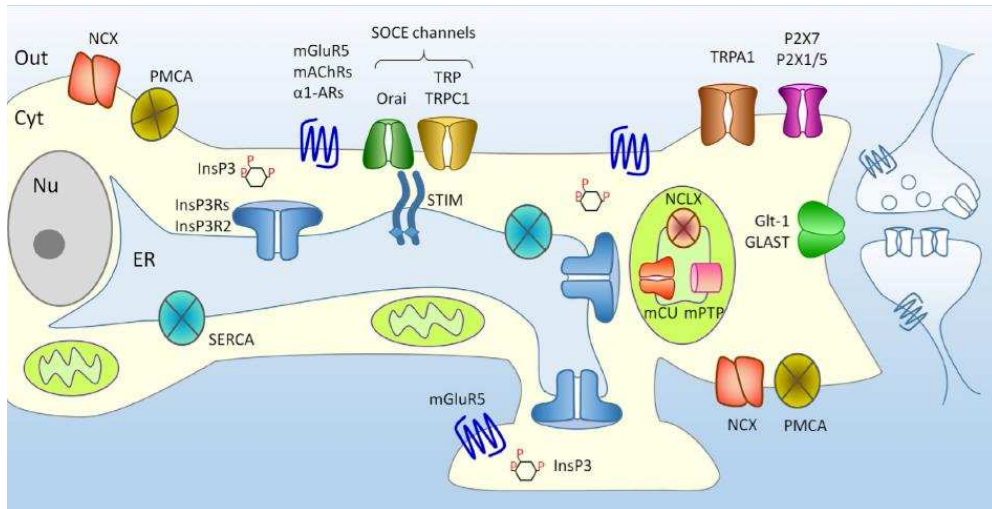
Figure 1.6: calcium tool kit in astrocytes. Schematic representation of calcium toolkit in astrocytes. [1].

Calcium signalling in astrocytes regulates different functions, among them some can be considered as "common functions", being described in almost all cell types, while other functions can be defined as cell type specific function [1].

Among the common functions we can report gene transcription, cell mobility and remodelling, indeed different proteins of the cytoskeleton are calcium regulated, and autophagy activation. Moreover, ER calcium homeostasis is crucial for protein folding: chaperone proteins, which also include the principal luminal Ca2+-binding proteins, CRT, BiP/Grp78 and PDI, are calcium regulated and responsible for protein folding and posttranslational protein modifications. Indeed, reduced $[Ca^{2+}]_{ER}$ is responsible for accumulation of unfolded proteins and consequent unfolded protein response (UPR) activation

(Lim 2023). In mitochondria calcium increases promote metabolic activity promoting the activity of four enzymes of Kreb cycle: FAD-glycerol phosphate dehydrogenase, Pyruvate dehydrogenase, Isocitrate dehydrogenase, Oxoglutarate dehydrogenase [44]. Moreover, via different experiments, both in tissue samples and isolated mitochondria, it has been demonstrated that calcium increases promote the activity of the F1F0 ATP synthase [44] (Fig.1.7).
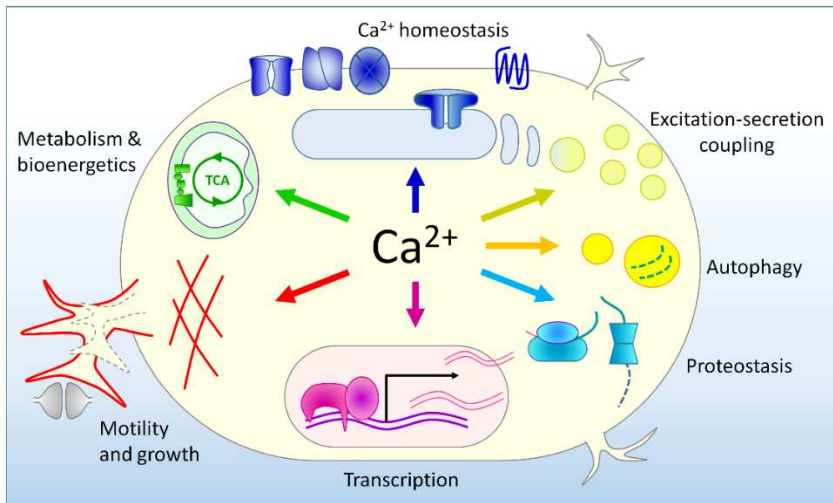
Figure 1.7. Common functions of astrocytic Ca2+ signals. Ca^{2+}, in astrocytes regales numerous functions that are described almost in all cell types [1].

Looking to the cell type specific function of calcium signalling in astrocytes, the most important function is the perception and decoding of the information from the external environment. These signals are crucial to adapt astrocytic physiology to neurons energetic and signalling demands [45]. In this context, astrocytic calcium signalling regulates secretion of gliotransmitters and trophic factors or nutrients. It is implicated in the modulation of cerebral blood flow and contributes to higher brain function such as memory formation, cognition respiration and sleep-awake cycle [46][47][48][49] (Fig.1.8).
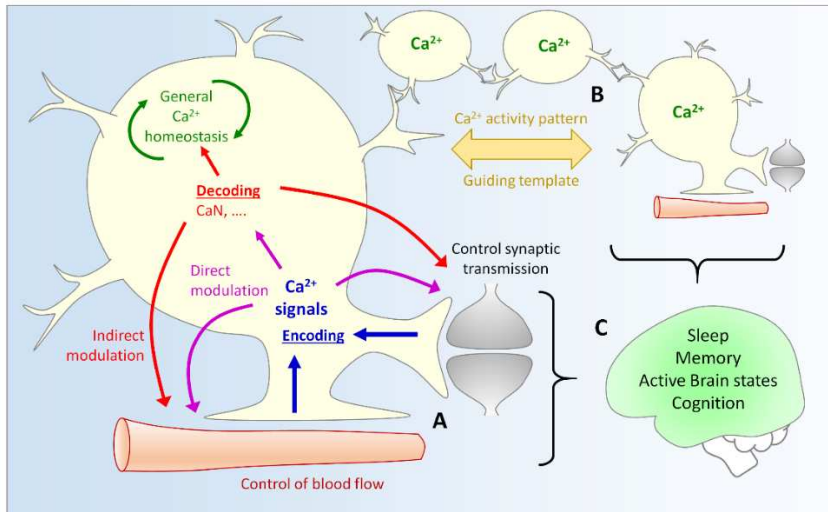
Figure 1.8. Astrocyte-specific Ca2+ signals. Calcium signalling in astrocytes has been associated with the fine regulation of numerous cell type specific functions, relate to CNS physiology [1].

Even if, calcium signalling role in astrocytic brain functions has been widely investigated, the mechanistic details of Ca^{2+} regulation in the different phenomena, and the details of the different levels of integration of the information remains to be further investigated.

1.4   CALCINEURIN

The Ca^{2+}/calmodulin (CaM)-activated serine/threonine phosphatase, calcineurin (CaN), is a heterodimer composed of a larger (59KDa) catalytic subunit (CaNA), and a smaller (19KDa) obligatory regulatory subunit B (CaNB). There have been identified several isoforms for each subunit:

- CaNAα, CaNAβ and CaNAγ encoded by the genes Ppp3ca, Ppp3cb and Ppp3cc, respectively.
- CaNB1 and CaNB2 encoded by the respective Ppp3r1 and Ppp3r2 genes.

The expression of some of these isoforms is tissue specific, for example, in the mammalian brain, only CaNB1, regulatory subunit is expressed. Neuron-specific CaNB1 KO had been produced to eliminate CaN activity in mouse forebrain neuron [50]. Deletion of CaNB1 can be used therefore for generation of cell-specific CaN KO models [51].

Calcineurin, at the sub-cellular level, can be found throughout the cytosol and the nucleus, and is also commonly associated with membrane receptors, ion channels, and pumps via physical interactions with a variety of anchoring proteins [52].

Calcineurin is a key element of the cellular response to Ca^{2+}. Indeed, when calcium levels increase, through an influx from the extracellular space, or by release from endoplasmic reticulum (ER), CaM, in a calcium-bound form, binds CaNA, contemporarily, CaNB binds Ca^{2+}. This cooperative action induces conformational changes in CaNA displacing the autoinhibitory C-terminal domain from the catalytic site, rendering CaN catalytically active [53].

Calcineurin was first discovered in brain tissue, where it is expressed at high levels [54]. CaN has been found in many other tissues, e.g., muscles and, notably, in lymphocytes, where most studies of CaN-regulated signalling pathways have been conducted [55]. From these studies emerge the prototypical functions of calcineurin: CaN mediates dephosphorylation of nuclear factor of activated T cells (NFAT) family of transcription factors, promoting their translocation to the nucleus, where they bound specific target gene promoters, coding for proteins involved in inflammatory response, such as IL2 and IL6 (Fig.1.9). This pathway has been largely studied, in different tissue, thanks to specific calcineurin inhibitors, in particular FK506 and Ciclosporin A, and the peptide VIVIT, that interferes directly with calcineurin/NFAT interaction [56].
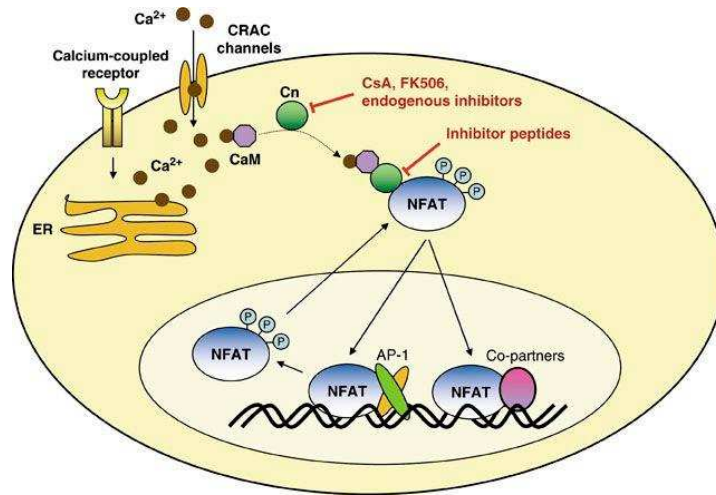
Figure 1.9 Scheme of NFAT activation by Ca^{2+} and CaN [57].

Studies performed from the mid-1980s to the beginning of 1990s reported high expression of CaN in neurons from hippocampus, neocortex, striatum and amygdala, with no expression observed in glial cells; only in late 1990s was found that CaN is also expressed in astrocytes *in situ* and in culture and, in particular, after inflammatory insults. In neurons CaN regulates neuronal excitability, synaptic transmission, and memory formation. In astrocytes, it was thought that CaN is principally involved in setting up reactive gliosis and neuro-inflammation in different neuropathological conditions [58]. For instance, greater numbers of CaN-positive astrocytes, in the hippocampus, have been found during ageing, injury, and Aβ deposition in both (APP/PS1) mice and tissue obtained from subjects diagnosed with Alzheimer's disease [52].

CaN mediates phenotype switching in astrocytes, with up regulation of the expression of GFAP (Glial Fibrillary Acid Protein), down regulation of EAATs, hypertrophy of astrocytes soma and processes, activating both, NFAT and NFkB transcription factors [58]. This astrocyte reactivity has been

extensively documented as a pervasive feature of almost every form of acute CNS injury as well as most chronic neurodegenerative disorders [59] (Fig.1.10).

It was demonstrated that, in hippocampal astrocytes, activation of CaN requires elevation of cytoplasmic $[Ca^{2+}]$. This increase could be mediated by Ca^{2+} entry from the external milieu, e.g. mediated by channel-like structures formed by Aβ in Alzheimer disease, or by Ca^{2+} release from the endoplasmic reticulum via IP_3Rs [60] (Fig.1.11). Moreover astrocytic CaN activation leads to modification in Ca^{2+}-mediated mechanisms, such as glio-transmission and reactive inflammation [58] [61].
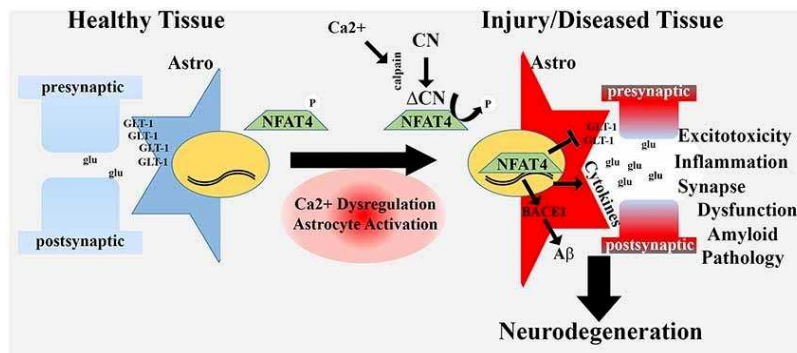
Figure 1.10 Astroglial activation and calcineurin/NFAT signalling in age-related neurodegenerative diseases [62].

In early work from our laboratory, it has been proposed that CaN mediates remodelling of astroglial Ca^{2+} signalling toolkit during Alzheimer disease

pathogenesis[63].
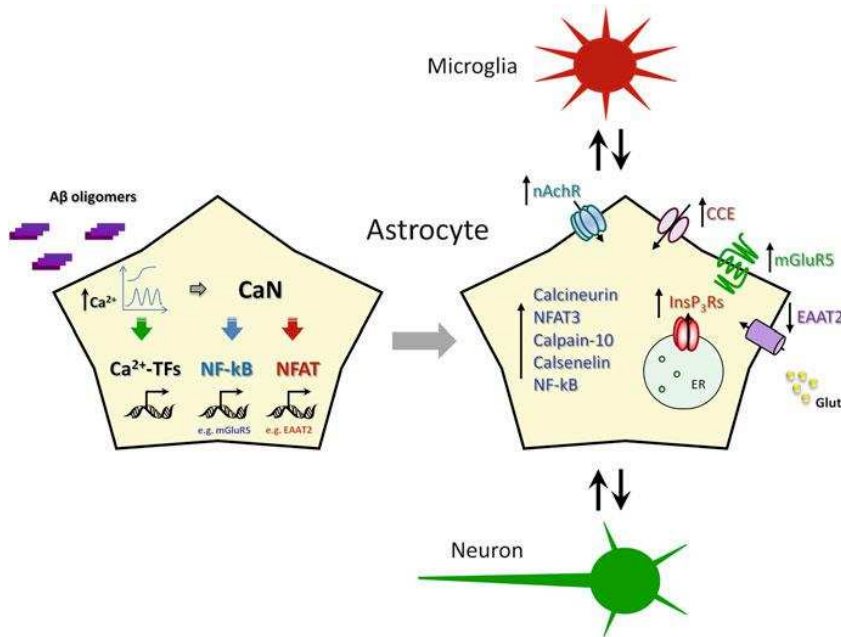
Figure 1.11 Glial calcium signalling in Alzheimer disease [63].

Among a clear implication of CaN in astrogliosis activation, in the last years, our laboratory described physiological roles of astroglial CaN, e.g., in modulating crucial astroglial function such as K^+ buffering and protein synthesis rate maintenance, and consequent regulation of neuronal excitability and the expression and localization of GLAST [51] [64].

1.5 MITOCHONDRIA – ENDOPLASMIC RETICULUM CONTACT SITES (MERCS)

In eukaryotic cells the endoplasmic reticulum (ER) provides an environment suitable for protein and phospholipids synthesis and represents the most

important organelle for Ca^{2+} storage [65]. As it has been already mentioned, mitochondria are responsible for the conversion of energy stored in the chemical bonds of nutrients into ATP, they also have a crucial role in the management of ROS and in the control of apoptotic pathway [66]. Ca^{2+} levels and dynamics are crucial for both ER and mitochondria functions. Correct ER luminal Ca^{2+} levels are important for proper protein folding and maturation, while ER Ca^{2+} overload may result in enhanced Ca^{2+} transients in the cytosol [67]. Ca^{2+} signals in the mitochondrial matrix are essential for the activity of several enzymes of Krebs cycle and for ATP synthase [44] (Fig.1.12).
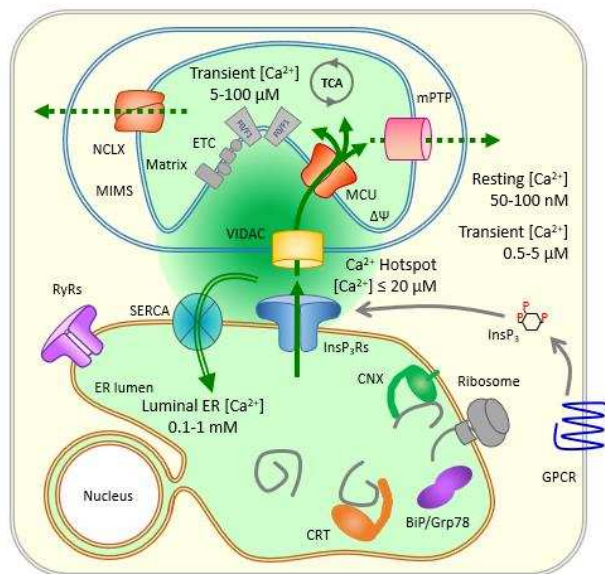
Figure 1.12 ER and mitochondrial Ca^{2+} signalling toolkit. Principal mechanisms regulating ER and mitochondria calcium dynamics are represented[6].

Intriguingly, during last decades, not only the single organelle, but the interaction between ER and mitochondria has emerged as the key regulator of cellular pathophysiology [68]. Indeed, already in the'50s interactions between organelles have been described in electron microscopy studies, but these

structures were considered as technical artefacts [69]. About 40 years required to demonstrate that ER-mitochondria contact sites represent an essential structure implicated in cellular physiological processes. In the 90's the presence of specific proteins responsible for the organization and stabilization of this structure have been demonstrated, indeed proteases treatment is required to physically separates ER fraction from mitochondria [70]. Nowadays, in literature, different proteins have been demonstrated to have a structural role in the composition of ER-mitochondria contact sites, keeping the distance between the ER membrane and the outer mitochondrial membrane such to allow efficient protein synthesis, transfer of proteins and lipids, and transfer of Ca^{2+} ions from ER to mitochondria [6]. At the interface between mitochondria and the ER, it is possible to find many different proteins that function as "tethers" between the two organelles [71] (Fig.1.13). One of the main tethering systems relies on the crosstalk between the OMM protein tyrosine phosphatase-interacting protein-51 (PTPIP51) and the vesicle-associated membrane protein B (VAPB), an ER-resident protein; PTPIP51/VAPB interaction was found to shape MERCS and to participate in autophagy regulation [72]. B cell receptor-associated protein 31 (Bap31) is an ER molecular chaperone able to interact with mitochondrial fission protein 1 (Fis1) on the OMM, building a platform involved in the response to apoptotic stimuli [73]. Other fundamental tethering mechanisms are based on mitofusin-mitofusin and IP3R-VDAC-Grp75 interactions and will be furtherly discussed below. Interestingly, apart from tethering systems, a whole set of additional proteins can be found at MERCs, embodying a plethora of different functions. Some of them interact with the aforementioned platforms (e.g., DJ-1 and TOM70 with IP3R-VDAC-Grp75 complex), increasing their stability and promoting their functionality [74] [75]. As membrane contact sites are critical compartments for lipid biogenesis and

transfer, many essential components of the related machineries are localized at MERCs, like phosphatidylserine (PS) synthases (PSS1 and PSS2), PS decarboxylases (PSD1 and PSD2), acetyl-coA cholesterol acyltransferase (ACAT1) or AAA domain-containing protein 3 (ATAD3) [71]. Moreover, MERCs house proteins involved in apoptosis (Bax, Bak, Bcl-2, Bcl-XL) and in autophagy (Pink1, Parkin, Atg5).
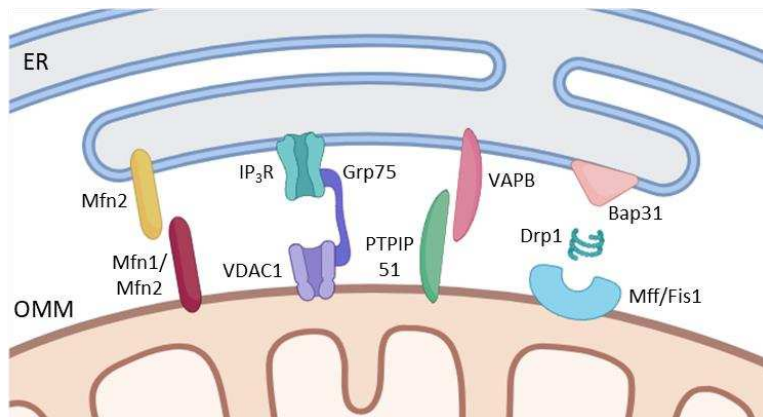
Figure 1.13 Schematic representation of some of the main tethering proteins/complexes present at the level of ER-mitochondria interface. a) Mfn1 and Mfn2 are able to interact together to drive mitochondrial fusion, but Mfn2 also behaves as a tether between the ER and the mitochondrion. b) Thanks to Grp75, IP3R on the ER couples with VDAC on the OMM to form a complex also involved in Ca2+ transfer. c) VAPB/PTPIP51 interaction guides autophagic processes. d) Bap31 is able to interact with Fis1, that in turn partners with Drp1 to initiate mitochondrial fission events.

- Mitofusins: Mitofusins are dynamin-related GTPases located on the OMM, and they are deeply involved in mechanisms of mitochondrial dynamics, in particular in the process of fusion. Mitofusin 1 (Mfn1) and mitofusin 2 (Mfn2) share high degree of similarity and both mediate mitochondrial fusion [76], but Mfn2 was also related to additional functions: de Brito and Scorrano showed, indeed, that not only Mfn2 is enriched at ER-mitochondria contact sites, but also that it tethers the two organelles by forming homotypic or heterotypic

interactions [77]. The role of Mfn2 in linking ER and mitochondria may be further investigated to uncover possible implications of this protein in the maintenance of the distance between these two organelles and, consequently, also in the calcium transfer occurring at this level [78].

- Dynamin-related protein 1 (Drp1): opposite to fusion, the other important process in mitochondrial dynamics is fission, which is mainly mediated by Drp1, a cytosolic GTPase that, upon recruitment on the OMM and oligomerization, drives constriction of the membrane, therefore marking the site of a future fission event [13]. Its recruitment on the membrane is orchestrated by dedicated receptors like Fis1 or mitochondrial fission factor (Mff), which are already present at the ER-mitochondria interface before the initiation of the fission event [71].

- Voltage-dependent anion channel (VDAC): this channel is the most abundant protein in the OMM, and it presents as a porin known to regulate the permeability of this portion of the mitochondrial membrane to ions and small (<5 kDa) metabolites [79]. VDAC is a transmembrane protein, structurally defined as a barrel-like pore resulting from the alignment of 19 β-sheets, oriented in an antiparallel fashion. VDAC is present in three different isoforms, with variable expression in different tissues; depending on the tissue and species of belonging, VDACs consist in 280-300 amino acids, and their molecular weight ranges between 30–35 kDa [80]. VDAC1 isoform is able to assemble into a supercomplex with IP3R and the molecular chaperone Grp75, leading to the formation of a sort of "tunnel" that allows the transfer of Ca2+ [81].

- Inositol-1,4,5-trisphosphate (IP3) receptor (IP3R): the IP3R family is the most ubiquitous among intracellular $Ca2+$ channels in non-striated muscle cells; it consists of 3 isoforms of ligand-gated channels sharing ~70% sequence homology, but with different tissue specificity and different sensitivity to IP3. Each receptor is made of three subdomains, slightly different among the three isoforms: the ligand-binding domain, located at the N-terminal region; the gatekeeper domain, responsible for the channel activity and formed by six transmembrane helices, located at the C-terminal region; a central cytosolic domain with regulatory activities, harbouring the binding sites for several interactors and regulators [82].

- 75-kDa Glucose-related protein (Grp75): Grp75 is a stress-induced molecular chaperone, belonging to the heat shock protein 70 family, involved in mitochondrial quality-control systems. Above its canonical function, it is also a member of the IP3R-VDAC-Grp75 supercomplex, the one responsible for the accommodation of the flux of $Ca2+$ from the ER to the mitochondria [83].

Ca^{2+} concentration in the mitochondrial matrix resembles the cytosolic one in resting conditions; despite this, mitochondria can uptake high amounts of calcium, up to the micromolar range [84]. Indeed, in the early '90s Rizzuto and colleagues demonstrated that mitochondria may accumulate Ca^{2+} as a consequence of cell stimulation and cytosolic $[Ca^{2+}]$ oscillations: they observed that when the ER and mitochondria are sufficiently close to each other, IP3-based intracellular stimuli produce local domains of high $[Ca^{2+}]$ at their interface [85] [86] (Fig.1.12). This huge amount of calcium can be uptaken reach the mitochondrial matrix through the mitochondrial calcium uniporter (MCU) complex. The MCU complex consists of a tetramer of pore-forming

MCU subunits; even though this complex contains several regulator proteins, just two of them, in addition to MCU subunits, are considered as part of the core of the complex: essential MCU regulator (EMRE) and mitochondrial calcium uptake 1/2 (MICU1/2) [87]. The MCU-EMRE-MICU core complex is sensitive to Ca^{2+} concentration in the intermembrane space and forms a channel that allows the flux of Ca^{2+} from this compartment to the mitochondrial matrix; this flux is driven by electrochemical potential gradient for Ca^{2+}, which results primarily from the mitochondrial membrane potential ($\Delta\Psi m$) and from low Ca^{2+} levels in the matrix at rest [88]. In this compartment, calcium signalling is finally coupled to mitochondrial metabolism and energy production. Actually, in physiological conditions the MCU complex has a low affinity for Ca^{2+}, with a Kd of 10–20 µM that shouldn't allow the passage of this ion through the channel; however, the controversial activity of the MCU has finally gained an explanation after the discovery of calcium microdomains at ER-mitochondria interface that can reach a sufficiently high (up to 40 µM) Ca2+ concentration to activate the MCU [86] [89]. Indeed, it has been postulated that for efficient transfer of Ca^{2+} ions between ER and mitochondria, and to guarantee the formation of high Ca^{2+} hotspot, able to overtake MCU activation threshold, a distance of ≈10-25 nm is required to allow formation of a protein complex composed of inositol-1,4,5-trisphosphate receptor (InsP3R), adaptor protein Grp75 and VDAC (voltage-dependent anion channel) [6] (Fig.1.14). Therefore, in healthy cells, the ER-mitochondria tethering ensures the propagation of IP3-linked Ca^{2+} signals to mitochondria, in other to coordinate ATP production with the stimulated state of the cell and to enable the mitochondrial Ca^{2+} buffering [44]. Indeed shorter (<10 nm) or wider (>25 nm) distance might drastically decrease the efficiency of Ca^{2+} transfer and may lead

to (i) ER Ca^{2+} overload and protein synthesis/degradation alterations and (ii) deficiency of mitochondrial Ca^{2+} signals resulting in bioenergetic deficit [67].
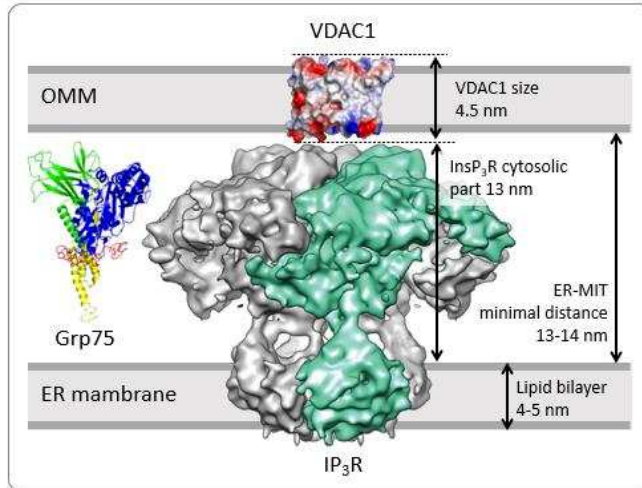
Figure 1.12 Organization of InsP$_3$R-Grp75-VDAC Ca^{2+} transferring unit: InsP$_3$R is a tetrameric complex that presents a Cytosolic domain leaning out of the ER membrane for ~ 13 nm, while Voltage-dependent anion channel 1 (VDAC1) is almost completely inserted in OMM. Molecules are represented in scale [67]

In this contest, in a recent publication, in an astroglial model of Alzheimer's disease (3xTg iAstro), we identified an increase in both ER and cytosolic [Ca2+], and a reduction of mitochondria Ca^{2+} uptake, indicating a defect in Ca^{2+} transfer from the ER to the mitochondria. These alterations in Ca^{2+} handling correlate with reduced protein synthesis, at the ER side, and reduced ATP production by mitochondria. The defect of Ca^{2+} transfer might be explained by the decreased distance at MIT and ER interface, that we identified in 3xTg iAstro, using the split-GFP contact site sensor (SPLICS) detecting a distance of about 8-10nm [36] [90].

Surprisingly, comparing our hypothesis with literature we found different works, in which the authors forced the shortening of the ER-mitochondria gap size by overexpressing an artificial linker, that fix the ER and OMM at a distance of ~ 6nm. Garrido-Maraver and colleagues show that overexpression of the ER-OMM linker in a Drosophila AD model mitigated β-amyloid toxicity and extended fly's lifespan [65]. Using the same animal model for studying Parkinson's disease, Basso and co-authors, demonstrated that the expression of the linker rescued motor deficit of flies [91]. In contrast, as presented in a very recent publication, the use of the same linker in MCR5 cells induces cell senescence. Also considering presenilins 1 and 2 (PS1 and 2) mutations, that are involved with Alzheimer's disease and that are localized at the ER mitochondria interface, I find a contradicting scenario both in the description of the role of PS1 and 2 in the ER and mitochondria Ca^{2+} handling. In this context appears crucial to clearly define the space between ER and mitochondria to allocate functional calcium transfer complexes and consequentially guarantee efficient mitochondrial calcium uptake.

BIBBLIOGRAPY

(1) Lim, D.; Semyanov, A.; Genazzani, A.; Verkhratsky, A. Calcium Signaling in Neuroglia. *Int. Rev. Cell Mol. Biol.* **2021**, *362*, 1–53. https://doi.org/10.1016/bs.ircmb.2021.01.003.

(2) Lim, D.; Ronco, V.; Grolla, A. A.; Verkhratsky, A.; Genazzani, A. A. Glial Calcium Signalling in Alzheimer's Disease. *Rev. Physiol. Biochem. Pharmacol.* **2014**, *167*, 45–65. https://doi.org/10.1007/112_2014_19.

(3) Glitsch, M. D.; Bakowski, D.; Parekh, A. B. Store-Operated Ca2+ Entry Depends on Mitochondrial Ca2+ Uptake. *EMBO J.* **2002**, *21* (24), 6744–6754. https://doi.org/10.1093/emboj/cdf675.

(4) Feno, S.; Rizzuto, R.; Raffaello, A.; Vecellio Reane, D. The Molecular Complexity of the Mitochondrial Calcium Uniporter. *Cell Calcium* **2021**, *93*, 102322. https://doi.org/10.1016/j.ceca.2020.102322.

(5) Di Marco, G.; Vallese, F.; Jourde, B.; Bergsdorf, C.; Sturlese, M.; De Mario, A.; Techer-Etienne, V.; Haasen, D.; Oberhauser, B.; Schleeger, S.; Minetti, G.; Moro, S.; Rizzuto, R.; De Stefani, D.; Fornaro, M.; Mammucari, C. A High-Throughput Screening Identifies MICU1 Targeting Compounds. *Cell Rep.* **2020**, *30* (7), 2321-2331.e6. https://doi.org/10.1016/j.celrep.2020.01.081.

(6) Lim, D.; Dematteis, G.; Tapella, L.; Genazzani, A. A.; Calì, T.; Brini, M.; Verkhratsky, A. Ca2+ Handling at the Mitochondria-ER Contact Sites in Neurodegeneration. *Cell Calcium* **2021**, *98*, 102453. https://doi.org/10.1016/j.ceca.2021.102453.

(7) Serrat, R.; Covelo, A.; Kouskoff, V.; Delcasso, S.; Ruiz-Calvo, A.; Chenouard, N.; Stella, C.; Blancard, C.; Salin, B.; Julio-Kalajzić, F.; Cannich, A.; Massa, F.; Varilh, M.; Deforges, S.; Robin, L. M.; De Stefani, D.; Busquets-Garcia, A.; Gambino, F.; Beyeler, A.; Pouvreau, S.; Marsicano, G. Astroglial ER-Mitochondria Calcium Transfer Mediates Endocannabinoid-Dependent Synaptic Integration. *Cell Rep.* **2021**, *37* (12), 110133. https://doi.org/10.1016/j.celrep.2021.110133.

(8) Rasola, A.; Bernardi, P. Mitochondrial Permeability Transition in Ca(2+)-Dependent Apoptosis and Necrosis. *Cell Calcium* **2011**, *50* (3), 222–233. https://doi.org/10.1016/j.ceca.2011.04.007.

(9) Ichas, F.; Mazat, J. P. From Calcium Signaling to Cell Death: Two Conformations for the Mitochondrial Permeability Transition Pore. Switching from Low- to High-Conductance State. *Biochim. Biophys. Acta* **1998**, *1366* (1–2), 33–50. https://doi.org/10.1016/s0005-2728(98)00119-4.

(10) Sambri, I.; Massa, F.; Gullo, F.; Meneghini, S.; Cassina, L.; Carraro, M.; Dina, G.; Quattrini, A.; Patanella, L.; Carissimo, A.; Iuliano, A.; Santorelli, F.; Codazzi, F.; Grohovaz, F.; Bernardi, P.; Becchetti, A.; Casari, G. Impaired Flickering of the Permeability Transition Pore Causes SPG7 Spastic Paraplegia. *EBioMedicine* **2020**, *61*, 103050. https://doi.org/10.1016/j.ebiom.2020.103050.

(11) Haworth, R. A.; Hunter, D. R. The Ca2+-Induced Membrane Transition in Mitochondria. II. Nature of the Ca2+ Trigger Site. *Arch. Biochem. Biophys.* **1979**, *195* (2), 460–467. https://doi.org/10.1016/0003-9861(79)90372-2.

(12) Baumgartner, H. K.; Gerasimenko, J. V.; Thorne, C.; Ferdek, P.; Pozzan, T.; Tepikin, A. V.; Petersen, O. H.; Sutton, R.; Watson, A. J. M.; Gerasimenko, O. V. Calcium Elevation in Mitochondria Is the Main Ca2+ Requirement for Mitochondrial Permeability Transition Pore (mPTP) Opening. *J. Biol. Chem.* **2009**, *284* (31), 20796–20803. https://doi.org/10.1074/jbc.M109.025353.

(13) Lange, S. C.; Bak, L. K.; Waagepetersen, H. S.; Schousboe, A.; Norenberg, M. D. Primary Cultures of Astrocytes: Their Value in Understanding Astrocytes in Health and Disease. *Neurochem. Res.* **2012**, *37* (11), 2569–2588. https://doi.org/10.1007/s11064-012-0868-0.

(14) Parpura, V.; Heneka, M. T.; Montana, V.; Oliet, S. H. R.; Schousboe, A.; Haydon, P. G.; Stout, R. F.; Spray, D. C.; Reichenbach, A.; Pannicke, T.; Pekny, M.; Pekna, M.; Zorec, R.; Verkhratsky, A. Glial Cells in (Patho)Physiology. *J. Neurochem.* **2012**, *121* (1), 4–27. https://doi.org/10.1111/j.1471-4159.2012.07664.x.

(15) Pekny, M.; Pekna, M.; Messing, A.; Steinhäuser, C.; Lee, J.-M.; Parpura, V.; Hol, E. M.; Sofroniew, M. V.; Verkhratsky, A. Astrocytes: A Central Element in Neurological Diseases. *Acta Neuropathol. (Berl.)* **2016**, *131* (3), 323–345. https://doi.org/10.1007/s00401-015-1513-1.

(16) Schober, A. L.; Wicki-Stordeur, L. E.; Murai, K. K.; Swayne, L. A. Foundations and Implications of Astrocyte Heterogeneity during Brain Development and Disease. *Trends Neurosci.* **2022**, *45* (9), 692–703. https://doi.org/10.1016/j.tins.2022.06.009.

(17) Verkhratsky, A.; Nedergaard, M. Physiology of Astroglia. *Physiol. Rev.* **2018**, *98* (1), 239–389. https://doi.org/10.1152/physrev.00042.2016.

(18) Halassa, M. M.; Fellin, T.; Takano, H.; Dong, J.-H.; Haydon, P. G. Synaptic Islands Defined by the Territory of a Single Astrocyte. *J. Neurosci. Off. J. Soc. Neurosci.* **2007**, *27* (24), 6473–6477. https://doi.org/10.1523/JNEUROSCI.1419-07.2007.

(19) Bélanger, M.; Magistretti, P. J. The Role of Astroglia in Neuroprotection. *Dialogues Clin. Neurosci.* **2009**, *11* (3), 281–295. https://doi.org/10.31887/DCNS.2009.11.3/mbelanger.

(20) Verkhratsky, A.; Nedergaard, M. Astroglial Cradle in the Life of the Synapse. *Philos. Trans. R. Soc. Lond. B. Biol. Sci.* **2014**, *369* (1654), 20130595. https://doi.org/10.1098/rstb.2013.0595.

(21) Andrade-Talavera, Y.; Duque-Feria, P.; Paulsen, O.; Rodríguez-Moreno, A. Presynaptic Spike Timing-Dependent Long-Term Depression in the Mouse Hippocampus. *Cereb. Cortex N. Y. N 1991* **2016**, *26* (8), 3637–3654. https://doi.org/10.1093/cercor/bhw172.

(22) Rial, D.; Lemos, C.; Pinheiro, H.; Duarte, J. M.; Gonçalves, F. Q.; Real, J. I.; Prediger, R. D.; Gonçalves, N.; Gomes, C. A.; Canas, P. M.; Agostinho, P.; Cunha, R. A. Depression as a Glial-Based Synaptic Dysfunction. *Front. Cell. Neurosci.* **2015**, *9*, 521. https://doi.org/10.3389/fncel.2015.00521.

(23) Verkhratsky, A.; Zorec, R.; Rodriguez, J. J.; Parpura, V. PATHOBIOLOGY OF NEURODEGENERATION: THE ROLE FOR ASTROGLIA. *Opera Medica Physiol.* **2016**, *1*, 13–22.

(24) Allen, N. J.; Eroglu, C. Cell Biology of Astrocyte-Synapse Interactions. *Neuron* **2017**, *96* (3), 697–708. https://doi.org/10.1016/j.neuron.2017.09.056.

(25) Larsen, B. R.; Stoica, A.; MacAulay, N. Managing Brain Extracellular K(+) during Neuronal Activity: The Physiological Role of the Na(+)/K(+)-ATPase Subunit Isoforms. *Front. Physiol.* **2016**, *7*, 141. https://doi.org/10.3389/fphys.2016.00141.

(26) Ballanyi, K.; Grafe, P.; ten Bruggencate, G. Ion Activities and Potassium Uptake Mechanisms of Glial Cells in Guinea-Pig Olfactory Cortex Slices. *J. Physiol.* **1987**, *382*, 159–174. https://doi.org/10.1113/jphysiol.1987.sp016361.

(27) Robinson, M. B.; Jackson, J. G. Astroglial Glutamate Transporters Coordinate Excitatory Signaling and Brain Energetics. *Neurochem. Int.* **2016**, *98*, 56–71. https://doi.org/10.1016/j.neuint.2016.03.014.

(28) Gegelashvili, G.; Schousboe, A. Cellular Distribution and Kinetic Properties of High-Affinity Glutamate Transporters. *Brain Res. Bull.* **1998**, *45* (3), 233–238. https://doi.org/10.1016/s0361-9230(97)00417-6.

(29) Danbolt, N. C. Glutamate Uptake. *Prog. Neurobiol.* **2001**, *65* (1), 1–105. https://doi.org/10.1016/s0301-0082(00)00067-8.

(30) Durkee, C. A.; Araque, A. DIVERSITY AND SPECIFICITY OF ASTROCYTE-NEURON COMMUNICATION. *Neuroscience* **2019**, *396*, 73–78. https://doi.org/10.1016/j.neuroscience.2018.11.010.

(31) Schwarz, Y.; Zhao, N.; Kirchhoff, F.; Bruns, D. Astrocytes Control Synaptic Strength by Two Distinct V-SNARE-Dependent Release Pathways. *Nat. Neurosci.* **2017**, *20* (11), 1529–1539. https://doi.org/10.1038/nn.4647.

(32) Andersson, M.; Blomstrand, F.; Hanse, E. Astrocytes Play a Critical Role in Transient Heterosynaptic Depression in the Rat Hippocampal CA1 Region. *J. Physiol.* **2007**, *585* (Pt 3), 843–852. https://doi.org/10.1113/jphysiol.2007.142737.

(33) Martín, R.; Bajo-Grañeras, R.; Moratalla, R.; Perea, G.; Araque, A. Circuit-Specific Signaling in Astrocyte-Neuron Networks in Basal Ganglia Pathways. *Science* **2015**, *349* (6249), 730–734. https://doi.org/10.1126/science.aaa7945.

(34) Jimenez-Blasco, D.; Busquets-Garcia, A.; Hebert-Chatelain, E.; Serrat, R.; Vicente-Gutierrez, C.; Ioannidou, C.; Gómez-Sotres, P.; Lopez-Fabuel, I.; Resch-Beusher, M.; Resel, E.; Arnouil, D.; Saraswat, D.; Varilh, M.; Cannich, A.; Julio-Kalajzic, F.; Bonilla-Del Río, I.; Almeida, A.; Puente, N.; Achicallende, S.; Lopez-Rodriguez, M.-L.; Jollé, C.; Déglon, N.; Pellerin, L.; Josephine, C.; Bonvento, G.; Panatier, A.; Lutz, B.; Piazza, P.-V.; Guzmán, M.; Bellocchio, L.; Bouzier-Sore, A.-K.;

Grandes, P.; Bolaños, J. P.; Marsicano, G. Glucose Metabolism Links Astroglial Mitochondria to Cannabinoid Effects. *Nature* **2020**, *583* (7817), 603–608. https://doi.org/10.1038/s41586-020-2470-y.

(35) Parpura, V.; Fisher, E. S.; Lechleiter, J. D.; Schousboe, A.; Waagepetersen, H. S.; Brunet, S.; Baltan, S.; Verkhratsky, A. Glutamate and ATP at the Interface Between Signaling and Metabolism in Astroglia: Examples from Pathology. *Neurochem. Res.* **2017**, *42* (1), 19–34. https://doi.org/10.1007/s11064-016-1848-6.

(36) Dematteis, G.; Vydmantaitė, G.; Ruffinatti, F. A.; Chahin, M.; Farruggio, S.; Barberis, E.; Ferrari, E.; Marengo, E.; Distasi, C.; Morkūnienė, R.; Genazzani, A. A.; Grilli, M.; Grossini, E.; Corazzari, M.; Manfredi, M.; Lim, D.; Jekabsone, A.; Tapella, L. Proteomic Analysis Links Alterations of Bioenergetics, Mitochondria-ER Interactions and Proteostasis in Hippocampal Astrocytes from 3xTg-AD Mice. *Cell Death Dis.* **2020**, *11* (8), 645. https://doi.org/10.1038/s41419-020-02911-1.

(37) Eraso-Pichot, A.; Pouvreau, S.; Olivera-Pinto, A.; Gomez-Sotres, P.; Skupio, U.; Marsicano, G. Endocannabinoid Signaling in Astrocytes. *Glia* **2023**, *71* (1), 44–59. https://doi.org/10.1002/glia.24246.

(38) Rizzoli, S.; Sharma, G.; Vijayaraghavan, S. Calcium Rise in Cultured Neurons from Medial Septum Elicits Calcium Waves in Surrounding Glial Cells. *Brain Res.* **2002**, *957* (2), 287–297. https://doi.org/10.1016/s0006-8993(02)03618-1.

(39) Bojarskaite, L.; Bjørnstad, D. M.; Pettersen, K. H.; Cunen, C.; Hermansen, G. H.; Åbjørsbråten, K. S.; Chambers, A. R.; Sprengel, R.; Vervaeke, K.; Tang, W.; Enger, R.; Nagelhus, E. A. Astrocytic Ca2+ Signaling Is Reduced during Sleep and Is Involved in the Regulation of Slow Wave Sleep. *Nat. Commun.* **2020**, *11* (1), 3240. https://doi.org/10.1038/s41467-020-17062-2.

(40) Sonoda, K.; Matsui, T.; Bito, H.; Ohki, K. Astrocytes in the Mouse Visual Cortex Reliably Respond to Visual Stimulation. *Biochem. Biophys. Res. Commun.* **2018**, *505* (4), 1216–1222. https://doi.org/10.1016/j.bbrc.2018.10.027.

(41) Stobart, J. L.; Ferrari, K. D.; Barrett, M. J. P.; Stobart, M. J.; Looser, Z. J.; Saab, A. S.; Weber, B. Long-Term In Vivo Calcium Imaging of Astrocytes Reveals Distinct Cellular Compartment Responses to Sensory Stimulation. *Cereb. Cortex N. Y. N 1991* **2018**, *28* (1), 184–198. https://doi.org/10.1093/cercor/bhw366.

(42) Verkhratsky, A.; Kettenmann, H. Calcium Signalling in Glial Cells. *Trends Neurosci.* **1996**, *19* (8), 346–352. https://doi.org/10.1016/0166-2236(96)10048-5.

(43) Parnis, J.; Montana, V.; Delgado-Martinez, I.; Matyash, V.; Parpura, V.; Kettenmann, H.; Sekler, I.; Nolte, C. Mitochondrial Exchanger NCLX Plays a Major Role in the Intracellular Ca2+ Signaling, Gliotransmission, and Proliferation of Astrocytes. *J. Neurosci. Off. J. Soc. Neurosci.* **2013**, *33* (17), 7206–7219. https://doi.org/10.1523/JNEUROSCI.5721-12.2013.

(44) Rossi, A.; Pizzo, P.; Filadi, R. Calcium, Mitochondria and Cell Metabolism: A Functional Triangle in Bioenergetics. *Biochim. Biophys. Acta BBA - Mol. Cell Res.* **2019**, *1866* (7), 1068–1078. https://doi.org/10.1016/j.bbamcr.2018.10.016.

(45) Verkhratsky, A.; Nedergaard, M. Physiology of Astroglia. *Physiol. Rev.* **2018**, *98* (1), 239–389. https://doi.org/10.1152/physrev.00042.2016.

(46) Marina, N.; Christie, I. N.; Korsak, A.; Doronin, M.; Brazhe, A.; Hosford, P. S.; Wells, J. A.; Sheikhbahaei, S.; Humoud, I.; Paton, J. F. R.; Lythgoe, M. F.; Semyanov, A.; Kasparov, S.; Gourine, A. V. Astrocytes Monitor Cerebral Perfusion and Control Systemic Circulation to Maintain Brain Blood Flow. *Nat. Commun.* **2020**, *11* (1), 131. https://doi.org/10.1038/s41467-019-13956-y.

(47) Semyanov, A.; Henneberger, C.; Agarwal, A. Making Sense of Astrocytic Calcium Signals - from Acquisition to Interpretation. *Nat. Rev. Neurosci.* **2020**, *21* (10), 551–564. https://doi.org/10.1038/s41583-020-0361-8.

(48) García-Cáceres, C.; Balland, E.; Prevot, V.; Luquet, S.; Woods, S. C.; Koch, M.; Horvath, T. L.; Yi, C.-X.; Chowen, J. A.; Verkhratsky, A.; Araque, A.; Bechmann, I.; Tschöp, M. H. Role of Astrocytes, Microglia, and Tanycytes in Brain Control of Systemic Metabolism. *Nat. Neurosci.* **2019**, *22* (1), 7–14. https://doi.org/10.1038/s41593-018-0286-y.

(49) Santello, M.; Toni, N.; Volterra, A. Astrocyte Function from Information Processing to Cognition and Cognitive Impairment. *Nat. Neurosci.* **2019**, *22* (2), 154–166. https://doi.org/10.1038/s41593-018-0325-8.

(50) Zeng, H.; Chattarji, S.; Barbarosie, M.; Rondi-Reig, L.; Philpot, B. D.; Miyakawa, T.; Bear, M. F.; Tonegawa, S. Forebrain-Specific Calcineurin Knockout Selectively Impairs Bidirectional Synaptic Plasticity and Working/Episodic-like Memory. *Cell* **2001**, *107* (5), 617–629. https://doi.org/10.1016/s0092-8674(01)00585-2.

(51) Tapella, L.; Soda, T.; Mapelli, L.; Bortolotto, V.; Bondi, H.; Ruffinatti, F. A.; Dematteis, G.; Stevano, A.; Dionisi, M.; Ummarino, S.; Di Ruscio, A.; Distasi, C.; Grilli, M.; Genazzani, A. A.; D'Angelo, E.; Moccia, F.; Lim, D. Deletion of Calcineurin from GFAP-Expressing Astrocytes Impairs Excitability of Cerebellar and Hippocampal Neurons through

Astroglial Na+ /K+ ATPase. *Glia* **2020**, *68* (3), 543–560. https://doi.org/10.1002/glia.23737.

(52) Furman, J. L.; Norris, C. M. Calcineurin and Glial Signaling: Neuroinflammation and Beyond. *J. Neuroinflammation* **2014**, *11*, 158. https://doi.org/10.1186/s12974-014-0158-7.

(53) Abdul, H. M.; Furman, J. L.; Sama, M. A.; Mathis, D. M.; Norris, C. M. NFATs and Alzheimer's Disease. *Mol. Cell. Pharmacol.* **2010**, *2* (1), 7– 14.

(54) Klee, C. B.; Krinks, M. H. Purification of Cyclic 3',5'-Nucleotide Phosphodiesterase Inhibitory Protein by Affinity Chromatography on Activator Protein Coupled to Sepharose. *Biochemistry* **1978**, *17* (1), 120– 126. https://doi.org/10.1021/bi00594a017.

(55) Canellada, A.; Ramirez, B. G.; Minami, T.; Redondo, J. M.; Cano, E. Calcium/Calcineurin Signaling in Primary Cortical Astrocyte Cultures: Rcan1-4 and Cyclooxygenase-2 as NFAT Target Genes. *Glia* **2008**, *56* (7), 709–722. https://doi.org/10.1002/glia.20647.

(56) Aramburu, J.; Yaffe, M. B.; López-Rodríguez, C.; Cantley, L. C.; Hogan, P. G.; Rao, A. Affinity-Driven Peptide Selection of an NFAT Inhibitor More Selective than Cyclosporin A. *Science* **1999**, *285* (5436), 2129– 2133. https://doi.org/10.1126/science.285.5436.2129.

(57) Olabisi, O. A.; Soto-Nieves, N.; Nieves, E.; Yang, T. T. C.; Yang, X.; Yu, R. Y. L.; Suk, H. Y.; Macian, F.; Chow, C.-W. Regulation of Transcription Factor NFAT by ADP-Ribosylation. *Mol. Cell. Biol.* **2008**, *28* (9), 2860–2871. https://doi.org/10.1128/MCB.01746-07.

(58) Lim, D.; Rodríguez-Arellano, J. J.; Parpura, V.; Zorec, R.; Zeidán-Chuliá, F.; Genazzani, A. A.; Verkhratsky, A. Calcium Signalling Toolkits in Astrocytes and Spatio-Temporal Progression of Alzheimer's Disease. *Curr. Alzheimer Res.* **2016**, *13* (4), 359–369. https://doi.org/10.2174/1567205013666151116130104.

(59) Ben Haim, L.; Ceyzériat, K.; Carrillo-de Sauvage, M. A.; Aubry, F.; Auregan, G.; Guillermier, M.; Ruiz, M.; Petit, F.; Houitte, D.; Faivre, E.; Vandesquille, M.; Aron-Badin, R.; Dhenain, M.; Déglon, N.; Hantraye, P.; Brouillet, E.; Bonvento, G.; Escartin, C. The JAK/STAT3 Pathway Is a Common Inducer of Astrocyte Reactivity in Alzheimer's and Huntington's Diseases. *J. Neurosci. Off. J. Soc. Neurosci.* **2015**, *35* (6), 2817–2829. https://doi.org/10.1523/JNEUROSCI.3516-14.2015.

(60) Grolla, A. A.; Fakhfouri, G.; Balzaretti, G.; Marcello, E.; Gardoni, F.; Canonico, P. L.; DiLuca, M.; Genazzani, A. A.; Lim, D. Aβ Leads to Ca^{2+} Signaling Alterations and Transcriptional Changes in Glial Cells. *Neurobiol. Aging* **2013**, *34* (2), 511–522. https://doi.org/10.1016/j.neurobiolaging.2012.05.005.

(61) Lim, D.; Iyer, A.; Ronco, V.; Grolla, A. A.; Canonico, P. L.; Aronica, E.; Genazzani, A. A. Amyloid Beta Deregulates Astroglial mGluR5-Mediated Calcium Signaling via Calcineurin and Nf-kB. *Glia* **2013**, *61* (7), 1134–1145. https://doi.org/10.1002/glia.22502.

(62) Sompol, P.; Norris, C. M. Ca2+, Astrocyte Activation and Calcineurin/NFAT Signaling in Age-Related Neurodegenerative Diseases. *Front. Aging Neurosci.* **2018**, *10*, 199. https://doi.org/10.3389/fnagi.2018.00199.

(63) Lim, D.; Ronco, V.; Grolla, A. A.; Verkhratsky, A.; Genazzani, A. A. Glial Calcium Signalling in Alzheimer's Disease. *Rev. Physiol. Biochem. Pharmacol.* **2014**, *167*, 45–65. https://doi.org/10.1007/112_2014_19.

(64) Dematteis, G.; Restelli, E.; Chiesa, R.; Aronica, E.; Genazzani, A. A.; Lim, D.; Tapella, L. Calcineurin Controls Expression of EAAT1/GLAST in Mouse and Human Cultured Astrocytes through Dynamic Regulation of Protein Synthesis and Degradation. *Int. J. Mol. Sci.* **2020**, *21* (6). https://doi.org/10.3390/ijms21062213.

(65) Garrido-Maraver, J.; Loh, S. H. Y.; Martins, L. M. Forcing Contacts between Mitochondria and the Endoplasmic Reticulum Extends Lifespan in a *Drosophila* Model of Alzheimer's Disease. *Biol. Open* **2019**, bio.047530. https://doi.org/10.1242/bio.047530.

(66) Maack, C. Orphaned Mitochondria in Heart Failure. *Cardiovasc. Res.* **2016**, *109* (1), 6–8. https://doi.org/10.1093/cvr/cvv262.

(67) Lim, D.; Tapella, L.; Dematteis, G.; Genazzani, A. A.; Corazzari, M.; Verkhratsky, A. The Endoplasmic Reticulum Stress and Unfolded Protein Response in Alzheimer's Disease: A Calcium Dyshomeostasis Perspective. *Ageing Res. Rev.* **2023**, *87*, 101914. https://doi.org/10.1016/j.arr.2023.101914.

(68) Paillusson, S.; Stoica, R.; Gomez-Suaga, P.; Lau, D. H. W.; Mueller, S.; Miller, T.; Miller, C. C. J. There's Something Wrong with My MAM; the ER-Mitochondria Axis and Neurodegenerative Diseases. *Trends Neurosci.* **2016**, *39* (3), 146–157. https://doi.org/10.1016/j.tins.2016.01.008.

(69) Herrera-Cruz, M. S.; Simmen, T. Over Six Decades of Discovery and Characterization of the Architecture at Mitochondria-Associated Membranes (MAMs). *Adv. Exp. Med. Biol.* **2017**, *997*, 13–31. https://doi.org/10.1007/978-981-10-4567-7_2.

(70) Rizzuto, R.; Pinton, P.; Carrington, W.; Fay, F. S.; Fogarty, K. E.; Lifshitz, L. M.; Tuft, R. A.; Pozzan, T. Close Contacts with the Endoplasmic Reticulum as Determinants of Mitochondrial Ca2+ Responses. *Science* **1998**, *280* (5370), 1763–1766. https://doi.org/10.1126/science.280.5370.1763.

(71) Barazzuol, L.; Giamogante, F.; Calì, T. Mitochondria Associated Membranes (MAMs): Architecture and Physiopathological Role. *Cell Calcium* **2021**, *94*, 102343. https://doi.org/10.1016/j.ceca.2020.102343.

(72) Gomez-Suaga, P.; Paillusson, S.; Miller, C. C. J. ER-Mitochondria Signaling Regulates Autophagy. *Autophagy* **2017**, *13* (7), 1250–1251. https://doi.org/10.1080/15548627.2017.1317913.

(73) Giamogante, F.; Barazzuol, L.; Brini, M.; Calì, T. ER-Mitochondria Contact Sites Reporters: Strengths and Weaknesses of the Available Approaches. *Int. J. Mol. Sci.* **2020**, *21* (21), 8157. https://doi.org/10.3390/ijms21218157.

(74) Filadi, R.; Leal, N. S.; Schreiner, B.; Rossi, A.; Dentoni, G.; Pinho, C. M.; Wiehager, B.; Cieri, D.; Calì, T.; Pizzo, P.; Ankarcrona, M. TOM70 Sustains Cell Bioenergetics by Promoting IP3R3-Mediated ER to Mitochondria Ca2+ Transfer. *Curr. Biol. CB* **2018**, *28* (3), 369-382.e6. https://doi.org/10.1016/j.cub.2017.12.047.

(75) Liu, Y.; Ma, X.; Fujioka, H.; Liu, J.; Chen, S.; Zhu, X. DJ-1 Regulates the Integrity and Function of ER-Mitochondria Association through Interaction with IP3R3-Grp75-VDAC1. *Proc. Natl. Acad. Sci. U. S. A.* **2019**, *116* (50), 25322–25328. https://doi.org/10.1073/pnas.1906565116.

(76) Joaquim, M.; Escobar-Henriques, M. Role of Mitofusins and Mitophagy in Life or Death Decisions. *Front. Cell Dev. Biol.* **2020**, *8*, 572182. https://doi.org/10.3389/fcell.2020.572182.

(77) de Brito, O. M.; Scorrano, L. Mitofusin 2 Tethers Endoplasmic Reticulum to Mitochondria. *Nature* **2008**, *456* (7222), 605–610. https://doi.org/10.1038/nature07534.

(78) Dorn, G. W. Mitofusins as Mitochondrial Anchors and Tethers. *J. Mol. Cell. Cardiol.* **2020**, *142*, 146–153. https://doi.org/10.1016/j.yjmcc.2020.04.016.

(79) Rosencrans, W. M.; Rajendran, M.; Bezrukov, S. M.; Rostovtseva, T. K. VDAC Regulation of Mitochondrial Calcium Flux: From Channel Biophysics to Disease. *Cell Calcium* **2021**, *94*, 102356. https://doi.org/10.1016/j.ceca.2021.102356.

(80) Sander, P.; Gudermann, T.; Schredelseker, J. A Calcium Guard in the Outer Membrane: Is VDAC a Regulated Gatekeeper of Mitochondrial Calcium Uptake? *Int. J. Mol. Sci.* **2021**, *22* (2), 946. https://doi.org/10.3390/ijms22020946.

(81) Szabadkai, G.; Bianchi, K.; Várnai, P.; De Stefani, D.; Wieckowski, M. R.; Cavagna, D.; Nagy, A. I.; Balla, T.; Rizzuto, R. Chaperone-Mediated Coupling of Endoplasmic Reticulum and Mitochondrial Ca2+ Channels. *J. Cell Biol.* **2006**, *175* (6), 901–911. https://doi.org/10.1083/jcb.200608073.

(82) Ahumada-Castro, U.; Bustos, G.; Silva-Pavez, E.; Puebla-Huerta, A.; Lovy, A.; Cárdenas, C. In the Right Place at the Right Time: Regulation of Cell Metabolism by IP3R-Mediated Inter-Organelle Ca2+ Fluxes. *Front. Cell Dev. Biol.* **2021**, *9*, 629522. https://doi.org/10.3389/fcell.2021.629522.

(83) Han, S.; Zhao, F.; Hsia, J.; Ma, X.; Liu, Y.; Torres, S.; Fujioka, H.; Zhu, X. The Role of Mfn2 in the Structure and Function of Endoplasmic Reticulum-Mitochondrial Tethering in Vivo. *J. Cell Sci.* **2021**, *134* (13), jcs253443. https://doi.org/10.1242/jcs.253443.

(84) Bootman, M. D.; Bultynck, G. Fundamentals of Cellular Calcium Signaling: A Primer. *Cold Spring Harb. Perspect. Biol.* **2020**, *12* (1), a038802. https://doi.org/10.1101/cshperspect.a038802.

(85) Rizzuto, R.; Simpson, A. W.; Brini, M.; Pozzan, T. Rapid Changes of Mitochondrial Ca2+ Revealed by Specifically Targeted Recombinant Aequorin. *Nature* **1992**, *358* (6384), 325–327. https://doi.org/10.1038/358325a0.

(86) Rizzuto, R.; Brini, M.; Murgia, M.; Pozzan, T. Microdomains with High Ca2+ Close to IP3-Sensitive Channels That Are Sensed by Neighboring Mitochondria. *Science* **1993**, *262* (5134), 744–747. https://doi.org/10.1126/science.8235595.

(87) Alevriadou, B. R.; Patel, A.; Noble, M.; Ghosh, S.; Gohil, V. M.; Stathopulos, P. B.; Madesh, M. Molecular Nature and Physiological Role of the Mitochondrial Calcium Uniporter Channel. *Am. J. Physiol. Cell Physiol.* **2021**, *320* (4), C465–C482. https://doi.org/10.1152/ajpcell.00502.2020.

(88) Duchen, M. R. Mitochondria and Ca(2+)in Cell Physiology and Pathophysiology. *Cell Calcium* **2000**, *28* (5–6), 339–348. https://doi.org/10.1054/ceca.2000.0170.

(89) Hajnóczky, G.; Csordás, G.; Krishnamurthy, R.; Szalai, G. Mitochondrial Calcium Signaling Driven by the IP3 Receptor. *J. Bioenerg. Biomembr.* **2000**, *32* (1), 15–25. https://doi.org/10.1023/a:1005504210587.

(90) Cieri, D.; Vicario, M.; Giacomello, M.; Vallese, F.; Filadi, R.; Wagner, T.; Pozzan, T.; Pizzo, P.; Scorrano, L.; Brini, M.; Calì, T. SPLICS: A Split Green Fluorescent Protein-Based Contact Site Sensor for Narrow and Wide Heterotypic Organelle Juxtaposition *Cell Death Differ.* **2018**, *25* (6), 1131–1145. https://doi.org/10.1038/s41418-017-0033-z.

(91) Basso, V.; Marchesan, E.; Peggion, C.; Chakraborty, J.; von Stockum, S.; Giacomello, M.; Ottolini, D.; Debattisti, V.; Caicci, F.; Tasca, E.; Pegoraro, V.; Angelini, C.; Antonini, A.; Bertoli, A.; Brini, M.; Ziviani, E. Regulation of ER-Mitochondria Contacts by Parkin via Mfn2.
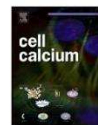
Pharmacol. Res. **2018**, *138*, 43–56. https://doi.org/10.1016/j.phrs.2018.09.006.

Chapter 2

ELSEVIER

Deletion of calcineurin from astrocytes reproduces proteome signature of Alzheimer's disease and epilepsy and predisposes to seizures

Laura Tapella [a,1], Giulia Dematteis [a,1], Federico Alessandro Ruffinatti [a,3], Luisa Ponzoni [b], Fabio Fiordaliso [c], Alessandro Corbelli [c], Enrico Albanese [a], Beatrice Pistolato [a], Jessica Pagano [d], Elettra Barberis [e,f], Emilio Marengo [e], Claudia Balducci [g], Gianluigi Forloni [g], Chiara Verpelli [d], Carlo Sala [d], Carla Distasi [a], Mariaelvina Sala [d], Marcello Manfredi [f,h,2], Armando A. Genazzani [a,2,*], Dmitry Lim [a,2,*]

[a] Department of Pharmaceutical Sciences, Università del Piemonte Orientale "Amedeo Avogadro", Via Bovio 6, 28100, Novara, Italy
[b] BIOMETRA, University of Milan and Fondazione Zardi-Gori, Milan, Italy
[c] Department of Molecular Biochemistry and Pharmacology, Istituto di Ricerche Farmacologiche Mario Negri IRCCS, Milan, Italy
[d] CNR Neuroscience Institute, Milan, Italy
[e] Department of Sciences and Technological Innovation, Università del Piemonte Orientale, Alessandria, Italy
[f] Department of Translational Medicine, University of Piemonte Orientale, Novara, Italy
[g] Department of Neuroscience, Istituto di Ricerche Farmacologiche Mario Negri IRCCS, Milan, Italy
[h] Center for Translational Research on Autoimmune and Allergic Diseases, University of Piemonte Orientale, Novara, Italy

ARTICLE INFO

ABSTRACT

Calcineurin (CaN), acting downstream of intracellular calcium signals, orchestrates cellular remodeling in many cellular types. In astrocytes, major homeostatic players in the central nervous system (CNS), CaN is involved in neuroinflammation and gliosis, while its role in healthy CNS or in early neuro-pathogenesis is poorly understood. Here we report that in mice with conditional deletion of CaN in GFAP-expressing astrocytes (astroglial calcineurin KO, ACN-KO), at 1 month of age, transcription was largely unchanged, while the proteome was deranged in the hippocampus and cerebellum. Gene ontology analysis revealed overrepresentation of annotations related to myelin sheath, mitochondria, ribosome and cytoskeleton. Over-represented pathways were related to protein synthesis, oxidative phosphorylation, mTOR and neurological disorders, including Alzheimer's disease (AD) and seizure disorder. Comparison with published proteomic datasets showed significant overlap with the proteome of a familial AD mouse model and of human subjects with drug-resistant seizures. ACN-KO mice showed no alterations of motor activity, equilibrium, anxiety or depressive state. However, in Barnes maze ACN-KO mice learned the task but adopted serial search strategy. Strikingly, beginning from about 5 months of age ACN-KO mice developed spontaneous tonic-clonic seizures with an inflammatory signature of epileptic brains. Altogether, our data suggest that the deletion of astroglial CaN produces features of neurological disorders and predisposes mice to seizures. We suggest that calcineurin in astrocytes may serve as a novel Ca^{2+}-sensitive switch which regulates protein expression and homeostasis in the central nervous system.

1. Introduction

Homeostatic support, provided by astrocytes, is of paramount importance for proper brain functioning [1]. During continuous interaction with neurons in the central nervous system (CNS), astrocytes generate intracellular calcium (Ca^{2+}) signals which are thought to mediate their homeostatic activities, including release of signalling molecules, control of cerebral blood flow, regulation of K^+ and

neurotransmitter uptake and control of neuronal activity [2,3]. Moreover, deregulation of astrocytic Ca^{2+} signals and downstream signalling processes are strongly associated with neuropathologies including Alzheimer's disease and epilepsy [4, 5, 6]. Much effort has been devoted to detection and characterization of astroglial Ca^{2+} signals themselves [7, 8], while how the Ca^{2+} signals in astrocytes are decoded, processed and translated to arrange a multitude of astroglial homeostatic activities is poorly understood [3].

Recently, we have generated a mouse with conditional KO of calcineurin (CaN), a Ca^{2+}/calmodulin-activated serine-threonine phosphatase (astroglial calcineurin KO, or ACN-KO) and showed that the deletion of astrocytic CaN (Astro-CaN) severely impairs intrinsic neuronal excitability in hippocampal pyramidal neurons and cerebellar granule cells through functional inactivation of astroglial Na^+/K^+ ATPase and deregulation of Na^+ and K^+ handling [9]. CaN drives Ca^{2+}-dependent cellular transcriptional and functional remodelling in different cellular types including lymphocytes [10], cardiomyocytes [11], skeletal muscle [12], bone cells [13] and neurons [14]. However, it is not known whether in healthy astrocytes CaN exerts similar activity.

In the present report we used a multiomics approach to comprehensively investigate alterations produced by the deletion of Astro-CaN at the transcriptional and proteome level. We report that the deletion of CaN from astrocytes, at one month of age, results in derangement of protein expression at the posttranscriptional level re-creating a similar protein profile to that associated with neurological and neurodegenerative diseases, in particular with AD and seizures. Later in life, beginning from about 5 months of age, ACN-KO mice display an increased risk to develop spontaneous tonic-clonic motor seizures. Collectively, our results suggest that Astro-CaN may serve as a Ca^{2+}-sensitive molecular hub which regulates protein expression and homeostasis in the CNS.

2. Results

2.1. Deletion of Astro-CaN deranges protein expression at posttranscriptional level

To investigate the effect of the deletion of CaN from astrocytes on gene and protein expression in the CNS, we performed Next Generation RNA sequencing (RNA-Seq) and shotgun mass spectrometry proteomics (SG-MS) analyses of the hippocampus and cerebellum (the brain areas in which all astrocytes are GFAP-positive and hence achieved full CaN KO) of one month-old ACN-KO and ACN-Ctr mice. RNA-Seq revealed only two genes that showed a fold change over 2 in whole tissue hippocampal and cerebellar preparations from ACN-KO compared with ACN-Ctr mice (Suppl. Fig. 1). This were Rab31 and Vapa in the hippocampus (-2.11 and -2.04 fold change, respectively) and Dsp and Rab31 in cerebellum (-2.62 and -2.14 fold change, respectively). In brief, therefore, the transcriptional profile was largely unchanged. SG-MS proteomics (Fig. 1A) identified 1661 and 1456 proteins in whole-tissue hippocampal (Wht-Hip) and cerebellar (Wht-Cb) preparations, respectively. In hippocampal (Syn-Hip) and cerebellar (Syn-Cb) synaptosomal fractions 525 and 471 proteins, respectively, were identified (Suppl. Table 1). Quantification and identification of differentially expressed proteins (DEPs) (FC > 50%, p-value < 0.05) yielded 21, 17, 134 and 40 DEPs in Wht-Hip, Wht-Cb, Syn-Hip and Syn-Cb samples, respectively (Fig. 1B and Suppl. Table 2). Surprisingly, there was very little, if any, overlap of DEPs between samples suggesting that the changes in protein expression produced by the deletion of Astro-CaN are brain region-specific. However, in of 40 DEPs in Syn-Cb, 12 proteins (30%) were common with Syn-Hip samples. Of these 12, only one protein is astrocyte-specific, GLAST (EAAT1, Slc1a3), which we have previously shown to be under
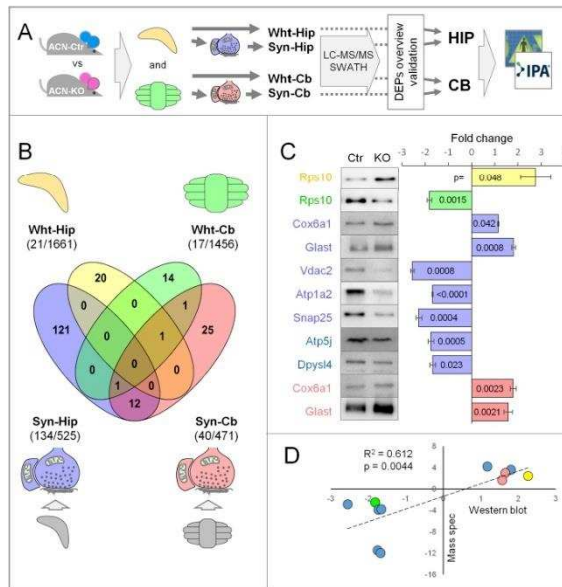
Fig. 1. Astrocyte-specific CaN knockout at 1 mo of age deranges protein expression differentially in the hippocampus and the cerebellum. (A) A scheme of the workflow: whole-tissue hippocampus (Wht-Hip) and cerebellum (Wht-Cb) and their respective synaptosomal fractions (Syn-Hip and Syn-Cb), prepared from ACN-Ctr and ACN-KO mice, were subjected to shotgun mass spectrometry (SG-MS) proteomics (LC-MS/MS – SWATH, 4- 6 mice per condition). RNA-Seq did not result in a significant transcriptional activity. SG-MS resulted in 21, 17, 134 and 40 differentially expressed proteins (DEPs) in Wht-Hip, Wht-Cb, Syn-Hip and Syn-Cb, respectively. For bioinformatic analysis, hippocampal and cerebellar preparations were pooled resulting in HIP (155 DEPs) and CB (54 DEPs). (B) Intersection of DEPs lists show very limited overlap between samples indicating on brain region-specific alterations produced by Astro-CaN-KO. (C) Validation of DEPs by Western blot (details of statistical analysis are reported in Suppl. Table 9); and (D) correlation of Western blot results with SG-MS (R^2 = 0.612, p = 0.0044). Colour codes: cyan, ACN-Ctr mice; magenta, ACN-KO mice; light-yellow, Wht-Hip, light-green, Wht-Cb; light-blue, Syn-Hip; light-red, Syn-Cb.

Table 1
Top 10 overrepresented IPA annotations.

HIPPOCAMPUS Canonical Pathways	p-value	# Hits	CEREBELLUM Canonical Pathways	p-value	# Hits
Synaptogenesis Signaling Pathway	3.16E-15	21	EIF2 Signaling	9.77E-07	7
Phagosome Maturation	6.31E-15	16	Glucocorticoid Receptor Signaling	1.41E-04	6
Sirtuin Signaling Pathway	1.26E-12	18	Regulation of eIF4 and p70S6K Signaling	5.25E-04	4
Mitochondrial Dysfunction	1.26E-14	14	Sirtuin Signaling Pathway	6.31E-04	5
Remodeling of Epithelial Adherens Junctions	3.16E-11	10	Mitochondrial Dysfunction	7.24E-04	4
14-3-3-mediated Signaling	6.31E-11	12	Breast Cancer Regulation by Stathmin1	1.29E-03	4
Oxidative Phosphorylation	2.09E-10	11	mTOR Signaling	1.55E-03	4
Huntington's Disease Signaling	8.71E-10	14	Oxidative Phosphorylation	2.24E-03	3
Epithelial Adherens Junction Signaling	7.41E-09	11	Acetyl-CoA Biosynthesis III (from Citrate)	2.40E-03	1
Glycolysis I	1.82E-08	6	CCR3 Signaling in Eosinophils	3.24E-03	3
Upstream Regulator	**p-value**	**# Hits**	**Upstream Regulator**	**p-value**	**# Hits**
MAPT	1.97E-65	60	MAPT	1.89E-09	11
PSEN1	3.63E-49	50	MYC	6.71E-08	15
APP	4.24E-37	57	RICTOR	2.94E-07	8
HTT	4.63E-19	34	5-fluorouracil	1.50E-06	8
torin1	2.73E-16	15	MYCN	5.95E-06	7
metribolone	2.67E-15	24	HDAC4	2.03E-05	5
FMR1	6.96E-15	16	ammonia	3.56E-05	2
RICTOR	5.47E-14	19	LONP1	3.88E-05	4
sirolimus	9.3E-14	25	ST1926	4.87E-05	5
BDNF	1.28E-11	18	TLE3	5.46E-05	4
Diseases or Functions Annotation: Epilepsy	**p-value**	**# Hits**	**Diseases or Functions Annotation**	**p-value**	**# Hits**
Seizure disorder	4.07E-14	29	Decay of mRNA	1.30E-08	7
Seizures	4.47E-12	25	Synthesis of protein	2.35E-08	13
Infantile or early childhood epileptic encephalopathy	6.86E-12	12	Expression of protein	1.14E-07	11
Developmental epileptic encephalopathy	7.69E-12	12	Parkinson's disease	1.30E-07	9
Familial generalized epilepsy	4.56E-11	12	Nonsense-mediated mRNA decay	2.66E-07	6
Early-onset epilepsy	9.62E-11	13	Progressive encephalopathy	1.25E-06	14
Tonic-clonic seizure	2.68E-10	13	Movement Disorders	1.26E-06	16
Childhood epilepsy	9.85E-10	12	Progressive neuromuscular disease	1.26E-06	10
Epilepsy	1.34E-09	19		1.48E-06	6

Table 1 (continued)

HIPPOCAMPUS Canonical Pathways	p-value	# Hits	CEREBELLUM Canonical Pathways	p-value	# Hits
			Initiation of translation of protein		
Epilepsy or neurodevelopmental disorder	4.79E-09	21	Disorder of basal ganglia	1.64E-06	13

control of CaN in astrocytes [15].

Validation of SG-MS results by WB (Fig. 1C) showed significant correlation ($R^2 = 0.612$, p = 0.0044) between SG-MS and WB (Fig. 1D). qPCR validation showed no alterations in mRNA levels except Vapa and Rab31, found to be downregulated in hippocampus confirming, thus, RNA-Seq results (Suppl. Fig. 2). Classification of DEPs for Cell component and Function categories revealed that in Wht-Hip and Wht-Cb Cell components of *cytosol* were the most abundant followed by *mitochondria, ribosome* and *vesicles*, while among Functions there were *metabolism, translation, OXPHOS* followed by *vesicle trafficking* and *transport across membrane*. In synaptosomal preparations Cell components were categorized as *cytosol, cytoskeleton, mitochondria, plasma membrane, vesicles* and *ribosome*; while among Functions were *signalling, metabolism, transport across membrane, structural proteins, OXPHOS, translation* and *vesicle trafficking* (Suppl. Fig. 3).

2.2. Deletion of Astro-CaN deranges protein expression in major brain cell types

The analysis of DEPs showed the presence of many neuronal proteins, e.g., Thy-1, Snap25, Synaptophysin and Tau suggesting that the deletion of CaN from astrocytes affects neuronal protein expression. Therefore, we analysed the cell-specificity of DEPs using a merged lists of Wht-Hip and Syn-Hip DEPs (Suppl. Table 2E). First, we primed the Human Protein Atlas (HPA) database (https://www.proteinatlas.org/) in which protein expression is comprehensively examined using ATLAS antibodies (Sigma) and the cell-specificity of expression in the hippocampal formation is scored in glial and neuronal cells. This analysis, revealed that, in the hippocampus, the majority of DEPs were neuron-specific (32.9%) or enriched in neurons (24.5%), while glia-specific proteins (6.5%) or proteins enriched in glia (2.6%) were less abundant (Fig. 2A). Next, we primed a brain cell-specific transcriptome database published by Ben Barres and colleagues [16]. The analysis revealed that DEPs specific for all principal brain cell types, including astrocytes (7 hits), neurons (12 hits), oligodendrocytes (7 hits), microglial cells (3 hits) and endothelial cells (1 hit) were differentially expressed in ACN-KO brain (Fig. 2B), corroborating and extending the results obtained using HPA.

Taken together, RNA-Seq and SG-MS analyses showed that at one month of age the deletion of Astro-CaN does not change transcription neither in the hippocampus nor in the cerebellum, while protein expression was altered differentially in these two brain regions, in all principal brain cellular types.

2.3. Deletion of Astro-CaN produces proteome signature of neuropathology and seizures

Next, we investigated the functional significance of protein expression alterations in ACN-KO mice. For this analysis, whole-tissue DEPs were pooled with synaptosomal DEPs resulting in two lists, related to the hippocampus (HIP) and the cerebellum (CB). Gene ontology analysis of HIP DEPs revealed overrepresentation of 175 GO terms (Suppl. Table 3A). The most significantly overrepresented hits from GO category Cellular Component (CC) were *myelin sheath* (44 DEPs), *extracellular exosome* (90 DEPs) and *mitochondrion* (46 DEPs), while KEGG pathways
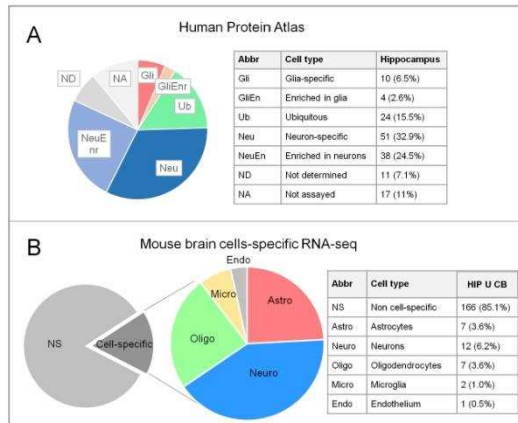
Fig. 2. Cell-specificity analysis of differentially expressed proteins. (A) Priming of Human Protein Atlas database (www.proteinatlas.org) of Hippocampal differentially expressed proteins (DEPs) revealed prevalence of neuronal DEPs. (B) Priming of mouse brain cell-specific RNA-Seq transcriptome revealed alterations in expression of proteins from all major CNS cell types, with prevalence of neuronal proteins.

were *OXPHOS* (17 DEPs), *Alzheimer's* (AD, 16 DEPs), *Parkinson's* (PD, 16 DEPs) and *Huntington's disease* (HD, 16 DEPs). Interestingly, intersection of *AD, PD, HD* and *OXPHOS* lists resulted in 12 common DEPs, all of which were components of the oxidative phosphorylation (OXPHOS) mitochondrial pathway (Suppl. Fig. 4). DAVID analysis of CB list returned 43 significantly overrepresented GO terms among which were KEGG pathway *ribosome* (7 DEPs) and CC *extracellular exosome* (33 DEPs), *intermediate filament* (7), *intracellular ribonucleoprotein complex* (9), *ribosome* (7) and *mitochondrion* (15) (Suppl. Table 3B). Presence of intermediate filaments of the keratin family was somewhat surprising, however priming databases Genecards (https://www.genecards.org/) and PaxDB (https://pax-db.org/) revealed presence of keratins in different brain proteome datasets (Suppl. Table 4).

Ingenuity pathway analysis (IPA) of HIP dataset resulted in a list of at least 500 significantly overrepresented annotations. Top Canonical Pathways were *Synaptogenesis Signaling Pathway, Phagosome Maturation, Sirtuin Signaling Pathway,* and *Mitochondrial Dysfunction* (Table 1). Overrepresented Disease And Functions annotations contained developmental and hereditary neurological disorders as well as psychiatric and neurodegenerative disorders (full list of annotations provided in Suppl. Table 5). Note the presence of annotations related to seizures and epilepsy (Table 1) which contained 29 proteins (listed in Suppl. Table 6). Top Upstream Regulators in HIP were proteins *MAPT, PSEN1, APP* and *HTT* (Table 1 and Suppl. Table 7A). Mutations of MAPT (tau), PSEN1 (presenilin 1) and APP (amyloid precursor protein) are the major causes of familial AD (FAD) [17], while mutation of HTT is a cause of Huntington's disease [18]. The relationships of MAPT, PSEN1 and APP with target proteins, calculated by IPA, are shown, respectively, in Suppl. Figs. 5, 6 and 7. Of 69 unique proteins in *MAPT, PS1, APP* lists, 47 were common (Suppl. Table 7B), falling in three clusters, generated using STRING unsupervised k-means clustering, (i) neuronal and synaptic, (ii) metabolic pathways, mitochondrial and OXPHOS, and (iii) cytoskeletal and adhesion proteins (Fig. 3, and Suppl. Table 7C). Top Canonical Pathways in CB list were *EIF2 Signaling, Glucocorticoid Receptor Signaling, Regulation of eIF4 and p70S6K Signaling, Sirtuin Signaling Pathway* and *Mitochondrial Dysfunction*. Top Upstream Regulators in CB were *MAPT, MYC* and *RICTOR*, while Disease And Functions annotations included

Decay of mRNA, Synthesis of protein, Parkinson's disease and *Progressive encephalopathy* (Table 1).

Altogether, GO and pathway analyses suggest that the deletion of Astro-CaN affects, among others, mitochondrial function, protein synthesis and mTOR signalling, showing significant association with neurological diseases, including AD and epilepsy.

2.4. ACN-KO proteome shows significant overlap with 5xFAD mouse AD model and with human drug-resistant epilepsy datasets

Given the emergence of AD and seizures, we compared all our HIP ACN-KO DEPs with published AD and epilepsy proteome datasets. For AD comparison, we chose a proteome dataset obtained on 8 months-old 5xFAD mouse AD model, which represents the early stage of AD-like pathology [19]. HIP ACN-KO dataset showed significant overlap with 5xFAD-vs-NonTg proteome reported by Neuner et al. (18 overlapped proteins, p = 7.02E-15; Fig. 4A, and Suppl. Table 8A).

For comparison with epileptic brains, a dataset contributed recently by Karen-Aviram and colleagues [20] was chosen. This dataset features DEPs from the resected high frequency epileptic foci compared with biopsies of non-epileptic regions from the same patients with drug-resistant epilepsy (denominated as HE). Of 155 DEPs of HIP ACN-KO list, 26 DEPs (16.8%) were common with HE showing significant overlap (p = 1.07E-24; Fig. 4B, Suppl. Table 8B).

Collectively, our omics data suggest that the deletion of CaN from astrocytes, at 1 mo of age, produces deregulation of protein expression resembling that of AD and epilepsy.

2.5. The absence of ultrastructural alterations in ACN-KO hippocampus

Previously, we reported no alterations in neurodevelopment and brain cytoarchitecture of ACN-KO mice [9], while bioinformatic analysis already at 1 month of age ACN-KO mice shows a proteome fingerprint of neurological diseases which may result in alterations at the synaptic level in the hippocampus. Therefore, we have investigated if there were ultrastructural alterations in the hippocampus of ACN-KO mice with consequent behavioural characterization including a
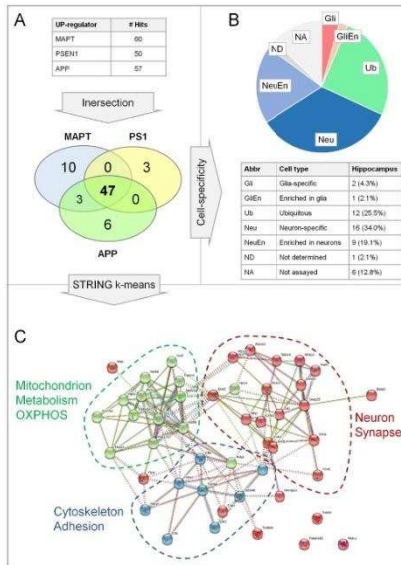
4

56

Fig. 3. Top 3 Cell-specificity and STRING k-means clustering of common targets of IPA pathway Upstream Regulators of Hippocampal DEPs MAPT, PS1 and APP. (A) Intersection of 60 MAPT, 50 PS1 and 57 APP putative regulated DEPs resulted in 47 common DEPs. (B) Cell-specificity analysis Human Protein Atlas (www.proteinatlas.org) database shows presence of mostly neuronal and neuron-enriched DEPs. (C) 47 common DEPs regulated by MAPT, PS1 and APP, putative upstream regulators found by IPA pathway analysis, were subjected to STRING protein-protein interaction analysis. STRING k-means unsupervised clustering revealed 3 clusters grouped in proteins related to: neuron and synapse (Cluster 1, red), mitochondrion, metabolism and OXPHOS (Cluster 2, green); and cytoskeleton and adhesion (Cluster 3, light-blue).

hippocampus-dependent task. Transmission electron microscope analysis revealed no ultrastructural alterations in neuropil of CA1 hippocampal region including synapses and mitochondria (Suppl. Fig. 8A). Likewise, quantification of dendritic spines in the hippocampus revealed no differences in spine density ($p = 0.78$, $n = 12$ for ACN-Ctr, $n = 15$ for ACN-KO), confirming that, at 1 mo of age, the deletion of CaN from astrocytes does not alter structural and morphological aspects of the CNS (Suppl. Fig. 8B).

2.6. ACN-KO mice adopt serial search strategy in Barnes maze

Next, we subjected mice to behavioural tests to assess if general parameters of behaviour and memory of ACN-KO mice were different from that of ACN-Ctr. Results of open field test showed that the distance travelled, the time spent and the average speed of movement in the external and internal parts of the field did not differ between ACN-Ctr and ACN-KO mice ($p = 0.73$, $n = 15$) (Suppl. Fig. 9). Similarly, no changes were found in nesting behaviour ($p = 0.145$, $n = 11$), hanging ($p = 0.56$, $n = 8$) and tail suspension tests ($p = 0.86$, $n = 18$). This indicates that ACN-KO mice do not have deficit of motor activity,

equilibrium or muscle strength, neither show anxious or depressive behaviour (Suppl. Fig. 9). Next, we subjected ACN-Ctr and ACN-KO mice to Barnes maze behavioural paradigm (Fig. 5A). No differences were observed across acquisition training (AT) sessions in primary latency (F $(1,18) = 0.0005$, $p = 0.98$, $n = 10$ per genotype; Fig. 5), entry latency (F $(1,18) = 0.45$, $p = 0.51$) and entry errors (F(1,18) $= 0.43$, $p = 0.52$). However, in AT1, ACN-KO mice made significantly more primary errors (13.6 ± 3.05 pokes for ACN-KO vs 6.0 ± 1.03 pokes for ACN-Ctr; $p = 0.023$) resulting in significative association with genotypes in two-way ANOVA for repeated measures (RM-ANOVA) (F(1,18) $= 8.53$; $p = 0.0091$). The difference in the number of primary errors was not due to alteration in locomotor activity as there were no differences in distance travelled ($p = 0.57$) and average speed ($p = 0.45$) during AT1 session. These results suggest that, in spite of the difference in the number of primary errors during AT1 session, ACN-KO mice learned the task and succeeded to locate the target hole with the same temporal efficiency as ACN-Ctr mice. During the acquisition probe (AP) session, in which the escape box was removed and mice were allowed to explore the maze for 90 sec., the primary latency ($p = 0.24$) and the number of primary errors ($p = 0.89$) to find the target hole in 90 sec were not different between ACN-Ctr and ACN-KO mice. However, the number of total pokes during the session were significantly higher in ACN-KO than in ACN-Ctr mice (37.1 ± 1.16, $n = 10$ vs 21.1 ± 3.44 pokes, $n = 9$, respectively; $p = 0.02$, unpaired t-test; Fig. 5D right). This may suggest on the differences in search strategy that mice adopt to locate target hole. To test this we have identified the following search strategies: direct (spatial), serial search and random (mixed) [21]. To these three classical search strategies, an additional strategy was discriminated when the mouse returned to the target hole from the first or second adjacent holes (called return) (see Methods section for detailed description of search strategies). In course of the AP session, when the first approach to the target hole was considered, only one (11.1%) of ACN-Ctr mice used serial search, while 3 (33.3%) and 5 (55.6%) mice used, respectively, random and direct search. Instead, 6 (60%) ACN-KO mice used serial search strategy during the first search, while 1 (10%) and 3 (30%) mice used, respectively, random and direct search ($p = 0.080$, χ^2, Fisher's exact test; Fig. 5E left). The trend of ACN-KO mice to use serial search during the acquisition probe was strengthened when the total number of the target hole searches during 90 sec of probe were counted: ACN-Ctr and ACN-KO mice used, respectively, 5 (17.2%) vs 23 (52.3%) times the serial search strategy, 6 (20.7%) and 7 (15.9%) times the random search, 4 (13.8%) vs 2 (4.5%) the return strategy, and 14 (48.3%) vs 12 (27.3%) spatial search to find the target hole. The differences were significative using χ^2, Fisher's exact test ($p = 0.020$; Fig. 5E right). These results suggest that ACN-KO mice learn the position of target hole using non-spatial but serial search strategy to locate it. Fig. 5F shows representative traces of ACN-Ctr and ACN-KO mice during AP session, from which is evident that the difference in search strategy is reflected by the time spent and the distance travelled by the mouse in the external part or in the center of the maze. We used these parameters to analyse if the serial search is an intrinsic property of ACN-KO mice linked to anxiety and is independent of learning, or this is the strategy that mice develop during the learning process because they are unable to adopt spatial search strategy. For this, the maze was divided in two zones, external and internal (Fig. 6A), and the distance and time spent in each zone was measured in two occurrences in which all mice spent equal time searching the maze, the habituation session, e. g., before learning, and the AP session. While there was no difference in total distance travelled during both habituation ($p = 0.57$) and AP session ($p = 0.084$) (Fig. 6B), ACN-KO mice travelled significantly more ($p = 0.015$) (Fig. 6C) and spent more time ($p = 0.009$) (Fig. 6D) in the external part of the maze than in the internal part in comparison with ACN-Ctr during the AP session but not the habituation.

Taken together, these results show that ACN-KO mice do not have motor alterations or anxiety while presenting alterations in spatial learning.
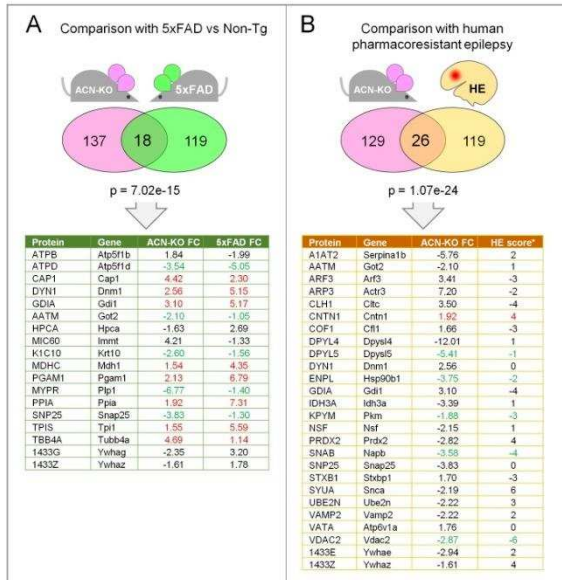
A Comparison with 5xFAD vs Non-Tg

Protein	Gene	ACN-KO FC	5xFAD FC
ATPB	Atp5f1b	1.84	-1.99
ATPD	Atp5f1d	-3.54	-5.05
CAP1	Cap1	4.42	2.30
DYN1	Dnm1	2.56	5.15
GDIA	Gdi1	3.10	5.17
AATM	Got2	-2.10	-1.05
HPCA	Hpca	-1.63	2.69
MIC60	Immt	4.21	-1.33
K1C10	Krt10	-2.60	-1.56
MDHC	Mdh1	1.54	4.35
PGAM1	Pgam1	2.13	6.79
MYPR	Plp1	-6.77	-1.40
PPIA	Ppia	1.92	7.31
SNP25	Snap25	-3.83	-1.30
TPIS	Tpi1	1.55	5.59
TBB4A	Tubb4a	4.69	1.14
1433G	Ywhag	-2.35	3.20
1433Z	Ywhaz	-1.61	1.78

p = 7.02e-15

B Comparison with human pharmacoresistant epilepsy

Protein	Gene	ACN-KO FC	HE score*
A1AT2	Serpina1b	-5.76	2
AATM	Got2	-2.10	1
ARF3	Arf3	3.41	-3
ARP3	Actr3	7.20	-2
CLH1	Cltc	3.50	-4
CNTN1	Cntn1	1.92	4
COF1	Cfl1	1.66	-3
DPYL4	Dpysl4	-12.01	1
DPYL5	Dpysl5	-5.41	-1
DYN1	Dnm1	2.56	0
ENPL	Hsp90b1	-3.75	-2
GDIA	Gdi1	3.10	-4
IDH3A	Idh3a	-3.39	1
KPYM	Pkm	-1.88	-3
NSF	Nsf	-2.15	1
PRDX2	Prdx2	-2.82	4
SNAB	Napb	-3.58	-4
SNP25	Snap25	-3.83	0
STXB1	Stxbp1	1.70	-3
SYUA	Snca	-2.19	6
UBE2N	Ube2n	-2.22	3
VAMP2	Vamp2	-2.22	2
VATA	Atp6v1a	1.76	0
VDAC2	Vdac2	-2.87	-6
1433E	Ywhae	-2.94	2
1433Z	Ywhaz	-1.61	4

p = 1.07e-24

Fig. 4. Comparison with 5xFAD mouse and human drug-resistant epilepsy proteome datasets. (A) Comparison with 8 mo old 5xFAD vs NonTg hippocampal proteome (18 common DEPs, listed in the table below; p = 7.02E-15) [19]. (B) Comparison with human drug-resistant epilepsy dataset contributed by [20] obtained on brain biopsies from high-frequency epileptic foci vs low-frequency regions from the same patients. 26 common proteins were found (p = 1.07E-24) listed in the table below. Colour labels: in red co-upregulated; in green: co-downregulated DEPs. Magenta, ACN-KO vs ACN-Ctr DEPs; green, 5xFAD vs NonTg DEPs; light-yellow, human epileptic (HE) DEPs. HE score was calculated as an algebraic sum of numerical values (from 1 to 2 for up-regulated proteins and from -1 to -2 for down-regulated proteins) assigned to DEPs categories according to [20].

2.7. ACN-KO mice develop tonic-clonic seizures and neuroinflammation starting from 5 months of age

The emergence of annotations related to epilepsy prompted us to investigate if there was an increased incidence of seizures during lifetime of ACN-KO mice. Monitoring of ACN-KO mice revealed that starting from about 5 months of age, both males and females of ACN-KO mice showed increasing risk to develop seizures. Seizures started either upon cage opening, or upon bothering of a mouse by slightly pulling the tail (Suppl. Video 1). The intensity of seizures corresponded to stages from 3 (forelimb clonus) to 5 (rearing and falling with forelimb clonus) according to Racine scale [22] (Suppl. Video 1) or to stages 6-7 according to Pinel and Rovner scale (forelimb clonus with multiple rearing and falling; jumping) [23] (Suppl. Video 2). The percentage of mice developing seizures grew steadily until 10 months after which the incidence did not increase further (Fig. 7A). There were no differences in the risk of seizure development between the three experimental groups, males (n = 50), non-breeding females (n = 36) and breeding females (n = 80) (long-rank Mantel-Cox test, $\chi^2 = 0.856$, df = 2, p = 0.6518) reaching 40% risk for males and 45% for females (Fig. 7A). We next attempted registration of EEG in ACN-KO males. However, epileptic mice did not developed seizure after implantation of electrodes (n = 4) which made it impossible to register EEG during seizures. Thus, we proceeded with registration of seizure-free mice. In all cases registered from ACN-KO mice there was a presence of aberrant electrical activity (100.8 ± 19.25 spikes/24h in ACN-KO vs 3.5 ± 0.50 spikes/24h in ACN-Ctr, p = 0.042, n = 5) resembling that of interictal spikes [24] (Fig. 7B).

Neuroinflammation is a key feature of human seizure disorders and mouse models of epilepsy [25]. Therefore, we investigated if in ACN-KO mice with seizures this key feature of epileptic brain was respected.

qPCR experiments on mRNA extracted from hippocampi of ACN-Ctr (labelled as Ctr in Fig. 7C), ACN-KO mice without seizures (labelled as Ns in Fig. 7C) and ACN-KO mice with recurrent seizures (labelled as Seiz in Fig. 7C) demonstrate that Il-1β, TNF, Cox2 and Gfap mRNA were significantly upregulated in ACN-KO mice with seizures (15.6 fold, p < 0.0001; 3.9 fold, p = 0.0003; 7.62 fold, p = 0.0001 and 1.29 fold, p = 0.0067, compared with ACN-Ctr, respectively), indicating an ongoing neuroinflammatory process. Together, our data suggest that the deletion of CaN from astrocytes results in development of delayed spontaneous tonic-clonic seizures from 5 months of age.

3. Discussion

The present study was designed to investigate the effect(s) of the deletion of Astro-CaN on global transcriptional and translational remodelling in the CNS of ACN-KO mice at 1 month of age, a time-point when the CaN KO is fully expressed, development and neuronal differentiation in the CNS are completed, while there are minimal compensatory effects of the deletion of Astro-CaN. The principal findings of this work are: (i) in resting conditions, Astro-CaN does not play a significant role in transcription; (ii) at 1 month of age, protein expression was altered in hippocampus and cerebellum of ACN-KO mice in a brain area-specific manner. In addition, a different set of proteins was found altered when specifically looking at hippocampal and cerebellar synaptosomes; (iii) changes in protein expression occurred in all principal cellular types of the CNS including astrocytes, neurons, oligodendrocytes, microglia and endothelial cells; (iv) bioinformatic analysis revealed over-representation of differentially expressed proteins related to CNS disorders, specifically to AD and seizure disorder; (v) comparisons with published proteome datasets indicate significant overlap of HIP ACN-KO
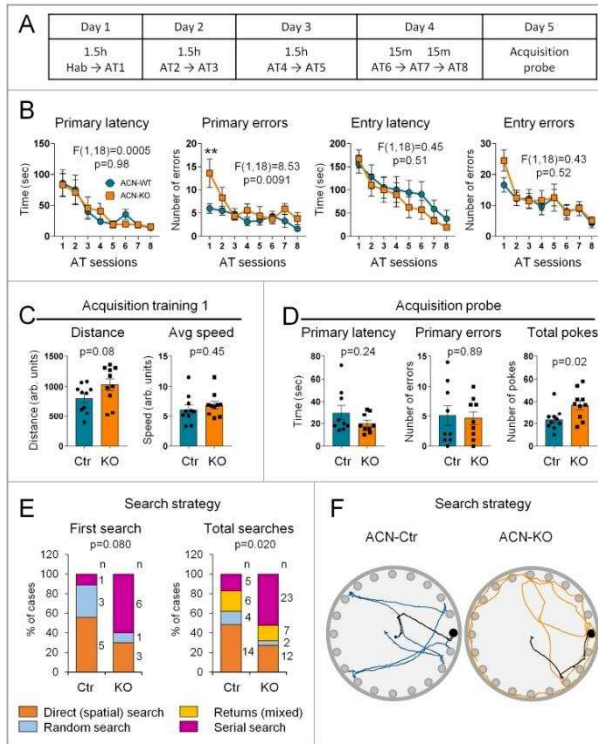
Fig. 5. ACN-KO mice learned the Barnes maze task, but use serial search strategy. (A) schematic representation of Barnes maze experiment protocol (Hab = habituation; AT = acquisition training). (B) Performance of ACN-Ctr and ACN-KO mice across AT sessions: no differences were found in primary latency (F $(1,18) = 0.0005$; p = 0.98), entry latency (F $(1,18) = 0.45$; p = 0.51) and entry errors (F $(1,18) = 0.43$; p = 0.52), in primary errors, only in AT1 session, significative difference between ACN-Ctr and ACN-KO mice was found (p = 0.0091). (C) the absence of significative differences in total distance travelled and average (Avg) speed, during AT1 (respectively: p = 0.57; p = 0.45), shows that there are no alterations in general motor and explorative activity in ACN-KO compare to ACN-Ctr mice. (D) ACN-Ctr and ACN-KO mice do not show differences, in the acquisition probe, considering both primary latency (p = 0.19) and primary errors (p = 0.83), but there is a significant difference in the number of total pokes during acquisition probe (p = 0.019). (E) Comparison of search strategies adopted by ACN-Ctr and ACN-KO mice during acquisition training: considering both first search and total searches strategies ACN-Ctr prefer direct search (orange), while ACN-KO prefer serial search (Magenta). (F) representative traces of ACN-Ctr (blue) and ACN-KO (orange) mice; first search is black coloured.

dataset with those related to AD and epilepsy; (vi) ACN-KO mice do not exhibit alterations in locomotor activity, signs of anxiety or depression; (vii) in Barnes maze, ACN-KO mice were able to locate the target hole with the same efficiency as ACN-Ctr mice but used non-spatial search strategy, serial search; and (vii) beginning from about 5 months of age ACN-KO mice show increased risk to develop tonic-clonic seizures.

3.1. Posttranscriptional nature of the Astro-CaN deletion effects

In astrocytes, CaN activity is mainly associated with transcriptional remodelling through activation of transcription factors NFAT and NF-kB. Such a transcriptional remodelling has been shown in several pathological conditions *in vivo* and *in vitro* in response to toxic or pro-inflammatory stimuli [26, 27, 28]. Neuronal activity-dependent activation of CaN followed by NFAT nuclear translocation has been demonstrated in pericytes after field stimulation of hippocampal slices [29], while *in vitro* our group has shown a robust Astro-CaN activation in mixed neuron-astrocytes hippocampal cultures upon chemical induction of long-term potentiation (LTP) [30]. Here we show that the remodelling of CNS proteome, as a result of the deletion of CaN from astrocytes, occurs in the absence of transcriptional alterations, suggesting that the

principal mean by which CaN acts in healthy astrocytes is through protein de-phosphorylation. However, it should be emphasized that for RNA-Seq and SG-MS analyses we used resting, not stimulated and not stressed animals. Therefore, at least in principle, a stress-or-stimulation-induced Astro-CaN-mediated transcriptional activity, as it occurs in neurons during late phase of LTP [14], cannot be *a priori* ruled-out. Nevertheless, we can speculate that, upon continuous modifications in homeostatic demand during dynamic neuronal activity, fast dephosphorylation/phosphorylation signalling would be more advantageous compared to a relatively slower process such as transcription.

3.2. Astro-CaN deletion predicts neuropathology, does it mean that neuropathology is caused by Astro-CaN dysfunction?

The central finding of this work is that, in response to the deletion of CaN from astrocytes, the molecular signature of neuropathology was evident already at 1 month of ACN-KO mouse age. As shown in the gene ontology analysis, the molecular signature resembles that of several neurological and neurodegenerative diseases, e.g., OXPHOS alterations were common between PD, HD and AD. However, IPA pathway analysis
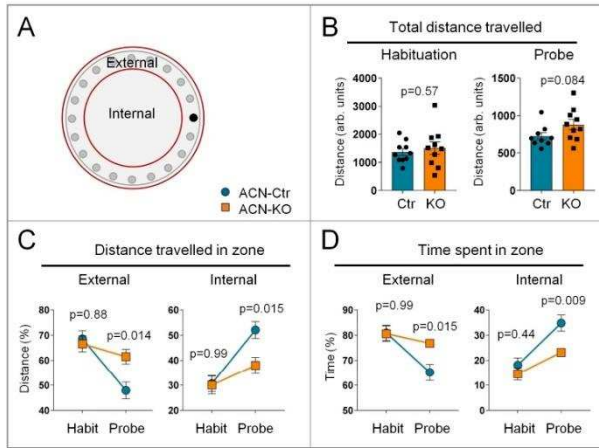
7

Fig. 6. Search strategies alteration is not an intrinsic feature of ACN-KO mice. (A) schematic representation of Barnes maze division in internal zone and external zone. (B) no differences between ACN-Ctr and ACN-KO mice emerged in the total distance travelled during, both, habituation and acquisition probe (respectively: p = 0.57; p = 0.084). (C) % of distance travelled by ACN-Ctr and ACN-KO mice, in external and internal zone, in the habituation (Hab) and probe sessions. (D) % of time spent by ACN-Ctr and ACN-KO mice, in external and internal zone, in the habituation (Hab) and probe sessions.
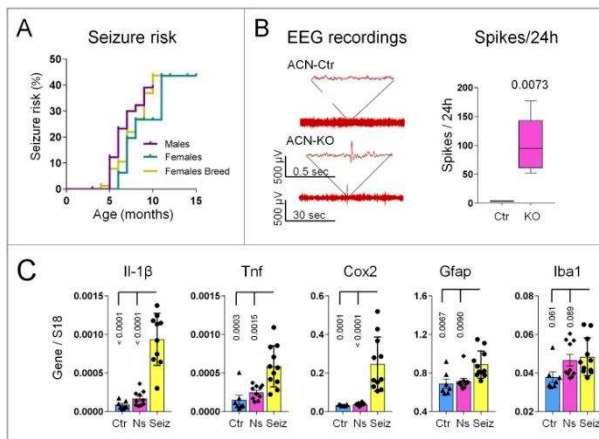

Fig. 7. Increased risk to develop tonic-clonic seizures in ACN-KO mice beginning from 5 months of age, and inflammatory phenotype in 9 months-old ACN-KO mice with seizures. (A) Starting from 5 mo of age, both males and females exhibit increasing risk of spontaneous tonic-clonic seizures (violet, males, n = 50; turquoise, females, n = 36; yellow, females in breeding, n = 80, long-rank Mantel-Cox test, $\chi^2 = 0.856$, df = 2, p = 0.6518). (B) No seizures have been observed in mice which underwent surgery for electrode implantation. However, in seizure-free mice there were aberrant EEG spikes as registered by 24 h recording (100.8 ± 19.25 spikes/24h in ACN-KO vs 3.5 ± 0.50 spikes/24h in ACN-Ctr, p = 0.0073, n = 5). (C) Hippocampi were dissected from ACN-Ctr (Ctr, cyan columns), ACN-KO mice which never had seizures (Ns, magenta columns) and from ACN-KO mice with seizures less than 5 min before sacrifice (Seiz, yellow columns). RNA was extracted and real-time PCR was performed using specific primers for pro-inflammatory cytokines (Il-1β, Tnf and Cox2) and markers of gliosis (Gfap and Iba1). Note upregulation of pro-inflammatory and gliotic markers specifically in ACN-KO mice with seizures (p < 0.0001, Seiz vs Ctr and Ns for Il-1β; p = 0.0003 and p = 0.0015, Seiz vs Ctr and Ns, respectively for Tnf; p = 0.0001 and p < 0.0001, Seiz vs Ctr and Ns, respectively for Cox2; p = 0.0067 and p =

0.0090, Seiz vs Ctr and Ns, respectively for Gfap; and p = 0.061 and p = 0.089, Seiz vs Ctr and Ns, respectively for Iba1). Details of statistical analysis are reported in Supplementary Table 9.

indicates on a particular link with AD. Strikingly, the top 3 Upstream Regulators found by IPA analysis were the three major causes of familiar AD, namely Tau (MAPT), PS1 and APP with 47 common proteins downstream of these hypothetical regulators (30.3% of HIP list, Suppl. Table 7B). Because of FAD mutated proteins have been traditionally regarded as neuronal proteins, one could draw a straightforward conclusion that the deletion of CaN from astrocytes predisposes neurons to harmful effects of FAD mutations partly recreating the fingerprint of FAD-related proteome. Analysis of cell-specificity of this list shows that the majority of proteins are, indeed, neuron-specific or enriched in

60

neurons (Fig. 3B).

Disrupted intracellular Ca^{2+} signalling, bioenergetic deficit and impairment of protein synthesis and degradation represent, perhaps, the most important features of early AD pathogenesis [31, 32, 33, 34]. It has been suggested that alterations of inter-organellar communication, in particular of the ER-mitochondrial Ca^{2+} transfer, may represent central event in AD cellular pathology [35, 36, 37, 38]. We speculate that, in AD astrocytes, alterations of CaN activity may provide a link between deregulation of Ca^{2+} homeostasis, bioenergetic deficit and cellular disproteostasis. This speculation is supported by reports suggesting that CaN directly regulates both protein synthesis and mitochondrial dynamics and bioenergetics [39, 40, 41]. In spite that transcriptional changes represent an important feature of AD astrocytes [42,43], our data suggest that such an effect may occur at the posttranscriptional level. Further support to this speculation comes from the comparison of our proteomics data with that of a mouse model of incipient AD, 8 months-old 5xFAD mice [19]. However, since ACN-KO mice do not bear FAD mutations, it is unlikely that ACN-KO mouse represents an AD mouse model. Instead, significant overlap with hippocampal proteome of 5xFAD mice suggest that the alterations of Astro-CaN activity may occur during AD pathogenesis. Moreover, we propose that it may constitute a common denominator for a group of neuropathological diseases as suggested by bioinformatic analysis. In this light, considering the increased risk of seizures in AD patients [44,45], the association of Astro-CaN specifically with AD and epilepsy assumes particular significance. Therefore, investigation of Astro-CaN activity and its association with central and peripheral markers at early disease stages may lead to the development of novel approaches in diagnosis, prevention and therapy.

3.3. Alterations in spatial memory in ACN-KO mice

Interestingly, at 1 mo of age, we did not find ultrastructural alteration in the hippocampal neuropil of ACN-KO mice, neither they have alterations in basic behavioural performances like locomotor activity, equilibrium and strength. In addition, ACN-KO mice did not exhibit anxious or depressive behaviour, as none of the parameters in open field, nesting or tail suspension tests was changed. However, alterations in navigational strategies which ACN-KO mice adopt to locate the target hole in Barnes maze test suggest a functional impairment of hippocampal circuits. Barnes maze is considered to be a hippocampus-dependent task in which the ability to use spatial memory is tested [46]. However, a mouse is able to find the target hole even without spatial orienteers, using the information inherent to maze exploring holes serially [47]. In these terms, one could conclude that ACN-KO mice, which adopt serial search to locate the target hole, have clear functional hippocampal impairment. However, lately, it has been argued that hippocampus is used for non-spatial memory processing due to its ability to time-parse elementary memory events to integrate temporal (when), episodic (what), spatial (where) information into memory traces [48,49]. In light of this paradigm it is plausible to conclude that ACN-KO mice fail to develop spatial search and avail to serial exploration of holes due to functional dissociation of temporal and spatial representations both of which are hippocampus-dependent [48]. Such a dissociation has been found in the hippocampus of an AD mouse model, rTg4510 mice, in which temporal sequences of neuronal firing can persist while spatial firing is disrupted [50]. This rational is supported by several studies of animal model of AD and epilepsy. Thus, Macedo and colleagues [51] showed that rats, after hippocampal infusion of β-amyloid peptides, used non-spatial strategies to solve the maze; similarly, in kainic acid model of temporal lobe epilepsy, mice understood the context and solved the maze using serial but not spatial search [52], suggesting that the inability to form spatial representations may be a common feature between AD and epilepsy.

Striking similarity was found in Barnes maze performance, specifically in the acquisition training profiles and the preference of serial

search strategy, between ACN-KO mice and a mouse with neuronal expression of Ca^{2+}-insensitive mutant of Ca^{2+}/calmodulin-dependent kinase II (CaMKII) in which long-term potentiation in theta-range (5-10 Hz) of stimulating frequencies was specifically impaired [53]. Speculatively, this may suggest a mechanistic link between Astro-CaN-regulated CNS proteostasis and neuronal activity and plasticity. Further thorough molecular and electrophysiological analysis of neuronal activity and plasticity is needed to investigate the link between Astro-CaN and neuronal CaMKII. While such investigation is beyond the aim of the present contribution, the link between neuronal excitability, found to be impaired in ACN-KO mice [9], and the activity of CaMKII in neurons is well documented [54].

3.4. Is ACN-KO mouse a novel model of spontaneous seizures and epilepsy?

Another important finding of this contribution regards the increased risk of ACN-KO mice to develop motor seizures in the period from 5 to 12 months of age. As we have previously reported, to 20th postnatal day ACN-KO mice develop full CaN KO in the hippocampus and the cerebellum [9]. Therefore, it is reasonable to suggest that the seizures are unlikely to be the direct effect of Astro-CaN KO. A delay of 5-10 month from the CaN-KO till seizure development suggests that a constellation of long-lasting alterations, downstream of Astro-CaN, may lead to seizure development. While the primary cause is represented by the Astro-CaN KO, the very cause of seizures is currently unknown. At the time of seizures ACN-KO mice show inflammatory phenotype closely resembling that observed in human disease and animal models of epilepsy [25]. However, despite that the onset and development of epilepsy are strongly associated with neuroinflammation [55], it is prematurely to conclude that the seizures in ACN-KO mice are caused by the inflammatory process. Moreover, at 1 month of age of ACN-KO mice, the molecular epileptic fingerprint does not evidence inflammatory component but strongly suggests the insufficiency of glial support to neurons because: (i) primary cause is the deletion of an astroglial enzyme; (ii) altered expression of astrocyte-specific membrane transporters as Glast [15], Glt-1 and Atp1a2; and (iii) overrepresentation of DEPs related to myelin sheath suggesting inadequate oligodendroctytic function. In support of this, compromised myelinisation of axons in hippocampus has been repeatedly associated with insurgence of seizure [56,57]. In this light, the significant overlap 1 mo-old ACN-KO mice proteome with that from human patients with intractable epilepsy [20] is of special interest. Indeed, Keren-Aviram and colleagues reported downregulation of GFAP in the epileptic foci and did not report appearance of other makers of neuroinflammation.

Lastly, a "spontaneous" nature of seizures discriminates ACN-KO mice from the majority of animal models of epilepsy [58]. We found that two third of ACN-KO mice do not develop seizures during their life-time, and the appearance of seizures cannot be predicted with absolute certainty. Manipulation with ACN-KO mice and/or surgical procedures decreases the probability to develop seizure to the extent that we were not able to register seizures in the electrode-implanted animals. All this renders ACN-KO mice time and cost-ineffective as a model of epilepsy [58]. However, "fast" and cost-effective animal models are not able to faithfully reproduce all aspects of the human seizure disorder [58]. This is particularly true for drug-resistant forms of epilepsy [59]. We, therefore, envisage that the results obtained from the thorough characterisation of epileptic phenotype of ACN-KO mice may outperform the time- and cost-related disadvantages of this novel and spontaneous model of seizure disorder.

4. Conclusions

The observations that glial cells change very early during neuropathology [60,61] led to hypothesize that an insufficient homeostatic support to other cells in the CNS may be among the primary events

which predispose neurons to dysfunction [61,62]. In this context, we have proposed that deregulation of astroglial Ca^{2+} signalling, downstream of CaN, may contribute to this homeostatic failure [4,6]. Our present data provide further support to this hypothesis suggesting that Astro-CaN may work as a Ca^{2+}-sensitive hub orchestrating homeostatic activities of astrocytes hence influencing functions of other cells in the CNS. This action may be exerted through the control of extracellular K^+ handling. Previously we have shown this for hippocampal pyramidal neurons and cerebellar granule cells [9], but dependence on extracellular potassium has also been shown for endothelial cells [63,64] by inward rectifier K^+ channels. Other mechanisms may include neurotransmitter control, e.g., glutamate, as we have shown that glutamate transporters and extracellular concentrations are regulated by astrocytic CaN [9,15]. In this regard, we also have suggested that endothelial cells are able to directly sense glutamate [65], which, speculatively, may be under the control of astroglial CaN. While molecular and signalling details of CaN activation and of Astro-CaN downstream signalling are a matter of future research, our results provide a framework for investigations suggesting that protein synthesis [15], myelination and mitochondria, alongside with mTOR signalling and with control of ion homeostasis [9], may represent principal components of Astro-CaN-controlled homeostatic network.

5. Methods

5.1. Generation and handling of ACN-KO mice

Generation and handling of conditional CaN knockout (KO) in GFAP-expressing astrocytes (astroglial calcineurin KO, ACN-KO) has been described previously [9]. Briefly, CaNB1$^{flox/flox}$ mice [66] (Jackson Laboratory strain B6;129S-Ppp3r1tm2Grc/J, stock number 017692) were crossed with GFAP-Cre mice [67] (Jackson Laboratory strain B6. Cg-Tg(Gfap-cre)77.6Mvs/2J, stock number 024098). The line was maintained by crossing CaNB1$^{flox/flox}$/GfapCre$^{-/-}$ (thereafter referred as to ACN-Ctr) males with CaNB1$^{flox/flox}$/GfapCre$^{+/-}$ (ACN-KO) females.

Mice were housed in the animal facility of the Università del Piemonte Orientale, with unlimited access to water and food. Animals were managed in accordance with European directive 2010/63/UE and with Italian law D.l. 26/2014. The procedures were approved by the local animal-health and ethical committee (Università del Piemonte Orientale) and were authorized by the national authority (Istituto Superiore di Sanità; authorization numbers N. 77-2017 and N. 214-2019). All efforts were made to reduce the number of animals bred and used.

5.2. Preparations of tissue homogenates and synaptosomal fractions

Tissues were homogenized using glass-Teflon 1 ml homogenizer in lysis buffer (50 mM Tris HCl (pH 7.4), sodium dodecyl sulfate (SDS) 0.5%, 5 mM EDTA). Synaptosomal fractions were prepared as reported previously [68] from hippocampal or cerebellar tissues pooled from two 1 month old ACN-Ctr or ACN-KO mice. Briefly, mice were anesthetized by intraperitoneal injection of Zoletil (80 mg/kg) and Xylazine (45 mg/kg) and sacrificed by decapitation. Hippocampi and cerebella were rapidly dissected and placed into ice-cold homogenization buffer containing 50 mM MOPS, pH 7.4, 320 mM sucrose, 0.2 mM DTT, 100 mM KCl, 0.5 mM MgCl$_2$, 0.01 mM EDTA, 1 mM EGTA, protease inhibitor cocktails (PIC, Calbiochem) and phosphatase inhibitor Na$_3$VO$_4$ (1μM). All subsequent steps were performed at 4°C. The tissues were minced and homogenized in 1:10 w/v homogenization buffer with 12 strokes in a Teflon-glass douncer. The homogenates were then centrifuged for 10 min at 800g followed by centrifugation of the supernatant at 9200g for 15 min. The resulting P2 pellet, representing the crude synaptosomal fraction, was solubilized in lysis buffer.

5.3. Western blot

20 μg proteins were resolved on 8% of 12% SDS-polyacrylamide gel. Proteins were transferred onto nitrocellulose membrane using Trans-Blot Turbo Transfer System (Bio-Rad), blocked in skim milk (5%, for 1 h; Cat. 70166; Sigma) and immunoblotted with indicated antibody. Mouse anti-Tubulin (1:5000, Cat. T7451) or anti-β-actin (1:10000, Cat. A1978), both from Sigma (Milan, Italy) were used to normalize protein load. Primary antibodies were: mouse anti-Sy38 (1:500, Cat. MAB-10321); rabbit anti-Cox6a1 (1:500, Cat. AB-83898); rabbit anti-Vdac2 (1:500, Cat. AB-83899); rabbit anti-Atp5j (1:500, Cat. AB-83897); rabbit anti-Dpysl4 (1:500, Cat. AB-83901); rabbit anti-Gfap (1:500, Cat. N. AB-10682), all from Immunological Sciences (Rome, Italy); rabbit anti-Rps10 (1:500, Cat. PA5-96460, Thermofisher, Milan, Italy); rabbit anti-Glast (1:500, Cat. NB100-1869, NovusBio, Milan, Italy); rabbit anti-Atp1a2 (1:1000, Cat. ANP-002, Alomone Labs, Jerusalem, Israel); mouse anti-PSD95, clone K28/43 (1: 1000, Cat. MABN68, Merck Millipore, Milan, Italy); mouse anti-Snap25 (1:600, Cat. sc-376713, Santa-Cruz, Dallas, Texas, USA). Goat anti-mouse IgG (H+L) horseradish peroxidase-conjugated secondary antibody (1: 8000; Cat. 170-6516, Bio-Rad, Milan, Italy) was used. The protein bands were developed using SuperSignal West Pico chemiluminescent substrate (Cat. 34078; Thermofisher). Densitometry analysis was performed using the Quantity One software (Bio-Rad).

5.4. Proteomic analysis

5.4.1. In solution digestion

Lysates were digested using the following protocol: samples were prepared to have 100 μg of protein in a final volume of 25 μL of 100 mM NH$_4$HCO$_3$. Proteins were reduced using 2.5 μl of dithiothreitol (200 mM DTT stock solution) (Sigma) at 90°C for 20 min, and alkylated with 10 μl of Cysteine Blocking Reagent (Iodoacetamide, IAM, 200 mM Sigma) for 1 h at room temperature in the dark. DTT stock solution was then added to destroy the excess of IAM. After dilution with 300 μL of water and 100 μL of NH$_4$HCO$_3$ to raise pH 7.5-8.0, 5 μg of trypsin (Promega, Sequence Grade) was added and digestion was performed overnight at 37°C. Trypsin activity was stopped by adding 2 μl of neat formic acid and samples were dried by Speed Vacuum [69].

The peptide digests were desalted on the Discovery® DSC-18 solid phase extraction (SPE) 96-well Plate (25 mg/well) (Sigma-Aldrich Inc., St. Louis, MO, USA). The SPE plate was preconditioned with 1 mL of acetonitrile and 2 mL of water. After the sample loading, the SPE was washed with 1 mL of water. The adsorbed proteins were eluted with 800 μL of acetonitrile:water (80:20). After desalting, samples were vacuum evaporated and reconstituted with 20 μl of 0.05% formic acid in water. Two μL of stable-isotope-labeled peptide standard (DPEVRPTSAVAA, Val- 13C5 15N1 at V10, Cellmano Biotech Limited, Anhui, China) was spiked into the samples before the LC-MS/MS analysis and used for instrument quality control.

5.4.2. Label-free proteomic analysis

LC–MS/MS analyses were performed using a micro-LC Eksigent Technologies (Dublin, USA) system with a stationary phase of a Halo Fused C18 column (0.5 × 100 mm, 2.7 μm; Eksigent Technologies, Dublin, USA). The injection volume was 4.0 μL and the oven temperature was set at 40°C. The mobile phase was a mixture of 0.1% (v/v) formic acid in water (A) and 0.1% (v/v) formic acid in acetonitrile (B), eluting at a flow-rate of 15.0 μL min^{-1} at an increasing concentration of solvent B from 2% to 40% in 30 min. The LC system was interfaced with a 5600+ TripleTOF system (AB Sciex, Concord, Canada) equipped with a DuoSpray Ion Source and CDS (Calibrant Delivery System). Samples used to generate the SWATH-MS (Sequential window acquisition of all theoretical mass spectra) spectral library were subjected to the traditional data-dependent acquisition (DDA): the mass spectrometer analysis was performed using a mass range of 100–1500 Da (TOF scan with

an accumulation time of 0.25 s), followed by a MS/MS product ion scan from 200 to 1250 Da (accumulation time of 5.0 ms) with the abundance threshold set at 30 cps (35 candidate ions can be monitored during every cycle). Samples were then subjected to cyclic data independent analysis (DIA) of the mass spectra, using a 25-Da window. A 50-ms survey scan (TOF-MS) was performed, followed by MS/MS experiments on all precursors. These MS/MS experiments were performed in a cyclic manner using an accumulation time of 40 ms per 25-Da swath (36 swaths in total) for a total cycle time of 1.5408 s. The ions were fragmented for each MS/MS experiment in the collision cell using the rolling collision energy. The MS data were acquired with Analyst TF 1.7 (SCIEX, Concord, Canada). Three instrumental replicates for each sample were subjected to the DIA analysis [70,71].

5.4.3. Protein database search

The mass spectrometry files were searched using Protein Pilot (AB SCIEX, Concord, Canada) and Mascot (Matrix Science Inc., Boston, USA). Samples were input in the Protein Pilot software v4.2 (AB SCIEX, Concord, Canada), which employs the Paragon algorithm, with the following parameters: cysteine alkylation, digestion by trypsin, no special factors and False Discovery Rate at 1%. The UniProt Swiss-Prot reviewed database containing mouse proteins (version 12/10/2018, containing 25137 sequence entries). The Mascot search was performed on Mascot v2.4, the digestion enzyme selected was trypsin, with 2 missed cleavages and a search tolerance of 50 ppm was specified for the peptide mass tolerance, and 0.1 Da for the MS/MS tolerance. The charges of the peptides to search for were set to $2+$, $3+$ and $4+$, and the search was set on monoisotopic mass. The instrument was set to ESI-QUAD-TOF and the following modifications were specified for the search: carbamidomethyl cysteines as fixed modification and oxidized methionine as variable modification.

5.4.4. Protein quantification

The quantification was performed by integrating the extracted ion chromatogram of all the unique ions for a given peptide. The quantification was carried out with PeakView 2.0 and MarkerView 1.2. (Sciex, Concord, ON, Canada). Six peptides per protein and six transitions per peptide were extracted from the SWATH files. Shared peptides were excluded as well as peptides with modifications. Peptides with FDR lower than 1.0% were exported in MarkerView for the t-test.

5.5. Bioinformatic analysis

For bioinformatic analysis, DEPs from whole tissue preparations were pooled with correspondent synaptosomal DEPs: Wht-Hip ∪ Syn-Hip = HIP; Wht-Cb∪Syn-Cb = CB. Wht-Hip and Syn-Hip did not contain common DEPs at |FC| > 1.5 and p-value < 0.05 and were pooled without modifications. Wht-Cb and Syn-Cb (|FC| > 1.5 and p-value < 0.05) contained 3 common DEPs. In this case the DEP with lower p-value regardless of its FC was taken for further analysis. This resulted 155 and 54 unique DEPs in HIP and CB lists, respectively.

5.5.1. DAVID gene ontology (GO) analysis

Gene ontology (GO) analysis was performed using The Database for Annotation, Visualization and Integrated Discovery (DAVID) v.6.8 tool (https://david.ncifcrf.gov/) [72]. Overrepresented GO terms which passed Benjamini correction (p < 0.05) were considered significant.

5.5.2. STRING protein-protein interaction analysis

For prediction of protein-protein interactions and clustering using K-means algorithm, Search Tool for the Retrieval of Interacting Genes/Proteins (STRING) v10.5 online software was used (https://string-db.org/) [73].

5.5.3. IPA pathway analysis

For pathway analysis, Ingenuity Pathway Analysis package (Content version: 49932394; Release Date: 2019-11-14) was used. Ingenuity Canonical Pathways, Disease and Bio Functions, Upstream Regulators and Causal Network Regulators were downloaded using default settings.

5.6. Comparison with AD and epilepsy datasets

HIP ACN-KO differential protein expression was compared with published mouse AD and human epilepsy proteome datasets. The proteomics analysis by Neuner et al. [19] on 8-month-old 5xFAD hippocampus mouse model was used as AD reference and DEPs were matched by primary accession number as retrieved from the UniProtKB/Swiss-Prot reviewed database (release 2020_01). The dataset provided by Keren-Aviram et al. [20] on human refractory epilepsy was used as epileptic reference. In this case, to allow interspecies comparison, BioMart tool (www.ensembl.org) was used to extract genes that were orthologous between human and mouse. Afterwards, DEPs were again matched by primary accession number. In both the cases, the significance of the overlap between sets was evaluated through hypergeometric test, using as background reference the number of protein-coding transcripts detected by RNA-Seq (N=14,333 genes). Human epilepsy (HE) score shown in Fig. 4 and Suppl. Table 8B was calculated as an algebraic sum of numerical values (from 1 to 2 for up-regulated proteins and from -1 to -2 for down-regulated proteins) assigned to DEPs categories according to Keren-Aviram et al., 2018.

5.7. Barnes maze test

Barnes maze test is used to assess spatial memory and different search strategies in rodents [21,47]. The maze was made from a circular, 6-mm thick, white acrylic slab with a diameter of 1 m. Twenty holes with a diameter of 5 cm were made on the perimeter at a distance of 2.5 cm from the edge. This circular platform was then mounted on top of a stool, 60 cm above the ground and balanced. The escape cage was made using a plastic dark box to be easily cleaned. A piece of paper was put in the escape cage, in order to make it more attractive for the mice, and it was changed after every animal test. The maze was placed in the center of a dedicated room and two 120 W lights were placed on the edges of the room facing towards the ceiling about 2 m of the way up from the floor. Four coloured-paper shapes (squares, triangles, circles) were mounted around the room as visual cues, in addition to the asymmetry of the room itself. After testing each mouse, the whole maze was thoroughly cleaned using 70% ethanol and the maze was rotated by 3 holes clockwise to avoid the formation of intra-maze odour cues. All sessions were recorded and videos were analysed with SMART V2.5.21 software. The animals interacted with the Barnes maze in three phases: habituation (Hab), acquisition training (AT), and acquisition probe (AP). After each experimental session the mouse is stored in an holding cage, and after all mice from one home cage completed testing for the day, they were placed back in their home cage together.

On the first day of testing, the habituation phase consisted in placing the mouse in the escape tunnel for 1 min. After that the mouse was placed in the middle of the maze and was allowed to freely explore the maze. The habituation session ended when the mouse entered the escape tunnel or after 5 min elapsed. During the habituation session bight light was turned on but buzzer was turned off. If the mouse did not enter on his own during that time, it was gently nudged to enter and left in the cage for 1 min. The first acquisition training session (AT1) was done 1.5 h after habituation. The mouse was brought in the maze room on an acrylic platform 25 × 25 cm covered by a cylindrical container. After positioning in the center of the maze and 10 s elapsed the buzzer was switched on, the container was lifted, and the mouse was free to explore the maze. The session ended when the mouse entered the escape tunnel or after 3 min elapsed. If the mouse did not enter the escape box in 3 min, it was gently nudged to enter and left inside for 30 sec. On days 2 (AT2, AT3) and 3 (AT4, AT5) two acquisition trainings per day were performed with 1.5 h of interval between sessions for each animal. On the

11

day 4, three acquisition training sessions were performed (AT6, AT7, AT8) with 15 min of interval between one another, for each animal. On the day 5 acquisition probe (AP) session was performed: the escape cage was removed, the mouse was brought to the center of the maze and, after 10 sec, the buzzer was turned on and the container was removed. Each mouse was given 90 sec to explore the maze, at the end of which, the buzzer was turned off and the mouse was returned to its holding cage.

The search strategies were categorized as follows. The direct (spatial) search was computed when the animal moved directly to the target hole or to an adjacent hole before the target (for the first search) or when mouse approaches target hole from at least 4 holes far away. The random search strategy was computed when at least three visits before the target hole happened in an unsystematic manner, i.e., the animal visited non-adjacent holes and/or crossed the maze. The serial search strategy was computed when there were visits to at least three sequential holes in clockwise or counter-clockwise manner from the target hole. Lastly, return strategy was identified when mouse returned to the target hole from 1-2 adjacent holes. The return strategy can be considered as an exploration of the area around the target hole. In Barnes maze, 10 ACN-Ctr and 10 ACN-KO male mice were tested. During AP session, one ACN-Ctr mouse was excluded because it fell down from the maze and after that showed increased anxiety.

5.8. Electro-encephalographic (EEG) recording

ACN-Ctr and ACN-KO mice were anesthetized with isoflurane (5% (v /v) in 1 L/min O_2. Four screw electrodes (Bilaney Consultants GMBH, Dusseldorf, Germany) were inserted bilaterally through the skull over the cortex (anteroposterior, +2.0–3.0 mm; left–right 2.0 mm from bregma); a further electrode was placed into the nasal bone as ground. The 5 electrodes were connected to a pedestal (Bilaney, Dusseldorf, Germany) and fixed with acrylic cement (Palavit, New Galetti and Rossi, Milan, Italy). The animals were allowed to recover for a week from surgery before the experiment. EEG activity was recorded in a Faraday chamber using a Power-Lab digital acquisition system (AD Instruments, Bella Vista, Australia; sampling rate 100 Hz, resolution 0.2 Hz) in freely moving awake mice. Basal cerebral activity was recorded continuously for 24 h (from 5 pm to 4 pm). Segments with movement artefacts or electrical noise were excluded from statistical analysis. All EEG traces were also analysed and scored for the presence of spikes, which were discriminated offline with the spike histogram extension of the software (LabChart v8 Pro Windows). Spikes were defined as having a duration < 200 ms with baseline amplitude set to 4.5 times the standard deviation of the EEG signal (determined during inter-spike activity periods, whereas repetitive spiking activity was defined as 3 or more spikes lasting < 5 s).

5.9. Statistical analysis

Statistical analysis was performed using GraphPad Prism software v7. For Western blot validation of SG-MS results (Fig. 1C), one sample t-test was used. For comparison of two sample groups, a two-tailed un-paired t-test (Fig. 7B; Suppl. Figs. 8B and 9B-D) or unpaired t test with Welch's correction (Suppl. Fig. 3) were used. For comparison of ACN-KO proteomics with 5xFAD and HE datasets (Fig. 4), hypergeometric test was used. Barnes maze results were analysed as follows: parameters of repeated AT sessions (Fig. 5B) were analysed using two-way ANOVA for repeated measures; single parameters of habituation, AT1 and AP sessions (Figs. 5C,D and 6B) were analysed using a two-tailed unpaired t-test; search strategies during AP session (Fig. 5E) were analysed using Chi-square (Fisher's exact) test; differences in distance and time travelled in external and internal zones of Barnes maze between genotypes (Fig. 6C,D) were analysed by two-way ANOVA Sidak's multiple comparisons test. Risk to develop seizure between groups was analysed using log-rank (Mantel-Cox) test. qPCR results in Fig. 7C were analysed using one-way ANOVA with Tukey's posthoc test. The distance, time and

speed of mice movements during Open field test (Suppl. Fig. 9A) were analysed using two-way ANOVA Sidak's multiple comparisons test. In all tests, differences were considered significant at p < 0.05. Detailed report on statistical methods and results is provided in Suppl. Table 9.

CRediT authorship contribution statement

Laura Tapella: Investigation, Methodology, Formal analysis, Writing – original draft, Writing – review & editing, Funding acquisition. **Giulia Dematteis:** Investigation, Methodology, Formal analysis, Writing – original draft, Writing – review & editing. **Federico Alessandro Ruffinatti:** Methodology, Formal analysis, Writing – review & editing. **Luisa Ponzoni:** Investigation, Methodology, Formal analysis. **Fabio Fiordaliso:** Investigation, Methodology, Formal analysis. **Alessandro Corbelli:** Investigation, Methodology, Formal analysis. **Enrico Albanese:** Investigation. **Beatrice Pistolato:** Investigation. **Jessica Pagano:** Investigation, Methodology, Formal analysis. **Elettra Barberis:** Investigation. **Emilio Marengo:** Resources, Software. **Claudia Balducci:** Investigation, Resources, Writing – review & editing. **Gianluigi Forloni:** Resources, Writing – review & editing. **Chiara Verpelli:** Investigation, Resources, Writing – review & editing. **Carlo Sala:** Resources, Writing – review & editing. **Carla Distasi:** Resources, Writing – review & editing. **Mariaelvina Sala:** Investigation, Resources, Writing – review & editing. **Marcello Manfredi:** Investigation, Methodology, Formal analysis, Data curation, Writing – review & editing, Funding acquisition. **Armando A. Genazzani:** Conceptualization, Supervision, Writing – review & editing, Funding acquisition. **Dmitry Lim:** Conceptualization, Formal analysis, Investigation, Writing – original draft, Writing – review & editing, Supervision, Project administration, Funding acquisition.

Declaration of Competing Interest

The authors declare no conflict of interests.

Acknowledgements

Supplementary materials

Supplementary material associated with this article can be found, in the online version, at doi:10.1016/j.ceca.2021.102480.

References

[1] A. Verkhratsky, M. Nedergaard, Physiology of Astroglia, Physiol. Rev. 98 (2018) 239–389, https://doi.org/10.1152/physrev.00042.2016.

[2] B.S. Khakh, M.V. Sofroniew, Diversity of astrocyte functions and phenotypes in neural circuits, Nat. Neurosci. 18 (2015) 942–952, https://doi.org/10.1038/nn.4043.

[3] D. Lim, A. Semyanov, A. Genazzani, A. Verkhratsky, Calcium signaling in neuroglia. International Review of Cell and Molecular Biology, Academic Press, 2021, https://doi.org/10.1016/bs.ircmb.2021.01.003.

[4] D. Lim, J.J. Rodríguez-Arellano, V. Parpura, R. Zorec, F. Zeidán-Chuliá, A. A. Genazzani, A. Verkhratsky, Calcium signalling toolkits in astrocytes and spatio-temporal progression of Alzheimer's disease, Curr. Alzheimer Res. 13 (2016) 359-369.

[5] L. Nikolic, P. Nobili, W. Shen, E. Audinat, Role of astrocyte purinergic signaling in epilepsy, Glia. (2019). 10.1002/glia.23747.

[6] D. Lim, V. Ronco, A.A. Grolla, A. Verkhratsky, A.A. Genazzani, Glial calcium signalling in Alzheimer's disease, Rev. Physiol. Biochem. Pharmacol. 167 (2014) 45–65, https://doi.org/10.1007/112_2014_19.

12

[7] T.A. Fiacco, C. Agulhon, K.D. McCarthy, Sorting out astrocyte physiology from pharmacology, Annu. Rev. Pharmacol. Toxicol. 49 (2009) 151–174, https://doi.org/10.1146/annurev.pharmtox.011008.145602.

[8] E. Bindocci, I. Savtchouk, N. Liaudet, D. Becker, G. Carriero, A. Volterra, Three-dimensional Ca2+ imaging advances understanding of astrocyte biology, Science 356 (2017), https://doi.org/10.1126/science.aai8185.

[9] L. Tapella, T. Soda, L. Mapelli, V. Bortolotto, H. Bondi, F.A. Ruffinatti, G. Dematteis, A. Stevano, M. Dionisi, S. Ummarino, A. Di Ruscio, C. Distasi, M. Grilli, A.A. Genazzani, E. D'Angelo, F. Moccia, D. Lim, Deletion of calcineurin from GFAP-expressing astrocytes impairs excitability of cerebellar and hippocampal neurons through astroglial Na+ /K+ ATPase, Glia 68 (2020) 543–560, https://doi.org/10.1002/glia.23737.

[10] M. Oh-hora, A. Rao, Calcium signaling in lymphocytes, Curr. Opin. Immunol. 20 (2008) 250–258, https://doi.org/10.1016/j.coi.2008.04.004.

[11] V. Parra, B.A. Rothermel, Calcineurin signaling in the heart: The importance of time and place, J. Mol. Cell. Cardiol. 103 (2017) 121–136, https://doi.org/10.1016/j.yjmcc.2016.12.006.

[12] M.K. Tu, J.B. Levin, A.M. Hamilton, L.N. Borodinsky, Calcium signaling in skeletal muscle development, maintenance and regeneration, Cell Calcium 59 (2016) 91–97, https://doi.org/10.1016/j.ceca.2016.02.005.

[13] D. Sitara, A.O. Aliprantis, Transcriptional regulation of bone and joint remodeling by NFAT, Immunol. Rev. 233 (2010) 286–300, https://doi.org/10.1111/j.0105-2896.2009.00849.x.

[14] K. Baumgärtel, I.M. Mansuy, Neural functions of calcineurin in synaptic plasticity and memory, Learn. Mem. 19 (2012) 375–384, https://doi.org/10.1101/lm.027201.112.

[15] G. Dematteis, E. Restelli, R. Chiesa, E. Aronica, A.A. Genazzani, D. Lim, L. Tapella, Calcineurin controls expression of EAAT1/GLAST in mouse and human cultured astrocytes through dynamic regulation of protein synthesis and degradation, Int. J. Mol. Sci. 21 (2020), https://doi.org/10.3390/ijms21062213.

[16] Y. Zhang, K. Chen, S.A. Sloan, M.L. Bennett, A.R. Scholze, S. O'Keeffe, H. P. Phatnani, P. Guarnieri, C. Caneda, N. Ruderisch, S. Deng, S.A. Liddelow, C. Zhang, R. Daneman, T. Maniatis, B.A. Barres, J.Q. Wu, An RNA-sequencing transcriptome and splicing database of glia, neurons, and vascular cells of the cerebral cortex, J. Neurosci. 34 (2014) 11929–11947, https://doi.org/10.1523/JNEUROSCI.1860-14.2014.

[17] C.T. Loy, P.R. Schofield, A.M. Turner, J.B.J. Kwok, Genetics of dementia, Lancet 383 (2014) 828–840, https://doi.org/10.1016/S0140-6736(13)60630-3.

[18] M.A. Nance, Genetics of Huntington disease, Handb Clin Neurol 144 (2017) 3–14, https://doi.org/10.1016/B978-0-12-801893-4.00001-8.

[19] S.M. Neuner, L.A. Wilmott, B.R. Hoffmann, K. Mozhui, C.C. Kaczorowski, Hippocampal proteomics defines pathways associated with memory decline and resilience in normal aging and Alzheimer's disease mouse models, Behav. Brain Res. 322 (2017) 288–298, https://doi.org/10.1016/j.bbr.2016.06.002.

[20] G. Keren-Aviram, F. Dachet, S. Bagla, K. Balan, J.A. Loeb, E.A. Dratz, Proteomic analysis of human epileptic neocortex predicts vascular and glial changes in epileptic regions, PLoS ONE 13 (2018), e0195639, https://doi.org/10.1371/journal.pone.0195639.

[21] K. Gawel, E. Gibula, M. Marszalek-Grabska, J. Filarowska, J.H. Kotlinska, Assessment of spatial learning and memory in the Barnes maze task in rodents-methodological consideration, Naunyn Schmiedebergs Arch. Pharmacol. 392 (2019) 1–18, https://doi.org/10.1007/s00210-018-1589-y.

[22] R.J. Racine, Modification of seizure activity by electrical stimulation. II. Motor seizure, Electroencephalogr Clin. Neurophysiol. 32 (1972) 281–294, https://doi.org/10.1016/0013-4694(72)90177-0.

[23] J.P. Pinel, L.I. Rovner, Experimental epileptogenesis: kindling-induced epilepsy in rats, Exp. Neurol. 58 (1978) 190–202, https://doi.org/10.1016/0014-4886(78)90133-4.

[24] M. Lévesque, P. Salami, Z. Shiri, M. Avoli, Interictal oscillations and focal epileptic disorders, Eur. J. Neurosci. 48 (2018) 2915–2927, https://doi.org/10.1111/ejn.13628.

[25] E.A. van Vliet, E. Aronica, A. Vezzani, T. Ravizza, Review: Neuroinflammatory pathways as treatment targets and biomarker candidates in epilepsy: emerging evidence from preclinical and clinical studies, Neuropathol. Appl. Neurobiol. 44 (2018) 91–111, https://doi.org/10.1111/nan.12444.

[26] A.M. Fernandez, S. Jimenez, M. Mecha, D. Dávila, C. Guaza, J. Vitorica, I. Torres-Aleman, Regulation of the phosphatase calcineurin by insulin-like growth factor I unveils a key role of astrocytes in Alzheimer's pathology, Mol. Psychiatry. 17 (2012) 705–718, https://doi.org/10.1038/mp.2011.128.

[27] J.L. Furman, C.M. Norris, Calcineurin and glial signaling: neuroinflammation and beyond, J. Neuroinflammation 11 (2014) 158, https://doi.org/10.1186/s12974-014-0158-7.

[28] D. Lim, F. Rocchio, M. Lisa, M. Fcancesco, From Pathology to Physiology to Calcineurin Signalling in Astrocytes, Opera Medica et Physiologica 2 (2016) 122–140, https://doi.org/10.20388/OMP2016.002.0029.

[29] J.A. Filosa, M.T. Nelson, L.V. Gonzalez Bosc, Activity-dependent NFATc3 nuclear accumulation in pericytes from cortical parenchymal microvessels, Am. J. Physiol., Cell Physiol. 293 (2007) C1797–C1805, https://doi.org/10.1152/ajpcell.00554.2006.

[30] D. Lim, L. Mapelli, P.L. Canonico, F. Moccia, A.A. Genazzani, Neuronal Activity-Dependent Activation of Astroglial Calcineurin in Mouse Primary Hippocampal Cultures, Int. J. Mol. Sci. 19 (2018), https://doi.org/10.3390/ijms19102997.

[31] Alzheimer's Association Calcium Hypothesis Workgroup, Calcium Hypothesis of Alzheimer's disease and brain aging: A framework for integrating new evidence into a comprehensive theory of pathogenesis, Alzheimers Dement. 13 (2017) 178–182, https://doi.org/10.1016/j.jalz.2016.12.006, e17.

[32] R.H. Swerdlow, Mitochondria and Mitochondrial Cascades in Alzheimer's Disease, J. Alzheimers Dis. 62 (2018) 1403–1416, https://doi.org/10.3233/JAD-170585.

[33] M.S. Hipp, P. Kasturi, F.U. Hartl, The proteostasis network and its decline in ageing, Nat. Rev. Mol. Cell Biol. 20 (2019) 421–435, https://doi.org/10.1038/s41580-019-0101-y.

[34] J. Cheng, B.J. North, T. Zhang, X. Dai, K. Tao, J. Guo, W. Wei, The emerging roles of protein homeostasis-governing pathways in Alzheimer's disease, Aging Cell 17 (2018) e12801, https://doi.org/10.1111/acel.12801.

[35] S. Paillusson, R. Stoica, P. Gomez-Suaga, D.H.W. Lau, S. Mueller, T. Miller, C.C. J. Miller, There's something wrong with my mam; the er-mitochondria axis and neurodegenerative diseases, Trends Neurosci. 39 (2016) 146–157, https://doi.org/10.1016/j.tins.2016.01.008.

[36] E. Area-Gomez, A. de Groof, E. Bonilla, J. Montesinos, K. Tanji, I. Boldogh, L. Pon, E.A. Schon, A key role for MAM in mediating mitochondrial dysfunction in Alzheimer disease, Cell Death Dis. 9 (2018) 335, https://doi.org/10.1038/s41419-017-0215-0.

[37] G. Dematteis, G. Vydmantaité, F.A. Ruffinatti, M. Chahin, S. Farruggio, E. Barberis, E. Ferrari, E. Marengo, C. Distasi, R. Morkūnienė, A.A. Genazzani, M. Grilli, E. Grossini, M. Corazzari, M. Manfredi, D. Lim, A. Jekabsone, L. Tapella, Proteomic analysis links alterations of bioenergetics, mitochondria-ER interactions and proteostasis in hippocampal astrocytes from 3xTg-AD mice, Cell Death Dis 11 (2020) 645, https://doi.org/10.1038/s41419-020-02911-1.

[38] D. Lim, G. Dematteis, L. Tapella, A.A. Genazzani, T. Calì, M. Brini, A. Verkhratsky, Ca2+ handling at the mitochondria-ER contact sites in neurodegeneration, Cell Calcium 98 (2021), 102453, https://doi.org/10.1016/j.ceca.2021.102453.

[39] M.D. Sans, J.A. Williams, Calcineurin is required for translational control of protein synthesis in rat pancreatic acini, Am. J. Physiol., Cell Physiol. 287 (2004) C310–C319, https://doi.org/10.1152/ajpcell.00534.2003.

[40] G.M. Cereghetti, A. Stangherlin, O. Martins de Brito, C.R. Chang, C. Blackstone, P. Bernardi, L. Scorrano, Dephosphorylation of Drp1 by calcineurin regulates translocation of Drp1 to mitochondria, Proc. Natl. Acad. Sci. U.S.A. 105 (2008) 15803–15808, https://doi.org/10.1073/pnas.0808249105.

[41] P.T. Pfluger, D.G. Kabra, M. Aichler, S.C. Schriever, K. Pfuhlmann, V.C. García, M. Lehti, J. Weber, M. Kutschke, J. Rozman, J.W. Elrod, A.L. Hevener, A. Feuchtinger, M. Hrabě de Angelis, A. Walch, S.M. Rollmann, B.J. Aronow, T. D. Müller, D. Perez-Tilve, M. Jastroch, M. De Luca, J.D. Molkentin, M.H. Tschöp, Calcineurin links mitochondrial elongation with energy metabolism, Cell Metab. 22 (2015) 838–850, https://doi.org/10.1016/j.cmet.2015.08.022.

[42] F. Ruffinatti, L. Tapella, I. Gregnanin, A. Stevano, G. Chiorino, P.L. Canonico, C. Distasi, A.A. Genazzani, D. Lim, Transcriptional remodeling in primary hippocampal astrocytes from an Alzheimer's disease mouse model, Curr. Alzheimer Res.. (2018). 10.2174/1567205015666180613113924.

[43] M. Orre, W. Kamphuis, L.M. Osborn, A.H.P. Jansen, L. Kooijman, K. Bossers, E. M. Hol, Isolation of glia from Alzheimer's mice reveals inflammation and dysfunction, Neurobiol Aging 35 (2014) 2746–2760, https://doi.org/10.1016/j.neurobiolaging.2014.06.004.

[44] N. Nicastro, F. Assal, M. Seeck, From here to epilepsy: the risk of seizure in patients with Alzheimer's disease, Epileptic Disord. 18 (2016) 1–12, https://doi.org/10.1684/epd.2016.0808.

[45] K.A. Vossel, M.C. Tartaglia, H.B. Nygaard, A.Z. Zeman, B.L. Miller, Epileptic activity in Alzheimer's disease: causes and clinical relevance, Lancet Neurol. 16 (2017) 311–322, https://doi.org/10.1016/S1474-4422(17)30044-3.

[46] S. Sharma, S. Rakoczy, H. Brown-Borg, Assessment of spatial memory in mice, Life Sci. 87 (2010) 521–536, https://doi.org/10.1016/j.lfs.2010.09.004.

[47] F.E. Harrison, R.S. Reiserer, A.J. Tomarken, M.P. McDonald, Spatial and nonspatial escape strategies in the Barnes maze, Learn. Mem. 13 (2006) 809–819, https://doi.org/10.1101/lm.334306.

[48] H. Eichenbaum, On the integration of space, time, and memory, Neuron 95 (2017) 1007–1018, https://doi.org/10.1016/j.neuron.2017.06.036.

[49] J. Sugar, M-B. Moser, Episodic memory: Neuronal codes for what, where, and when, Hippocampus 29 (2019) 1190–1205, https://doi.org/10.1002/hipo.23132.

[50] J. Cheng, D. Ji, Rigid firing sequences undermine spatial memory codes in a neurodegenerative mouse model, Elife 2 (2013) e00647, https://doi.org/10.7554/eLife.00647.

[51] P.T. Macêdo, A.C.Q. Aquino, Y.S.R. Meurer, L.E.M. Brandão, C.L.C. Campêlo, R. H. Lima, M.R. Costa, A.M. Ribeiro, R.H. Silva, Subtle alterations in spatial memory induced by amyloid peptides infusion in rats, Front. Aging Neurosci. 10 (2018) 18, https://doi.org/10.3389/fnagi.2018.00018.

[52] Y. Van Den Herrewegen, L. Denewet, A. Buckinx, G. Albertini, A. Van Eeckhaut, I. Smolders, D. De Bundel, The barnes maze task reveals specific impairment of spatial learning strategy in the intrahippocampal kainic acid model for temporal lobe epilepsy, Neurochem. Res. 44 (2019) 600–608, https://doi.org/10.1007/s11064-018-2610-z.

[53] M.E. Bach, R.D. Hawkins, M. Osman, E.R. Kandel, M. Mayford, Impairment of spatial but not contextual memory in CaMKII mutant mice with a selective loss of hippocampal LTP in the range of the theta frequency, Cell 81 (1995) 905–915, https://doi.org/10.1016/0092-8674(95)90010-1.

[54] X.-B. Liu, K.D. Murray, Neuronal excitability and calcium/calmodulin-dependent protein kinase type II: location, location, location, Epilepsia 53 (Suppl 1) (2012) 45–52, https://doi.org/10.1111/j.1528-1167.2012.03474.x.

[55] A. Vezzani, S. Balosso, T. Ravizza, Neuroinflammatory pathways as treatment targets and biomarkers in epilepsy, Nat. Rev. Neurol. 15 (2019) 459–472, https://doi.org/10.1038/s41582-019-0217-x.

[56] Y. Ye, J. Xiong, J. Hu, M. Kong, L. Cheng, H. Chen, T. Li, L. Jiang, Altered hippocampal myelinated fiber integrity in a lithium-pilocarpine model of temporal

13

lobe epilepsy: a histopathological and stereological investigation, Brain Res. 1522 (2013) 76–87, https://doi.org/10.1016/j.brainres.2013.05.026.

[57] X.-J. Song, W. Han, R. He, T.-Y. Li, L.-L. Xie, L. Cheng, H.-S. Chen, L. Jiang, Alterations of hippocampal myelin sheath and axon sprouting by status convulsion and regulating lingo-1 expression with RNA interference in immature and adult rats, Neurochem. Res. 43 (2018) 721–735, https://doi.org/10.1007/s11064-018-2474-2.

[58] L. Kandratavicius, P.A. Balista, C. Lopes-Aguiar, R.N. Ruggiero, E.H. Umeoka, N. Garcia-Cairasco, L.S. Bueno-Junior, J.P. Leite, Animal models of epilepsy: use and limitations, Neuropsychiatr Dis. Treat. 10 (2014) 1693–1705, https://doi.org/10.2147/NDT.S50371.

[59] F. Tang, A.M.S. Hartz, B. Bauer, Drug-Resistant Epilepsy: Multiple Hypotheses, Few Answers, Front. Neurol. 8 (2017) 301, https://doi.org/10.3389/fneur.2017.00301.

[60] J.J. Rodríguez, C.-Y. Yeh, S. Terzieva, M. Olabarria, M. Kulijewicz-Nawrot, A. Verkhratsky, Complex and region-specific changes in astroglial markers in the aging brain, Neurobiol. Aging. 35 (2014) 15–23, https://doi.org/10.1016/j.neurobiolaging.2013.07.002.

[61] A. Verkhratsky, R. Zorec, J.J. Rodríguez, V. Parpura, Astroglia dynamics in ageing and Alzheimer's disease, Curr. Opin. Pharmacol. 26 (2016) 74–79, https://doi.org/10.1016/j.coph.2015.09.011.

[62] A. Verkhratsky, J.J. Rodrigues, A. Pivoriunas, R. Zorec, A. Semyanov, Astroglial atrophy in Alzheimer's disease, Pflugers Arch. (2019). 10.1007/s00424-019-02310-2.

[63] S. Negri, P. Faris, T. Soda, F. Moccia, Endothelial signaling at the core of neurovascular coupling: The emerging role of endothelial inward-rectifier K+ (Kir2.1) channels and N-methyl-d-aspartate receptors in the regulation of cerebral blood flow, Int. J. Biochem. Cell Biol. 135 (2021), 105983, https://doi.org/10.1016/j.biocel.2021.105983.

[64] T.A. Longden, F. Dabertrand, M. Koide, A.L. Gonzales, N.R. Tykocki, J.E. Brayden, D. Hill-Eubanks, M.T. Nelson, Capillary K+-sensing initiates retrograde hyperpolarization to increase local cerebral blood flow, Nat. Neurosci. 20 (2017) 717–726, https://doi.org/10.1038/nn.4533.

[65] E. Zuccolo, D.A. Kheder, D. Lim, A. Perna, F.D. Nezza, L. Botta, G. Scarpellino, S. Negri, S. Martinotti, T. Soda, G. Forcaia, L. Riboni, E. Ranzato, G. Sancini, L. Ambrosone, E. D'Angelo, G. Guerra, F. Moccia, Glutamate triggers intracellular Ca2+ oscillations and nitric oxide release by inducing NAADP- and InsP3

-dependent Ca2+ release in mouse brain endothelial cells, J. Cell. Physiol. 234 (2019) 3538–3554, https://doi.org/10.1002/jcp.26953.

[66] J.R. Neilson, M.M. Winslow, E.M. Hur, G.R. Crabtree, Calcineurin B1 is essential for positive but not negative selection during thymocyte development, Immunity 20 (2004) 255–266.

[67] C. Gregorian, J. Nakashima, J.Le Belle, J. Ohab, R. Kim, A. Liu, K.B. Smith, M. Groszer, A.D. Garcia, M.V. Sofroniew, S.T. Carmichael, H.I. Kornblum, X. Liu, H. Wu, Pten deletion in adult neural stem/progenitor cells enhances constitutive neurogenesis, J. Neurosci. 29 (2009) 1874–1886, https://doi.org/10.1523/JNEUROSCI.3095-08.2009.

[68] F. Gillardon, Differential mitochondrial protein expression profiling in neurodegenerative diseases, Electrophoresis 27 (2006) 2814–2818, https://doi.org/10.1002/elps.200500911.

[69] F. Rocchio, L. Tapella, M. Manfredi, M. Chisari, F. Ronco, F.A. Ruffinatti, E. Conte, P.L. Canonico, M.A. Sortino, M. Grilli, E. Marengo, A.A. Genazzani, D. Lim, Gene expression, proteome and calcium signaling alterations in immortalized hippocampal astrocytes from an Alzheimer's disease mouse model, Cell Death Dis. 10 (2019) 24, https://doi.org/10.1038/s41419-018-1264-8.

[70] S. Martinotti, M. Patrone, M. Manfredi, F. Gosetti, M. Pedrazzi, E. Marengo, E. Ranzato, HMGB1 Osteo-Modulatory Action on Osteosarcoma SaOS-2 Cell Line: An Integrated Study From Biochemical and -Omics Approaches, J. Cell. Biochem. 117 (2016) 2559–2569, https://doi.org/10.1002/jcb.25549.

[71] E. Dalla Pozza, M. Manfredi, J. Brandi, A. Buzzi, E. Conte, R. Pacchiana, D. Cecconi, E. Marengo, M. Donadelli, Trichostatin A alters cytoskeleton and energy metabolism of pancreatic adenocarcinoma cells: an in depth proteomic study, J. Cell. Biochem. 119 (2018) 2696–2707, https://doi.org/10.1002/jcb.26436.

[72] D.W. Huang, B.T. Sherman, R.A. Lempicki, Systematic and integrative analysis of large gene lists using DAVID bioinformatics resources, Nat. Protoc. 4 (2009) 44–57, https://doi.org/10.1038/nprot.2008.211.

[73] D. Szklarczyk, J.H. Morris, H. Cook, M. Kuhn, S. Wyder, M. Simonovic, A. Santos, N.T. Doncheva, A. Roth, P. Bork, L.J. Jensen, C. von Mering, The STRING database in 2017: quality-controlled protein-protein association networks, made broadly accessible, Nucleic Acids Res. 45 (2017) D362–D368, https://doi.org/10.1093/nar/gkw937.

14

Chapter 3

Article

Calcineurin Controls Cellular Prion Protein Expression in Mouse Astrocytes

Giulia Dematteis [1], Elena Restelli [2], Virginia Vita Vanella [3], Marcello Manfredi [3], Emilio Marengo [4], Marco Corazzari [5], Armando A. Genazzani [1], Roberto Chiesa [2], Dmitry Lim [1,*] and Laura Tapella [1,*]

[1] Department of Pharmaceutical Sciences, Università del Piemonte Orientale "Amedeo Avogadro", 28100 Novara, Italy; giulia.dematteis@uniupo.it (G.D.); armando.genazzani@uniupo.it (A.A.G.)
[2] Department of Neuroscience, Istituto di Ricerche Farmacologiche Mario Negri IRCCS, 20156 Milan, Italy; elena.restelli@marionegri.it (E.R.); roberto.chiesa@marionegri.it (R.C.)
[3] Department of Translational Medicine, Center for Translational Research on Autoimmune and Allergic Disease (CAAD), Università del Piemonte Orientale "Amedeo Avogadro", 28100 Novara, Italy; virginia.vanella@uniupo.it (V.V.V.); marcello.manfredi@uniupo.it (M.M.)
[4] Department of Sciences and Technological Innovation, Università del Piemonte Orientale "Amedeo Avogadro", 28100 Novara, Italy; emilio.marengo@uniupo.it
[5] Department of Health Science (DSS), Center for Translational Research on Autoimmune and Allergic Disease (CAAD) & Interdisciplinary Research Center of Autoimmune Diseases (IRCAD), Università del Piemonte Orientale "Amedeo Avogadro", 28100 Novara, Italy; marco.corazzari@uniupo.it
* Correspondence: dmitry.lim@uniupo.it (D.L.); laura.tapella@uniupo.it (L.T.); Tel.: +39-0321-375822 (L.T.)

Abstract: Prion diseases arise from the conformational conversion of the cellular prion protein (PrP^C) into a self-replicating prion isoform (PrP^{Sc}). Although this process has been studied mostly in neurons, a growing body of evidence suggests that astrocytes express PrP^C and are able to replicate and accumulate PrP^{Sc}. Currently, prion diseases remain incurable, while downregulation of PrP^C represents the most promising therapy due to the reduction of the substrate for prion conversion. Here we show that the astrocyte-specific genetic ablation or pharmacological inhibition of the calcium-activated phosphatase calcineurin (CaN) reduces PrP^C expression in astrocytes. Immunocytochemical analysis of cultured CaN-KO astrocytes and isolation of synaptosomal compartments from the hippocampi of astrocyte-specific CaN-KO (ACN-KO) mice suggest that PrP^C is downregulated both in vitro and in vivo. The downregulation occurs without affecting the glycosylation of PrP^C and without alteration of its proteasomal or lysosomal degradation. Direct assessment of the protein synthesis rate and shotgun mass spectrometry proteomics analysis suggest that the reduction of PrP^C is related to the impairment of global protein synthesis in CaN-KO astrocytes. When WT-PrP and PrP-D177N, a mouse homologue of a human mutation associated with the inherited prion disease fatal familial insomnia, were expressed in astrocytes, CaN-KO astrocytes showed an aberrant localization of both WT-PrP and PrP-D177N variants with predominant localization to the Golgi apparatus, suggesting that ablation of CaN affects both WT and mutant PrP proteins. These results provide new mechanistic details in relation to the regulation of PrP expression in astrocytes, suggesting the therapeutic potential of astroglial cells.

Keywords: astrocytes; calcineurin; FK506; prion protein; protein synthesis; calcium; neuroinflammation

1. Introduction

Prion diseases are a group of neurodegenerative diseases affecting humans and animals characterized by the accumulation of a misfolded isoform of the cellular prion protein (PrP^C), commonly referred to as PrP^{Sc}, in the brain [1]. Human prion diseases include (I) iatrogenic forms, e.g., Kuru, iatrogenic Creutzfeldt–Jakob disease (iCJD) and variant CJD; (II) sporadic forms, e.g., sporadic CJD and fatal insomnia (sFI); and (III) familial forms carrying point or insertional mutations in the *PRNP* gene encoding PrP^C, such as genetic CJD,

69

fatal familial insomnia (FFI) and Gerstmann–Straussler–Scheinker (GSS) syndrome [2,3]. Prion diseases have a long incubation period before clinical manifestation. Patients develop heterogeneous symptoms, such as dementia, ataxia, myoclonus and other motor and neuropsychiatric manifestations, that lead to a fatal outcome. Spongiform vacuolation of the grey matter, neuronal loss and chronic inflammation, with astrogliosis and microgliosis, are the main neuropathological hallmarks of prion diseases [4].

In prion research, many different mouse and cellular models have been described to understand the pathological mechanism and to define a possible therapeutic strategy [5–7], with the main efforts focused on neurons. However, a growing body of evidence suggests that astroglial cells can contribute to the pathogenesis of prion diseases [8,9].

Astrocytes are the principal homeostatic cells of the central nervous system (CNS). They are responsible for structural, functional and metabolic support to neurons and other cells in the CNS [10–12]. In prion diseases, astrocytes become reactive, losing their ability to control the CNS environment [6,13]. Reactive gliosis is an early pathological marker of neuropathology, which develops in concomitance with prion deposition and leads to neuronal dysfunction [13]. It has been reported that the expression of PrP^C in astrocytes contributes to their differentiation and is necessary for correct neuronal function [14–16].

Calcium (Ca^{2+}) signals are essential for cell life, and, if not properly controlled, aberrant Ca^{2+} signals may result in cell malfunction or even cell death [17,18]. To induce specific downstream signaling events, Ca^{2+} signals are decoded by specialized Ca^{2+}-binding proteins, the most important of which is, perhaps, the Ca^{2+}/calmodulin-activated phosphatase calcineurin (CaN). Structurally, CaN is a heterodimer, composed of a catalytic CaNA subunit and an obligatory regulatory CaNB subunit. Binding of Ca^{2+} ions to CaNB and concomitant interaction of the Ca^{2+}/calmodulin complex with CaNA lead to displacement of the autoinhibitory domain, enabling the interaction of CaN with its substrates. In the brain, CaN is expressed at high levels in neurons, in which it plays a fundamental role during neuronal plasticity [17]. However, CaN expressed in astroglial cells receives continuously increasing attention due to its key role in processes of neuroinflammation and reactive astrogliosis, which are characteristics of virtually all chronic neuropathological conditions. CaN acts through both direct protein dephosphorylation and activation of gene transcription, e.g., through the direct activation of transcription factors of activated T-cells (NFAT) [10,19,20]. Over-activation of CaN plays a pivotal role in reactive gliosis and neuroinflammation in Alzheimer's disease (AD) [10,11,20–24]. A preclinical alteration of CaN has been reported in the TgPG14 mouse model of inherited prion disease [25,26], and treatment of prion-infected mice with the CaN inhibitor FK506 delays disease onset and promotes PrP degradation [27–29]. Moreover, PrP expression level influences the incubation period and disease duration in both prion-infected and mutant PrP mice [30–34]. Recently, a physiological role for CaN in astrocytes has been proposed, correlated with the control of neuronal excitability and astrocytic protein synthesis [35–37].

A growing body of evidence suggests that reduction of PrP^C expression represents a promising strategy to mitigate the conversion of PrP^C into PrP^{Sc} [38–43]. Here we show that genetic or pharmacological ablation of CaN in astrocytes reduces PrP^C expression at a post-transcriptional level. This regulation occurs at the level of ribosomal protein synthesis and localization of PrP^C at the plasma membrane and does not involve PrP^C degradation. Altogether, our data suggest that astroglial CaN may represent a novel target for manipulation with PrP^C expression and mitigation of prion diseases.

2. Materials and Methods

2.1. Astrocyte-Specific CaN-KO Mice (ACN-KO)

The generation and handling of a mouse line with conditional CaN knockout (KO) in GFAP-expressing astrocytes has been described previously [36]. The mice were housed in the animal facility of the Università del Piemonte Orientale, with unlimited access to water and food. Animals were managed in accordance with European directive 2010/63/UE and with Italian law D.l. 26/2014. The procedures were approved by the local animal-health

and ethical committee (Università del Piemonte Orientale) and were authorized by the national authority (Istituto Superiore di Sanità; authorization numbers N. 214-2019 and N. 1136-2020). All efforts were made to reduce the number of animals by following the 3Rs rule.

2.2. Primary Hippocampal Astrocytic and Neuronal Cultures

Primary astroglial cultures were obtained by extracting hippocampi from either control (ACN-Ctr) or ACN-KO mouse pups at postnatal day 1–5 (P1–P5). Hippocampi were dissected in cold HBSS from the pups' brains and dissociated by incubation with trypsin (0.5 mg/mL, 37 °C, 20 min) followed by gentle trituration and resuspension in Dulbecco's Modified Eagle's Medium (DMEM, Sigma, St Louis, MO, USA, Cat. D5671)—high glucose, supplemented with 10% foetal bovine serum (FBS, Gibco, Thermo Fisher Scientific, Milan, Italy, Cat. 10270-106), 2 mg/mL glutamine (Sigma, MERK Life Sciences srl, Milan, Italy, Cat. G7513), 10 U/mL penicillin and 100 mg/mL streptomycin (Sigma, MERK Life Sciences srl, Milan, Italy, Cat. P0781). Each pup was processed separately and samples were plated on 6-well plates pre-treated with 0.1 mg/mL poly-L-lysine (PLL, Sigma, MERK Life Sciences srl, Milan, Italy, Cat. P2636). At sub-confluence (5–10 days in vitro), cells were detached with trypsin and pleated for experiments. Neuron cultures were prepared as described [35,36,44].

2.3. Pharmacological Treatments

At passage 2 (P2), astroglial primary cells were plated at 60% of confluence in PLL-coated 6-well plates. Treatment was started 24 h later using 200 nM FK506 (TOCRIS, biotecne, Minneapolis, MN, USA, Cat. 3631). Cells were lysed after 1 week of treatment. To inhibit proteasome activity, 3 h before lysis, cells were treated with 1 µM (R)-MG132 (TOCRIS, biotecne, Minneapolis, MN, USA, Cat. 6033). To inhibit lysosome activity, 1 h before lysis, cells were treated with 20 µM chloroquine (Sigma, MERK Life Sciences srl, Milan, Italy, C6628-25G).

2.4. Assessment of Protein Synthesis

The global protein synthesis rate was assessed using the surface sensing of translation (SUnSET) method published previously [35,45]. Briefly, primary astroglial cells were incubated with 4 µM puromycin dihydrochloride (Sigma, MERK Life Sciences srl, Milan, Italy, Cat. P8833) in complete DMEM at 37 °C with 5% CO_2 for 3 h [45]. Subsequently, cell lysates were fixed for immune fluorescence (IF) analysis with an anti-puromycin antibody.

2.5. Immunofluorescence

Primary Ctr and CaN-KO astrocytes, grown on 13 mm glass coverslips, were treated as previously explained. IF was performed as follows.

Puromycin IF. Cells were fixed in 4% paraformaldehyde and 4% sucrose, permeabilized (7 min in 0.1% Triton X-100 in phosphate-buffered saline (PBS)), blocked in 0.1% gelatine and immunoprobed with an appropriate primary antibody overnight at 4 °C. After three washes in PBS, an Alexa-conjugated secondary antibody (1:200) was applied for 1 h at RT. The following primary antibodies were used: anti-puromycin [35]. Secondary antibodies were as follows: Alexa Fluor 488 anti-mouse IgG. Nuclei were counter-stained with 4′,6-diamidino-2-phenylindole (DAPI).

PrP IF. Astrocytes were fixed in 4% paraformaldehyde for 7 min at room temperature and incubated in blocking solution (0.05% saponin, 0.5% bovine serum albumin (BSA), 10% FBS and 50 mM NH_4Cl in PBS) for 30 min at room temperature (RT). The cells were then incubated with the anti-PrP antibody 12B2 (kindly provided by Dr. J.P. Langeveld, Central Veterinary Institute of Wageningen University, Lelystad, The Netherlands, to Dr. Roberto Chiesa) and diluted 1:400 in blocking solution overnight at 4 °C. After three washes in PBS, cells were incubated with a biotinylated anti-IgG secondary antibody (Vector; 1:200) for 1 h

71

at RT, then reacted with Alexa Fluor 488-conjugated streptavidin (Thermo Fisher Scientific, Milan, Italy; 1:500) for 30 min at RT.

ER and Golgi markers IF. After fixation and blocking, cells were incubated with the primary antibodies diluted in blocking solution for 2–3 h at RT, then washed three times in PBS and incubated with a fluorescent conjugated anti-IgG secondary antibody for 1 h at RT. The following antibodies were used: mouse monoclonal anti-GM130 and rabbit polyclonal anti-BAP31. Secondary antibodies were conjugated with Alexa-594 or Alexa-647 fluorophores (Thermo Fisher Scientific, Milan, Italy; 1:500). Primary antibodies were listed in Table 1.

Table 1. Primary antibodies used for IF analysis.

Antibodies	Dilution	House	Cat.
Anti-puromycin	1:200	Millipore	MABE343
12B2	1:400	Central Veterinary Institute	/
Anti-GM130	1:500	Transduction Laboratories	610823
Anti-BAP31	1:200	Proteintech	11200-1-AP

2.6. Quantitative Fluorescence Image Analysis

Images were acquired using a FV-1000 Olympus laser confocal scanning system (Olympus, Tokyo, Japan) and Leica Thunder imager 3D live cell and Leica SP8 LIGHTNING Confocal Microscope imaging systems (Leica Microsystems srl, Milan, Italy). Images were acquired under non-saturating conditions (pixel fluorescence below 255 arbitrary units) and analyzed with Fiji ImageJ v.1.52p software. To determine the amount of total PrP, the PrP fluorescence density was measured for the entire cell area excluding the nucleus as a corrected total cell fluorescence (CTCFcell) = integrated density—(area of selected cell $\times$ mean background fluorescence) [35]. To determine the level of PrP on the plasma membrane, the CTCF of PrP on the plasma membrane was selected (CTCFpm) and a CTCFpm/CTCFcell ratio was calculated. To determine the amount of PrP in the Golgi apparatus, the CTCF of the PrP fluorescence was measured for the Golgi area of the cell identified by GM130 immunostaining (CTCFgolgi) and for the entire area of that cell excluding the Golgi (CTCFcyt) and the CTCFgolgi/CTCFcyt ratio was calculated. Data are expressed as fold changes relative to control.

2.7. Cell Transfection

WT and CaN-KO astrocytes were plated onto 13 mm glass coverslips in 24-well plates (3×10^4 cells/well). Then, 24 h after plating, cells were transfected with plasmids, eGFP PrP or eGFP FFI, in a 1:1 ratio using Lipofectamine 2000 (Thermo Fisher Scientific, Milan, Italy) in Optimem (11058-021; Gibco, Thermo Fisher Scientific, Milan, Italy). The transfection medium complete DMEM was replaced after 12 h, and 48 h after transfection, the cells were washed with PBS and fixed in 4% formaldehyde (Sigma, Milan, Italy). Constructs: the PrP-EGFP constructs eGFP PrP and eGFP FFI, expressing, respectively, mouse PrP (WT-PrP) and mouse D177N/M128 mutant PrP (FFI-PrP), were generated by inserting a monomerized version of EGFP containing a GS linker (GGGGS, repeated four times) at its 3′ end, after codon 34 of 3F4-tagged mouse PrP [46].

2.8. Western Blotting

Astroglial cultures were lysed with 100 μL of lysis buffer (50 mM Tris-HCl (pH 7.4), sodium dodecyl sulphate (SDS) 0.5%, 5 mM EDTA), 10 μL of protease inhibitor cocktail (PIC, Millipore, MERK Life Sciences srl, Milan, Italy, Cat. 539133) and phosphatase inhibitor cocktail (Thermo Fisher Scientific, Milan, Italy, Cat. 78428) and collected in a 1.5 mL tube. Lysates were boiled at 96 °C for 5 min and then quantified with a QuantiPro BCA Assay Kit (Sigma, MERK Life Sciences srl, Milan, Italy, Cat. SLBF3463). Then, 40 μg of proteins were mixed with the right amount of Laemmli Sample Buffer 4X (Bio-Rad, Hercules, CA, USA) and boiled. Samples were loaded on a 12% polyacrylamide–sodium dodecyl sulphate

gel for SDS-PAGE. Proteins were transferred onto nitrocellulose membrane using Mini Transfer Packs or Midi Transfer Packs with Trans-Blot® Turbo ™ (Bio-Rad, Hercules, CA, USA), according to the manufacturer's instructions (Bio-Rad, Hercules, CA, USA). The membranes were blocked in 5% skim milk (Sigma, MERK Life Sciences srl, Milan, Italy, Cat. 70166) for 45′ at room temperature. Subsequently, membranes were incubated with indicated primary antibody overnight at 4 °C. The primary antibodies used were anti-mouse monoclonal antibodies 12B2, 94B4; anti-β-Actin was used to normalize protein loading (listed in Table 2). Goat anti-mouse IgG (H + L) horseradish peroxidase-conjugated secondary antibody (1:5000; Cat. 170-6516, Bio-Rad, Hercules, California, USA) and Goat anti-mouse IgG (H + L) horseradish peroxidase-conjugated secondary antibody (1:5000; Cat. 170-6515, Bio-Rad) were used. Detection was carried out with SuperSignal™ West Pico/femto PLUS Chemiluminescent Substrate (Thermo Scientific, Milan, Italy), based on the chemiluminescence of luminol and developed using the ChemiDoc™ Imaging System (Bio-Rad, Hercules, CA, USA).

Table 2. Primary antibodies used for WB analysis.

Antibodies	Dilution	House	Cat.
94B4	1:1000	Wageningen University & Research	mAbPrP94B4
12B2	1:500	Central Veterinary Institute	/
Anti-β-Actin	1:800	Sigma	A1978

2.9. Preparation of Synaptosomes and Astrocyte Sub-Cellular Fractionation

Synaptosomal fractions were isolated by differential centrifugation using the standard protocol [47]. Briefly, mice were sacrificed followed by decapitation. The brains were rapidly removed and placed into ice-cold homogenization buffer containing 50 mM MOPS, pH 7.4, 320 mM sucrose, 0.2 mM DTT, 100 mM KCl, 0.5 mM MgCl2, 0.01 mM EDTA, 1 mM EGTA, protease inhibitor cocktails (PIC, Millipore, Cat. 539133) and phosphatase inhibitor cocktails (Thermo Fisher Scientific, Milan, Italy, Cat. 78428). All subsequent steps were performed at 4 °C. The hippocampi were microdissected and homogenized in 1:10 w/v homogenization buffer with 12 strokes in a Teflon glass Douncer. The homogenates were centrifuged for 10 min at $800 \times g$ followed by centrifugation of the supernatant at $9200 \times g$ for 15 min. The resulting p pellet, representing the crude synaptosomal fraction, was solubilized in lysis buffer [37].

Astrocyte primary cultures were subjected to the corresponding fractionation to obtain subcellular PrP^C distribution, starting from an 80% confluent 100 mm dish of P2 astrocytes, Crt and CaN KO. Cells were lysed in homogenization buffer with 12 strokes in a Teflon glass Douncer. The total lysates (t) were centrifuged for 10 min at $800 \times g$, obtaining the post-nuclear supernatant fraction, called s1. The s1 fraction was centrifugated at $9200 \times g$ for 15 min, obtaining s2, the soluble fraction, and p, the membrane fraction. The resulting p pellet was solubilized in lysis buffer [35,37,48].

2.10. Deglycosylation Assay

PrP^C was de-glycosylated by incubating cell lysates with PNGase F (Sigma, MERK Life Sciences srl, Milan, Italy, Cat. P7367) according to the manufacturer's instructions. Samples, treated and not treated with PNGase F, were analysed by western blotting.

2.11. Total RNA Extraction and Real-Time PCR

Total mRNA was extracted from 1.0×10^6 cells using TRIzol Lysis Reagent (Invitrogen, Thermo Fisher Scientific, Milan, Italy, Cat. 15596026) according to the manufacturer's instruction. The first strand of cDNA was synthesized from 0.5–1 μg of total RNA using Im-Prom-II system (Promega, Madison, WI, USA, Cat. A3800). Real-Time PCR was performed using iTaq qPCR master mix, according to the manufacturer's instructions (Bio-Rad, Hercules, CA, USA, Cat. 1725124), in a SFX96 real-time system (Bio-Rad, Hercules, CA,

USA). To normalize raw real-time PCR data, an S18 ribosomal subunit was used. Primers used were listed in Table 3. Data are expressed as delta-C (t) of the gene of interest to S18, allowing appreciation of single gene expression levels.

Table 3. Oligonucleotide primers used for real-time PCR.

Protein	Gene	Forward/Reverse	Accession No.
S18	*Rps18*	TGCGAGTACTCAACACCAACA CTGCTTTCCTCAACACCACA	NM_011296
PrP	*Prnp*	GAACCATTTCAACCGAGCTGA TAGTCACAAAGAGGGCCAGC	NM_011170.3

2.12. Proteomic Analysis

Ctr and CaN-KO astrocytes cells were collected, washed and digested with trypsin. Then, 100 μg of protein in 25 μL of 100 mM NH_4HCO_3 was reduced with 2.5 μL of 200 mM DTT (Sigma, MERK Life Sciences srl, Milan, Italy) at 90 °C for 20 min and alkylated with 10 μL 200 mM iodoacetamide (Sigma, MERK Life Sciences srl, Milan, Italy, Cat. I5161) for 1 h at RT protected from light. Any excess of iodoacetamide was removed by the addition of 200 mM DTT. The samples were then digested with 5 μg of trypsin (Promega, Madison, WI, USA, Sequence Grade). After an overnight (ON) incubation at 37 °C, 2 μL of neat formic acid was added to stop trypsin activity and the digested samples were dried by speed vacuum [49]. The peptide digests were desalted on a Discovery® DSC-18 solid phase extraction (SPE) 96-well plate (25 mg/well) (Sigma-Aldrich Inc., St. Louis, MO, USA), as reported elsewhere [50].

LC–MS/MS analyses were performed using a micro-LC Eksigent Technologies (Dublin, OH, USA) system with a stationary phase of a Halo Fused C18 column (0.5 × 100 mm, 2.7 μm; Eksigent Technologies, Dublin, OH, USA). The injection volume was 4.0 μL and the oven temperature was set at 40 °C. The mobile phase was a mixture of 0.1% (*v/v*) formic acid in water (A) and 0.1% (*v/v*) formic acid in acetonitrile (B), eluting at a flow rate of 15.0 μL/min at increasing concentrations of B from 2–40% in 30 min. The LC system was interfaced with a 5600+ TripleTOF system (AB Sciex, Vaughan, ON, Canada) equipped with a DuoSpray Ion Source. Samples were subjected to the traditional data-dependent acquisition (DDA), as previously described [51]. The MS data were acquired with Analyst TF 1.7 (SCIEX, Vaughan, ON, Canada). Three instrumental replicates for each sample were subjected to the DIA analysis [52]. The MS files were searched using the software Mascot v.2.4 (Matrix Science Inc., Boston, MA, USA) using trypsin as enzyme, with 2 missed cleavages, and a search tolerance of 50 ppm was specified for the peptide mass tolerance and 0.1 Da for the MS/MS tolerance; charges of the peptides to search for were set to 2+, 3+ and 4+, and the search was set on monoisotopic mass and FDR at 1%. The instrument was set to ESI-QUAD-TOF, and the following modifications were specified for the search: carbamidomethyl cysteines as fixed modification and oxidized methionine as variable modification. The UniProt/Swiss-Prot reviewed database containing mouse proteins (version 12/10/2018, containing 25,137 sequence entries) was used.

2.13. Statistical Analysis

The statistical analysis was performed and related graphical representations were produced using GraphPad Prism v.7. A two-tailed unpaired Student's *t*-test or one-way Anova test were used. Differences were considered significant at $p < 0.05$.

3. Results

3.1. CaN KO and FK506 Treatment Reduced PrP^C Expression in Mouse Hippocampal Astrocytes

Previously, we have shown that CaN in astrocytes regulates the expression of plasma membrane proteins, e.g., glial high-affinity glutamate–aspartate transporter (GLAST) [35]. Given the emerging role of astrocytic PrP^C [8,9], we have investigated whether PrP^C could

be regulated by CaN. First, we evaluated the protein expression levels of PrP^C in primary cultures of hippocampal astrocytes from control and astrocyte-specific CaN-KO (ACN-Ctr and ACN-KO) mice, hereafter referred to as Ctr and CaN-KO astrocytes. We found that CaN-KO astrocytes had a reduced expression of PrP^C compared to Ctr astrocytes by about 50% (Figure 1a). We observed that, in total cell lysates, the major PrP^C signal resulted from diglycosylated bands, as shown in Figure 1a, while the mono-glycosylated or non-glycosylated forms were less expressed in both Ctr and CaN-KO astrocytes. As expected, deglycosylation with PNGaseF produced a single deglycosylated band of approximately 23 KDa in both Ctr and CaN-KO astrocytes (Figure 1b).
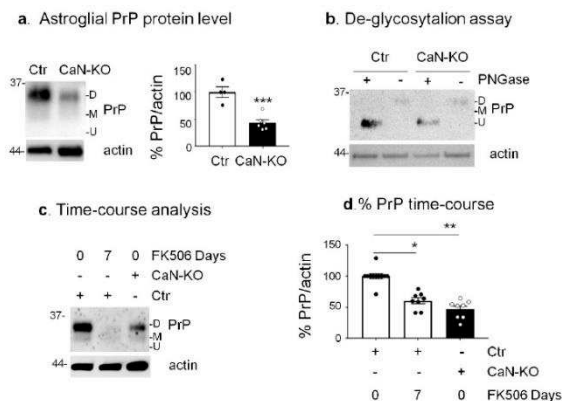

Figure 1. Analysis of PrP^C expression in Ctr, FK506-treated Ctr and CaN-KO primary hippocampal astrocytes. (**a**) Expression levels of PrP^C in Ctr and CaN-KO astrocytes. WB analysis of protein extracts with anti-PrP^C 12B2 and anti-actin antibodies and quantification of actin-normalized PrP^C levels expressed as percentages of Ctr. Data are the means ± SEM of Ctr (*n* = 4) and KO (*n* = 6) replicate astrocyte cultures. *** $p < 0.001$ by unpaired *t*-test. (**b**) Deglycosylation assay in Ctr and CaN-KO astroglial lysates. Ctr and CaN-KO astroglial lysates were treated with PNGase F and analysed by WB with anti-PrP 12B2 and anti-actin antibodies. (**c**) Time-course analysis with FK506 in Ctr and CaN-KO astrocytes. Ctr astrocytes were left untreated or treated with FK506 200 nM for 7 days and analyzed by WB with anti-PrP 12B2 and anti-actin antibodies, along with CaN-KO astrocyte lysates. (**d**) Quantification of actin-normalized PrP^C levels in WB like the one shown in (**c**). Data are the means ± SEM, (*n* = 6–11); * $p < 0.05$, ** $p < 0.01$ vs. Ctr by one-way Anova, multiple comparison Kruskal–Wallis test.

Next, we decided to verify if the pharmacological inhibition of CaN reduced PrP^C levels like in astrocytes with genetic CaN ablation. Treatment of Ctr astrocytes with FK506 (200 nM for 7 days) resulted in a significant decrease of PrP^C of about 45% (Figure 1c,d), confirming that the reduction of endogenous PrP^C proteins in CaN-KO astrocytes was due to the inhibition of CaN activity.

3.2. Total and Membrane PrP^C Downregulation

Expression of PrP^C at the plasma membrane has been specifically associated with its ability to be converted to misfolded PrP and to the development of pathology, both in vitro and in vivo [53,54]. Therefore, our next question was whether the reduction of PrP^C in CaN-KO astrocytes occurs specifically at the plasma membrane level. For this, we have fractionated cell lysates to isolate soluble and membrane proteins by centrifugation, as

has previously been performed on tissue [37]. Briefly, the total cell lysate was centrifuged to obtain a post-nuclear supernatant (s1), which subsequently was separated into the soluble fraction (s2) and the membrane fraction (p). As shown in Figure 2a,b, in total lysates the PrP^C signal was reduced in CaN-KO astrocytes compared to Ctr. The sub-cellular fractionation procedure showed an enrichment of PrP^C in fraction p both in Ctr and CaN-KO compared to total lysate, s1 or s2, while a reduction of PrP levels, specifically in the p fraction of CaN-KO astrocytes, was observed compared to the p fraction from Ctr cells, indicating the reduction of membrane-associated PrP^C. To strengthen the results, we immunostained CaN-KO (or FK506-treated) astrocytes with anti-PrP antibody and quantified the ratio of membrane and total PrP^C. As shown in Figure 2c, both genetic and pharmacological ablation of CaN in astrocytes resulted in a marked reduction of the total and of the membrane PrP^C signal compared to Ctr.

Next, we investigated whether CaN-dependent PrP^C reduction could be detected in vivo in total hippocampal homogenates from ACN-Ctr and ACN-KO mice at 1 month of age, i.e., the age-point when mice develop deregulation of neuronal excitability and protein expression [36,37]. As reported in Figure 3a, an equal level of PrP^C was expressed in whole-tissue hippocampal homogenates from ACN-Ctr and ACN-KO mice, which can be attributed to higher PrP^C neuronal protein expression, which was in apparent contradiction with in vitro data. One of the morpho-functional units of astrocytes is represented by the fine astrocytic processes surrounding synapses, peri-synaptic processes, in which ion and metabolite transporters and other proteins are enriched and which may represent the site of localization of PrP^C in astrocytes in vivo. To test this hypothesis, we prepared synaptosomal fractions from ACN-Ctr and ACN-KO hippocampi, using a previously reported protocol which preserves and enriches perisynaptic astrocytic processes [35,37]. Indeed, we found a significant reduction of PrP^C in the synaptosomal preparation from hippocampi of ACN-KO compared to ACN-Crt mice (Figure 3b). To rule out the neuronal PrP^C contribution to the reduction of PrP levels in synaptosomes, we assessed PrP^C expression in primary hippocampal neurons from ACN-Ctr and ACN-KO mice. We observed that Ctr and CaN-KO neurons expressed equal levels of PrP^C (Figure 3c), supporting the view that the reduction of PrP^C in vivo occurs in astrocytes but not in neurons.

3.3. CaN Ablation-Induced PrP^C Downregulation Is not due to Alterations of Gene Expression or Protein Degradation

In many cell types, including astrocytes, CaN is known to control expression, first of all, through regulation of gene transcription [10,20,55]. Therefore, we checked if CaN deletion or pharmacological inhibition could alter *Prnp* gene transcription.

As shown in Figure 4a, *Prnp* mRNA levels were unchanged in: (i) Ctr astrocytes treated for 1 week with FK506 vs. Ctr astrocytes; (ii) cultured CaN-KO vs. Ctr astrocytes; and (iii) hippocampal tissues from ACN-KO vs. ACN-Ctr mice, ruling out the possibility of transcriptional regulation. Next, we investigated if CaN-dependent PrP^C reduction was due to alteration of proteasomal or lysosomal degradation [28,35], since it has been shown that in neurons lysosomes contribute to degradation of PrP^C [35]. For this, we treated astrocytes either with MG132, a specific proteosomal inhibitor, or with CQ, an anti-malaric agent and a commonly used inhibitor of lysosomal degradation. As for proteasomal degradation, PrP expression increased when Ctr astrocytes were treated with MG132, suggesting an accumulation of synthetized but not degraded PrP^C. However, MG132 failed to rescue the downregulated PrP^C expression in CaN-KO astrocytes or in astrocytes treated with FK506 (Figure 4b). CQ treatment did not alter significatively the levels of PrP^C expression in control astrocytes and failed to rescue decreased PrP^C expression in CaN-KO astrocytes (Figure 5). Altogether, these data suggest that the CaN ablation-dependent reduction of PrP^C expression in astrocytes is neither due to altered transcription nor due to augmented degradation of the protein.
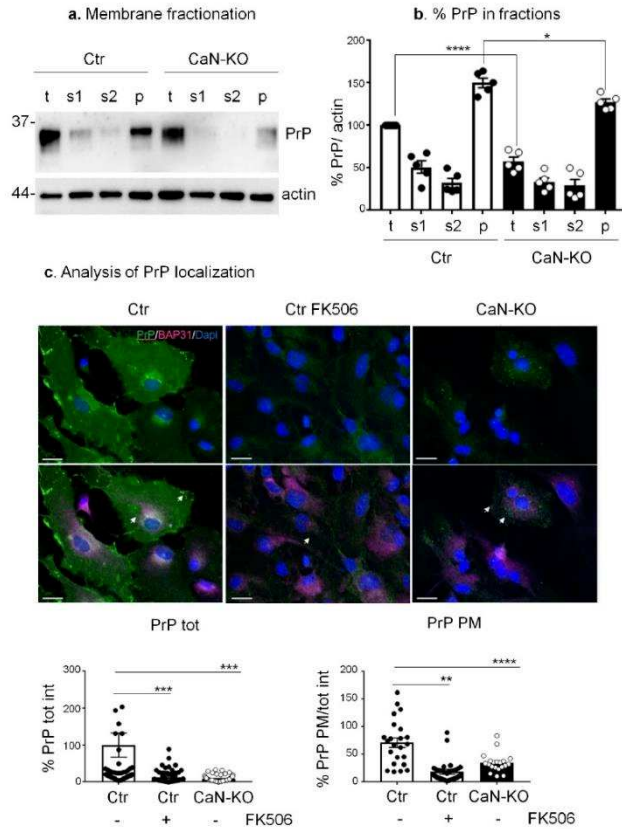
Figure 2. Analysis of PrP^C localization in Ctr, FK506-treated Ctr and CaN-KO primary hippocampal astrocytes. (**a**) Fractionation of Ctr and CaN-KO astrocytic lysates by centrifugation and evaluation of PrP^C relative abundance by WB with anti-PrP in t (total cell lysates), s1 (post nuclear supernatant), s2 (soluble fraction), p (membrane fraction) fractions. (**b**) Quantification of membrane fractionation is expressed as means ± SEM, $n = 5$; **** $p < 0.0001$, * $p < 0.05$ by one-way Anova, Sidak's multiple comparison. (**c**) Immunofluoresce analysis on Ctr, FK506-treated Ctr and CaN-KO astrocytes with anti-PrP (green), anti-BAP31 (pink) antibodies and reacted with DAPI to stain the nuclei (blue). Confocal microscope analysis, scale bar 20 μm. Quantification of total PrP (PrP tot) or plasma membrane PrP (PrP PM) fluorescence density expressed as percentages of Ctr from Ctr $n = 54$ cells, FK506-treated Ctr $n = 67$ and CaN-KO $n = 70$ cells, from four to five replicates, ** $p < 0.01$, *** $p < 0.001$ and **** $p < 0.0001$.
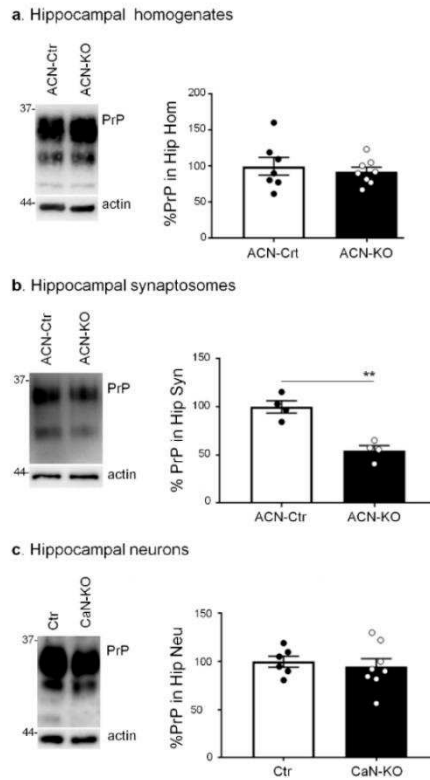
Figure 3. Analysis of PrP^C expression in hippocampal tissues from ACN-Ctr and ACN-KO mice at one month of age. (**a**) WB analysis with anti-PrP and anti-actin antibodies of hippocampal homogenates from ACN-Ctr and ACN-KO mice. Quantification of the actin-normalized PrP signal expressed as percentage of Ctr. Data are the means $\pm$ SEM, ACN-Ctr $n = 7$, ACN-KO $n = 8$, unpaired *t*-test, ns. (**b**) Synaptosomal fractions from hippocampi of ACN-Ctr and ACN-KO mice were analyzed by WB with anti-PrP and anti-actin antibodies. Quantification of the actin-normalized PrP signal expressed as percentage of Ctr. Data are the means $\pm$ SEM, ACN-Ctr $n = 4$, ACN-KO $n = 4$, unpaired *t*-test, ** $p = 0.0015$. (**c**) WB analysis with anti-PrP and anti-actin antibodies of hippocampal neurons from ACN-Ctr (Ctr) and ACN-KO (CaN-KO) mice. Quantification of the actin-normalized PrP signal expressed as percentages of Ctr. Data are the means $\pm$ SEM, Ctr $n = 6$, CaN-KO $n = 8$, unpaired *t*-test, ns.
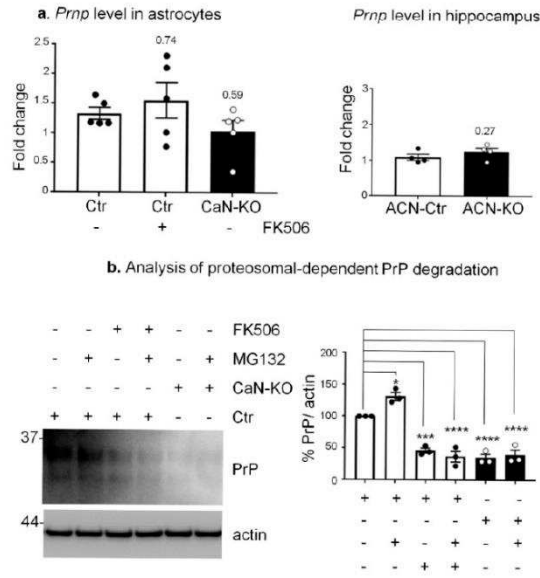
Figure 4. Real-time PCR, proteasomal degradation analysis of Ctr, FK506-treated Ctr and CaN-KO astrocytes. (**a**) Real-time PCR of *Prnp* on primary astrocytes, Ctr, FK506 (200 nM for 7 days)-treated and CaN-KO. Values represent means ± SEM ∆C(t) of gene/S18 of five independent experiments for each condition. (**b**) WB analysis of PrP^C and actin, protein degradation in hippocampal astrocytes from Ctr, FK506 (200 nM for 7 days)-treated and CaN-KO. Where indicated, MG132 was added 3 h before lysis. Data are expressed as means ± SEM, three independent cultures were used, one-way Anova, multiple comparison, * $p < 0.05$, *** $p < 0.001$ and **** $p < 0.0001$.

3.4. Reduction of PrP^C Expression in CaN-KO Astrocytes Results from Deregulation of Global Protein Synthesis

Recently, we have shown that both genetic and pharmacological ablation of CaN in astrocytes suppresses global protein synthesis [35]. In the absence of transcriptional and post-translational alterations (see above), it is reasonable to suggest that the impairment of protein synthesis alone could account for the reduced PrP^C protein expression in CaN-KO and FK506-treated astrocytes. To pursue this hypothesis, first we confirmed, using an immunocytochemical variant of the puromycin incorporation assay [45], that active ribosomes in CaN-KO astrocytes and Ctr astrocytes treated with FK506 incorporated less puromycin, suggesting an impairment of global protein synthesis (Figure 6). Protein synthesis is a complex multistep process in which CaN has been suggested to regulate several steps [56]. To shed light on possible mechanisms of protein synthesis deregulation in CaN-KO astrocytes, we performed shotgun mass spectrometry proteomics followed by bioinformatic analysis.
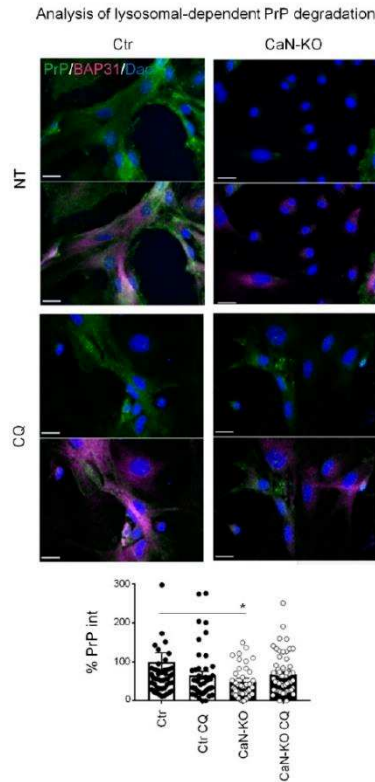
79

Analysis of lysosomal-dependent PrP degradation

Figure 5. Analysis of lysosomal-dependent PrP^C degradation. Ctr and CaN-KO astrocytes were untreated or treated with chloroquine (CQ) before immunofluorescence with anti PrP (green), BAP31 (pink) antibodies and reacted with DAPI to stain the nuclei (blue). Confocal microscope analysis, scale bar 20 μm. Quantification of total PrP^C fluorescence density expressed as percentage of Ctr. Data are the means ± SEM of Ctr n = 49 cells, Ctr CQ n = 46 and KO n = 58 cells; KO CQ = 62, from three to seven coverslips from three independent experiments, * $p < 0.05$.

As shown in Table S1a, 1212 and 823 proteins were identified, respectively, in Ctr and CaN-KO astrocytes. Of these, 609 were commonly expressed by both types of astrocytes, while 603 and 214 were identified only in Ctr or CaN-KO astrocytes, respectively (see also Table S1a,b). The analysis using the DAVID online gene ontology (GO) tool revealed that the most significantly overrepresented GO terms in Ctr astrocytes were related to translation, ribosomes, focal adhesion and components of the extracellular matrix, and the most significantly overrepresented KEGG pathway was Ribosome (Table S1b). GO terms, overrepresented in CaN-KO astrocytes, were related to RNA splicing, RNA binding, focal adhesion and the extracellular matrix (Table S1c). Overall, this analysis suggests that

ribosome-mediated translation may be specifically impaired in CaN-KO astrocytes, which links the downregulation of PrP^C in CaN-KO astrocytes to protein synthesis.
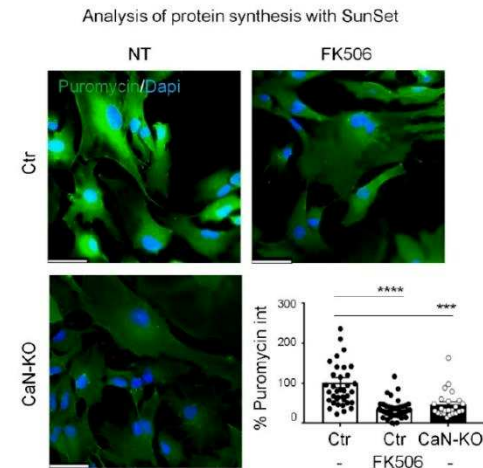
Analysis of protein synthesis with SunSet

Figure 6. Protein synthesis analysis in Ctr, FK506-treated Ctr and CaN-KO astrocytes. Ctr, FK506-treated Ctr and CaN-KO astrocytes were pulsed with 4 μM puromycin, fixed and analysed by IF with anti-puromycin antibody (green) and reacted with DAPI to stain the nuclei (blue). Images were acquired with a Leica Thunder imager 3D live cell microscope, scale bar 41.6 μm. Data are expressed as means ± SEM of *n* cells Ctr = 37, FK506-treated Ctr = 44, CaN-KO = 24, from three independent experiments. one-way Anova, Dunnett's multiple comparison analysis, *** $p < 0.001$ and **** $p < 0.0001$.

3.5. FK506 and CaN-KO Reduced the Expression and Plasma Membrane Localization of WT and Mutant PrP Associated with Human Inherited Prion Diseases

Since prion diseases include genetic variants caused by mutations in the PrP gene, including the PrP$_{D177N}$ mutation associated with FFI human disease [31,46,57,58], it was of interest to investigate whether the effect of CaN KO in astrocytes differs between wildtype PrP^C and the mutant variant.

For this, we transiently transfected Ctr and CaN-KO astrocytes with eGFP-tagged PrP$_{WT}$ or PrP$_{D177N}$ [57]. In neurons, it has been shown that overexpressed PrP proteins, including mutant variants, are partially retained in the Golgi apparatus compartment. Therefore, using confocal microscopy, we quantified the ratio between plasma membrane-localized PrP and PrP localized in the Golgi compartment. The analysis showed that both PrP$_{WT}$ and PrP$_{D177N}$ were expressed significantly less at the plasma membrane of CaN-KO as compared with Ctr astrocytes, suggesting that the effect of CaN KO is maintained also in mutant variants of PrP (Figure 7).
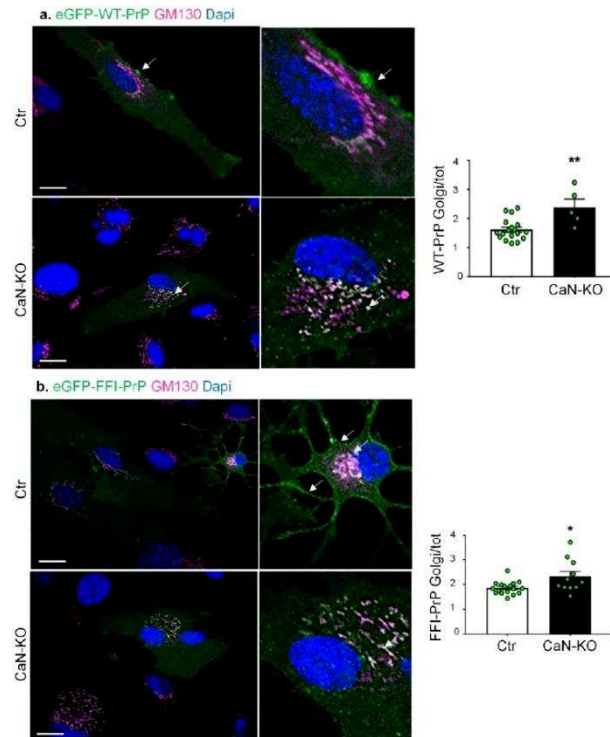
Figure 7. Analysis of WT and D177N PrP transient expression in Ctr and CaN-KO astrocytes. Ctr and CaN-KO astrocytes were transfected with eGFP-WT PrP (**a**) and eGFP-D177N PrP (**b**) fusion proteins (green), immunostained with an anti-GM130 (pink) to mark the Golgi apparatus and reacted with DAPI to stain the nuclei (blue). Images were acquired with a confocal microscope, scale bar 20 μm. PrP fluorescent density in the Golgi apparatus is expressed as mean ± SEM, from four independent coverslips, * $p < 0.05$ and ** $p < 0.01$.

4. Discussion

Previously, we have reported that CaN controls the expression of membrane proteins, e.g., GLAST, through a dynamic regulation of protein synthesis and degradation [35]. The aim of this study, therefore, was to see if CaN could also be involved in the control of PrP^C expression. The main results of this study are as follows: (i) genetic ablation of CaN from astrocytes as well as chronic treatment of cultured astrocytes with a CaN inhibitor reduced PrP^C expression in astrocytes but not in neurons; (ii) the reduction of PrP^C in astrocytes was due to the impairment of protein synthesis machinery but not due to alterations of transcription or protein degradation; (iii) the reduction of PrP^C protein expression in astrocytes is associated with the reduction of its presence on the plasma membrane, which is true for both WT PrP^C and mutant FFI-related PrP.

In spite of significant progress in the field, the downregulation of PrP^C remains one of the most promising approaches to mitigate the conversion of PrP^C in PrP^{Sc} and the burden of prion disease [38,39,41–43,59]. However, it has been suggested that PrP^C regulates many cellular functions, including neuronal excitability, differentiation, ion homeostasis and mitochondrial functions and that it also plays a role in immune cells [60]. In neurons, PrP^C has been proposed to serve as a molecular scaffold for the transduction of signals across the plasma membrane [61,62]. We and other groups have shown that endogenous PrP^C regulates neuronal calcium signalling, in particular, store-operated calcium entry and glutamate-induced mitochondrial accumulation of Ca^{2+} [63–66]. Therefore, systemic downregulation of PrP^C may result in harmful drawbacks for the cell due to ablation of its physiological activity. In this framework, the data presented here, in correlation with reports on the role of astrocytic PrP^C in spreading the prion pathology, suggest that astrocytic CaN may represent a valuable strategy to counteract prion diseases.

Inhibitors of CaN have already been suggested to mitigate neuropathology in models of Alzheimer's disease, strokes and, importantly, in mouse models of acquired prion disease [27–29,67–72]. In the context of neuropathology, overactivation and/or overexpression of CaN, specifically in astrocytes, has been associated mainly with reactive gliosis and neuroinflammation. Thus, the role of the CaN-mediated activation of transcriptional activity of NFAT and its association with neuroinflammation has been largely discussed in the context of Alzheimer's disease [11,20,73,74], highlighting the benefits of astrocyte-specific targeting.

In this context, it is important to emphasize that the CaN ablation-mediated downregulation of PrP^C is not related to pro-inflammatory effects of CaN or to transcriptional activation. Instead, we suggest that CaN, through protein dephosphorylation, regulates translational machinery, as has been already proposed [56,75,76]. Previously, we have shown that, in resting conditions, astrocytic CaN does not regulate gene transcription, acting through dephosphorylation of target proteins, and that one of the target processes may be the assembly of ribosomal complexes and initiation of translation [36,37,56,75,76]. One of the results of such deregulation is the impairment of the expression of ribosomal proteins in CaN-KO astrocytes, which is supported by our present proteomics analysis (Table S1). We have also shown that CaN ablation regulates expression of the astrocytic glutamate transporter, GLAST, at a post-transcriptional level through a disequilibrium between protein synthesis and degradation [35]. Both genetic and chronic pharmacological CaN inhibition resulted in upregulation of GLAST, an opposite effect to that found here for PrP^C. This suggests that the deregulation of protein expression upon CaN inhibition is protein-specific and may result in either upregulation or downregulation of protein expression [37].

In conclusion, our results are in line with the suggestion that anti-CaN treatment may be beneficial in prion diseases. At the same time, the results provide mechanistic insight into astrocyte-specific PrP^C regulation, highlighting the possibility of a non-neuronal yet cell-specific approach to reduce the burden of misfolded PrP and mitigate the development of prion diseases.

References

1. Prusiner, S.B. Prions. *Proc. Natl. Acad. Sci. USA* **1998**, *95*, 13363–13383. [CrossRef] [PubMed]
2. Puoti, G.; Bizzi, A.; Forloni, G.; Safar, J.G.; Tagliavini, F.; Gambetti, P. Sporadic Human Prion Diseases: Molecular Insights and Diagnosis. *Lancet Neurol.* **2012**, *11*, 618–628. [CrossRef]
3. Sy, M.-S.; Gambetti, P.; Wong, B.-S. Human Prion Diseases. *Med. Clin. N. Am.* **2002**, *86*, 551–571. [CrossRef]
4. Takada, L.T.; Kim, M.-O.; Metcalf, S.; Gala, I.I.; Geschwind, M.D. Chapter 29—Prion Disease. In *Handbook of Clinical Neurology*; Geschwind, D.H., Paulson, H.L., Klein, C., Eds.; Neurogenetics, Part II.; Elsevier: Amsterdam, The Netherlands, 2018; Volume 148, pp. 441–464.
5. Marín-Moreno, A.; Espinosa, J.C.; Torres, J.M. Transgenic Mouse Models for the Study of Prion Diseases. *Prog. Mol. Biol. Transl. Sci.* **2020**, *175*, 147–177. [CrossRef]
6. Orge, L.; Lima, C.; Machado, C.; Tavares, P.; Mendonça, P.; Carvalho, P.; Silva, J.; Pinto, M.d.L.; Bastos, E.; Pereira, J.C.; et al. Neuropathology of Animal Prion Diseases. *Biomolecules* **2021**, *11*, 466. [CrossRef]
7. Vorberg, I.; Chiesa, R. Experimental Models to Study Prion Disease Pathogenesis and Identify Potential Therapeutic Compounds. *Curr. Opin. Pharmacol.* **2019**, *44*, 28–38. [CrossRef] [PubMed]
8. Scheckel, C.; Imeri, M.; Schwarz, P.; Aguzzi, A. Ribosomal Profiling during Prion Disease Uncovers Progressive Translational Derangement in Glia but Not in Neurons. *eLife* **2020**, *9*, e62911. [CrossRef]
9. Smith, H.L.; Freeman, O.J.; Butcher, A.J.; Holmqvist, S.; Humoud, I.; Schätzl, T.; Hughes, D.T.; Verity, N.C.; Swinden, D.P.; Hayes, J.; et al. Astrocyte Unfolded Protein Response Induces a Specific Reactivity State That Causes Non-Cell-Autonomous Neuronal Degeneration. *Neuron* **2020**, *105*, 855–866.e5. [CrossRef]
10. Lim, D.; Rodríguez-Arellano, J.J.; Parpura, V.; Zorec, R.; Zeidán-Chuliá, F.; Genazzani, A.A.; Verkhratsky, A. Calcium Signalling Toolkits in Astrocytes and Spatio-Temporal Progression of Alzheimer's Disease. *Curr. Alzheimer Res.* **2016**, *13*, 359–369. [CrossRef]
11. Lim, D.; Ronco, V.; Grolla, A.A.; Verkhratsky, A.; Genazzani, A.A. Glial Calcium Signalling in Alzheimer's Disease. *Rev. Physiol. Biochem. Pharmacol.* **2014**, *167*, 45–65. [CrossRef]
12. Verkhratsky, A.; Sofroniew, M.V.; Messing, A.; deLanerolle, N.C.; Rempe, D.; Rodríguez, J.J.; Nedergaard, M. Neurological Diseases as Primary Gliopathies: A Reassessment of Neurocentrism. *ASN Neuro* **2012**, *4*, AN20120010. [CrossRef]
13. Li, B.; Chen, M.; Zhu, C. Neuroinflammation in Prion Disease. *Int. J. Mol. Sci.* **2021**, *22*, 2196. [CrossRef]
14. Hartmann, C.A.; Martins, V.R.; Lima, F.R.S. High Levels of Cellular Prion Protein Improve Astrocyte Development. *FEBS Lett.* **2013**, *587*, 238–244. [CrossRef] [PubMed]
15. Kushwaha, R.; Sinha, A.; Makarava, N.; Molesworth, K.; Baskakov, I.V. Non-Cell Autonomous Astrocyte-Mediated Neuronal Toxicity in Prion Diseases. *Acta Neuropathol. Commun.* **2021**, *9*, 22. [CrossRef] [PubMed]
16. Lima, F.R.S.; Arantes, C.P.; Muras, A.G.; Nomizo, R.; Brentani, R.R.; Martins, V.R. Cellular Prion Protein Expression in Astrocytes Modulates Neuronal Survival and Differentiation. *J. Neurochem.* **2007**, *103*, 2164–2176. [CrossRef]
17. Baumgärtel, K.; Mansuy, I.M. Neural Functions of Calcineurin in Synaptic Plasticity and Memory. *Learn. Mem.* **2012**, *19*, 375–384. [CrossRef] [PubMed]
18. Brini, M.; Ottolini, D.; Calì, T.; Carafoli, E. Calcium in Health and Disease. *Met. Ions. Life Sci.* **2013**, *13*, 81–137. [CrossRef] [PubMed]
19. Creamer, T.P. Calcineurin. *Cell Commun. Signal.* **2020**, *18*, 137. [CrossRef]
20. Furman, J.L.; Norris, C.M. Calcineurin and Glial Signaling: Neuroinflammation and Beyond. *J. Neuroinflamm.* **2014**, *11*, 158. [CrossRef]
21. Abdul, H.M.; Sama, M.A.; Furman, J.L.; Mathis, D.M.; Beckett, T.L.; Weidner, A.M.; Patel, E.S.; Baig, I.; Murphy, M.P.; LeVine, H.; et al. Cognitive Decline in Alzheimer's Disease Is Associated with Selective Changes in Calcineurin/NFAT Signaling. *J. Neurosci.* **2009**, *29*, 12957–12969. [CrossRef]
22. Agostinho, P.; Lopes, J.P.; Velez, Z.; Oliveira, C.R. Overactivation of Calcineurin Induced by Amyloid-Beta and Prion Proteins. *Neurochem. Int.* **2008**, *52*, 1226–1233. [CrossRef]

23. Moon, J.-H.; Hong, J.-M.; Park, S.-Y. Calcineurin Activation by Prion Protein Induces Neurotoxicity via Mitochondrial Reactive Oxygen Species. *Oxid. Med. Cell. Longev.* **2021**, *2021*, 5572129. [CrossRef] [PubMed]
24. Shah, S.Z.A.; Hussain, T.; Zhao, D.; Yang, L. A Central Role for Calcineurin in Protein Misfolding Neurodegenerative Diseases. *Cell. Mol. Life Sci.* **2017**, *74*, 1061–1074. [CrossRef] [PubMed]
25. Biasini, E.; Massignan, T.; Fioriti, L.; Rossi, V.; Dossena, S.; Salmona, M.; Forloni, G.; Bonetto, V.; Chiesa, R. Analysis of the cerebellar proteome in a transgenic mouse model of inherited prion disease reveals preclinical alteration of calcineurin activity. *Proteomics* **2006**, *6*, 2823–2834. [CrossRef]
26. Chiesa, R.; Piccardo, P.; Ghetti, B.; Harris, D.A. Neurological Illness in Transgenic Mice Expressing a Prion Protein with an Insertional Mutation. *Neuron* **1998**, *21*, 1339–1351. [CrossRef]
27. Nakagaki, T.; Ishibashi, D.; Mori, T.; Miyazaki, Y.; Takatsuki, H.; Tange, H.; Taguchi, Y.; Satoh, K.; Atarashi, R.; Nishida, N. Administration of FK506 from Late Stage of Disease Prolongs Survival of Human Prion-Inoculated Mice. *Neurotherapeutics* **2020**, *17*, 1850–1860. [CrossRef]
28. Nakagaki, T.; Satoh, K.; Ishibashi, D.; Fuse, T.; Sano, K.; Kamatari, Y.O.; Kuwata, K.; Shigematsu, K.; Iwamaru, Y.; Takenouchi, T.; et al. FK506 Reduces Abnormal Prion Protein through the Activation of Autolysosomal Degradation and Prolongs Survival in Prion-Infected Mice. *Autophagy* **2013**, *9*, 1386–1394. [CrossRef]
29. Mukherjee, A.; Morales-Scheihing, D.; Gonzalez-Romero, D.; Green, K.; Taglialatela, G.; Soto, C. Calcineurin Inhibition at the Clinical Phase of Prion Disease Reduces Neurodegeneration, Improves Behavioral Alterations and Increases Animal Survival. *PLoS Pathog.* **2010**, *6*, e1001138. [CrossRef]
30. Chiesa, R.; Restelli, E.; Comerio, L.; Del Gallo, F.; Imeri, L. Transgenic Mice Recapitulate the Phenotypic Heterogeneity of Genetic Prion Diseases without Developing Prion Infectivity: Role of Intracellular PrP Retention in Neurotoxicity. *Prion* **2016**, *10*, 93–102. [CrossRef]
31. Bouybayoune, I.; Mantovani, S.; Del Gallo, F.; Bertani, I.; Restelli, E.; Comerio, L.; Tapella, L.; Baracchi, F.; Fernández-Borges, N.; Mangieri, M.; et al. Transgenic Fatal Familial Insomnia Mice Indicate Prion Infectivity-Independent Mechanisms of Pathogenesis and Phenotypic Expression of Disease. *PLoS Pathog.* **2015**, *11*, e1004796. [CrossRef]
32. Dossena, S.; Imeri, L.; Mangieri, M.; Garofoli, A.; Ferrari, L.; Senatore, A.; Restelli, E.; Balducci, C.; Fiordaliso, F.; Salio, M.; et al. Mutant Prion Protein Expression Causes Motor and Memory Deficits and Abnormal Sleep Patterns in a Transgenic Mouse Model. *Neuron* **2008**, *60*, 598–609. [CrossRef] [PubMed]
33. Chiesa, R.; Drisaldi, B.; Quaglio, E.; Migheli, A.; Piccardo, P.; Ghetti, B.; Harris, D.A. Accumulation of Protease-Resistant Prion Protein (PrP) and Apoptosis of Cerebellar Granule Cells in Transgenic Mice Expressing a PrP Insertional Mutation. *Proc. Natl. Acad. Sci. USA* **2000**, *97*, 5574–5579. [CrossRef] [PubMed]
34. Büeler, H.; Raeber, A.; Sailer, A.; Fischer, M.; Aguzzi, A.; Weissmann, C. High Prion and PrP^{Sc} Levels but Delayed Onset of Disease in Scrapie-Inoculated Mice Heterozygous for a Disrupted PrP Gene. *Mol. Med.* **1994**, *1*, 19–30. [CrossRef]
35. Dematteis, G.; Restelli, E.; Chiesa, R.; Aronica, E.; Genazzani, A.A.; Lim, D.; Tapella, L. Calcineurin Controls Expression of EAAT1/GLAST in Mouse and Human Cultured Astrocytes through Dynamic Regulation of Protein Synthesis and Degradation. *Int. J. Mol. Sci.* **2020**, *21*, 2213. [CrossRef] [PubMed]
36. Tapella, L.; Soda, T.; Mapelli, L.; Bortolotto, V.; Bondi, H.; Ruffinatti, F.A.; Dematteis, G.; Stevano, A.; Dionisi, M.; Ummarino, S.; et al. Deletion of Calcineurin from GFAP-Expressing Astrocytes Impairs Excitability of Cerebellar and Hippocampal Neurons through Astroglial Na+/K+ ATPase. *Glia* **2020**, *68*, 543–560. [CrossRef] [PubMed]
37. Tapella, L.; Dematteis, G.; Ruffinatti, F.A.; Ponzoni, L.; Fiordaliso, F.; Corbelli, A.; Albanese, E.; Pistolato, B.; Pagano, J.; Barberis, E.; et al. Deletion of Calcineurin from Astrocytes Reproduces Proteome Signature of Alzheimer's Disease and Epilepsy and Predisposes to Seizures. *Cell Calcium* **2021**, *100*, 102480. [CrossRef]
38. Biggi, S.; Pancher, M.; Stincardini, C.; Luotti, S.; Massignan, T.; Dalle Vedove, A.; Astolfi, A.; Gatto, P.; Lolli, G.; Barreca, M.L.; et al. Identification of Compounds Inhibiting Prion Replication and Toxicity by Removing PrPC from the Cell Surface. *J. Neurochem.* **2020**, *152*, 136–150. [CrossRef]
39. White, M.D.; Farmer, M.; Mirabile, I.; Brandner, S.; Collinge, J.; Mallucci, G.R. Single Treatment with RNAi against Prion Protein Rescues Early Neuronal Dysfunction and Prolongs Survival in Mice with Prion Disease. *Proc. Natl. Acad. Sci. USA* **2008**, *105*, 10238–10243. [CrossRef]
40. White, M.D.; Mallucci, G.R. RNAi for the Treatment of Prion Disease: A Window for Intervention in Neurodegeneration? *CNS Neurol. Disord. Drug Targets* **2009**, *8*, 342–352. [CrossRef]
41. Minikel, E.V.; Zhao, H.T.; Le, J.; O'Moore, J.; Pitstick, R.; Graffam, S.; Carlson, G.A.; Kavanaugh, M.P.; Kriz, J.; Kim, J.B.; et al. Prion Protein Lowering Is a Disease-Modifying Therapy across Prion Disease Stages, Strains and Endpoints. *Nucleic Acids Res.* **2020**, *48*, 10615–10631. [CrossRef]
42. Nazor Friberg, K.; Hung, G.; Wancewicz, E.; Giles, K.; Black, C.; Freier, S.; Bennett, F.; Dearmond, S.J.; Freyman, Y.; Lessard, P.; et al. Intracerebral Infusion of Antisense Oligonucleotides into Prion-Infected Mice. *Mol. Ther. Nucleic Acids* **2012**, *1*, e9. [CrossRef]
43. Raymond, G.J.; Zhao, H.T.; Race, B.; Raymond, L.D.; Williams, K.; Swayze, E.E.; Graffam, S.; Le, J.; Caron, T.; Stathopoulos, J.; et al. Antisense Oligonucleotides Extend Survival of Prion-Infected Mice. *JCI Insight* **2019**, *5*, 131175. [CrossRef] [PubMed]
44. Tapella, L.; Cerruti, M.; Biocotino, I.; Stevano, A.; Rocchio, F.; Canonico, P.L.; Grilli, M.; Genazzani, A.A.; Lim, D. TGF-B2 and TGF-B3 from Cultured β-Amyloid-Treated or 3xTg-AD-Derived Astrocytes May Mediate Astrocyte-Neuron Communication. *Eur. J. Neurosci.* **2018**, *47*, 211–221. [CrossRef] [PubMed]

45. Schmidt, E.K.; Clavarino, G.; Ceppi, M.; Pierre, P. SUnSET, a Nonradioactive Method to Monitor Protein Synthesis. *Nat. Methods* **2009**, *6*, 275–277. [CrossRef] [PubMed]

46. Massignan, T.; Biasini, E.; Lauranzano, E.; Veglianese, P.; Pignataro, M.; Fioriti, L.; Harris, D.A.; Salmona, M.; Chiesa, R.; Bonetto, V. Mutant Prion Protein Expression Is Associated with an Alteration of the Rab GDP Dissociation Inhibitor Alpha (GDI)/Rab11 Pathway. *Mol. Cell. Proteom.* **2010**, *9*, 611–622. [CrossRef]

47. Gillardon, F. Differential Mitochondrial Protein Expression Profiling in Neurodegenerative Diseases. *Electrophoresis* **2006**, *27*, 2814–2818. [CrossRef]

48. Rocchio, F.; Tapella, L.; Manfredi, M.; Chisari, M.; Ronco, F.; Ruffinatti, F.A.; Conte, E.; Canonico, P.L.; Sortino, M.A.; Grilli, M.; et al. Gene Expression, Proteome and Calcium Signaling Alterations in Immortalized Hippocampal Astrocytes from an Alzheimer's Disease Mouse Model. *Cell Death Dis.* **2019**, *10*, 24. [CrossRef]

49. Dalla Pozza, E.; Manfredi, M.; Brandi, J.; Buzzi, A.; Conte, E.; Pacchiana, R.; Cecconi, D.; Marengo, E.; Donadelli, M. Trichostatin A Alters Cytoskeleton and Energy Metabolism of Pancreatic Adenocarcinoma Cells: An in Depth Proteomic Study. *J. Cell. Biochem.* **2018**, *119*, 2696–2707. [CrossRef]

50. Manfredi, M.; Robotti, E.; Bearman, G.; France, F.; Barberis, E.; Shor, P.; Marengo, E. Direct Analysis in Real Time Mass Spectrometry for the Nondestructive Investigation of Conservation Treatments of Cultural Heritage. *J. Anal. Methods Chem.* **2016**, *2016*, 6853591. [CrossRef]

51. Manfredi, M.; Brandi, J.; Di Carlo, C.; Vita Vanella, V.; Barberis, E.; Marengo, E.; Patrone, M.; Cecconi, D. Mining Cancer Biology through Bioinformatic Analysis of Proteomic Data. *Expert Rev. Proteom.* **2019**, *16*, 733–747. [CrossRef]

52. Albanese, P.; Nield, J.; Tabares, J.A.M.; Chiodoni, A.; Manfredi, M.; Gosetti, F.; Marengo, E.; Saracco, G.; Barber, J.; Pagliano, C. Isolation of Novel PSII-LHCII Megacomplexes from Pea Plants Characterized by a Combination of Proteomics and Electron Microscopy. *Photosynth. Res.* **2016**, *130*, 19–31. [CrossRef] [PubMed]

53. Saá, P.; Harris, D.A.; Cervenakova, L. Mechanisms of Prion-Induced Neurodegeneration. *Expert Rev. Mol. Med.* **2016**, *18*, e5. [CrossRef] [PubMed]

54. Sarnataro, D.; Pepe, A.; Zurzolo, C. Chapter Three—Cell Biology of Prion Protein. In *Progress in Molecular Biology and Translational Science*; Legname, G., Vanni, S., Eds.; Prion Protein; Academic Press: Cambridge, MA, USA, 2017; Volume 150, pp. 57–82.

55. Hogan, P.G.; Chen, L.; Nardone, J.; Rao, A. Transcriptional Regulation by Calcium, Calcineurin, and NFAT. *Genes Dev.* **2003**, *17*, 2205–2232. [CrossRef] [PubMed]

56. Sans, M.D.; Williams, J.A. Calcineurin Is Required for Translational Control of Protein Synthesis in Rat Pancreatic Acini. *Am. J. Physiol. Cell Physiol.* **2004**, *287*, C310–C319. [CrossRef] [PubMed]

57. Restelli, E.; Capone, V.; Pozzoli, M.; Ortolan, D.; Quaglio, E.; Corbelli, A.; Fiordaliso, F.; Beznoussenko, G.V.; Artuso, V.; Roiter, I.; et al. Activation of Src Family Kinase Ameliorates Secretory Trafficking in Mutant Prion Protein Cells. *J. Biol. Chem.* **2021**, *296*, 100490. [CrossRef]

58. Fioriti, L.; Dossena, S.; Stewart, L.R.; Stewart, R.S.; Harris, D.A.; Forloni, G.; Chiesa, R. Cytosolic Prion Protein (PrP) Is Not Toxic in N2a Cells and Primary Neurons Expressing Pathogenic PrP Mutations. *J. Biol. Chem.* **2005**, *280*, 11320–11328. [CrossRef]

59. Mallucci, G.R.; White, M.D.; Farmer, M.; Dickinson, A.; Khatun, H.; Powell, A.D.; Brandner, S.; Jefferys, J.G.R.; Collinge, J. Targeting Cellular Prion Protein Reverses Early Cognitive Deficits and Neurophysiological Dysfunction in Prion-Infected Mice. *Neuron* **2007**, *53*, 325–335. [CrossRef]

60. Castle, A.R.; Gill, A.C. Physiological Functions of the Cellular Prion Protein. *Front. Mol. Biosci.* **2017**, *4*, 19. [CrossRef]

61. Legname, G. Elucidating the Function of the Prion Protein. *PLOS Pathog.* **2017**, *13*, e1006458. [CrossRef]

62. Linden, R. The Biological Function of the Prion Protein: A Cell Surface Scaffold of Signaling Modules. *Front. Mol. Neurosci.* **2017**, *10*, 77. [CrossRef]

63. De Mario, A.; Peggion, C.; Massimino, M.L.; Viviani, F.; Castellani, A.; Giacomello, M.; Lim, D.; Bertoli, A.; Sorgato, M.C. The Prion Protein Regulates Glutamate-Mediated Ca^{2+} Entry and Mitochondrial Ca^{2+} Accumulation in Neurons. *J. Cell Sci.* **2017**, *130*, 2736–2746. [CrossRef] [PubMed]

64. De Mario, A.; Castellani, A.; Peggion, C.; Massimino, M.L.; Lim, D.; Hill, A.F.; Sorgato, M.C.; Bertoli, A. The Prion Protein Constitutively Controls Neuronal Store-Operated Ca^{2+} Entry through Fyn Kinase. *Front. Cell. Neurosci.* **2015**, *9*, 416. [CrossRef] [PubMed]

65. Lazzari, C.; Peggion, C.; Stella, R.; Massimino, M.L.; Lim, D.; Bertoli, A.; Sorgato, M.C. Cellular Prion Protein Is Implicated in the Regulation of Local Ca^{2+} Movements in Cerebellar Granule Neurons. *J. Neurochem.* **2011**, *116*, 881–890. [CrossRef] [PubMed]

66. Lim, D.; Bertoli, A.; Sorgato, M.C.; Moccia, F. Generation and Usage of Aequorin Lentiviral Vectors for Ca^{2+} Measurement in Sub-Cellular Compartments of Hard-to-Transfect Cells. *Cell Calcium* **2016**, *59*, 228–239. [CrossRef] [PubMed]

67. Butcher, S.P.; Henshall, D.C.; Teramura, Y.; Iwasaki, K.; Sharkey, J. Neuroprotective Actions of FK506 in Experimental Stroke: In Vivo Evidence against an Antiexcitotoxic Mechanism. *J. Neurosci.* **1997**, *17*, 6939–6946. [CrossRef]

68. Cai, J.; Sun, Y.; Yin, Z.; Wang, D.; Shi, K.; Fu, Y.; Cao, X.; Ge, Y. Analysis of FK506-Mediated Functional Recovery and Neuroprotection in a Rat Model of Spinal Cord Injury Indicates That EGF Is Modulated in Astrocytes. *Exp. Ther. Med.* **2018**, *16*, 501–510. [CrossRef]

69. Hong, H.-S.; Hwang, J.-Y.; Son, S.-M.; Kim, Y.-H.; Moon, M.; Inhee, M.-J. FK506 Reduces Amyloid Plaque Burden and Induces MMP-9 in AβPP/PS1 Double Transgenic Mice. *J. Alzheimers Dis.* **2010**, *22*, 97–105. [CrossRef]

70. Labrande, C.; Velly, L.; Canolle, B.; Guillet, B.; Masmejean, F.; Nieoullon, A.; Pisano, P. Neuroprotective Effects of Tacrolimus (FK506) in a Model of Ischemic Cortical Cell Cultures: Role of Glutamate Uptake and FK506 Binding Protein 12 KDa. *Neuroscience* **2006**, *137*, 231–239. [CrossRef]

71. Saganová, K.; Gálik, J.; Blaško, J.; Korimová, A.; Račeková, E.; Vanický, I. Immunosuppressant FK506: Focusing on Neuroprotective Effects Following Brain and Spinal Cord Injury. *Life Sci.* **2012**, *91*, 77–82. [CrossRef]

72. Zawadzka, M.; Kaminska, B. A Novel Mechanism of FK506-Mediated Neuroprotection: Downregulation of Cytokine Expression in Glial Cells. *Glia* **2005**, *49*, 36–51. [CrossRef]

73. Kraner, S.D.; Norris, C.M. Astrocyte Activation and the Calcineurin/NFAT Pathway in Cerebrovascular Disease. *Front. Aging Neurosci.* **2018**, *10*, 287. [CrossRef] [PubMed]

74. Lim, D.; Rocchio, F.; Mapelli, L.; Moccia, F. From Pathology to Physiology of Calcineurin Signalling in Astrocytes. *Opera Med. Physiol.* **2016**, *2*, 122–140.

75. Bollo, M.; Paredes, R.M.; Holstein, D.; Zheleznova, N.; Camacho, P.; Lechleiter, J.D. Calcineurin Interacts with PERK and Dephosphorylates Calnexin to Relieve ER Stress in Mammals and Frogs. *PLoS ONE* **2010**, *5*, e11925. [CrossRef] [PubMed]

76. Tosello, V.; Saccomani, V.; Yu, J.; Bordin, F.; Amadori, A.; Piovan, E. Calcineurin Complex Isolated from T-Cell Acute Lymphoblastic Leukemia (T-ALL) Cells Identifies New Signaling Pathways Including MTOR/AKT/S6K Whose Inhibition Synergize with Calcineurin Inhibition to Promote T-ALL Cell Death. *Oncotarget* **2016**, *7*, 45715–45729. [CrossRef] [PubMed]

Chapter 4

Genetic deletion of astrocytic calcineurin B1 prevents cognitive impairment and neuropathology development in acute and chronic mouse models of Alzheimer's disease. (IN REVISION)

Running head: Astrocyte calcineurin in Alzheimer's disease

Laura Tapella[1]#, Giulia Dematteis[1]#, Pietro La Vitola[2], Susanna Leva[2], Elisa Tonelli[1], Marco Raddi[1], Marta Delconti[1], Letizia Dacomo[2], Mariagrazia Grilli[1], Laura Colombo[2], Mario Salmona[2], Gianluigi Forloni[2], Armando A Genazzani[1]*, Claudia Balducci[2]*, Dmitry Lim[1]*

co-first,

* corresponding

armando.genazzani@uniupo.it; Phone(Office): +39 0321 375827

claudia.balducci@marionegri.it; Phone(Office): +39.02.39014395

dmitry.lim@uniupo.it; Phone(Office): +39 0321 375822

Affiliations

[1] Department of Pharmaceutical Sciences, Università del Piemonte Orientale, Via Bovio 6, 28100, Novara, Italy

[2] Department of Neuroscience, Istituto di Ricerche Farmacologiche Mario Negri IRCCS, via Mario Negri 2, 20156 Milano (Italy)

Word count: 7443

Statements relating to our ethics and integrity policies

ABSTRACT

Alzheimer's disease (AD) represents an urgent yet unmet challenge for modern society, calling for exploration of innovative targets and therapeutic approaches. Astrocytes, main homeostatic cells in the CNS, represent promising cell-target. Our aim was to investigate if deletion of the regulatory CaNB1 subunit of calcineurin in astrocytes could mitigate AD-related memory deficits, neuropathology and neuroinflammation. We have generated two, acute and chronic, AD mouse models with astrocytic CaNB1 ablation (ACN-KO). In the former we evaluated the ability of β-amyloid oligomers (AβOs) to impair memory and activate glial cells once injected in the cerebral ventricle of conditional ACN-KO mice. Next, we generated a tamoxifen-inducible astrocyte-specific CaNB1 knock-out in 3xTg-AD mice (indACNKO-AD). CaNB1 was deleted, by tamoxifen injection, in 11.7-month-old 3xTg-AD mice for 4.7 months. Spatial memory was evaluated using the Barnes maze; β-amyloid plaques burden, neurofibrillary tangle deposition, reactive gliosis and neuroinflammation were also assessed. The acute model showed that ICV injected AβOs in 2-month-old wild type mice impaired recognition memory and fostered a pro-inflammatory microglia phenotype, whereas in ACN-KO mice, AβOs were inactive. In indACNKO-AD mice, 4.7 months after CaNB1 depletion we found preservation of spatial memory and cognitive flexibility, abolishment of amyloidosis and reduction of neurofibrillary tangles, gliosis and neuroinflammation. Our results suggest that ACN is crucial for the development of cognitive impairment, AD neuropathology and neuroinflammation. Astrocyte-specific CaNB1 deletion is beneficial for both the abolishment of AβO-mediated detrimental effects and treatment of ongoing AD-related pathology, hence representing an intriguing target for AD therapy.

Main points:

- Depletion of astrocytic calcineurin B1 (ACN-KO) abolishes β-amyloid oligomer-mediated memory impairment and microglia activation.
- Inducible ACN-KO in 3xTg-AD mice prevents disease development.
- ACN represents a valuable target for AD therapy.

INTRODUCTION

Alzheimer's disease (AD) remains an urgent yet unmet challenge [96]. In spite of significant progresses made in deciphering the mechanisms of action of the main recognized culprit such as the β-amyloid peptide (Aβ), including synaptic, cognitive dysfunction, and neuronal cell death, clinical trials against these targets have failed [97]. Recently, breakthrough discoveries highlighted the primary role of glial cells and neuroinflammation as driving force of AD [98]. Of note, astrocytes are primary target of Aβ oligomers (AβOs) - the main neurotoxic species fostering synaptic/cognitive dysfunction and gliosis [99,100] - already at initial disease stages. They play crucial roles in brain metabolism, inter-neuronal signaling, vascular regulation, and defense [101]. Calcium (Ca^{2+}) homeostasis dysregulation in reactive astrocytes appears as a crucial disease event [102]. Furthermore, astrocytes acquire a pro-inflammatory phenotype responsible for neurodegeneration,[103] a cascade of events requiring the activation of astroglial calcineurin (CaN) → nuclear factor of activated T-cells (NFAT) axis, which is responsible for the transcription and release of harmful pro-inflammatory molecules [104–107].

CaN is a ubiquitous serine-threonine phosphatase composed of a catalytic subunit A (CaNA) and an obligatory regulatory subunit B1 (CaNB1). Genetic elimination of CaNB1 in neurons was shown to ablate CaN activity [108,109]. Activation of CaN occurs in several steps upon Ca^{2+} binding to the EF-hand Ca^{2+} binding domains of CaNB, and the Ca^{2+}/calmodulin (CaM) complex to the CaM-binding domain (CaMBD) at the C-terminal of the CaNA autoinhibitory tail. Displacement of the autoinhibitory tail allows the access of the catalytic site to substrate proteins.

In the healthy brain, CaN is mostly expressed in neurons where it is essential for synaptic plasticity and memory formation [110], but much less in astrocytes

[109] where it regulates neuronal excitability and protein expression at the post-transcriptional level [109,111–113]. During AD, CaN is overactivated mainly in astrocytes and by interacting with NFAT induces synaptic/cognitive dysfunction, glutamate dysregulation and neuroinflammation [114]. CaN inhibition with tacrolimus (FK506) in AD mice reverts cognitive and synaptic dysfunction [115,116]. Astrocyte-specific inhibition of CaN→NFAT axis in AD mice mitigates astrogliosis and neuroinflammation, reduces deposition of Aβ plaques and ameliorates memory [117]. In addition, organ transplanted subjects chronically treated with FK506 have a lower AD risk [118].

However, neither genetic ablation of CaN specifically in astrocytes in AD mouse models, nor the specific targeting of the regulatory CaNB1 subunit have been investigated so far. We have thus developed two AD mouse models with a KO of CaNB1 subunit in GFAP-expressing astrocytes. In conditional astrocyte-specific CaN-KO (ACN-KO) mice we tested the effects of AβOs injected in the cerebral ventricle, on memory and glial cells [99,109,119,120]. In an inducible ACN KO model on the background of 3xTg-AD mice we evaluated learning and memory abilities as well as the extent of neuropathology.

MATERIALS AND METHODS

Animals

Conditional astrocyte-specific CaN KO mice.

Generation and characterization of ACN-Ctr and ACN-KO mice with a conditional astrocyte-specific KO of CaN was reported elsewhere [109]. Mice used at the Mario Negri Institute for Pharmacological Research (IRFMN) were all drug and behavioral test naïve and the experiments were conducted during the light cycle. Animals were housed in a SPF facility in standard mouse cages

containing sawdust with food (2018S Envigo diet) and water ad libitum, under conventional laboratory conditions (room temperature: $20 \pm 2°C$; humidity: 60%) and a 12/12-hour light/dark cycle (7:00 am – 7:00 pm). For all the experiments male mice were used. The IRFMN adheres to the principles set out in the following laws, regulation, and policies governing the Care and Use of Laboratory Animals: Italian Governing Law (D.lgs 26/2014; Authorization n.19/2008-A issued March 6, 2008 by Ministry of Health); Mario Negri Institutional Regulations and Policies providing internal authorization for persons conducting animal experiments (Quality Management System Certificate – UNI EN ISO 9001:2015 – Reg. N° 6121); the NIH Guide for the Care and Use of Laboratory Animals (2011 edition) and EU directives and guidelines (EEC Council Directive 2010/63/UE). The statement of Compliance (Assurance) with the Public Health Service (PHS) Policy on Human Care and Use of Laboratory Animals has been reviewed (9/9/2014; Animal Welfare Assurance #A5023-01). All animals were managed in accordance with European directive 2010/63/UE and with Italian law D.l. 26/2014. The procedures were approved by the local animal-health and ethical committee (Università del Piemonte Orientale and Mario Negri Insitute for Pharmacological Research) and were authorized by the national authority (Istituto Superiore di Sanità; authorization numbers N. 77-2017, 648-2018 and N. 818/2018-PR). All efforts were made to reduce the number of animals by following the 3R's rule.

Generation of inducible astrocytic CaN KO in 3xTg-AD mice

Inducible astrocytic CaN KO was generated by crossing CaNB1[flox/flox] mice [108] (Jackson Laboratory strain B6;129S-Ppp3r1tm2Grc/J, stock number 017692), with ROSA26tdTomato[flox/flox]/GfapCreERT2^{+/-} (GFAP-CreERT2-R26tdT)

mouse line bearing human glial fibrillary acidic protein (GFAP) promoter driving the expression of a fusion protein consisting of bacterial Cre recombinase and a ligand-binding domain of estrogen receptor (CreERT2). The mice contained also tdTomato reporter gene preceded by a loxP-flanked STOP sequence into the ubiquitously active ROSA26 locus to allow optical temporal and spatial control of CreERT2-induced recombination. GFAP-CreERT2-R26tdT mice, which were on a C57Bl/6 background, were kindly provided by Prof. Frank Kirchhoff, CIPMM, University of Saarland, Homburg, Germany[121]. Resulting mouse line CaNB1$^{flox/flox}$/ROSA26tdTomato$^{flox/flox}$/GfapCreERT2$^{+/-}$ (abbreviated as indACNKO) was crossed with 3xTg-AD mice harboring knock-in point mutation of presenilin 1 gene PS1$_{M146V}$, and two transgenes (amyloid precursor protein Swedish mutation KM670/671NL, APP$_{Swe}$ and tau$_{P301L}$) under Thy1.2 promoter[122]. Resulting mice with genotype CaNB1$^{flox/flox}$/ROSA26tdTomato$^{flox/flox}$/GfapCreERT2$^{+/-}$ /PS1$_{M146V}$$^{KI/KI}$/APP$_{Swe}$^{Tg}/tau$_{P301L}$^{Tg}, abbreviated as indACNKO-AD, were maintained on mixed C57Bl/6:129X1/SvJ;129S1/Sv background. Mice were housed in the animal facility of the Università del Piemonte Orientale, 2-5 mice/cage, with unlimited access to water and food. The induction of the CreERT2 nuclear translocation and, therefore CaN KO and tdTomato expression, was induced by tamoxifen (TAM; Cayman Chemical, Ann Arbor, Michigan, USA, Cat. 13258), dissolved in 90% corn oil, 10% ethanol at a 10 mg/ml final concentration. Each mouse received at 11.7 months intraperitoneal (i.p.) injection of 50 mg/kg TAM once a day for 8 consecutive days [121].

Intracerebroventricular incannulation.

Mice were anesthetized with Forane (Abbott) using stereotaxic apparatus (model 900, David Kopf, CA) a 7 mm-long guide cannula was implanted into

the cerebral lateral ventricle (L ± 1.0 and DV -3.0 from dura with incisor bar at 0°) and secured to the skull with two stainless steel screws and dental cement. To avoid infections the animals received intraperitoneal injections of 150 mg/kg/day Amplital (Pfizer) for three consecutive days after surgery. Mice were allowed 10-15 days to recover from surgery before the experiment.

$A\beta_{1-42}$ treatment.

The $A\beta_{1-42}$ preparations, checked by AFM [119], were infused into the lateral cerebral ventricle using an injection unit inserted into the guide cannula. The $A\beta_{1-42}$ were diluted to 1 µM in 5 mM PBS, pH 7.4, and 7.5 µL were infused using a Hamilton syringe in a total time of 5 minutes. The injection unit was left in place for 2 minutes more to allow the solution to diffuse. Two hours after the AβO injection mice entered the familiarization phase of the NORT.

Novel object recognition test

Mice were tested in their home cage (30 x 13 cm) to reduce stress related to the exposure to a new environment. The following objects were used: a black plastic cylinder (4 x 5 cm), a glass vial with a white cup filled with water (3 x 6 cm) and a metal cube (3 x 5 cm). The task started with a 10 min familiarization trial during which exploration was recorded by an investigator blinded to the strain. Sniffing, touching and stretching the head toward the object at a distance not more than 2 cm were scored as object investigation. Twenty-four hours later (test trial) mice were exposed for 10 min to two objects: one familiar and a new, different one (novel object), and the time spent exploring the objects was recorded. Memory was expressed as a discrimination index, i.e. (seconds on novel – seconds on familiar)/(tot time on objects). [119,123]

Barnes maze (BM)

The Barnes maze is made of a circular white acrylic slab with a diameter of 1 m and twenty holes with a diameter of 5 cm on its perimeter at a distance of 2.5 cm from the edge. The maze was placed on the top of a stool, 60 cm above the ground in the center of a dedicated room, with colored-paper shapes as visual cues. Two 120 W lights were placed on the edges of the room. The escape box was made of a plastic dark box. The maze was cleaned using 70% ethanol after each trial. All sessions were recorded and analyzed with the SMART V2.5.21 software. Before TAM injections for ACN-KO induction mice were exposed to the BM (pre-TAM) in two phases: habituation (Hab) and acquisition training (AT). Post-TAM Barnes maze test included 3 different phases: Hab, AT and the Reversal Acquisition training (RAT). Hab and AT1 session were run on the same day, while the remaining as 3 sessions/day for 5 consecutive days with an interval of 15-30 min/mouse. For RAT, to test cognitive flexibility, the escape box was moved seven holes anti-clockwise. After each trial mice were returned to their home cage. For characterization of mice shown in Suppl. Figs. 2 and 3, n=7 and n=5 indACNKO-NT and indACNKO-AD mice were used, respectively. In Barnes maze experiment described in Fig. 4, n=10 for indACNctr-AD and n=6 for indACNKO-AD mice were used.

Intracardiac perfusion and brain tissue preparation.

Animals were anesthetized with a mixture of ketamine/medetomidine (1.5 mg/kg and 1.0 mg/kg respectively; i.p.), and ACN-Ctr/KO mice intracardially perfused with PBS 1X and 4% paraformaldehyde (PFA), post-fixed in 4% PFA (2 h, 4°C) and then cryo-protected in 20% sucrose (4°C, 24 h), frozen in n-pentane (-45°C) and stored at -80°C until use. IndACN mice were perfused with PBS, brains removed and divided in two halves: the left half was fixed in

4% PFA (48h), transferred in sucrose and frozen. The hippocampus from the right part was dissected, snap-frozen and conserved at -80°C.

Immunohistochemistry

Plaques, astrocytes, microglia. Mouse brain slices (n= 3/mouse) were incubated with H_2O_2 (1%) for 10 min followed by 1 h incubation at 4°C with blocking solutions [6E10 (plaques) 10% NGS; GFAP (astrocytes): 3% NGS+0.3% Triton X-100; Cd11b (microglia): 3% NGS + 0.4% Triton X-100). They were subsequently incubated overnight (O/N) with primary antibodies: mouse anti-6E10 (1:500, Signet), mouse anti-GFAP (1:3500, Chemicon Int. Inc., Temecula, USA); rabbit anti-CD11b (1:1000, Wako). After incubation with the biotinylated secondary antibody (1:200; Vector Laboratories), immunoreactivity was developed by avidin–biotin–peroxidase technique (Vectastain ABC kit, Vector Labs, USA), using 3′,3′-diaminobenzidine (DAB; Sigma, Munich, Germany) as chromogen.

Immunofluorescence. Brain sections (40 µm) were cut throughout the temporal extension of the hippocampus, then collected in 100 mM PBS for a double-immunofluorescence analysis for Iba1 and CD16/32. The primary antibodies (CD16/32 1:600, BD Pharmigen, USA; Iba1 1:1000, Wako; Japan) were applied after blocking solution (10% NGS + 0.3% Triton X-100 1h at RT) and kept o/n, followed by the fluorescent secondary antibodies (1:500, 1 h, RT) conjugated respectively with Alexa 488 and 546 (Molecular Probes).

Image analysis.

Quantitative analyses were done by an operator blind to genotype and treatment and normalizing on the quantified area. Area of selection was the whole hippocampus (3 slices/mouse). Brain images for DAB-stained slices were acquired using the Olympus Virtual Stage microscope (20X magnification). Immunofluorescence was acquired using an IX81 microscope and a FV500 confocal scan unit with 3 laser lines and an ultraviolet diode. 3D images were acquired at 40X magnification (10.45 µm z-axis, 0.95 µm step size). Marker immunoreactivity and the colocalization were quantified by applying dedicated home-made macros through Fiji software [124].

Imaging of tdTomato-positive astrocyte for quantitative analysis was done using Zeiss 710 confocal laser scanning microscope equipped with Plan-Neofluar 40x/1.30 Oil DIC M27 objective and Zen software. Stacks of fluorescent images were taken across slice thickness (20 images, 1 µm step) and merged using major projection algorithm. Quantification was performed offline using Fiji Image J software. Automatic threshold was applied with following quantification of area occupied by tdTomato.

To colocalize tdTomato-positive astrocytes with GFAP, slices were stained using mouse anti-GFAP antibody (1:100, Santa Cruz Biotechnology, USA, Cat. SC6170) followed by staining with secondary anti-goat biotinylated antibody (1:200, Vector Biolabs, USA, Cat. BA9500) and staining with Alexa-633-conjugated streptavidin (1:200, Invitrogen, S21375). Nuclei were counterstaned with DAPI. Stacks of fluorescent images were taken using Leica STELLARIS 8 confocal laser scanning microscope equipped with white light laser, HCX PL APO 40X/1.25-075 OIL CL objective and LAS X software.

Western blot

Hippocampi were homogenized (10% w/v) in lysis buffer containing 50mM Tris-HCl (pH 7.4), 150mM NaCl, Nonidet P-40 (NP-40) 0.5%, Sodium Deoxycholate (Na-Doc) 0.5%, 5mM EDTA, protease inhibitors cocktail (PIC, Millipore, cat. 539133) and phosphatase inhibitor cocktail (Thermo Fisher Scientific, cat. 78428). Lysates were quantified with QuantiPro BCA Assay Kit (Sigma, cat. SLBF3463). 20 µg of proteins were mixed with Laemmli Sample Buffer 4X (Bio-Rad), and boiled. Then samples were loaded on a 12% polyacrylamide-sodium dodecyl sulphate gel for SDS-PAGE. Proteins were transferred onto nitrocellulose membrane, using Mini Transfer Packs with Trans-Blot® Turbo TM (Bio-Rad). The membranes were blocked in 5% milk (Sigma, Cat. 70166; 45', RT). Subsequently, membranes were incubated with anti-GFAP (MAB-12029, Immunological Sciences) antibody (4°C, o/n). The goat anti-rabbit Igg (H+L)-HRP secondary antibody (1:5000; Cat. 170-6515, Bio-Rad) was used. Detection was carried out with SuperSignalTM West Pico/femto PLUS Chemiluminescent Substrate (Thermo Scientific) and developed using ChemiDocTM Imaging System (Bio-Rad). Anti-β-Actin (A1978, Sigma Aldrich) was used for protein normalization.

Total RNA extraction and real-time PCR

Total RNA was extracted using Trizol Reagent (Invitrogel, Cat. 15596026) as reported elsewhere [125]. 0.5-1 µg of total RNA was transcribed using SensiFast kit (BioLine, London, UK, Cat. BIO-65054). Real-time quantitative PCR (qPCR) was performed using iTaq qPCR master mix (Bio-Rad, Cat. 1725124) on a SFX96 Real-time system (Bio-Rad). To normalize raw real time PCR data, S18 ribosomal subunit was used. Primer sequences are provided in

Supplementary Table 1. Data are expressed as delta-C(t) of gene of interest to S18 allowing appreciation of single gene expression level.

Statistical analysis

Data were expressed as mean ± standard error of the mean (SEM) and analyzed using GraphPad Prism software. Data normal distribution was ascertained so to select either parametric or non- parametric analyses. The results of Barnes maze test were analyzed using two-way ANOVA, mixed-effect model using GraphPad Prism v.9.3.0. In the presence of a significant effect of treatment or a significant interaction the appropriate post-hoc tests were applied. A p-value < 0.05 was considered significant.

RESULTS

Conditional deletion of CaNB1 in astrocytes protects from the actions of AβOs.

AβOs are responsible for synaptic dysfunction, memory impairment and glial cell activation. We proved that a single ICV injection of AβOs produces memory impairment associated with a neuroinflammatory reaction [99,119,120]. To explore if astrocytic CaNB1 deletion could prevent AβO-induced toxicity, we used newly generated conditional astroglial CaNB1 KO (ACN-KO) mice [109]. According to the endogenous pattern of GFAP expression, CaNB1 deletion starts from the second post-natal week. At the age of the experiment (8 weeks), ACN-KO mice do not have visible phenotype and object recognition memory is not altered (Fig. 1). In these mice we ICV injected AβOs and compared their effects on memory, in the NORT (Fig. 1A), and on glial cells with those observed in ACN-Ctr mice. As shown in Fig. 1 B, AβOs produced significant

impairment in object recognition ability of ACN-Ctr mice, which was fully preserved in ACN-KO mice.

To investigate whether memory protection in ACN-KO mice was associated also with the absence of glial cell activation, ACN-Ctr and ACN-KO mice, receiving vehicle (VEH) or AβOs were sacrificed at 2, 8 or 24 h post-injection for brain histology. These time points were selected based on our previous data describing the timing of AβO-induced glial cell activation [99]. As shown in Figure 1 C, GFAP was increased, although not significantly, in both ACN-Ctr and ACN-KO mice receiving AβO. However, when we evaluated microglial activation we found that the response in ACN-Ctr and ACN-KO mice was significantly different. As shown in Figure 2 A, B at 2 and 8 h post-infusion AβOs fostered a significant increase in Iba1-marked area (microglial cells) only in ACN-Ctr mice; a slight, not significant increase was observed in ACN-KO mice at 24 h. Furthermore, when we addressed the expression of CD16/32, a maker of the pro-inflammatory phenotype, we found it was expressed only in ACN-Ctr microglial cells, but not in those of ACN-KO mice (Fig. 3 A-C), thus indicating that ACN favours a pro-inflammatory phenotype of microglial cells in the presence of AβOs.

Generation of inducible astrocyte-specific CaN-KO on the background of 3xTg-AD mice.

In order to investigate the effects of ACN ablation on the in vivo development of AD-like pathogenesis, we induced CaNB1 depletion in the 3xTg AD mice. We crossed a previously characterized strain CaNB1 $^{flox/flox}$, in +which three exons of the regulatory subunit CaNB1 were flanked by *Lox*P sites [108,109], with a mouse expressing two transgenic cassettes: GFAP-CreERT2 cassette allowing expression of CreERT2 fusion protein in GFAP-expressing cells and

a flox-stop-floxt dTomato-expressing cassette which allows optical detection of CreERT2-expressing cells [121]. The resulting mice, hereafter referred as indACNKO, were crossed with 3xTg-AD mice [122] (Suppl. Fig. S1). As a result of selection, four lines were generated with genotypes listed in (Table 1), abbreviated as indACNctr-NT, indACNKO-NT, representing, respectively, non-transgenic control with inducible CaNB1 in astrocytes; and indACNctr-AD and indACNKO-AD, representing, respectively, control 3xTg-AD mice and 3xTg-AD bearing inducible KO of CaNB1 in GFAP-expressing astrocytes (Table 1). To analyze the efficiency of CreERT2-induced recombination, both male and female mice were administered i.p. with 10 mg/kg TAM once a day for 8 consecutive days starting at 10 months of age and were sacrificed 5 months later. As shown in Suppl. Fig. S2, 5 months after induction, tdTomato-positive astrocytes were found throughout the brain in GfapCreERT2$^{+/-}$ mice. In the hippocampus, central in this paper, 67% and 60% of astrocytes were tdTomato positive respectively in indACNKO-NT and indACNKO-AD mice, and hence, achieved KO of CaN, confirming the efficiency of CreERT2 methodology in adult AD mice. Co-localization with GFAP showed that all tdTomato astrocytes were positive for GFAP, confirming the cell-specificity of recombination (Suppl. Fig. S3). After the deletion of CaNB1 from astrocytes, neither indACNKO-NT nor indACNKO-AD mice present visible phenotype alterations at least for a period of 5 month. For subsequent experiments, CreERT2-mediated recombination was induced at an average of 11.7 ± 1.3 months by i.p. TAM injection once a day for 8 consecutive days [121]. Prior to the induction (~11 months of age) and post-induction (~15.7 months of age), spatial memory of indACNctr-AD and indACNKO-AD mice was tested in the BM. Mice were sacrificed at 16.1 ± 1.3 months, 4.4 months after first TAM injection (Fig. 4 A).

Improvement of spatial memory and cognitive flexibility in indACNKO-AD mice.

Loss of memory is one of the key symptoms in AD patients. Specifically, impairment of episodic spatial memory and cognitive flexibility in 3xTg-AD mice has been reported by many studies using different paradigms including Morris water maze, NORT and BM. To assess memory abilities in our mice we choose the BM, because it offers a multi-parametric behavioral assessment, including motor activity, and is relatively non-stressful for mice. As shown on the experimental setup scheme (Fig. 4 A), mice were subjected to BM test twice: the first one to document the absence of differences in motor and learning performance between indACNctr-AD and indACNKO-AD mice pre-TAM induction (namely pre-TAM test). The second one, post-TAM test, was run about 4 months after TAM induction at 15.7 months of age (post-TAM test) (Fig. 4 A). To avoid preconditioning of mice to reversal training, the pre-TAM test consisted in habituation (Hab) and 11 acquisition training sessions (AT) until the primary latency (time used for locating the target hole) decreased below 60 seconds in three consecutive sessions (a criterion adopted also for later tests). As shown on Fig. 4 B, both indACNctr-AD and indACNKO-AD, in the pre-TAM test, progressively learned the position of target hole ($F(10,268) = 13.50$, p = <0.0001 between sessions) with no differences in in learning profile ($F(1,27) = 0.06618$, p = 0.8 between genotypes, n=10 and n=6 for indACNctr-AD and indACNKO-AD, respectively), confirming similar learning abilities in the two genotypes. The post-TAM test included one Hab and 16 AT sessions (Fig. 4 C). From the very first sessions indACNKO-AD mice located the target hole in a shorter time, suggesting a better consolidation of the pre-TAM test compared with

indACNctr-AD mice. After 12 sessions, only indACNKO-AD mice reached the criterion (AT12-AT16), clearly highlighting higher spatial memory abilities compared to indACNctr-AD mice. Two-way ANOVA for repeated measures found significant differences between genotypes ($F_{(1,14)} = 6.738$, p = 0.0212) but not between sessions ($F_{(15, 210)} = 1.404$, p 0.1472; n=10 and n=6 for indACNctr-AD and indACNKO-AD, respectively).

Once the AT session blocks were completed, we moved the target hole by 7 positions anti-clockwise, and run a series of 12 RAT sessions, during which mice had to learn the new target location. Fig. 4 D shows that while indACNctr-AD mice did not show significant progressive primary latency reduction to locate the new target - with none session below 60 sec - indACNKO-AD mice showed progressive learning during the last 6 RAT sessions ($F_{(4.775,66.85)} = 6.519$, p = <0.0001 between sessions; $F_{(11,154)} = 1.983$, p = 0.0335 across sessions between genotypes; n=10 and n=6 for indACNctr-AD and indACNKO-AD, respectively). These results suggest that CaNB1 ablation in adult 3xTg-AD mice prevents the deterioration of learning and spatial memory abilities. Notably, differences in cognitive abilities were not due to the presence of motor deficits as ascertained by the measurement of mouse speed and distance travelled inside the maze, fully comparable between groups (Suppl. Fig. 4, 5).

Absence of Aβ plaques, and lower tau pathology and glial reactivity in indACNKO-AD mice.

Based on encouraging functional data in indACNKO-AD mice, we then investigated whether astrocytic ablation of CaNB1 had affected also their neuropathology. When we assessed plaque deposition pre-TAM none was detectable in both groups of mice, indicating that amyloidosis had not started yet (11.7-month; Fig. 5 A, pre-TAM) as previously documented in 3xTg-AD

male mice at this age [126]. In contrast, when plaques were labelled post-TAM induction, none of the 6 analyzed mouse brains had detectable Aβ deposits indACNKO-AD mice compared with indACNctr-AD (Fig. 5 B, post-TAM). Because of a greater consistency in the presence of plaques in the subiculum of the hippocampus of all mice analyzed, previously described at this mouse age [127–129], plaques were quantified only within this area (Fig. 5 C post-TAM), which confirmed qualitative observations showing a highly significant difference in the % of 6E10-marked area between the two groups.

Intracellular neurofibrillary tangles made of deposited hyper-phosphorylated tau represent the other key hallmark of AD highly correlating with cognitive impairment [130]. By assessing the extent of hippocampal tau pathology pre-TAM, at 11.7 months of age no signal was detectable in the two groups (Fig. 6 A, Pre-TAM). Notably, after TAM, tau pathology was clearly detectable only in the hippocampus of indACNctr-AD mice, in indACNKO-AD it was undetectable (Fig. 6 B post-TAM). The quantitative analysis confirmed histological observations (Fig. 6 C, post-TAM).

Next, we analyzed the expression of GFAP for astrocytes, and Iba1 for microglia. We observed an increase of GFAP immunoreactivity specifically around Aβ deposits (Fig. 7 A). Interestingly, GFAP immunoreactivity was significantly reduced in indACNKO-AD mice compared to that of indACNctr-AD as confirmed by GFAP-marked area quantification (Fig. 7 B). Accordingly, a significant increase of hippocampal GFAP protein expression was detected by Western blot analysis in indACNctr-AD vs. indACNctr-NT animals; in indACNKO-AD, GFAP protein levels were reduced down to the levels of indACNctr-NT mice (Suppl. Fig. S6). Similarly, staining with the microglial marker Iba1 revealed a higher immunoreactivity in indACNctr-AD

mice, which was significantly lower at both qualitative and quantitative level in indACNKO-AD mice (Fig. 7 C, D).

Reduction of neuroinflammation in indACNKO-AD mice.

Transcriptional alterations are features of AD astrocytes both *in vivo* and *in vitro* [125,131]. To assess if depletion of CaNB1 in 3xTg-AD mice had an effect on the general neuroinflammatory status we performed qPCR on RNAs extracted from whole hippocampi of indACNctr-NT, indACNKO-NT, indACNctr-AD and indACNKO-AD mice using primers for markers of reactive astrogliosis (GFAP, S100b, Vimentin), microgliosis (Iba1 and CD11b) and phagocytosis (CD68), or neuroinflammation-related cytokines (Il1β, Tnfα) and receptors (Tlr4). As shown in Fig. 8 A-G, GFAP, CD68, Il1β and Il6 mRNA were significantly increased in indACNctr-AD compared to indACNctr-NT or indACNKO-NT, while their levels were significantly decreased in indACNKO-AD mice.

DISCUSSION

This study was designed to test if genetic ablation of CaNB1 in astrocytes could counteract the effects of AβOs on memory and glial cells in an acute mouse model, as well as learning and memory deficits and the extent of AD-related neuropathology in 3xTg-AD mice. Two approaches have been pursued: i) ICV delivery of AβOs into constitutive ACN-KO mice (acute AD model), ii) generation and characterization of a novel mouse model with inducible ACN-KO in 3xTg-AD mice for evaluation of cognitive and neuropathological outcomes (chronic AD model).

Our results demonstrate that: (1) AβOs lose their ability to impair memory and induce neuroinflammation in the absence of ACN; (2) inducible ablation of CaNB1 in 3xTg-AD mouse astrocytes from 11.7 to 16.1 months of age: i) preserved cognitive abilities, (ii) prevented amyloidosis and tau pathology, iii) reduced gliosis and neuroinflammation.

Deletion of CaNB1 from astrocytes abolishes AβO-mediated detrimental effects on memory and glial cell activation.

AβOs are the most harmful species capable of disrupting the plasma membrane integrity and directly impact on synaptic and cognitive functions through several mechanisms [132,133]. Our previous work demonstrated that a single ICV infusion of AβOs fosters memory impairment associated with glial activation [499,119,120] which impacts on neuronal functions [99,134,135]. Here we applied this strategy to ACN-KO mice [109]. At this age ACN-KO mice do not show reactive gliosis or neuroinflammation and perform normally in the NORT [113], making them suitable to test AβO toxicity. Strikingly, we found that in 2-month-old ACN-KO mice, AβOs did not impair memory and we also confirmed that AβOs produced memory impairment in association with an activation of glial cells exclusively in ACN-Ctr mice; in ACN-KO mice the activation was evidenced at a later time point (24h), but it was slighter and not significant. In addition, by assessing the presence of a pro-inflammatory phenotype upon AβO injection, by labeling CD16/32, we found that microglia of ACN-Ctr mice were CD16/32$^+$. This suggests that deletion of CaNB1 from astrocytes is protective, and that activation of ACN is permissive for both AβO-mediated memory impairment and microgliosis. Despite we observed no differences in astrocytic activation between Ctr and ACNKO mice upon AβO injection, it is clear that the lack of ACN does significantly influence the action of the oligomers on memory and on microglia response. We have no explanation for

the response of astrocytes in the acute model, but future experiments will help to clarify this aspect and further characterize glial phenotype in the presence and the absence of ACN upon AβOs exposure. We are aware that AβO model does not represent AD pathogenesis. However, it allows to dissect the effects of oligomers on memory and glial cells. AβO injection has been used to study the effect of systemic CaN inhibition by FK506 on AβO-induced neuronal dysfunction [136], while here we show that the deletion of CaN from astrocytes is sufficient to counteract AβO-induced glial activation and memory impairment.

Deletion of ACN fully prevents cognitive impairment and neuropathology in 3xTg-AD mice.

To demonstrate that CaNB1 in astrocytes is a main driver of disease in its complexity, we have generated an inducible CaNB1 KO on the background of 3xTg-AD mice, a model which develops cognitive impairment, amyloidosis and tau pathology [122], as well as neuroinflammation, similar to human pathology.

Our results clearly show that CaNB1 deletion from astrocytes in 3xTg-AD mice preserves learning abilities and cognitive flexibility; completely abolishes plaque deposition and drastically reduced tau hyper-phosphorylation.

Several evidence indicates that Aβ toxicity and deposition are strongly associated with reactive gliosis and neuroinflammation [134,135,137]. Accordingly, the absence of plaques in our KO mice was accompanied by a significant decrease in the extent of gliosis. The functional significance of gliosis in AD remains unclear [138], from one side it is required for Aβ clearance, whereas its overactivation compromises cell homeostatic activities and Aβ uptake, creating a pathogenic, uncontrollable loop of glial overactivation and Aβ

buildup [139]. Furthermore, activated glial cells deprive neurons of a regulatory control necessary for memory processing [140]. We thus assume that concomitant reduction of amyloidosis and tau pathology together with mitigation of glial cell activation in our IndACNKO-AD mice might explain the preservation of their cognitive abilities.

Tau pathology amelioration in our IndACNKO-AD mice is of particular interest for two main reasons: (i) cognitive decline and neuronal death better correlate with the progression of tau neuropathology rather than with the abundance of Aβ deposits during the different stages of AD [130]. Therefore, prevention/mitigation of tau-pathology may itself represent an efficacious strategy to counteract cognitive decline in AD. It is, thus, conceivable to assume that astrocytic CaN might be considered as a promising target for disease-modifying pharmacological intervention, capable of interfering also with tau-pathology. (ii) Tau pathology is an umbrella term covering a wide group of diseases featured by the presence of tau inclusions in neurons and glia [141] which makes CaNB1 in astrocytes a versatile therapeutic target.

Astroglial CaN as a central hub of neuroinflammation and homeostasis: a mechanistic aspect.

All together our data corroborate the emerging role of astrocytic Ca^{2+}- CaN signaling in the onset and progression of AD neuropathology [105,106]. At the state of the art, it is difficult to provide a precise mechanistic explanation for the multiple protective actions we herein described. Nevertheless, several hypotheses could be suggested. Because of a persistent loop of mutual activation between astrocytes and microglia, subsequently influencing neuronal activity and memory, it is likely that ACN inhibition might be sufficient to interrupt such a vicious cycle, preserving neuronal function.

Reduced neuroinflammation can be, indeed, positively associated with the preservation of cognitive abilities we observed both in the AβO-induced and in indACNKO-AD mice, because of the strong association described between glial activation, neuroinflammation and synaptic plasticity and memory [99,140,142–146].

In our previous works, we, indeed, demonstrated that pre-treatment with anti-inflammatory drugs abolishes the action of AβOs or α-synuclein oligomers on memory [99].

Also, in the APP/PS1 AD mice it has been demonstrated that inhibition of ACN/NFAT pathway through the AAV vector expressing the NFAT inhibitor VIVIT under the GFAP promoter, improved basal hippocampal synaptic strength, long-term potentiation and cognition [117]. Prevention of reactive astrogliosis and neuroinflammation through inhibition of NFAT and NF-kB activation may play a role. Indeed, it is well known that the release of pro-inflammatory cytokines is responsible for an increase in Aβ production, and that this phenomenon relies on the activity of ACN-NFAT pathway. Thus, depletion of ACN in our mice might have turned into a reduction in Aβ production, thus explaining the impressively lower number of plaques deposited in IndACN-KO mice.

Recent data also suggest an interaction between ACN and the forkhead transcription factor FOX03 leading to its dephosphorylation and association with NFκB. The CAN/ FOX03/ NFκB association will promote gene programs responsible for neuroinflammation [147,148]. Of note, in our IndACN-KO mice neuroinflammatory markers were significantly decreased, which encourages to investigate this specific pathway in future work.

Recently, physiological functions of ACN have been linked to a number of homeostatic and signaling functions including metabolism and clearance of Aβ

and tau, that could be traced back to CaN control over astrocytic proteostasis [105,106,109,111–113]. It could be, thus, speculated that the CaN-dependent alterations of astrocytic proteostasis might turn into a reduced homeostatic support, e.g., through an alteration in the expression and release of neurotrophic, neuroprotective and signaling factors [102,106]. In this context, we have shown that astrocytes from 3xTg-AD mice show an impairment of protein synthesis and degradation machineries which turned into a reduced secretion of neurotrophic SPARC and neuroprotective HSP90 and HSP73 [149–151]. Whether CaN activation/dysfunction in AD astrocytes is linked to altered proteostasis, from which insufficient support to neurons, will be a matter of future investigations; however, such a link has already been suggested for a model of prion-induced neurodegeneration [152].

Last, ACN-KO may interfere with amyloidogenic process. Numerous reports suggest that Ca^{2+} signals control APP processing and release of $A\beta$ [153–156]. Likely, such a modulation, with participation of CaN occurs within pathogenic loop initiated by FAD-linked mutations and/or accumulation of $A\beta$Os, with consequent CaN-dependent transcriptional remodeling [134,157].

Altogether, all the above reported mechanisms and our results support the primary role of astrocytes in AD, which have been recently placed at the forefront in its pathogenesis, and suggest that CaNB1 - specifically in astrocytes - might be considered as a promising target for the development of cell targeting anti-AD therapies, capable of counteracting the multiple core neuropathological events of AD.

Data sharing plan: The data supporting the findings of this study are available upon reasonable request to the corresponding author.

Potential Conflicts of Interest: Nothing to report.

REFERENCES

1. Scheltens P, De Strooper B, Kivipelto M, et al. Alzheimer's disease. Lancet 2021;397(10284):1577–1590.
2. van Bokhoven P, de Wilde A, Vermunt L, et al. The Alzheimer's disease drug development landscape. Alzheimers Res Ther 2021;13(1):186.
3. Kwon HS, Koh S-H. Neuroinflammation in neurodegenerative disorders: the roles of microglia and astrocytes. Transl Neurodegener 2020;9(1):42.
4. Balducci C, Frasca A, Zotti M, et al. Toll-like receptor 4-dependent glial cell activation mediates the impairment in memory establishment induced by β-amyloid oligomers in an acute mouse model of Alzheimer's disease. Brain Behav Immun 2017;60:188–197.
5. Michelucci A, Heurtaux T, Grandbarbe L, et al. Characterization of the microglial phenotype under specific pro-inflammatory and anti-inflammatory conditions: Effects of oligomeric and fibrillar amyloid-beta. J Neuroimmunol 2009;210(1–2):3–12.
6. Verkhratsky A, Nedergaard M. Physiology of Astroglia. Physiol. Rev. 2018;98(1):239–389.
7. Verkhratsky A, Parpura V, Rodriguez-Arellano JJ, Zorec R. Astroglia in Alzheimer's Disease. Adv Exp Med Biol 2019;1175:273–324.
8. Liddelow SA, Guttenplan KA, Clarke LE, et al. Neurotoxic reactive astrocytes are induced by activated microglia. Nature 2017;541(7638):481–487.
9. Fernandez AM, Fernandez S, Carrero P, et al. Calcineurin in reactive astrocytes plays a key role in the interplay between proinflammatory and anti-inflammatory signals. J. Neurosci. 2007;27(33):8745–8756.
10. Furman JL, Norris CM. Calcineurin and glial signaling: neuroinflammation and beyond. J Neuroinflammation 2014;11:158.
11. Lim D, Tapella L, Dematteis G, et al. Calcineurin Signalling in Astrocytes: From Pathology to Physiology and Control of Neuronal Functions. Neurochem Res 2022;
12. Tapella L, Cerruti M, Biocotino I, et al. TGF-β2 and TGF-β3 from cultured β-amyloid-treated or 3xTg-AD-derived astrocytes may mediate astrocyte-neuron communication. Eur. J. Neurosci. 2018;47(3):211–221.
13. Neilson JR, Winslow MM, Hur EM, Crabtree GR. Calcineurin B1 is essential for positive but not negative selection during thymocyte development. Immunity 2004;20(3):255–266.
14. Tapella L, Soda T, Mapelli L, et al. Deletion of calcineurin from GFAP-expressing astrocytes impairs excitability of cerebellar and hippocampal neurons through astroglial Na+/K+ ATPase. Glia 2020;68(3):543–560.

15. Baumgärtel K, Mansuy IM. Neural functions of calcineurin in synaptic plasticity and memory. Learn. Mem. 2012;19(9):375–384.
16. Dematteis G, Restelli E, Chiesa R, et al. Calcineurin Controls Expression of EAAT1/GLAST in Mouse and Human Cultured Astrocytes through Dynamic Regulation of Protein Synthesis and Degradation. Int J Mol Sci 2020;21(6)
17. Dematteis G, Restelli E, Vanella VV, et al. Calcineurin Controls Cellular Prion Protein Expression in Mouse Astrocytes. Cells 2022;11(4):609.
18. Tapella L, Dematteis G, Ruffinatti FA, et al. Deletion of calcineurin from astrocytes reproduces proteome signature of Alzheimer's disease and epilepsy and predisposes to seizures. Cell Calcium 2021;100:102480.
19. Sompol P, Norris CM. Ca2+, Astrocyte Activation and Calcineurin/NFAT Signaling in Age-Related Neurodegenerative Diseases. Front Aging Neurosci 2018;10:199.
20. Cavallucci V, Berretta N, Nobili A, et al. Calcineurin inhibition rescues early synaptic plasticity deficits in a mouse model of Alzheimer's disease. Neuromolecular Med 2013;15(3):541–548.
21. Dineley KT, Hogan D, Zhang W-R, Taglialatela G. Acute inhibition of calcineurin restores associative learning and memory in Tg2576 APP transgenic mice. Neurobiol Learn Mem 2007;88(2):217–224.
22. Furman JL, Sama DM, Gant JC, et al. Targeting astrocytes ameliorates neurologic changes in a mouse model of Alzheimer's disease. J. Neurosci. 2012;32(46):16129–16140.
23. Taglialatela G, Rastellini C, Cicalese L. Reduced Incidence of Dementia in Solid Organ Transplant Patients Treated with Calcineurin Inhibitors. J. Alzheimers Dis. 2015;47(2):329–333.
24. Balducci C, Beeg M, Stravalaci M, et al. Synthetic amyloid-β oligomers impair long-term memory independently of cellular prion protein. PNAS 2010;107(5):2295–2300.
25. Balducci C, Forloni G. In vivo application of beta amyloid oligomers: a simple tool to evaluate mechanisms of action and new therapeutic approaches. Curr Pharm Des 2014;20(15):2491–2505.
26. Hirrlinger PG, Scheller A, Braun C, et al. Temporal control of gene recombination in astrocytes by transgenic expression of the tamoxifen-inducible DNA recombinase variant CreERT2. Glia 2006;54(1):11–20.
27. Oddo S, Caccamo A, Shepherd JD, et al. Triple-transgenic model of Alzheimer's disease with plaques and tangles: intracellular Abeta and synaptic dysfunction. Neuron 2003;39(3):409–421.
28. Balducci C, Santamaria G, La Vitola P, et al. Doxycycline counteracts neuroinflammation restoring memory in Alzheimer's disease mouse models. Neurobiol Aging 2018;70:128–139.

29. Schindelin J, Arganda-Carreras I, Frise E, et al. Fiji: an open-source platform for biological-image analysis. Nat Methods 2012;9(7):676–682.

30. Ruffinatti F, Tapella L, Gregnanin I, et al. Transcriptional remodeling in primary hippocampal astrocytes from an Alzheimer's disease mouse model. Curr Alzheimer Res 2018;

31. Hu Y-T, Chen X-L, Zhang Y-N, et al. Sex differences in hippocampal β-amyloid accumulation in the triple-transgenic mouse model of Alzheimer's disease and the potential role of local estrogens. Front Neurosci 2023;17:1117584.

32. Dionisio-Santos DA, Karaahmet B, Belcher EK, et al. Evaluating Effects of Glatiramer Acetate Treatment on Amyloid Deposition and Tau Phosphorylation in the 3xTg Mouse Model of Alzheimer's Disease. Front Neurosci 2021;15:758677.

33. Lambracht-Washington D, Fu M, Manouchehri N, et al. Glial cell transcriptome analyses in 3xTg-AD mice: Effects of aging, disease progression, and anti-Aβ immunotherapy. Aging Brain 2023;3:100066.

34. Rosenberg RN, Fu M, Lambracht-Washington D. Active full-length DNA Aβ42 immunization in 3xTg-AD mice reduces not only amyloid deposition but also tau pathology. Alzheimers Res Ther 2018;10(1):115.

35. Theofilas P, Ehrenberg AJ, Nguy A, et al. Probing the correlation of neuronal loss, neurofibrillary tangles, and cell death markers across the Alzheimer's disease Braak stages: a quantitative study in humans. Neurobiol Aging 2018;61:1–12.

36. Orre M, Kamphuis W, Osborn LM, et al. Isolation of glia from Alzheimer's mice reveals inflammation and dysfunction. Neurobiol Aging 2014;35(12):2746–2760.

37. Benilova I, Karran E, De Strooper B. The toxic Aβ oligomer and Alzheimer's disease: an emperor in need of clothes. Nat Neurosci 2012;15(3):349–357.

38. Forloni G, Balducci C. Alzheimer's Disease, Oligomers, and Inflammation. J Alzheimers Dis 2018;62(3):1261–1276.

39. Grolla AA, Fakhfouri G, Balzaretti G, et al. Aβ leads to Ca^{2+} signaling alterations and transcriptional changes in glial cells. Neurobiol. Aging 2013;34(2):511–522.

40. Narayan P, Holmström KM, Kim D-H, et al. Rare individual amyloid-β oligomers act on astrocytes to initiate neuronal damage. Biochemistry 2014;53(15):2442–2453.

41. Dineley KT, Kayed R, Neugebauer V, et al. Amyloid-beta oligomers impair fear conditioned memory in a calcineurin-dependent fashion in mice. J Neurosci Res 2010;88(13):2923–2932.

42. Minter MR, Taylor JM, Crack PJ. The contribution of neuroinflammation to amyloid toxicity in Alzheimer's disease. J Neurochem 2016;136(3):457–474.

43. Escartin C, Galea E, Lakatos A, et al. Reactive astrocyte nomenclature, definitions, and future directions. Nat Neurosci 2021;24(3):312–325.

44. Heneka MT, Carson MJ, El Khoury J, et al. Neuroinflammation in Alzheimer's disease. Lancet Neurol 2015;14(4):388–405.

45. Morris GP, Clark IA, Zinn R, Vissel B. Microglia: a new frontier for synaptic plasticity, learning and memory, and neurodegenerative disease research. Neurobiol Learn Mem 2013;105:40–53.

46. Götz J, Halliday G, Nisbet RM. Molecular Pathogenesis of the Tauopathies. Annu Rev Pathol 2019;14:239–261.

47. Al-Onaizi M, Al-Sarraf A, Braysh K, et al. Impaired spatial navigation and age-dependent hippocampal synaptic dysfunction are associated with chronic inflammatory response in db/db mice. Eur J Neurosci 2022;

48. Amirahmadi S, Farimani FD, Akbarian M, et al. Minocycline attenuates cholinergic dysfunction and neuro-inflammation-mediated cognitive impairment in scopolamine-induced Alzheimer's rat model. Inflammopharmacology 2022;

49. Hong S, Beja-Glasser VF, Nfonoyim BM, et al. Complement and microglia mediate early synapse loss in Alzheimer mouse models. Science 2016;352(6286):712–716.

50. Sandhu M, Irfan HM, Shah SA, et al. Friedelin Attenuates Neuronal Dysfunction and Memory Impairment by Inhibition of the Activated JNK/NF-κB Signalling Pathway in Scopolamine-Induced Mice Model of Neurodegeneration. Molecules 2022;27(14):4513.

51. Zhang Y, Liu D, Yao X, et al. DMTHB ameliorates memory impairment in Alzheimer's disease mice through regulation of neuroinflammation. Neurosci Lett 2022;785:136770.

52. Fernandez AM, Hervas R, Dominguez-Fraile M, et al. Blockade of the Interaction of Calcineurin with FOXO in Astrocytes Protects Against Amyloid-β-Induced Neuronal Death. J Alzheimers Dis 2016;52(4):1471–1478.

53. Fernandez AM, Jimenez S, Mecha M, et al. Regulation of the phosphatase calcineurin by insulin-like growth factor I unveils a key role of astrocytes in Alzheimer's pathology. Mol. Psychiatry 2012;17(7):705–718.

54. Dematteis G, Vydmantaitė G, Ruffinatti FA, et al. Proteomic analysis links alterations of bioenergetics, mitochondria-ER interactions and proteostasis in hippocampal astrocytes from 3xTg-AD mice. Cell Death Dis 2020;11(8):645.

55. Tapella L, Dematteis G, Moro M, et al. Protein synthesis inhibition and loss of homeostatic functions in astrocytes from an Alzheimer's disease mouse model: a role for ER-mitochondria interaction. Cell Death Dis 2022;13(10):878.

56. Gong C, Bonfili L, Zheng Y, et al. Immortalized Alzheimer's Disease Astrocytes: Characterization of Their Proteolytic Systems. Mol Neurobiol 2023;

57. Smith HL, Freeman OJ, Butcher AJ, et al. Astrocyte Unfolded Protein Response Induces a Specific Reactivity State that Causes Non-Cell-Autonomous Neuronal Degeneration. Neuron 2020;105(5):855-866.e5.

58. Zeiger W, Vetrivel KS, Buggia-Prévot V, et al. Ca2+ influx through store-operated Ca2+ channels reduces Alzheimer disease β-amyloid peptide secretion. J Biol Chem 2013;288(37):26955–26966.

59. Bussiere R, Lacampagne A, Reiken S, et al. Amyloid β production is regulated by β2-adrenergic signaling-mediated post-translational modifications of the ryanodine receptor. J Biol Chem 2017;292(24):10153–10168.

60. Guan P-P, Cao L-L, Wang P. Elevating the Levels of Calcium Ions Exacerbate Alzheimer's Disease via Inducing the Production and Aggregation of β-Amyloid Protein and Phosphorylated Tau. Int J Mol Sci 2021;22(11):5900.

61. Green KN, LaFerla FM. Linking calcium to Abeta and Alzheimer's disease. Neuron 2008;59(2):190–194.

62. Lim D, Iyer A, Ronco V, et al. Amyloid beta deregulates astroglial mGluR5-mediated calcium signaling via calcineurin and Nf-kB. Glia 2013;61(7):1134–1145.

Figures and legends

FIGURE 1
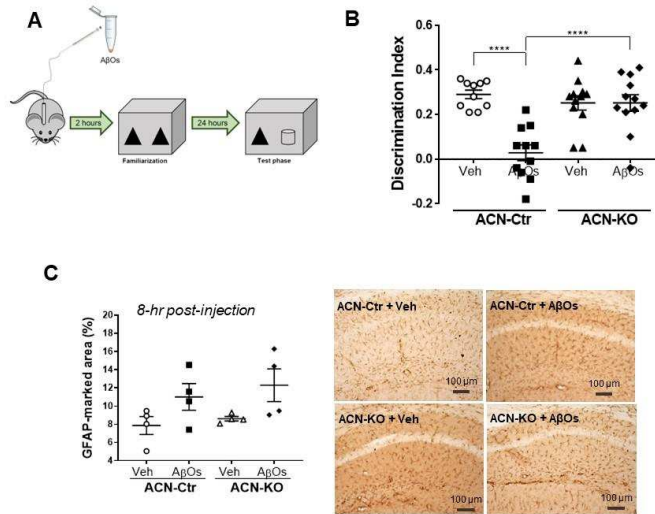
Figure 1. ACN-KO mice are protected from AβOs-induced memory impairment. (A) Experimental scheme. **(B)** Scatter plots are mean ± SEM of the discrimination index of AβO (1 μM) ICV-injected ACN-ctr and ACN-KO mice subsequently tested in the NORT. Two-way ANOVA found a significant interaction: $F_{(1,41)} = 16,13$, p = 0.0002. **(C)** Astroglial activation: scatter plots are mean ± SEM of the GFAP-marked area in Veh- and AβO-treated ACN-ctr and ACN-KO mice at 8h post-AβO injection.

FIGURE 2
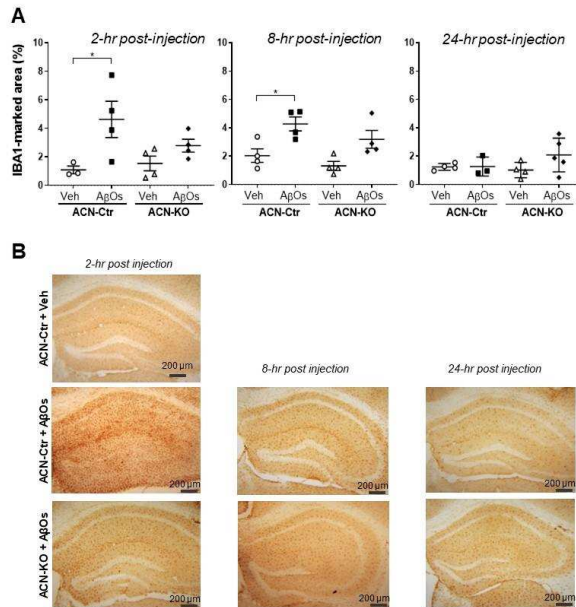
Figure 2. ACN-KO mice are protected from AβOs-induced microglial activation. (A) Time course of microglial activation: scatter plots are mean ± SEM of the IBA1-marked area in Veh- and AβO-treated ACN-ctr and ACN-KO mice at 2, 8 and 24 hrs post-injection. Two-way ANOVA found a significant effect of treatment (2 hrs): $F_{(1,11)}$ = 9,14, p = 0.0116; (8 hrs): $F_{(1,12)}$ = 17.43, p = 0.0013. **(B)** Images are mouse hippocampi immunostained with the anti-IBA1 antibody labeling microglia. *p < 0.05, ***p < 0.001, ****p < 0.0001 Tukey's post-hoc test.

FIGURE 3
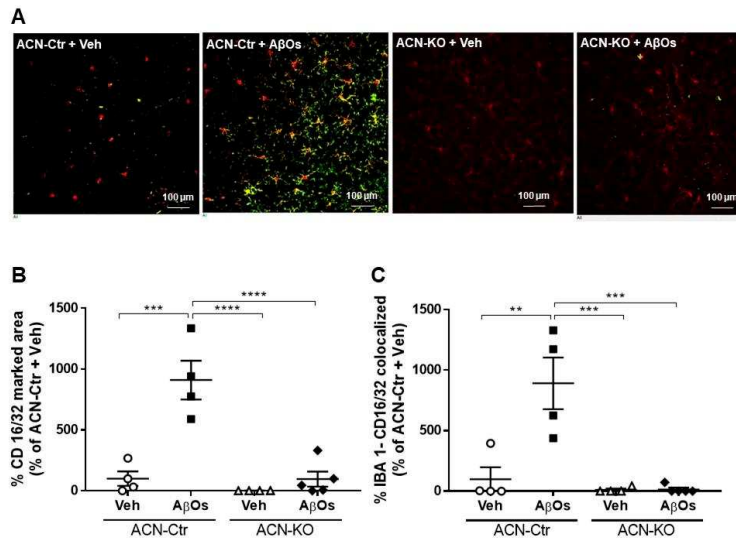
Figure 3. CD16/32 expression is highly detectable in AβO-treated ACN-ctr but not in ACN-KO mice. (A) Images are representative hippocampal slices co-labeled for CD16/32 (green) and the microglial marker IBA1 (red), which highlights a pro-inflammatory M1 phenotype in AβO-injected ACN-ctr but not AβO-injected ACN-KO mice. **(B)** Scatter plots are mean ± SEM of the % of CD16/32 hippocampal-marked area. Two-way ANOVA found a significant interaction: $F_{(1,13)} = 16.58$, $p = 0.0013$. **(C)** Scatter plots are mean ± SEM of the % of IBA1-CD16/32 co-localization in the experimental groups. Two-way ANOVA found a significant interaction: $F_{(1,13)} = 12.70$, $p = 0.0035$. **p < 0.01, ***p < 0.001, ****p < 0.0001 Tukey's post-hoc test.

FIGURE 4
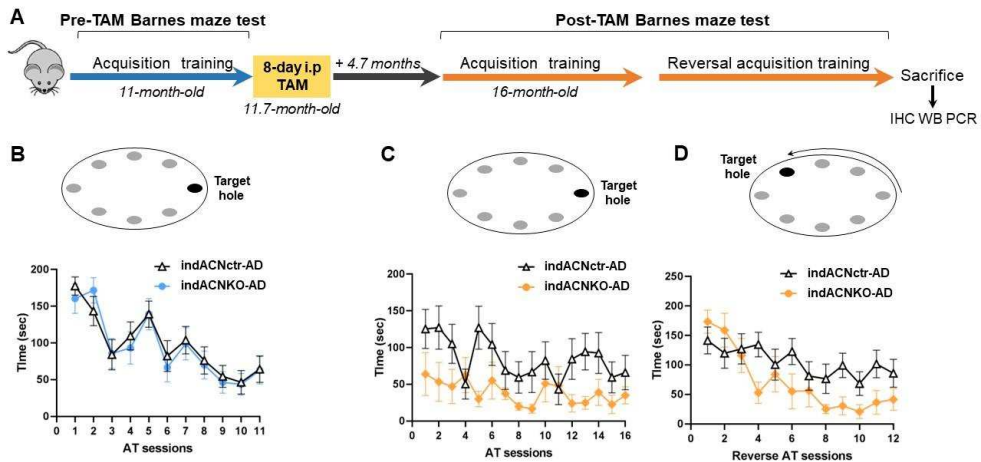
Figure 4. IndACNKO-AD mice are protected from the development of spatial memory and learning deficits. (A) Scheme of the experimental schedule. **(B)** Primary latency during Barnes maze Acquisition training in indACNctr-AD and indACNKO-AD mice prior to i.p. injection of TAM (pre-TAM). Two-way ANOVA for repeated measures found significant interaction between sessions ($F_{(10,268)} = 13.50$, $p = <0.0001$), but not between genotypes ($F_{(1,27)} = 0.06618$, $p = 0.8$). **(C)** Primary latency during post-TAM Acquisition training. Two-way ANOVA for repeated measures found significant interaction between genotypes ($F_{(1,14)} = 6.738$, $p = 0.0212$). **(D)** Primary latency during post-TAM Reversal Acquisition training sessions. Two-way ANOVA for repeated measures found significant interaction both between sessions ($F_{(4.775,66.85)} = 6.519$, $p = <0.0001$), and across sessions between genotypes ($F_{(11,154)} = 1.983$, $p = 0.0335$). Data are expressed as mean ± SEM of n=10 indACNctr-AD and n=6 indACNKO-AD mice.

FIGURE 5
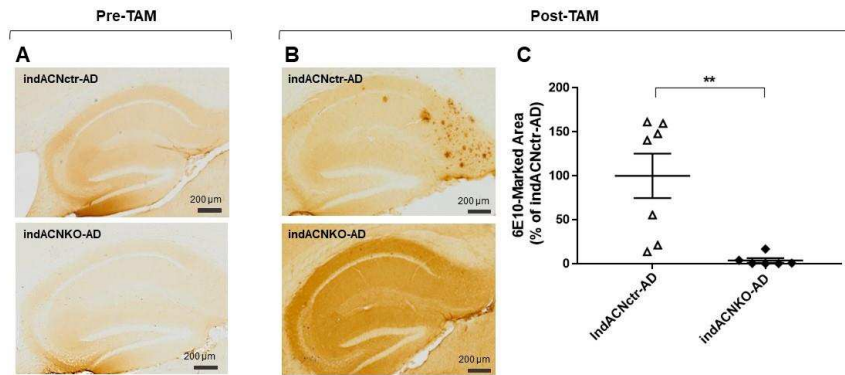
Figure 5. IndACNKO-AD mice do not develop Aβ plaques. Images in **(A)** are representative mouse hippocampi immunostained with the anti-6E10 antibody to label Aβ plaques in pre-TAM mice and in **(B)** in post-TAM indACNctr-AD and indACNKO-AD mice. **(C)** Scatter plots are mean ± SEM of the % of 6E10-marked area. **p < 0.01 Mann-Whitney's post-hoc test. Images in

FIGURE 6
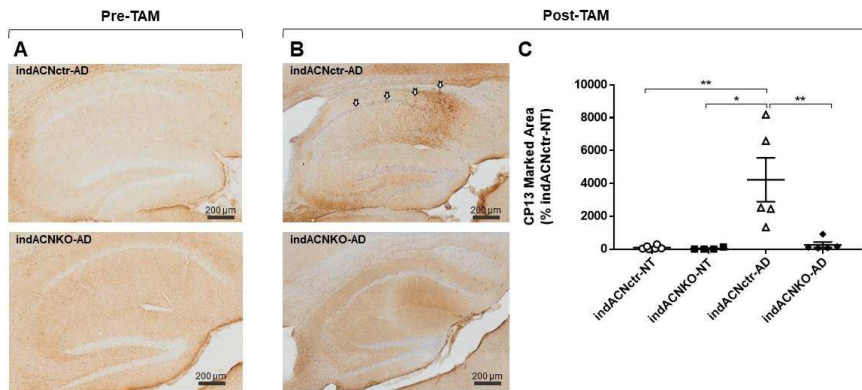
Figure 6. IndACNKO-AD mice do not develop tau pathology. Images in **(A)** are representative mouse hippocampi immunostained with the anti-CP13 antibody to label p-Tau in pre-TAM mice and in **(B)** post-TAM indACNctr-AD and indACNKO-AD mice. Arrows indicate accumulation of p-Tau-positive neurons. **(C)** Scatter plots are mean ± SEM of the % of CP13-marked area. One-way ANOVA (Kruskal-Wallis test): p = 0.0049; *p < 0.05, **p < 0.01, Mann-Whitney's post-hoc test.

FIGURE 7
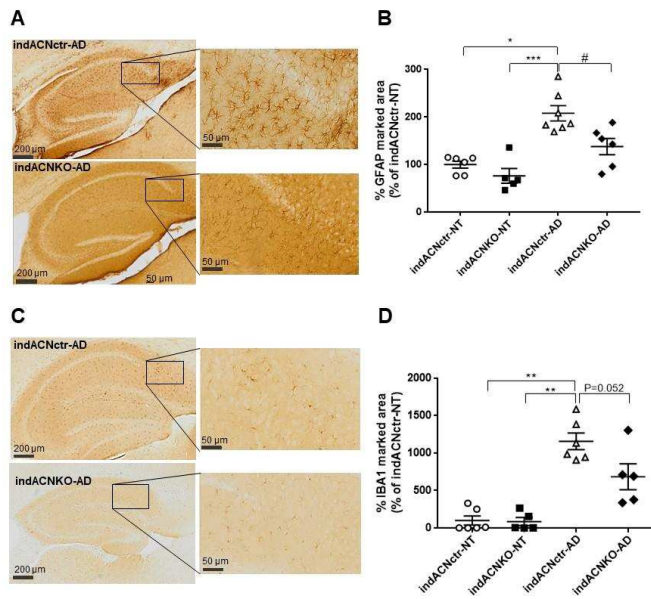
Figure 7. Gliosis is significantly reduced in IndACNKO-AD mice. Images in **(A)** are mouse hippocampi immunostained with the anti-GFAP antibody to label astrocytes in indACNctr-AD and indACNKO-AD mice. **(B)** Scatter plots are mean ± SEM of the GFAP-marked area. One-way ANOVA (Kruskal-Wallis test): p = 0.008. **(C)** Images are representative mouse hippocampi immunostained with the anti-IBA1 antibody to label microglia in indACNctr-AD and indACNKO-AD mice. **(D)** Scatter plots are mean ± SEM of the IBA1-marked area. One-way ANOVA (Kruskal-Wallis test): p = 0.008.

FIGURE 7
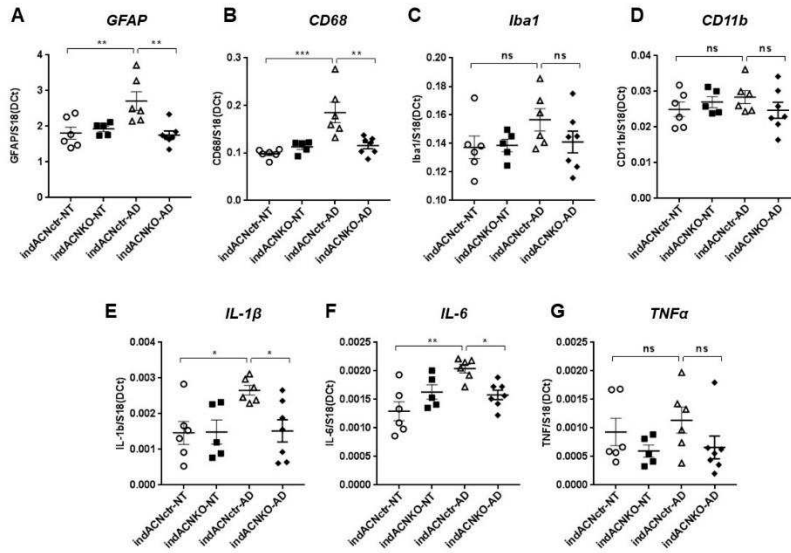
Figure 8. Neuroinflammation is significantly reduced in IndACNKO-AD mice. Scatter plots are mean ± SEM of 5-7 biological replicates for each genotype. One-way ANOVA: $p = 0.0025$, $F = 6.776$, $R^2 = 0.5041$ for GFAP; $p = 0.0002$, $F = 10.8$, $R^2 = 0.6183$ for CD68; $p = 0.2608$, $F = 1.44$, $R^2 = 0.1777$ for Iba1; $p = 0.5118$, $F = 0.7936$, $R^2 = 0.1064$ for CD11b; $p = 0.0205$, $F = 4.083$, $R^2 = 0.3798$ for Il-1b; $p = 0.0205$, $F = 4.083$, $R^2 = 0.3798$ for Il-1β; $p = 0.002$, $F = 7.079$, $R^2 = 0.515$ for Il-6; $p = 0.2670$, $F = 1.418$, $R^2 = 0.1754$ for TNFα. Tukey post-hoc test: *$p < 0.05$; **$p < 0.01$; ***$p < 0.001$.

SUPPLEMENTARY MATERIAL

Genetic deletion of astrocytic calcineurin B1 prevents cognitive impairment and neuropathology development in acute and chronic mouse models of Alzheimer's disease.

Running head: Astrocyte calcineurin in Alzheimer's disease

Laura Tapella[1]#, Giulia Dematteis[1]#, Pietro La Vitola[2], Susanna Leva[2], Elisa Tonelli[1], Marco Raddi[1], Marta Delconti[1], Letizia Dacomo[2], Mariagrazia Grilli[1], Laura Colombo[2], Mario Salmona[2], Gianluigi Forloni[2], Armando A Genazzani[1]*, Claudia Balducci[2]*, Dmitry Lim[1]*

co-first,

* corresponding

armando.genazzani@uniupo.it; Phone(Office): +39 0321 375827

claudia.balducci@marionegri.it; Phone(Office): +39.02.39014395

dmitry.lim@uniupo.it; Phone(Office): +39 0321 375822

Affiliations

[1] Department of Pharmaceutical Sciences, Università del Piemonte Orientale, Via Bovio 6, 28100, Novara, Italy

[2] Department of Neuroscience, Istituto di Ricerche Farmacologiche Mario Negri IRCCS, via Mario Negri 2, 20156 Milano (Italy)

Supplementary Table S1. List of oligonucleotide primers used for real-time PCR.

Protein Name	Gene Name	Forward/reverse	Accession No.
S18	Rps18	TGCGAGTACTCAACACCAACA CTGCTTTCCTCAACACCACA	NM_011296
GFAP	Gfap	GCTCCAAGATGAAACCAACC GAACTGGATCTCCTCCTCCA	NM_001131020.1
CD68			
Iba1	Aif1	CCGTCCAAACTTGAAGCCTT ACCCCAAGTTTCTCCAGCAT	NM_019467.2
CD11b			
Il-1β	Il1b	AAGTTGACGGACCCCAAAAGA TGTTGATGTGCTGCTGCGA	NM_008361.3
Il-6			
TNF	Tnf	ACTGAACTTCGGGGTGATCG CTCCTCCACTTGGTGGTTTG	NM_013693.2

Supplementary figures
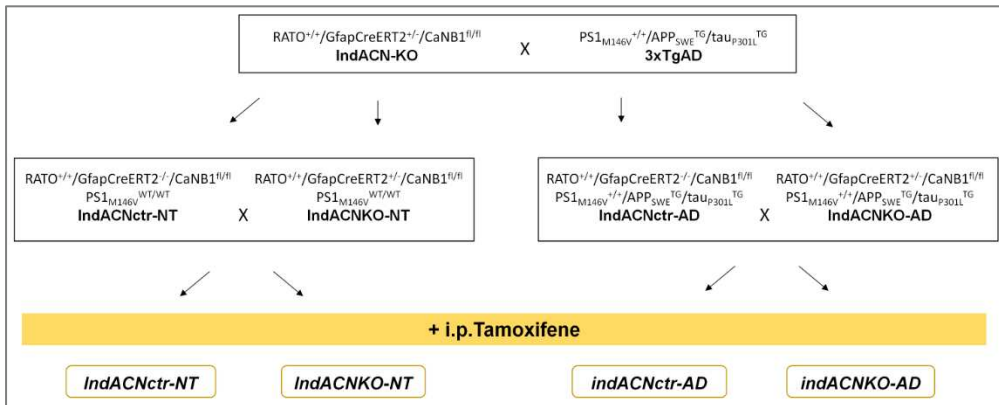
Supplementary Figure S1. Scheme of generation of inducible astrocyte-specific CaNB1 KO on the background of 3xTg-AD mice.
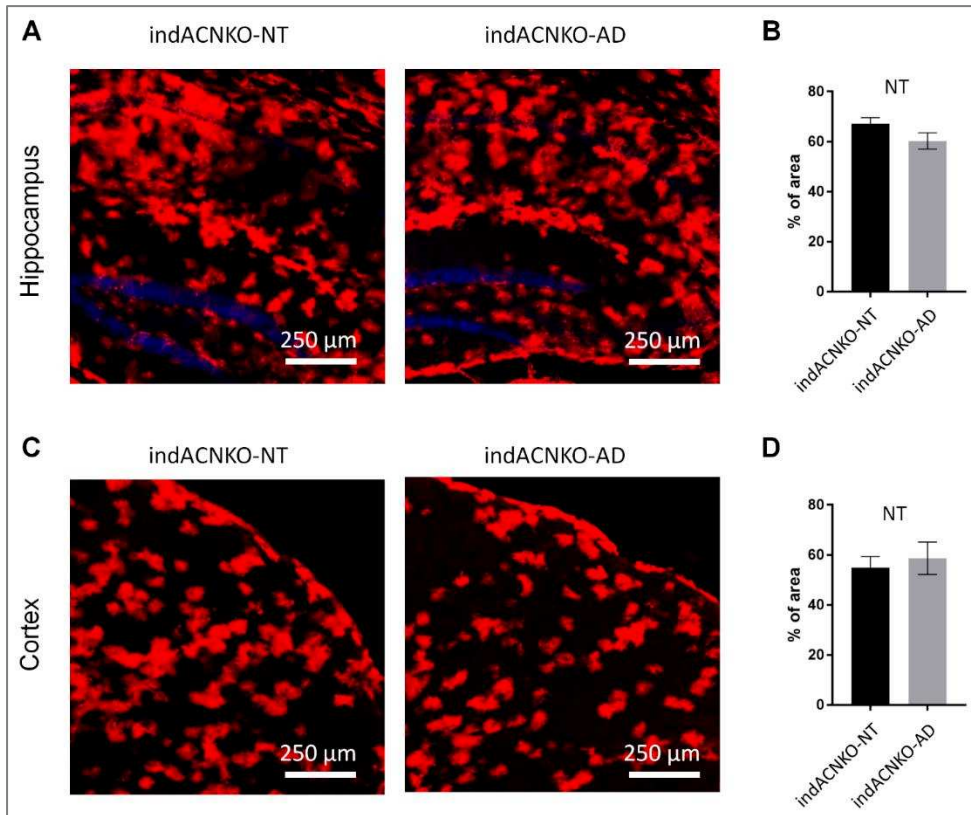
Supplementary Figure S2. Efficiency of astrocytic CaNB1 KO after induction with TAM. Confocal images of tdTomato fluorescence in hippocampal region (**A** and **B**) and frontal cortex (**C** and **D**) in indACNKO-NT and indACNKO-AD mice 5 months after TAM administration. Data in B and D are calculated as % of area occupied by tdTomato and expressed as mean ± SEM of n=5 sliced from 2 animals for each condition; unpaired two tailed Student's t-test. Scale bar: 300 µm.

A indACNKO-NT

| tdTomato | GFAP | tdTomato/GFAP/DAPI |

CA1

DG

100 µm

100 µm

B 3xTg-AD

| tdTomato | GFAP | tdTomato/GFAP/DAPI |

CA1

DG

100 µm

100 µm
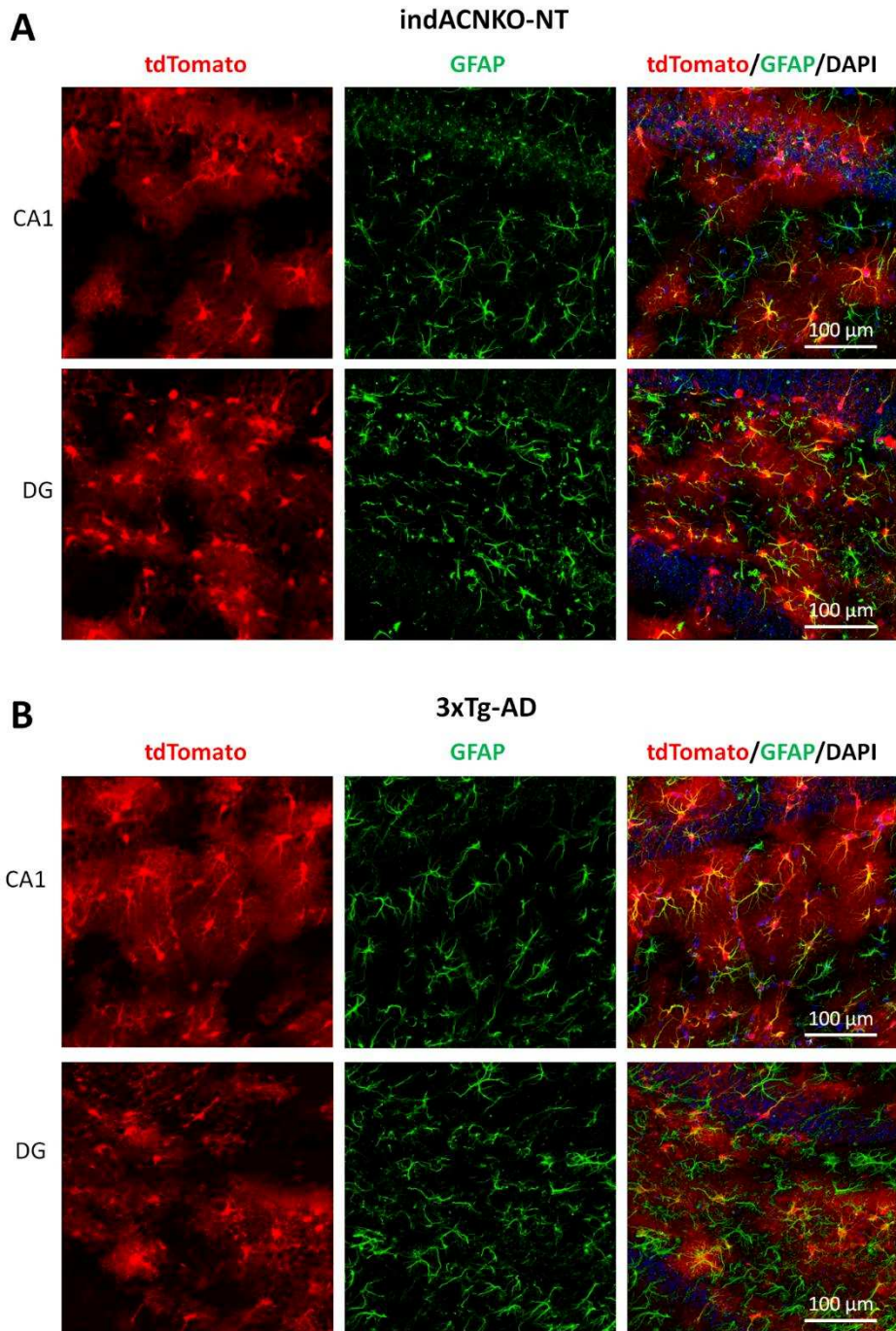
Supplementary Figure S3. **Colocalization of tdTomato reporter with GFAP immunostaining**. Confocal images of tdTomato fluorescence (red) and

Alexa-633-immunostained (green pseudocolored) astrocytes in CA1 and dentate gyrus regions of hippocampal formation from indACNKO-NT (**A**) and indACNKO-AD (**B**) mice. Note that all tdTomato-positive astrocytes are also GFAP-positive. Representative images are shown 3 animals for each condition. Scale bar: 100 µm.
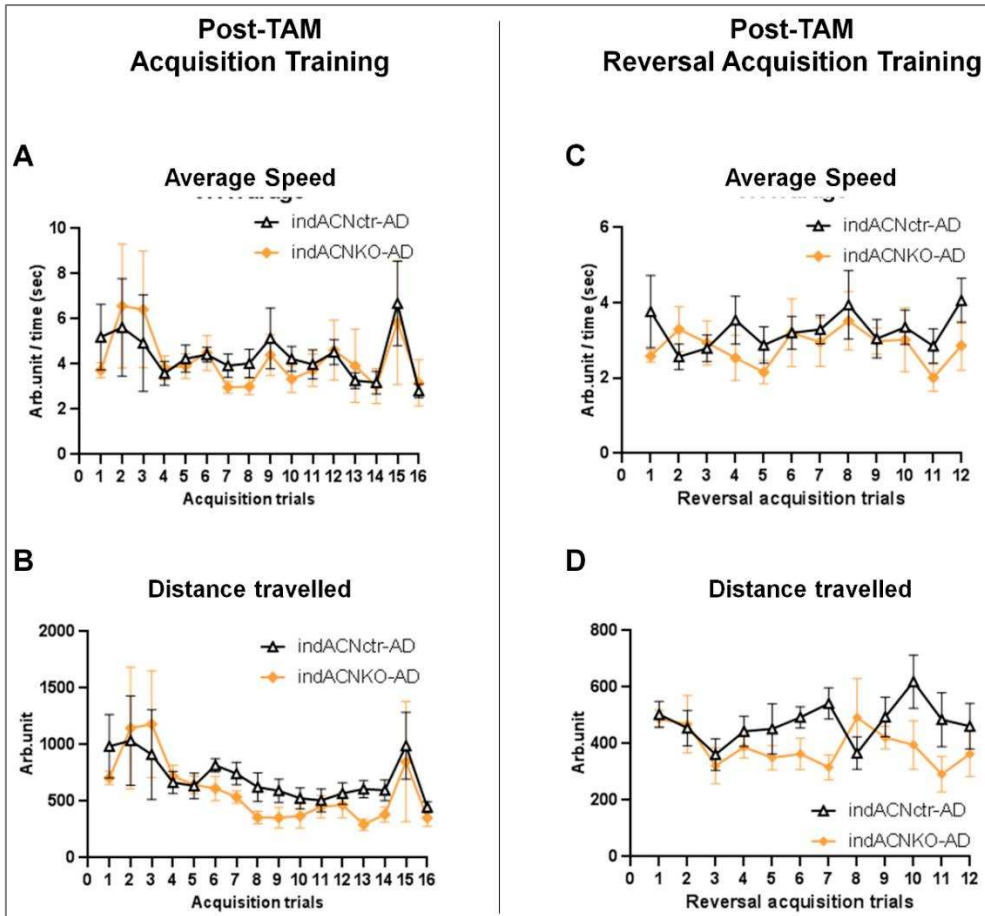
Supplementary Figure S4. Absence of differences in motor performance in post-TAM indACNctr-AD and indACNKO-AD mice. Average speed (**A** and **C**) during post-TAM Acquisition training or Reversal Acquisition Training sessions of post-TAM Barnes maze test. Two-way ANOVA for repeated measures did not found significant interaction between genotypes both in Acquisition Training ($F_{(1,14)}$ = 0.03974, p = 0.8849) and Reversal Acquisition Training ($F_{(1,14)}$ = 0.7519, p = 0.4005) . Neither significant interaction between sessions was found in Acquisition Training ($F_{(4.775, 66.85)}$ =1.641, p = 0.1826) nor in Reversal Acquisition Training ($F_{(4.775, 66.85)}$ =1.018,

p = 0.4108). Distance travelled (**B** and **D**) during Acquisition Training or Reversal Acquisition Training sessions of post-TAM Barnes maze test. Two-way ANOVA for repeated measures do not found significant interaction between genotypes both in Acquisition Training ($F_{(1,14)}$ = 1.224, p = 0.2871) and Reversal Acquisition Training ($F_{(1,14)}$ = 2.904, p = 0.1105) . Neither significant interaction between sessions was reported in Acquisition Training ($F_{(4.775,66.85)}$ =2.237, p = 0.0948) nor in Reversal Acquisition Training ($F_{(4.775,66.85)}$ =09921, p = 0.4347). Data are expressed as mean ± SEM of n=10 indACNctr-AD and n=6 indACNKO-AD mice.
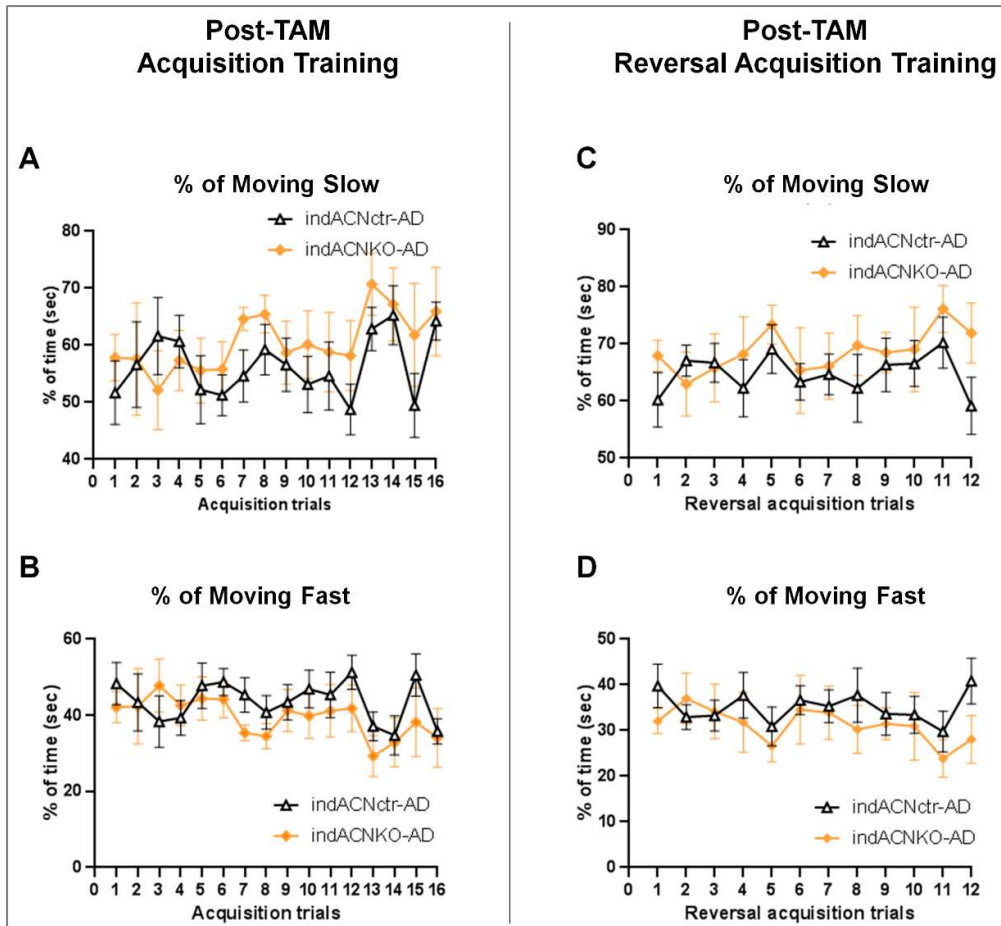
Supplementary Figure S5. Absence of differences in motor performance in post-TAM indACNctr-AD and indACNKO-AD mice. Percentage of Moving Slow (**A** and **C**) during post-TAM Acquisition training or Reversal Acquisition Training sessions of post-TAM Barnes maze test. Two-way ANOVA for repeated measures did not found significant interaction between genotypes both in Acquisition Training ($F_{(1,14)}$ = 0.7168, p = 0.4114) and Reversal Acquisition Training ($F_{(1,14)}$ = 0.9065, p = 0.3572) . Neither significant interaction between sessions was reported in Acquisition Training ($F_{(4.775,66.85)}$ =1.759, p = 0.1286) nor in Reversal Acquisition Training ($F_{(4.775,66.85)}$ = 0.9384, p = 0.4586). Percentage of Moving Fast (**B** and **D**) during

Acquisition Training or Reversal Acquisition Training sessions of post-TAM Barnes maze test. Two-way ANOVA for repeated measures do not found significant interaction between genotypes both in Acquisition Training ($F_{(1,14)}$ = 0.7168, p = 0.4114) and Reversal Acquisition Training ($F_{(1,14)}$ = 2.904, p = 0.1105) . Neither significant interaction between sessions was reported in Acquisition Training ($F_{(4.775,66.85)}$ = 0.9384, p = 0.4586) nor in Reversal Acquisition Training ($F_{(4.775,66.85)}$ = 0.9065, p = 0.3572). Data are expressed as mean ± SEM of n=10 indACNctr-AD and n=6 indACNKO-AD mice.
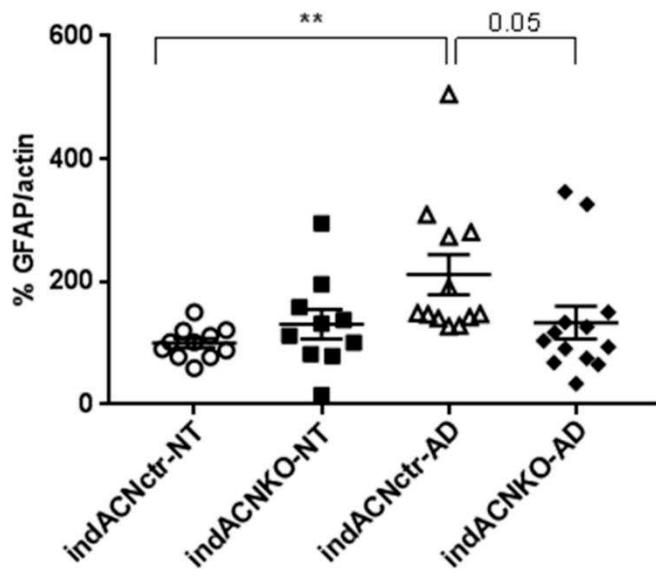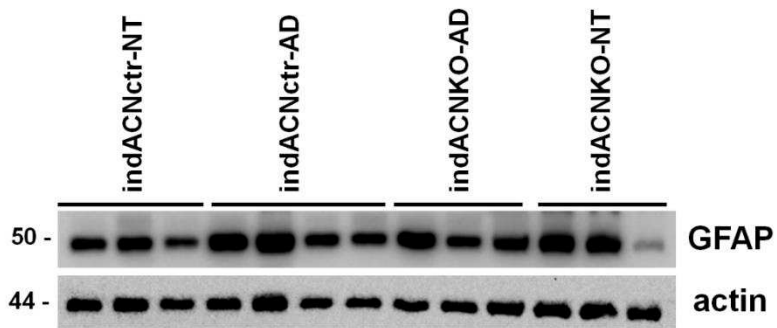
Supplementary Figure S6. Western blot bands and relative quantification of GFAP and actin of indACNctr-NT, indACNKO-NT, indACNctr-AD and indACNKO-AD mouse hippocampi. Scatter plots are mean ± SEM of the optical density. **$p < 0.01$, Dunn's post-hoc test.

Chapter 5

ARTICLE OPEN

Check for updates

Protein synthesis inhibition and loss of homeostatic functions in astrocytes from an Alzheimer's disease mouse model: a role for ER-mitochondria interaction

Laura Tapella [1,8], Giulia Dematteis [1,8], Marianna Moro[1], Beatrice Pistolato[1], Elisa Tonelli[1], Virginia Vita Vanella[2], Daniele Giustina[1], Aleida La Forgia[1], Elena Restelli[3,7], Elettra Barberis[2], Tito Cali [4], Marisa Brini [5], Salvatore Villani[1], Erika Del Grosso[1], Mariagrazia Grilli [1], Marcello Manfredi[2], Marco Corazzari [6], Ambra A. Grolla[1], Armando A. Genazzani[1✉] and Dmitry Lim [1✉]

© The Author(s) 2022

Deregulation of protein synthesis and ER stress/unfolded protein response (ER stress/UPR) have been reported in astrocytes. However, the relationships between protein synthesis deregulation and ER stress/UPR, as well as their role in the altered homeostatic support of Alzheimer's disease (AD) astrocytes remain poorly understood. Previously, we reported that in astrocytic cell lines from 3xTg-AD mice (3Tg-iAstro) protein synthesis was impaired and ER-mitochondria distance was reduced. Here we show that impaired protein synthesis in 3Tg-iAstro is associated with an increase of p-eIF2α and downregulation of GADD34. Although mRNA levels of ER stress/UPR markers were increased two-three-fold, we found neither activation of PERK nor downstream induction of ATF4 protein. Strikingly, the overexpression of a synthetic ER-mitochondrial linker (EML) resulted in a reduced protein synthesis and augmented p-eIF2α without any effect on ER stress/UPR marker genes. In vivo, in hippocampi of 3xTg-AD mice, reduced protein synthesis, increased p-eIF2α and downregulated GADD34 protein were found, while no increase of p-PERK or ATF4 proteins was observed, suggesting that in AD astrocytes, both in vitro and in vivo, phosphorylation of eIF2α and impairment of protein synthesis are PERK-independent. Next, we investigated the ability of 3xTg-AD astrocytes to support metabolism and function of other cells of the central nervous system. Astrocyte-conditioned medium (ACM) from 3Tg-iAstro cells significantly reduced protein synthesis rate in primary hippocampal neurons. When added as a part of pericyte/endothelial cell (EC)/astrocyte 3D co-culture, 3Tg-iAstro, but not WT-iAstro, severely impaired formation and ramification of tubules, the effect, replicated by EML overexpression in WT-iAstro cells. Finally, a chemical chaperone 4-phenylbutyric acid (4-PBA) rescued protein synthesis, p-eIF2α levels in 3Tg-iAstro cells and tubulogenesis in pericyte/EC/3Tg-iAstro co-culture. Collectively, our results suggest that a PERK-independent, p-eIF2α-associated impairment of protein synthesis compromises astrocytic homeostatic functions, and this may be caused by the altered ER-mitochondria interaction.

INTRODUCTION
Early cellular dysfunction during AD pathogenesis includes deregulation of Ca^{2+} homeostasis, mitochondrial dysfunction and bioenergetic deficit, oxidative stress and altered cell–cell communication. Such alterations may be traced back to the deregulation of protein synthesis, associated with the activation of endoplasmic reticulum (ER) stress/unfolded protein response (UPR), proposed as targets for the development of AD therapy [1–3]. Activation of ER stress/UPR has been reported in patients with advanced AD stages [4–7]. In cellular and animal AD models, heterogeneous and somewhat contrasting data have been reported and activation of

ER stress/UPR in AD models has been debated [8]. The central element which links ER stress/UPR to the accumulation of misfolded proteins is represented by PRKR-like endoplasmic reticulum kinase (PERK)-dependent phosphorylation of eukaryotic initiation factor 2α (eIF2α). In turn, this protein inhibits assembly of ribosomal 43S preinitiation complex and imposes a global translational block, with a profound impact on neural cell physiology [9, 10]. However, non-canonical variants of ER stress/UPR and their role in AD pathogenesis have been discussed [11, 12]. While most of the reports consider neuronal mechanisms of ER stress/UPR in AD, contribution of astrocytes has been generally overlooked.

[1]Department of Pharmaceutical Sciences, Università del Piemonte Orientale "Amedeo Avogadro", Via Bovio 6, 28100 Novara, Italy. [2]Department of Translational Medicine, Center for Translational Research on Autoimmune and Allergic Diseases (CAAD), Università del Piemonte Orientale "Amedeo Avogadro", Novara, Italy. [3]Istituto di Ricerche Farmacologiche Mario Negri IRCCS, via Mario Negri 2, 20156 Milan, Italy. [4]Department of Biomedical Sciences, Neuroscience Center (PNC), Centro Studi per la Neurodegenerazione (CESNE), University of Padua, Padua, Italy. [5]Department of Biology, Centro Studi per la Neurodegenerazione (CESNE), University of Padua, Padua, Italy. [6]Department of Health Science (DSS), Center for Translational Research on Autoimmune and Allergic Disease (CAAD) & Interdisciplinary Research Center of Autoimmune Diseases (IRCAD), Università del Piemonte Orientale "Amedeo Avogadro", Novara, Italy. [7]Present address: Human Technopole, Milan, Italy. [8]These Authors contributed equally: Laura Tapella, Giulia Dematteis. ✉email: armando.genazzani@uniupo.it; dmitry.lim@uniupo.it
Edited by Dr Pier Giorgio Mastroberardino

2

Astrocytes are homeostatic and secretory cells, whose function is to warrant the stability of the extracellular space, the development and correct functional integration of the CNS components in an environment which has recently been called the "active milieu" [13]. Therefore, the activation of ER stress/UPR and deregulation of protein synthesis in astrocytes would be particularly important for their potential role in CNS pathologies in terms of cellular dysfunction and loss of supportive functions. For example, local translation of mRNA in astrocytic processes is suggested to be important for shaping the repertoire of astrocytic plasma membrane and secreted proteins warranting support to neurons [14, 15]. A derangement of ribosomal protein synthesis machinery in AD astrocytes has already been documented [4]. While a canonical [PERK → p-eIF2α → protein synthesis block] pathway is postulated in astrocytes, only fragmentary data are available. Moreover the relationships between ER stress/UPR and protein synthesis in astrocytes during AD progression remain largely unexplored [16].

Recently, we proposed immortalized hippocampal astrocytes from 3xTg-AD mice (3Tg-iAstro cells) as a novel cellular model which shows features of AD-like pathology, i.e., transcriptional and translations alterations, deregulation of Ca^{2+} signaling, bioenergetic deficit, elevated ROS and augmented ER-mitochondria interaction [17–21]. The central finding, linking the astrocytic cell pathology with possible deficit of homeostatic support, was protein synthesis impairment and a modest increase of ER stress/UPR related genes [19, 20]. Herein we further investigated, both in vitro and in vivo, if reduction of protein synthesis in 3xTg-AD astrocytes was due to ER stress/UPR. Our results suggest that a PERK-independent, p-eIF2α-associated impairment of protein synthesis alters secretome of AD astrocytes and compromises their supportive and defensive functions, possibly through altered ER-mitochondria interaction.

RESULTS
Protein synthesis impairment in AD astrocytes is associated with PERK-independent phosphorylation of eIF2α in 3Tg-iAstro cells

To investigate if protein synthesis impairment in 3Tg-iAstro cells was due to activation of [PERK → eIF2α → activating transcription factor 4 (ATF4)] axis, we first of all confirmed that 3Tg-iAstro have a significant reduction of protein synthesis, compared to WT-iAstro cells, using both immunocytochemical (ICC) (Fig. 1a) and Western blot (WB) analysis (Fig. 1b) of puromycin incorporation in neo-synthetized peptides (SUrface SEnsing of Translation (SUnSET) method [22, 23]) (Fig. 1). Next, we investigated expression levels of p-eIF2α, whose de-phosphorylation is essential for the assembly of pre-initiation complex and initiation of translation [10]. As shown in Fig. 2a, the levels of p-eIF2α were significantly higher in 3Tg-iAstro compared with WT-iAstro cells, and comparable to the levels identified in WT-iAstro and 3Tg-iAstro treated with thapsigargin (THG), an established ER stress/UPR inducer. We also measured expression levels of growth arrest and DNA damage-inducible gene 34 GADD34, a protein which provides a scaffold for eIF2α de-phosphorylation by protein phosphatase 1 (PP1) [9]. Surprisingly, GADD34 protein levels were significantly lower in 3Tg-iAstro compared to WT-iAstro cells (Fig. 2a). Next, we asked if augmented levels of p-eIF2α correlated with activation of PERK, in our cellular model. However, the levels of p-PERK were not different in WT-iAstro and 3Tg-iAstro cells (Fig. 2b). During ER stress/UPR, activated and auto-phosphorylated PERK phosphorylates eIF2α and induces p-eIF2α-dependent upregulation of transcription factor ATF4 [9]. However, in 3Tg-iAstro levels of ATF4 were not different from those in WT-iAstro cells (Fig. 2b). Altogether these data suggested that phosphorylation of eIF2α in 3Tg-iAstro cells was not due to activation of [PERK → eIF2α/GADD34 → ATF4] axis. These results are in apparent contrast with

our previous report of a two-three-fold transcriptional upregulation of ER stress/UPR-induced genes Atf4, spliced variant of X-box-binding protein 1 (Xbp1s) and homocysteine inducible ER protein with ubiquitin like domain 1 (Herpud1) in 3Tg-iAstro cells compared to its WT counterpart [20]. Therefore, we compared the induction of ER stress/UPR markers in 3Tg-iAstro cells with those induced by THG, which produces maximal induction of ER stress/UPR markers. We confirmed that in 3Tg-iAstro cells mRNA of the three ER stress/UPR markers significantly increased, and the increase was in line with our previous publications [20] (Fig. 3, middle histograms). However, the maximal upregulation of all three transcripts was much higher in THG-treated (1 μM, 4 h) vs non-treated cells than that in 3Tg-iAstro vs WT-iAstro (by 4.8 fold for Atf4, by 50–70 fold for Xbp1s and 18–25 fold for Herpud1) (Fig. 3, right histograms). Of note, there was a tendency to a lower THG-induced upregulation of Xbp1s and Herpud1 (mRNA, Fig. 3b, c right histograms), and ATF4 (protein, Fig. 2b) in 3Tg-iAstro compared with WT-iAstro, although the differences were not significative in the current experimental setting. To strengthen the result we assessed mRNA levels of other genes involved in different arms of ER stress/UPR response as well as UPR-inducible chaperons including Atf6, Ddit3/CHOP, Bip/Grp78, calreticulin and Dnajb9/ERdj4. As shown in Supplemental Fig. 1, essentially the same result was obtained. We concluded that eIF2α phosphorylation and the reduction of protein synthesis in 3Tg-iAstro cells were PERK-independent, however a low-grade chronic ER stress cannot be ruled out.

Fig. 1 Protein synthesis analysis in WT- and 3Tg-iAstro cells. a Cells were pulsed with puromycin (4 μM, 1.5 h), fixed and analysed by IF with anti-puromycin antibody (green) and with DAPI to stain nuclei (blue). Images were acquired with Leica Thunder imager 3D live cell microscope, scale bar = 25 μm. Data are expressed as mean ± SEM, WT-iAstro cells $n = 40$, 3Tg-iAstro cells $n = 40$, from 4 independent experiments; ****$p < 0.05$ by unpaired t-test. **b** WB with anti-puromycin antibody and ponceau staining on cells treated with 4 μM puromycin. Data are expressed as mean ± SEM of 12 independent experiments; ****$p < 0.0001$ by unpaired t-test.

148

a

b

Fig. 2 PERK-independent activation of p-eIF2α. a Analysis of eIF2α phosphorylation and GADD34 expression on WT and 3Tg-iAstro. Cells were treated or not with 1 μM THG for 1 h, lysed and analysed by WB with anti- p-eIF2α, eIF2α, GADD34 and actin antibodies. Data are expressed as mean ± SEM of $n = 4$ (3Tg-iAstro + THG), $n = 5$ (3Tg-iAstro) or $n = 6$ (WT- and WT-iAstro + THG) independent experiments; *$p < 0.05$ by one-way ANOVA, Sidak's multiple comparison; ***$p < 0.001$ Dunnet's multiple comparisons. **b** Analysis of PERK phosphorylation and ATF4 induction on WT- and 3Tg-iAstro cells. WB analysis of cells treated as in **a** with anti-p-PERK, PERK, ATF4 and actin antibodies. Data are expressed as mean ± SEM from $n = 3$ (p-PERK and ATF) or $n = 8$ (PERK) independent experiments. *$p < 0.05$, **$p < 0.01$ and ***$p < 0.001$ by one-way ANOVA, Sidak's multiple comparison.
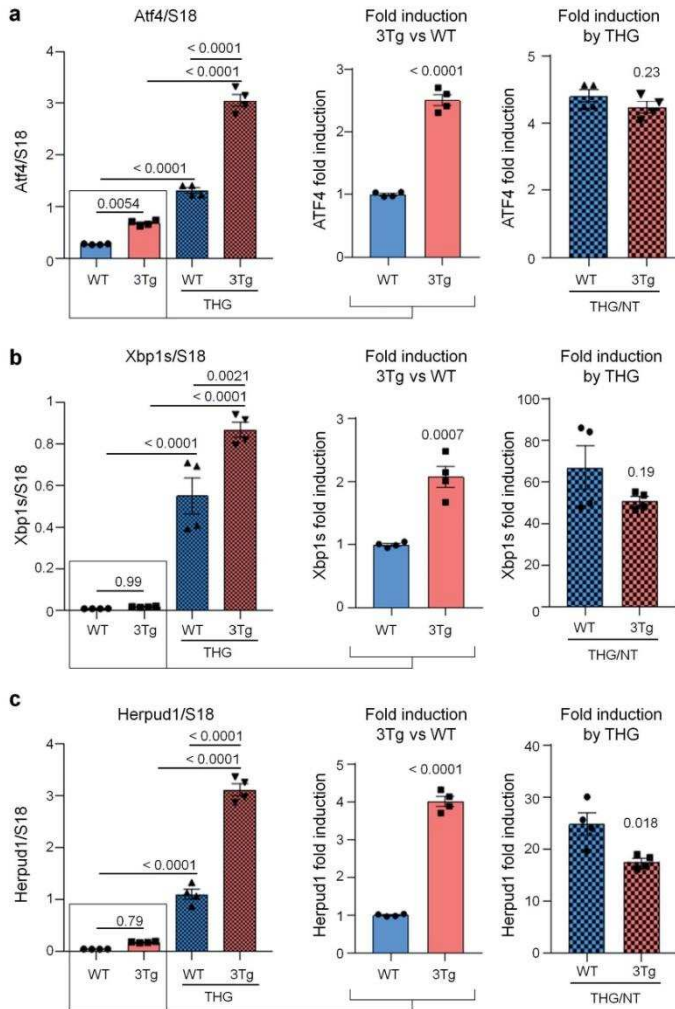
Fig. 3 ER stress/UPR genes induction in WT- and 3Tg-iAstro cells. Real-time PCR of Atf4 (**a**), Xbp1s (**b**) and Herpud1 (**c**) transcripts in cells treated or not with 1 µM THG for 4 h. Data of untreated WT- and 3Tg-iAstro cells (middle plots) and THG treated /untreated cell (right plots) are presented separately. Values represent mean ± SEM ΔC(t) of gene/S18 of four independent experiments for each condition. Left plots were analyzed using ANOVA, with Tukey posthoc test; middle and right plots were analyzed using unpaired two-tail Student's t-test.

Reduction of protein synthesis and increase of p-eIF2α in astrocytes expressing a 10 nm ER-mitochondrial linker

Previously, we reported that ER-mitochondrial interaction, measured by SPLICS (split-GFP-based Contact site Sensor), a recently developed ER-mitochondria contact sites sensor [24–26], is increased in 3Tg-iAstro compared with WT-iAstro cells, suggesting a correlation between ER-mitochondrial distance and reduction of protein synthesis [20]. To test the hypothesis of the causal role of the shorter ER-mitochondria distance on protein synthesis reduction we transfected WT-iAstro cells with a synthetic linker which fixes the ER-mitochondria distance at about 10–12 nm (named as 10 nm-EML) (a kind gift from György Csordás and György Hajnóczky, Thomas Jefferson University). The linker was composed of monomeric red fluorescent protein (mRFP) and an amino acidic liner, flanked at the N-terminal side by an ER-targeting sequence, and at the C-terminal side by an outer mitochondrial membrane-targeting sequence [27]. We found that the expression of 10 nm-EML significantly reduced protein synthesis rate as tested in the SUnSET assay, either by WB (Fig. 4a) or ICC (Fig. 4c). Strikingly, 10 nm-EML expression also significantly augmented p-eIF2α levels (Fig. 4b). At this point, we checked if the reduction of protein synthesis and increase of p-eIF2α were paralleled by an induction of ER stress/UPR marker genes. However, expression of Atf4, Xbp1s and Herpud1 transcripts were not different between Ctr (WT-iAstro transfected with mRFP) and 10 nm-EML-expressing WT-iAstro cells. Altogether these data, in line with alterations found in 3Tg-iAstro cells, suggest that increased interaction between ER and mitochondria augments phosphorylation of eIF2α and reduces protein synthesis by an UPR-independent mechanism.

PERK-independent increase of p-eIF2α and protein synthesis reduction in vivo in 3xTg-AD mouse astrocytes

Next, we assessed if similar alterations in protein synthesis, p-eIF2α and ER stress markers could be found also in vivo in the hippocampus of 3xTg-AD and WT mice. To assess protein synthesis rate, 3xTg-AD mice were injected with puromycin (225 mg/Kg body weight) intraperitoneally (i.p.) for 1.5 h. Then hippocampi were harvested and puromycin incorporation was analysed by WB and immunohistochemical analysis (IHC). As shown in Fig. 5a, WB analysis showed a significantly reduced puromicyn-positive signal in 3xTg-AD mice compared with WT. The result was confirmed by anti-puromycin staining of brain cryosections (Fig. 5b). Assessment of [PERK → eIF2α/ GADD34 → ATF4] axis activation by WB revealed significant increase of p-eIF2α, reduction of GADD34 protein, while total PERK and ATF4 were not changed. Under the same experimental conditions, p-PERK was undetectable by WB analysis in both genotype samples (Fig. 6a). This result, and the absence of total PERK mobility shift, which accompany THG-induced PERK phosphorylation in astrocytes (Fig. 2b), suggest that PERK is not activated in hippocampi of 3xTg-AD mice. IHC analysis confirmed upregulation of p-eIF2α specifically in CA1 neuropil astrocytes of 3xTg-AD mice (Fig. 6b), while GADD34 staining was diffused and was significantly reduced in the CA1 neuropil (Fig. 6c). qPCR analysis on whole hippocampal lysates revealed no changes in Atf4, Xbp1s, and Herpud1 transcript levels (Fig. 6d). Altogether, these data suggest that in AD astrocytes, both in vitro and in vivo, p-eIF2α-associated reduction of protein synthesis is independent of PERK activation but may be associated with alterations in ER-mitochondria interaction.

3Tg-iAstro cells do not support neuronal protein synthesis and pericyte-endothelial cell (EC) tubulogenesis in vitro, the effect, replicated by 10 nm-EML

Growing body of evidence suggest that non-cell autonomous mechanisms of neuronal degeneration during AD pathogenesis could be mediated by astroglial dysfunction and reduced homeostatic support to neurons and other cells in the CNS. Therefore, we assessed the effect of 3Tg-iAstro cells on neurons and a three-cell pericyte/EC/astrocyte 3D co-culture. 3Tg-iAstro-Conditioned Medium (ACM) transfer, but not WT-iAstro-ACM, onto primary murine hippocampal cultured neurons resulted in a significant reduction of neuronal protein synthesis, an early sign of neuronal dysfunction [28–31] (Fig. 7a, b). Treatment of neurons with ACM from WT-iAstro cells overexpressing 10 nm-EML had also reduced protein synthesis rate (Fig. 7c). When WT-iAstro or 3Tg-iAstro cells were added as a component of pericyte/EC/ astrocyte 3D co-culture, WT-iAstro, but not 3Tg-iAstro, supported formation of vessel-like tubules by pericyte and EC (Fig. 7d). Strikingly, the effect of 3Tg-iAstro was reproduced by co-culture with 10 nm-EML-overexpressing WT-iAstro cells (Fig. 7d). These results suggest that alterations of astrocyte-derived soluble factors and cell–cell contact may account for 3Tg-iAstro inability to support neuronal protein synthesis and pericyte/EC tubulogenesis and that ER-mitochondria interaction may have a role.

Analysis of secretome from 3Tg-iAstro cells suggests impairment of neurogenic, neuroprotective functions and inter-cellular interaction

In search of astrocyte-derived soluble factors we performed shotgun mass spectrometry proteomics of ACM from WT-iAstro and 3Tg-iAstro cells, followed by bioinformatic analysis. As shown in Supplemental Table 1, 120 and 84 proteins were identified, respectively, in WT- and 3Tg-iAstro cells ACM. Of these, 55 were expressed by both types of astrocytes, while 65 and 29 were identified only in WT- or 3Tg-iAstro cells ACM, respectively. Two pipelines of analysis have been performed. Firstly, proteins were quantified and differentially expressed proteins (DEPs) in 3Tg-iAstro vs WT-iAstro cells were identified (Supplemental Table 2). Five DEPs were identified. Of those, one, fatty acid-binding protein 3 (Fabp3) was upregulated, while four proteins, secreted protein acidic and cysteine rich (SPARC), heat shock protein 90 (HSP90), heat shock protein 73 (HSP73) and α1-tubulin, were significantly downregulated in 3Tg-iAstro compared with WT-iAstro cells (Fig. 8, left table). SPARC is a pro-neurogenic factor released by astrocytes which promotes neuronal differentiation [32]. Extra-cellular heat shock proteins are known to be neuroprotective [33]. Specifically, extracellular HSP90 protects neurons from oxidative stress [34]. Therefore, our proteomic results suggest that neurogenic and neuroprotective support in 3Tg-iAstro cells may be reduced compared with the WT counterpart. In a separate analysis, uniquely identified proteins were considered and subjected to gene ontology (GO) analysis using DAVID online tool in search of overrepresented groups of proteins. This analysis revealed that WT-iAstro, but not 3Tg-iAstro secretome, was enriched in proteins involved in cell–cell contacts, focal adhesion contacts and constituents of extracellular matrix (ECM), suggesting that support of cell–cell communication and ECM formation may be impaired in 3Tg-iAstro cells (Fig. 8, right upper table). Next we investigated if manipulation with ER-mitochondrial distance or normalization of protein folding had an effect on the secreted proteins. 10 nm-EML overexpression in WT-iAstro cells did not influence the identified proteins (Supplemental Table 3). However, treatment of 3Tg-iAstro cells with a chemical chaperone 4-PBA (4-phenil butyric acid) rescued the presence of proteins responsible for extracellular matrix formation (Fig. 8 right bottom table and Supplemental Table 4).

A chemical chaperone rescues protein synthesis alterations, ER-mitochondrial interaction, and homeostatic defects of 3Tg-iAstro cells

Our data suggest that impairment of protein synthesis may represent a key feature of astrocytic dysfunction in AD, which was accompanied by the increased interaction between ER and mitochondria [20, 21]. Therefore we investigated if the correction
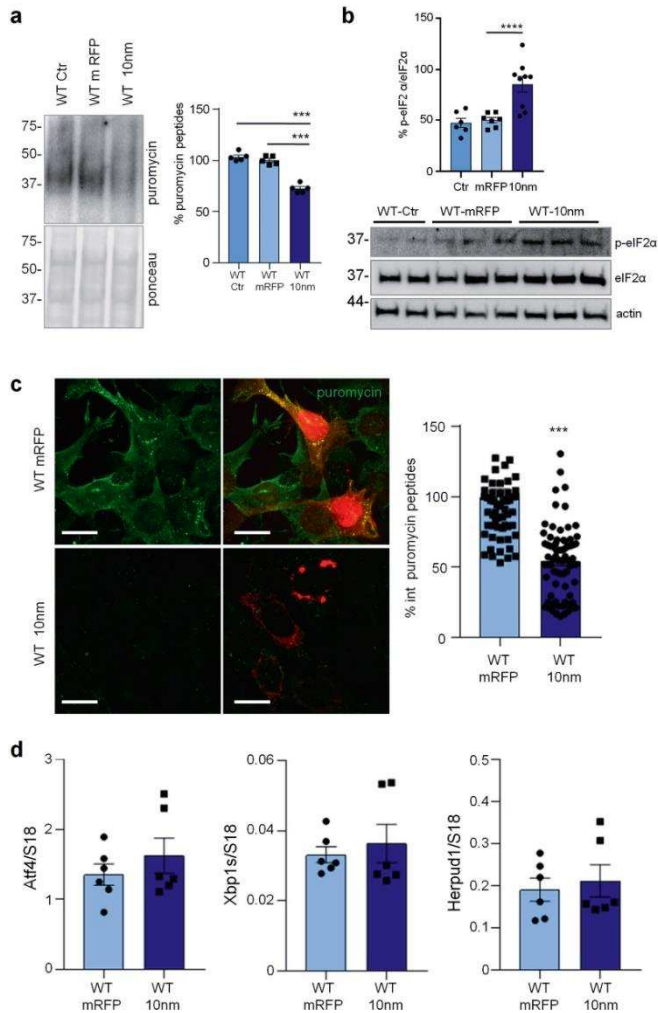
Fig. 4 Forced ER-mitochondria interaction causes impairment of protein synthesis in WT-iAstro cells. WT-iAstro cells were non-transfected (WT Ctr) or transfected with mRFP (WT mRFP) and 10-nm ER- mitochondrial linker (WT 10 nm). **a** WB with anti-puromycin antibody and ponceau staining on lysates of cells treated with 4 µM puromycin (1.5 h); data are expressed as mean ± SEM of three independent experiments; ***$p < 0.001$ by one-way ANOVA, Sidak's multiple comparison. **b** WB analysis of eIF2α phosphorylation. Data are expressed as mean ± SEM of four independent experiments; ****$p < 0.0001$ by one-way ANOVA, Sidak's multiple comparison. **c** Cells pulsed with 4 µM puromycin (1.5 h) were fixed and analysed by IF with anti-puromycin antibody (green). Images were acquired with Zeiss 710 confocal laser scanning microscope, data are expressed as mean ± SEM of three independent coverslip; ***$p < 0.001$ by unpaired t-test. Scale bar = 25 µm. **d** Real-time PCR of Atf4, Xbp1s and Herpud1 transcripts in cells transfected with mRFP and 10-nm ER-mitochondrial linker; data are expressed as mean ± SEM of four independent wells.

Differentially expressed proteins 3Tg vs WT

Protein	Uniprot_ID	FC	p.v.
FABP3	FABPH_MOUSE	+4.7	0.04
SPARC	SPRC_MOUSE	-1.6	0.03
HSP90	HS90B_MOUSE	-2.1	0.04
HSP73	HS7C_MOUSE	-2.3	0.04
Tub-α1b	TBA1B_MOUSE	-3.9	0.02

Identified proteins

WT-iAstro (120): 65, 55

3Tg-iAstro (84): 29, 38, 46

3Tg-iAstro + 4-PBA (102): 56

GO terms overrepresented in WT but not in 3Tg

Term	Count	Fold Enr	Adj.p.v.
GOTERM: Cellular Component			
GO:0031012~extracellular matrix	16	16.7	1.18E-12
GO:0005925~focal adhesion	15	11.8	8.76E-10
GO:0005913~cell-cell adherens junction	12	11.7	1.43E-07
GOTERM: Molecular Function			
GO:0098641~cadherin binding involved in cell-cell adhesion	12	12.1	6.92E-10
GOTERM: KEGG Pathway			
mmu04510:Focal adhesion	8	6.1	0.012

GO terms overrepresented in 3Tg + 4-PBA but not in 3Tg

Term	Count	Fold Enr	Adj.p.v.
GOTERM: Biological Process			
GO:0042060~wound healing	6	20.0	0.0054
GO:0030199~collagen fibril organization	5	33.7	0.0054
GOTERM: Cellular Component			
GO:0005615~extracellular space	24	4.6	2.40E-08
GO:0031012~extracellular matrix	8	10.6	2.94E-04
GO:0005581~collagen trimer	5	23.3	0.0017
GOTERM: Molecular Function			
GO:0030020~extracellular matrix structural constituent	4	38.0	0.0056
GO:0005201~extracellular matrix structural constituent	5	15.0	0.0099
GO:0005518~collagen binding	4	17.8	0.033

Fig. 8 Proteomic analysis of WT- and 3Tg-iAstro secretome. ACM (10 ml) was collected from 48 h culture of WT-iAstro, 3Tg-iAstro and 3Tg-iAstro cells treated with 4-PBA (3 µM, 48 h). Proteins were precipitated by TCA and processed as described in Methods section. 120, 84 and 102 proteins were identified in WT-iAstro, 3Tg-iAstro and 3Tg-iAstro + 4-PBA ACM, respectively. Protein quantification of 3Tg-iAstro vs WT-iAstro ACM returned five differentially regulated proteins (1.3 fold change cut-off, $p < 0.05$) (le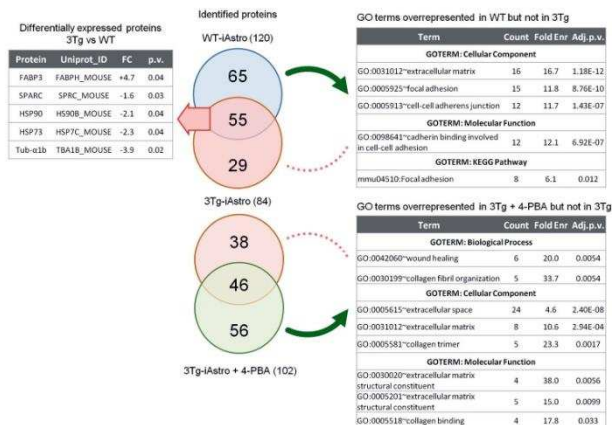ft upper table). Gene ontology analysis of proteins, unique for WT-iAstro or 3Tg-iAstro + 4-PBA both compared with 3Tg-iAstro ACM, returned GO terms related to extracellular matrix, focal adhesion and cadherin binding overrepresented in both WT-iAstro and 3Tg-iAstro + 4-PBA, but not in 3Tg-iAstro cells (right bottom table).

other CNS cells. This has been illustrated by us and other groups, e.g., showing that ACM from AD model mice produces dysfunction and degeneration of cultured primary neurons [51–53]. In this frame, herein we show that, unlike WT-iAstro ACM, ACM collected from 3Tg-iAstro cells impairs protein synthesis in cultured neurons. Moreover, when plated together with pericytes and EC in a 3D three-cell co-culture, unlike WT-iAstro, 3Tg-iAstro cells do not allow formation of tubular structures, characteristic of "angiogenic" pericyte-EC co-cultures. Astrocytes are known to secret factors supporting neurons in development and differentiation like thrombospondin 1, SPARC, Sparcl1, and lipocalin-2 [32, 54, 55]. Astrocytes also secrete an array of proteins, including heat shock proteins, acting as protective factors against different stress factors, including oxidative stress [33, 56–58]. They also express components of the ECM and adhesion molecules which support cell–cell communication and cellular dynamics [59–61]. Strikingly, neurogenic SPARC and protective HSP90 and HSP73 were significantly reduced in 3Tg-iAstro ACM compared with WT-iAstro ACM. In addition, proteins of cell adhesion and ECM were overrepresented in WT- but not in 3Tg-iAstro ACM. Therefore, the proteomic analysis of 3Tg-iAstro secretome strengthens the hypothesis of a reduced neurogenic and protective support and provides candidate molecules and signals to be further studied and tested for the development of AD therapy.

Rescue of p-eIF2α, protein synthesis, ER-mitochondrial interaction and homeostatic support by 4-PBA

Our results suggest that a low-grade chronic ER stress, with a somewhat lower UPR response, albeit without PERK activation, might exist in 3xTg-AD astrocytes. Although this is corroborated by rescue of protein synthesis defect and p-eIF2α levels by a small chemical chaperone 4-PBA, these data are in an apparent contradiction, because activation of PERK is regarded as an obligatory step in a protein misfolding-associated UPR induction [9]. Of note, in this regard, that a low-grade chronic ER stress is characteristic for melanoma cancer cells, and eIF2α phosphorylation may occur without ER stress [62, 63]. Furthermore, although 4-PBA is thought to act through prevention of protein aggregation in the ER, the full spectrum of its actions is not completely understood [64]. Growing body of evidence suggest that the effect of 4-PBA can also be explained from a Ca^{2+} handling point of view. 4-PBA has been shown to rescue THG- and tunicamycin-induced ER Ca^{2+} depletion [65], to normalize ER-mitochondrial Ca^{2+} fluxes in the intervertebral discs nucleus pulposus cells subjected to a compression-induced ER-stress [66], to abolish THG-induced cytosolic Ca^{2+} signals in pancreatic acini [67] and to normalize cytosolic Ca^{2+} levels in 3-Chloro-1,2-propanediol (3-MCPD)-treated HEK293 cells [68]. Moreover, 4-PBA has been shown to increase expression of SIGMA1R, a component and modulator of MERCS [21, 69]. These findings suggest that a direct or indirect action of 4-PBA on Ca^{2+} homeostasis and/or ER-mitochondrial interaction could also be hypothesized. Indeed, here we show that the increased ER-mitochondrial interaction in 3Tg-iAstro cells was fully rescued by 4-PBA. 4-PBA is an FDA approved drug and it has been shown to ameliorate cognitive performance and AD-related neuropathology in AD mouse models, holding a promise in AD therapy [35, 36]. Therefore, a more detailed investigation of the 4-PBA modulation of Ca^{2+} homeostasis and ER-mitochondria interaction is warranted.

CONCLUSIONS

ER stress/UPR has gained much attention as a possible target for drug development in AD [2, 35, 70–73]. However, somewhat paradoxical results and discrepancies between models and human data on the activation of components of the pathway, made the activation of ER stress/UPR in AD in its canonical form disputable [2, 8, 12]. To add to the complexity of the phenomenon, ER stress/UPR in neurodegenerative diseases has mostly been studied or interpreted through the lens of a neuronal dysfunction, while for

a

b

c

| WT-iAstro | 3Tg-iAstro | 3Tg-iAstro + 4-PBA |

d

| Ctr | 4-PBA |
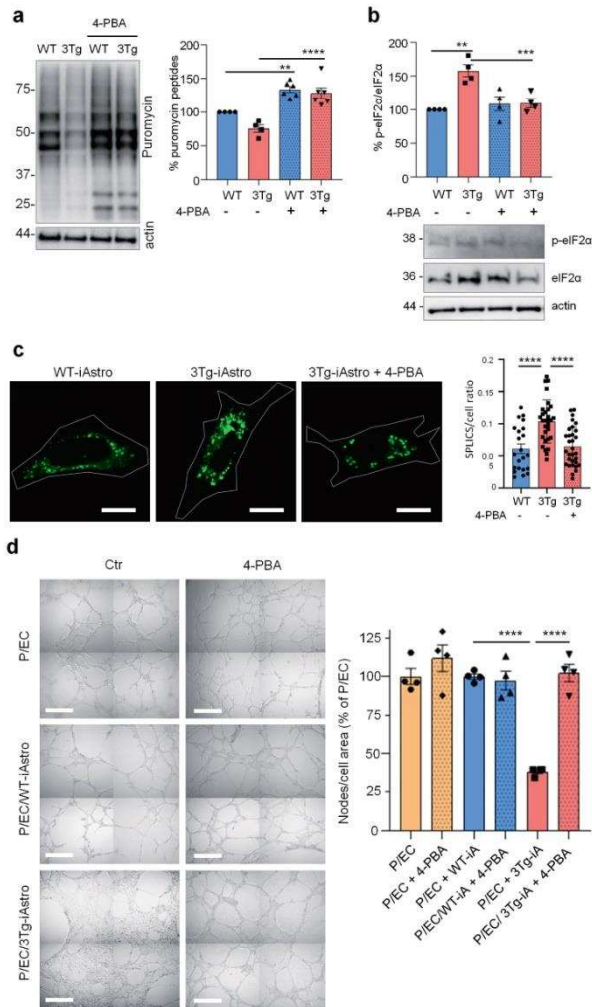
other CNS cells, in particular astrocytes, only fragmentary data are available, which makes it difficult to draw a "whole picture" [16]. Although deregulation of protein synthesis is well documented as an early feature of AD astrocytes, the relationships between p-eIF2α, disproteostasis, and their link to ER-mitochondria communication, remain poorly understood. Our data suggest that the deregulation of protein synthesis in a model of AD astrocytes may involve p-eIF2α-associated inhibition of protein synthesis without an overt activation of PERK-mediated UPR. Herein we propose that this defective pathway may be caused by a complex

L. Tapella et al.

Fig. 9 4-PBA rescues protein synthesis and p-eIF2α in 3Tg i-Astro and tubulogenesis in pericyte/EC co-cultures. a WT- and Tg-iAstro were treated or not with 4-PBA 3 µM, for 48 h, cells were pulsed with puromycin 4 µM and analysed by WB with anti-puromycin antibody and ponceau staining. Data are expressed as mean ± SEM from 6–4 independent experiments; **$p < 0.01$; ***$p < 0.001$, one-way ANOVA, Sidak's multiple comparisons. **b** WB analysis of eIF2α phosphorylation on WT-iAstro and 3Tg-iAstro, treated or not with 4-PBA 3 µM, for 48 h. Data are expressed as mean ± SEM from four independent experiments; **$p < 0.01$, one-way ANOVA, Sidak's multiple comparisons. **c** Representative images and quantification of SPLICS fluorescence, indicating ER-mitochondrial contacts at ~8–10 nm distance, in WT-iAstro, 3Tg-iAstro, and in 3Tg-iAstro treated with 4-PBA (3 µM, for 48 h). Data are expressed as mean ± SEM of $n = 22$ (WT-iAstro), $n = 30$ (Tg-iAstro), $n = 32$ (Tg-iAstro + 4-PBA), from three independent coverslip, ****$p < 0.0001$, one-way ANOVA, Sidak's multiple comparisons. Scale bar = 20 µM. **d** Co-cultures of pericytes, endothelial cells and WT-iAstro or 3Tg-iAstro (pre-treated or not with 4-PBA for 48 h) were plated in a layer of Matrigel in presence or absence of 4-PBA (3 µM). After 8 h, bright field images were taken using a Zeiss 710 confocal laser scanning microscope, scale bar = 500 µm. Data are expressed as mean ± SEM, $n = 4$ from two independent experiments; ***$p < 0.001$ by one-way ANOVA, Sidak's multiple comparisons.
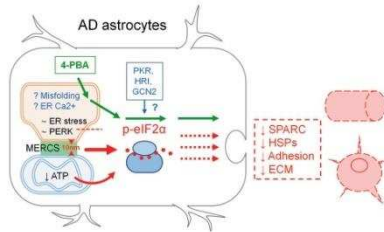

Fig. 10 Schematic representation of the role of impaired proteins synthesis in the loss of homeostatic functions by AD astrocytes. Phosphorylation of eIF2α and reduction of protein synthesis in AD astrocytes occurs without induction of overt ER stress/UPR and activation of PERK (~ER stress, ~PERK and intermittent red line). A role of PKR, HRI and GCN2 kinases is to be determined (blue arrow and question mark). Alteration of ER-mitochondrial interaction could be a plausible candidate (10 nm, red arrowheads and red thick arrow), as well as a reduced ATP supply by mitochondria (curved red arrow). A role of protein misfolding and ER Ca²⁺ dyshomeostasis is hypothesized (? Misfolding, ? ER Ca²⁺). The deregulation of proteins synthesis may potentially result in impaired secretion (red inter-mittent arrows) of neurotrophic and neuroprotective molecules as well as impaired formation of extracellular matrix (SPARC, heat shock proteins (HSPs), Adhesion, ECM). Protein synthesis, p-eIF2α levels and homeostatic functions can be rescued by the chemical chaperone 4-PBA (green arrows).

array of events, including altered ER-mitochondria interaction (Fig. 10).

MATERIALS AND METHODS
3xTg-AD mice
3xTg-AD mice and non-transgenic controls (WT) were housed in the animal facility of the Università del Piemonte Orientale, with unlimited access to water and food. Animals were managed in accordance with European directive 2010/63/UE and with Italian law D.l. 26/2014. The procedures were approved by the local animal-health and ethical committee (Università del Piemonte Orientale) and were authorized by the national authority (Istituto Superiore di Sanità; authorization numbers N. 22/2013). All efforts were made to reduce the number of animals by following the 3R's rule.

Immortalized hippocampal astrocytes from WT and 3xTg-AD mice. Gen-eration of immortalized astrocytes from hippocampi of WT and 3xTg-AD mice (WT- and 3Tg-iAstro cells) was described elsewhere [19]. iAstro lines were maintained in complete culture media containing Dulbecco's modified Eagle's medium (DMEM; Sigma-Aldrich, Cat. D5671) supplemen-ted with 10% fetal bovine serum (Gibco, Cat. 10270) (FBS), 2 mM L-glutamine (Sigma-Aldrich), and 1% penicillin/streptomycin solution (Sigma-Aldrich). Cells were passaged once a week and used for experiments between passages 12 and 20 from establishment.

Pericytes and endothelial cells. Human immortalized pericytes (CL 05008-CLTH) and endothelial cells EA.hy926 (CRL-2922™) were cultured in Dulbecco's modified Eagle's medium (DMEM; Sigma-Aldrich, Cat. No. D5671) supplemented with 10% fetal bovine serum (Gibco, Cat. No. 10270) (FBS), 2 mM L-glutamine (Sigma-Aldrich), and 1% penicillin/streptomycin solution (Sigma-Aldrich) at 37 ℃ in 5% CO2. Cells were used between passages 5 to 15 and passed twice a week.

Hippocampal neuronal cultures. Mouse neuronal primary cultures were prepared as described previously [17, 52, 74] with slight modifications. After enzymatic and mechanical dissociation, final cellular pellet was resuspended in neurobasal A medium (Invitrogen, Cat. 10888022) supplemented with 2% B27 supplement (Invitrogen, Cat. 17504044), 2 mg/mL glutamine, 10 U/mL penicillin, and 100 mg/mL streptomycin, and plated as described above. Half of medium volume was changed every third day and the cells were lysed at days in vitro (DIV) 15.

Cell transfection. 3×10^4 cells/well (WT- or 3Tg-Astro) were resuspended in 250 µl of complete DMEM and 250 µl of transfection mix, and plated onto 13 mm glass coverslips in 24 well plates. For the transfection mix Lipofectamine 2000 (Thermo Fisher Scientific, Cat. 11668-019) and plasmid, in ratio 1:1, were mixed in Optimem (Gibco, Cat. 11058-021); after 3 h, transfection medium was replaced with complete medium. After 48 h, cells were washed with PBS and fixed in 4% formaldehyde (Sigma, Milan, Italy). A 10 nm ER-mitochondrial linker, which fixes the ER-mitochondrial distance at 10–12 nm, a modification of a 5 nm ER-mitochondrial linker [27], was a kind gift from Drs György Csordás and György Hajnóczky (Thomas Jefferson University). Generation of split-GFP contact sites sensor (SPLICS) was described elsewhere [24, 25].

Astrocytes Conditioned Medium (ACM) preparation. For the preparation of ACM, 5×10^4 WT-iAstro and 3Tg-iAstro cells were plated in a 6 well-plate. After 24 h the media was changed with DMEM completed with FBS, 2 mg/mL glutamine, 10 U/mL penicillin, and 100 mg/mL streptomycin, or neurobasal A medium (Invitrogen, Cat. 10888022) supplemented with 2% B27 supplement (Invitrogen, Cat. 17504044), 2 mg/mL glutamine, 10 U/mL penicillin, and 100 mg/mL streptomycin. Forty-eight hour later, the media were collected and centrifuged at 12,000 g, for 10 min at 4 ℃. ACM was stored at −80 ℃ [52, 54].

Cell treatment with 4-phenylbutiric acid (4-PBA). WT-iAstro and 3Tg-iAstro cells were plated, and after 24h were treated with 3 µM 4-PBA (Sant Cruz Biotechnology, Cat. sc-232961) [62, 75]. Forty-eight hour later cells were lysated and then used for WB analysis.

Cell treatment with thapsigargin. 5×10^4 WT-iAstro or 3Tg-iAstro cells were plated in a 6MW dish. Forty-eight hour later they were acutely treated with thapsigargin (Tocris, Cat. 1138) (THG). For WB analysis cells were treated with THG 1 µM, for 1 h; for RNA extraction cells were treated with THG 1 µM for 4 h [62].

Pericytes/EC/astrocyte co-culture. For tubulogenesis assessment, a Matri-gel synthetic extracellular matrix (Corning, Cat. 356234) was used. 96 well plates were coated with 50 µl of Matrigel, gelatinized at 37 ℃ for 30 min. Pericytes (CL 05008-CLTH, Celther Polska, Lodz, Poland), EA.hy926 (CRL-2922, ATCC) and WT-iAstro or 3Tg-iAstro cells, in ratio 1:1:1 were resuspended in 100 µl of complete DMEM and plate on the matrix at the density of 1×10^4 cells/well, and incubated for 8 h. Phase contrast images were acquired with a Zeiss 710 confocal laser scanning microscope.

Table. 1. List of primary antibodies.

Primary antibody	Dilition WB	Dilution ICC/IHC	Cat. N.	House
Anti-ATF 4	1:500		390063	Santa Cruz
Anti-eIF2α	1:500		133132	Santa Cruz
Anti-p-eIF2α	1:500	1:200	ABP-0745	Immunological Sciences
Anti-Gadd 34	1:550	1:100	OTI2B11	Abcam
Anti-GFAP		1:100	MAB-12029	Immunological Sciences
Anti-PERK	1:500		C33E10	Cell Signaling Technology
Anti-p-PERK	1:500		16F8	Cell Signaling Technology
Anti-Puromycin	1:1000	1:200	MABE343	Millipore
Anti-β-actin	1:2000		A1978	Sigma-Aldrich

SUnSET for assessment of protein synthesis. Global protein synthesis rate was assessed using the Surface Sensing of Translation (SUnSET) method, as previously published [76]. Briefly, cells were incubated with 4 µM puromycin dihydrochloride (Sigma, Cat. P8833) supplemented in normal medium at 37 °C with 5% CO_2 for 1.5 h (iAstro cells) or 1 h (primary neurons). Subsequently, cell lysates were fixed for immune fluorescence analysis or western blot analysis [20, 22]. WT and 3xTgAD mice were i.p. injectd with puromycin dihydrochloride 225 mg/Kg body weight, $n = 2$ WT or 3xTgAD [77]. After 1.5 h, mice were anesthetized with i.p. injection of Zoletil (80 mg/kg) and Xylazine (45 mg/kg) and intracardially perfused with cold PBS. Brains were dissected and half of brains were used for WB analysis and the other halves of brain were post-fixed in 4% paraformaldehyde. Coronal 40 µm thick cryosections were used for immunochemical staining.

Immunofluorescence (IF). WT-iAstro and 3Tg-iAstro cells, grown onto 13 mm glass coverslips, were treated as previously explained. Immunofluorescence was done as follows. Cells were fixed in 4% paraformaldehyde and 4% sucrose, permeabilized (7 min in 0.1% Triton X-100 in phosphate-buffered saline (PBS)), blocked in 0,1% gelatine, and immunoprobed with an appropriate primary antibody over night at 4 °C. After three times washing in PBS, an Alexa-conjugated secondary antibody (1:200) was applied for 1 h at room temperature (RT). The following primary antibody was used: anti-Puromycin (Millipore, Cat. MABE343). Secondary antibody was Alexa Fluor 488 anti-mouse IgG. Nuclei were counter-stained with 4′,6-diamidino-2-phenylindole (DAPI).

Quantitative fluorescence image analysis. Images were acquired using a FV-1000 Olympus laser confocal scanning system, Zeiss 710 confocal laser scanning microscope, Leica SP8 LIGHTNING Confocal Microscope imaging systems and Leica Thunder imager 3D live cell. Images were acquired under non saturating conditions and analysed with Fiji ImageJ 1.52p software. To determine the amount of the puromycin labeled peptides on i-Astro, the puromycin mean fluorescence was measured for each selected cells excluding nucleus and expressed as fold change relative to control. To determine the amount of the puromycin labeled peptides on neuronal cultures and transfected i-Astro, the puromycin fluorescence was measured for the entire cell area excluding nucleus as a corrected total cell fluorescence (CTCF) = Integrated Density—(Area of selected cell X Mean background fluorescence). Data are expressed as fold change relative to control. For Puromycin IHC quantification, the puromycin mean fluorescence was measured by setting threshold analysis. Data are expressed as fold change relative to Ctr. For tubulogenesis assessment, the number of nodes taken with Leica Metafluor software was divided for the area covered by cells, analysed with Fiji ImageJ 1.52p software. The area covered by cells was expressed as the difference between the entire area and the closed area delimited by the tubules. Quantification of SPLICS fluorescence was performed as described elsewhere [20].

Western blot. Astroglial cultures or neuronal cultures were lysed with 100 µL of lysis buffer (50mM Tris-HCl (pH 7.4), sodium dodecyl sulphate (SDS) 0.5%, 5mM EDTA, 10 µL of protease inhibitors cocktail (PIC, Millipore, Cat. 539133) and phosphatase inhibitor cocktail (Thermo Fisher Scientific, Cat. 78428)) and collected in a 1.5 ml tube. Lysates were boiled at 96 °C for 5 min and then quantified with QuantiPro BCA Assay Kit (Sigma, Cat. SLBF3463). 40 µg of proteins were mixed with the right amount of Laemmli Sample Buffer 4X (Bio-Rad), and boiled. Then samples were loaded on a

12% polyacrylamide-sodium dodecyl sulphate gel for SDS-PAGE. Proteins were transferred onto nitrocellulose membrane, using Mini Transfer Packs or Midi Transfer Packs, with Trans-Blot® Turbo ™ (Bio-Rad) according to manufacturer's instructions (Bio-Rad). The membranes were blocked in 5% skim milk (Sigma, Cat. 70166) for 45′ at room temperature. Subsequently membranes were incubated with indicated primary antibody, overnight at 4 °C. Primary antibodies used are listed in Table 1, anti-β-Actin was used to normalize protein loading.

Goat anti-mouse IgG (H+L) horseradish peroxidase-conjugated secondary antibody (Bio-Rad, 1:5000; Cat. 170-6516,) and Goat anti-rabbit Igg (H +L) horseradish peroxidase-conjugated secondary antibody (Bio-Rad, 1:5000; Cat. 170-6515,) were used as secondary antibodies. Detection was carried out with SuperSignal™ West Pico/femto PLUS Chemiluminescent Substrate (Thermo Scientific), based on the chemiluminescence of luminol and developed using ChemiDoc™ Imaging System (Bio-Rad). Full length uncropped original western blots used in their manuscript are provided as a single Supplemental Material file.

IHC. Ctr and 3xTg-AD mice were anesthetized with i.p. injection of Zoletil (80 mg/kg) and Xylazine (45 mg/kg) and intracardial perfused with cold PBS1x. Brains were dissected and sagittal sections were post-fixed in 4% paraformaldehyde in PBS1x. 40 µm slices were cut at microtome at −25 °C and store at −20 °C in 50% PBS1x, 25% ethylene- glycol and 25% glycerol. Free-floating staining of slices were performed. Briefly, slices were incubated with blocking solution, contains 10% serum, 1% BSA, 0,5% Triton X-100 in TBS1x, for 1h at T room. Then, primary antibodies were applied o/n at 4 °C in blocking solution. After three washes in TBS1x, slices were incubated with corresponding secondary antibodies for 1 h at T room, washed with TBS1x three times and then, counter-stained with DAPI. For co-staining, GFAP labeling was performed first and amplified with secondary antibodies plus streptavidin-Cy3 (Vector, cat. SA 1300). Then, other proteins detection was performed using corresponding primary antibodies (as p-eIF2α and GADD34) and secondary antibodies-488. Images were acquired using Leica SP8 LIGHTNING Confocal Microscope imaging systems. Images were acquired under non saturating conditions and analysed with Fiji ImageJ 1.52p software.

Primary antibodies used are anti- GFAP, Anti-p-eIF2α, Anti-Gadd 34 and Anti-Puromycin, indicated in Table 1. Secondary antibodies are horse anti-goat biotinylated antibodies (Vector, cat. BA 9500), anti-mouse (Invitrogen, cat. A 11029) and anti-rabbit-488 antibodies (Invitrogen, cat. A32731).

Total RNA extraction and real-time PCR. Total mRNA was extracted from 1.0×10^6 cells using TRIzol Lysis Reagent (Invitrogel, Cat. 15596026) according to manufacturer's instruction. First strand of cDNA was synthesized from 0.5–1 µg of total RNA using Im-Prom-II system (Promega, Cat. A3800). Real-Time PCR was performed using iTaq qPCR master mix according to manufacturer's instructions (Bio-Rad, Cat. 1725124) on a SFX96 Real-time system (Bio-Rad). To normalize raw real-time PCR data, S18 ribosomal subunit was used. Data are expressed as delta-C (t) of gene of interest to S18 allowing appreciation of single gene expression level. Oligonucleotide primers were as follows: Atf4 (NM_009716.3), forward: GTTTAGAGCTAGGCAGTGAAG, reverse: CCTTTACACATGGAGGGATTAG; Xbp1 spliced (Xbp1s, NM_001271730.1), forward: AGTCCGCAGCAGGTG, reverse: GGTCCAACTTGTCCAGAATG; Herpud1 (NM_022331.2), forward: GTGGAGGAAGATGATGAGATAAA, reverse: CTCAGCGAGGAGTAGAAGTA; S18 (NM_011296), forward: TGCGAGTACTCAACACCAACA, reverse: CTGC TTTCCTCAACACCACA.

L. Tapella et al.

Proteomic analysis on astrocytes conditioned media

Astrocyte-conditioned media from WT-iAstro and 3Tg-iAstro cells, the cells treated with 4-PBA (3 µM, 48 h) or expressing 10nm-EML (8–10 ml from three independently plated 10 cm Petri dish per condition) were collected, proteins were precipitated by TCA, washed and digested with trypsin. 100 µg of protein in 25 µl of 100 mM NH4HCO3 were reduced with 2.5 µL of 200 mM DTT (Sigma) at 90 °C for 20 min and alkylated with 10 µL 200 mM iodoacetamide (Sigma) for 1h at RT protected from light. Any excess of iodoacetamide was removed by the addition of 200 mM DTT. The samples were then digested with 5 µg of trypsin (Promega, Sequence Grade). After an ON incubation at 37 °C, 2 µL of neat formic acid were added to stop trypsin activity and the digested samples were dried by Speed Vacuum [78]. The peptide digests were desalted on the Discovery® DSC-18 solid phase extraction (SPE) 96-well plate (25 mg/well) (Sigma-Aldrich Inc., St. Louis, MO, USA) [79].

LC–MS/MS analyses were performed using a micro-LC Eksigent Technologies (Dublin, USA) system with a stationary phase of a Halo Fused C18 column (0.5 × 100 mm, 2.7 µm; Eksigent Technologies, Dublin, USA). The injection volume was 4.0 µL and the oven temperature was set at 40 °C. The mobile phase was a mixture of 0.1% (v/v) formic acid in water (A) and 0.1% (v/v) formic acid in acetonitrile (B), eluting at a flow-rate of 15.0 µL/min at increasing concentrations of B from 2–40% in 30 min. The LC system was interfaced with a 5600+ TripleTOF system (AB Sciex, Concord, Canada) equipped with a DuoSpray Ion Source. Samples were subjected to the traditional data-dependent acquisition (DDA) as previously described [80]. The MS data were acquired with Analyst TF 1.7 (SCIEX, Concord, Canada). Three instrumental replicates for each sample were subjected to the DIA analysis [81]. The MS files were searched using the software Mascot v. 2.4 (Matrix Science Inc., Boston, USA) using trypsin as enzyme, with two missed cleavages and a search tolerance of 50 ppm was specified for the peptide mass tolerance, and 0.1 Da for the MS/MS tolerance, charges of the peptides to search for were set to 2 +, 3 + and 4 +, and the search was set on monoisotopic mass and FDR at 1%. The instrument was set to ESI-QUAD-TOF and the following modifications were specified for the search: carbamido-methyl cysteines as fixed modification and oxidized methionine as variable modification. The UniProt/Swiss-Prot reviewed database containing mouse proteins (version 12/10/2018, containing 25137 sequence entries) was used.

The quantification was performed by integrating the extracted ion chromatogram of all the unique ions for a given peptide. The quantification was carried out with PeakView 2.0 and MarkerView 1.2. (Sciex, Concord, ON, Canada). Six peptides per protein and six transitions per peptide were extracted from the SWATH files. Shared peptides were excluded as well as peptides with modifications. Peptides with FDR <1.0% were exported in MarkerView for the t-test.

Statistical analysis

Statistical analysis and related graphical representations was done using GraphPad Prism v.7. A two-tailed unpaired Student's t-test or one-way ANOVA test were used. No samples/results were excluded from the analysis. Differences were considered significant at $p < 0.05$.

DATA AVAILABILITY

The datasets generated during and/or analyzed during the current study are available from the corresponding author on reasonable request.

REFERENCES

1. Muneer A, Shamsher Khan RM. Endoplasmic reticulum stress: implications for neuropsychiatric disorders. Chonnam Med J. 2019;55:8–19.
2. Scheper W, Hoozemans JJM. The unfolded protein response in neurodegenerative diseases: a neuropathological perspective. Acta Neuropathol. 2015;130:315–31.
3. Halliday M, Radford H, Zents KAM, Molloy C, Moreno JA, Verity NC, et al. Repurposed drugs targeting eIF2α-P-mediated translational repression prevent neurodegeneration in mice. Brain. 2017;140:1768–83.
4. Garcia-Esparcia P, Sideris-Lampretsas G, Hernandez-Ortega K, Grau-Rivera O, Sklaviadis T, Gelpi E, et al. Altered mechanisms of protein synthesis in frontal cortex in Alzheimer disease and a mouse model. Am J Neurodegener Dis. 2017;6:15–25.
5. Buchanan H, Mackay M, Palmer K, Tothová L, Katsur M, Platt B, et al. Synaptic loss, ER Stress and neuro-inflammation emerge late in the lateral temporal cortex and associate with progressive Tau pathology in Alzheimer's disease. Mol Neurobiol. 2020;57:3258–72.
6. Duran-Aniotz C, Cornejo VH, Espinoza S, Ardiles ÁO, Medinas DB, Salazar C, et al. IRE1 signaling exacerbates Alzheimer's disease pathogenesis. Acta Neuropathol. 2017;134:489–506.
7. Ma T, Trinh MA, Wexler AJ, Bourbon C, Gatti E, Pierre P, et al. Suppression of eIF2α kinases alleviates Alzheimer's disease-related plasticity and memory deficits. Nat Neurosci. 2013;16:1299–305.
8. Hashimoto S, Saido TC. Critical review: involvement of endoplasmic reticulum stress in the aetiology of Alzheimer's disease. Open Biol. 2018. https://doi.org/10.1098/rsob.180024.
9. Pakos-Zebrucka K, Koryga I, Mnich K, Ljujic M, Samali A, Gorman AM. The integrated stress response. EMBO Rep. 2016;17:1374–95.
10. Costa-Mattioli M, Walter P. The integrated stress response: from mechanism to disease. Science. 2020;368:eaat5314.
11. Hetz C, Zhang K, Kaufman RJ. Mechanisms, regulation and functions of the unfolded protein response. Nat Rev Mol Cell Biol. 2020;21:421–38.
12. Kumar V, Maity SER. Stress-sensor proteins and ER-mitochondrial crosstalk-signaling beyond (ER) stress response. Biomolecules. 2021;11:173.
13. Semyanov A, Verkhratsky A. Astrocytic processes: from tripartite synapses to the active milieu. Trends Neurosci. 2021;44:781–92.
14. Sakers K, Lake AM, Khazanchi R, Ouwenga R, Vasek MJ, Dani A, et al. Astrocytes locally translate transcripts in their peripheral processes. Proc Natl Acad Sci USA. 2017;114:E3830–E3838.
15. Boulay A-C, Saubaméa B, Adam N, Chasseigneaux S, Mazaré N, Gilbert A, et al. Translation in astrocyte distal processes sets molecular heterogeneity at the gliovascular interface. Cell Disco. 2017;3:17005.
16. Sims SG, Cisney RN, Lipscomb MM, Meares GP. The role of endoplasmic reticulum stress in astrocytes. Glia. 2022;70:5–19.
17. Lim D, Iyer A, Ronco V, Grolla AA, Canonico PL, Aronica E, et al. Amyloid beta deregulates astroglial mGluR5-mediated calcium signaling via calcineurin and Nf-kB. Glia. 2013;61:1134–45.
18. Ruffinatti F, Tapella L, Gregnanin I, Stevano A, Chiorino G, Canonico PL et al. Transcriptional remodeling in primary Alzheimer's disease mouse model. Curr Alzheimer Res. 2018. https://doi.org/10.2174/1567205015666180613113924.
19. Rocchio F, Tapella L, Manfredi M, Chisari M, Ronco F, Alessandro RF, et al. Gene expression, proteome and calcium signaling alterations in immortalized hippocampal astrocytes from an Alzheimer's disease mouse model. CELL DEATH DIS-EASE. 2019;10:24.
20. Dematteis G, Vydmantaité G, Ruffinatti FA, Chahin M, Farruggio S, Barberis E, et al. Proteomic analysis links alterations of bioenergetics, mitochondria-ER interactions and proteostasis in hippocampal astrocytes from 3xTg-AD mice. Cell Death Dis. 2020;11:645.
21. Lim D, Dematteis G, Tapella L, Genazzani AA, Calì T, Brini M, et al. Ca2+ handling at the mitochondria-ER contact sites in neurodegeneration. Cell Calcium. 2021;98:102453.
22. Dematteis G, Restelli E, Chiesa R, Aronica E, Genazzani AA, Lim D, et al. Calcineurin controls expression of EAAT1/GLAST in mouse and human cultured astrocytes through dynamic regulation of protein synthesis and degradation. Int J Mol Sci. 2020;21:2213.
23. Dematteis G, Restelli E, Vanella VV, Manfredi M, Marengo E, Corazzari M, et al. Calcineurin controls cellular prion protein expression in mouse astrocytes. Cells. 2022;11:609.
24. Cieri D, Vicario M, Giacomello M, Vallese F, Filadi R, Wagner T, et al. SPLICS: a split green fluorescent protein-based contact site sensor for narrow and wide heterotypic organelle juxtaposition. Cell Death Differ. 2018;25:1131–45.
25. Vallese F, Catoni C, Cieri D, Barazzuol L, Ramirez O, Calore V, et al. An expanded palette of improved SPLICS reporters detects multiple organelle contacts in vitro and in vivo. Nat Commun. 2020;11:6069.
26. Calì T, Brini M. Quantification of organelle contact sites by split-GFP-based contact site sensors (SPLICS) in living cells. Nat Protoc. 2021;16:5287–308.
27. Csordás G, Renken C, Várnai P, Walter L, Weaver D, Buttle KF, et al. Structural and functional features and significance of the physical linkage between ER and mitochondria. J Cell Biol. 2006;174:915–21.
28. Ding Q, Markesbery WR, Chen Q, Li F, Keller JN. Ribosome dysfunction as an early event in Alzheimer's disease. J Neurosci. 2005;25:9171–5.
29. Ma T. Dysregulation of neuronal protein synthesis in Alzheimer's disease. In: Sossin WS, editor. The Oxford handbook of neuronal protein synthesis. USA: Oxford University Press; 2021. p. 533–50.
30. Santini E, Huynh TN, Klann E. Mechanisms of translation control underlying long-lasting synaptic plasticity and the consolidation of long-term memory. Prog Mol Biol Transl Sci. 2014;122:131–67.
31. Rosenberg T, Gal-Ben-Ari S, Dieterich DC, Kreutz MR, Ziv NE, Gundelfinger ED, et al. The roles of protein expression in synaptic plasticity and memory consolidation. Front Mol Neurosci 2014;7:86.

32. Kucukdereli H, Allen NJ, Lee AT, Feng A, Ozlu MI, Conatser LM, et al. Control of excitatory CNS synaptogenesis by astrocyte-secreted proteins Hevin and SPARC. PNAS. 2011;108:E440–49.

33. Lyon MS, Milligan C. Extracellular heat shock proteins in neurodegenerative diseases: new perspectives. Neurosci Lett. 2019;711:134462.

34. Calderwood SK, Borges TJ, Eguchi T, Lang BJ, Murshid A, Okusha Y, et al. Extracellular Hsp90 and protection of neuronal cells through Nrf2. Biochem Soc Trans. 2021;49:2299–306.

35. Cuadrado-Tejedor M, García-Osta A, Ricobaraza A, Oyarzabal J, Franco R. Defining the mechanism of action of 4-phenylbutyrate to develop a small-molecule-based therapy for Alzheimer's disease. Curr Med Chem. 2011;18:5545–53.

36. Cuadrado-Tejedor M, Ricobaraza AL, Torrijo R, Franco R, Garcia-Osta A. Phenylbutyrate is a multifaceted drug that exerts neuroprotective effects and reverses the Alzheimer's disease-like phenotype of a commonly used mouse model. Curr Pharm Des. 2013;19:5076–84.

37. Groenendyk J, Agellon LB, Michalak M. Calcium signaling and endoplasmic reticulum stress. Int Rev Cell Mol Biol. 2021. https://doi.org/10.1016/bs.ircmb.2021.03.003.

38. Bullido MJ, Martínez-García A, Tenorio R, Sastre I, Muñoz DG, Frank A, et al. Double stranded RNA activated EIF2 alpha kinase (EIF2AK2; PKR) is associated with Alzheimer's disease. Neurobiol Aging. 2008;29:1160–6.

39. Moradi Majd R, Mayeli M, Rahmani F. Pathogenesis and promising therapeutics of Alzheimer disease through eIF2α pathway and correspondent kinases. Metab Brain Dis. 2020;35:1241–50.

40. Hugon J, Paquet C. The PKR/P38/RIPK1 signaling pathway as a therapeutic target in Alzheimer's disease. Int J Mol Sci. 2021;22:3136.

41. Area-Gomez E, Schon EA. On the pathogenesis of Alzheimer's disease: the MAM hypothesis. FASEB J. 2017;31:864–7.

42. Paillusson S, Stoica R, Gomez-Suaga P, Lau DHW, Mueller S, Miller T, et al. There's something wrong with my MAM; the ER-mitochondria axis and neurodegenerative diseases. Trends Neurosci. 2016;39:146–57.

43. Lim D, Ronco V, Grolla AA, Verkhratsky A, Genazzani AA. Glial calcium signalling in Alzheimer's disease. Rev Physiol Biochem Pharm. 2014;167:45–65.

44. Lim D, Rodríguez-Arellano JJ, Parpura V, Zorec R, Zeidán-Chuliá F, Genazzani AA, et al. Calcium signalling toolkits in astrocytes and spatio-temporal progression of Alzheimer's disease. Curr Alzheimer Res. 2016;13:359–60.

45. Lim D, Semyanov A, Genazzani A, Verkhratsky A. Calcium signaling in neuroglia. Int Rev Cell Mol Biol. 2021. https://doi.org/10.1016/bs.ircmb.2021.01.003.

46. De Strooper B, Karran E. The cellular phase of Alzheimer's disease. Cell. 2016;164:603–15.

47. Hipp MS, Kasturi P, Hartl FU. The proteostasis network and its decline in ageing. Nat Rev Mol Cell Biol. 2019;20:421–35.

48. Kurtishi A, Rosen B, Patil KS, Alves GW, Møller SG. Cellular proteostasis in neurodegeneration. Mol Neurobiol. 2019;56:3676–89.

49. Griffiths EJ, Rutter GA. Mitochondrial calcium as a key regulator of mitochondrial ATP production in mammalian cells. Biochim Biophys Acta. 2009;1787:1324–33.

50. Bier DM. The energy costs of protein metabolism: lean and mean on uncle Sam's team. Washington, D.C.: National Academies Press (US); 1999. https://www.ncbi.nlm.nih.gov/books/NBK224633/.

51. Qiao J, Wang J, Wang H, Zhang Y, Zhu S, Adilijiang A, et al. Regulation of astrocyte pathology by fluoxetine prevents the deterioration of Alzheimer phenotypes in an APP/PS1 mouse model. Glia. 2016;64:240–54.

52. Tapella LPF, Cerruti M, Biocotino I, Stevano A, Rocchio F, Canonico PL, et al. TGF-β2 and TGF-β3 from cultured β-amyloid-treated or 3xTg-AD-derived astrocytes may mediate astrocyte-neuron communication. Eur J Neurosci. 2018;47:211–21.

53. Zhong N, Ramaswamy G, Weisgraber KH. Apolipoprotein E4 domain interaction induces endoplasmic reticulum stress and impairs astrocyte function. J Biol Chem. 2009;284:27273–80.

54. Cvijetic S, Bortolotto V, Manfredi M, Ranzato E, Marengo E, Salem R, et al. Cell autonomous and noncell-autonomous role of NF-κB p50 in astrocyte-mediated fate specification of adult neural progenitor cells. Glia. 2017;65:169–81.

55. Risher WC, Kim N, Koh S, Choi J-E, Mitev P, Spence EF, et al. Thrombospondin receptor α2δ-1 promotes synaptogenesis and spinogenesis via postsynaptic Rac1. J Cell Biol. 2018;217:3747–65.

56. Chaplot K, Jarvela TS, Lindberg I. Secreted chaperones in neurodegeneration. Front Aging Neurosci. 2020;12:268.

57. Lackie RE, Maciejewski A, Ostapchenko VG, Marques-Lopes J, Choy W-Y, Duennwald ML, et al. The Hsp70/Hsp90 chaperone machinery in neurodegenerative diseases. Front Neurosci. 2017;11:254.

58. Upadhya R, Zingg W, Shetty S, Shetty AK. Astrocyte-derived extracellular vesicles: Neuroreparative properties and role in the pathogenesis of neurodegenerative disorders. J Control Release. 2020;323:225–39.

59. Baeten KM, Akassoglou K. Extracellular matrix and matrix receptors in blood-brain barrier formation and stroke. Dev Neurobiol. 2011;71:1018–39.

60. Benarroch EE. Extracellular matrix in the CNS: dynamic structure and clinical correlations. Neurology. 2015;85:1417–27.

61. Wiese S, Karus M, Faissner A. Astrocytes as a source for extracellular matrix molecules and cytokines. Front Pharm. 2012;3:120.

62. Corazzari M, Rapino F, Ciccosanti F, Giglio P, Antonioli M, Conti B, et al. Oncogenic BRAF induces chronic ER stress condition resulting in increased basal autophagy and apoptotic resistance of cutaneous melanoma. Cell Death Differ. 2015;22:946–58.

63. Giglio P, Gagliardi M, Tumino N, Antunes F, Smaili S, Cotella D, et al. PKR and GCN2 stress kinases promote an ER stress-independent eIF2α phosphorylation responsible for calreticulin exposure in melanoma cells. Oncoimmunology. 2018;7:e1466765.

64. Kolb PS, Ayaub EA, Zhou W, Yum V, Dickhout JG, Ask K. The therapeutic effects of 4-phenylbutyric acid in maintaining proteostasis. Int J Biochem Cell Biol. 2015;61:45–52.

65. Lebeau PF, Platko K, Byun JH, Austin RC. Calcium as a reliable marker for the quantitative assessment of endoplasmic reticulum stress in live cells. J Biol Chem. 2021;296:100779.

66. Lin H, Peng Y, Li J, Wang Z, Chen S, Qing X, et al. Reactive oxygen species regulate endoplasmic reticulum stress and ER-mitochondrial Ca2+ crosstalk to promote programmed necrosis of rat nucleus pulposus cells under compression. Oxid Med Cell Longev. 2021;2021:8810698.

67. Malo A, Krüger B, Göke B, Kubisch CH. 4-Phenylbutyric acid reduces endoplasmic reticulum stress, trypsin activation, and acinar cell apoptosis while increasing secretion in rat pancreatic acini. Pancreas. 2013;42:92–101.

68. Zhong Y, Jin C, Han J, Zhu J, Liu Q, Sun D, et al. Inhibition of ER stress attenuates kidney injury and apoptosis induced by 3-MCPD via regulating mitochondrial fission/fusion and Ca2+ homeostasis. Cell Biol Toxicol. 2021;37:795–809.

69. Sharma M, Naura AS, Singla SK. A deleterious interplay between endoplasmic reticulum stress and its functional linkage to mitochondria in nephrolithiasis. Free Radic Biol Med. 2021;168:70–80.

70. Gerakis Y, Hetz C. Emerging roles of ER stress in the etiology and pathogenesis of Alzheimer's disease. FEBS J. 2018;285:995–1011.

71. Remondelli P, Renna M. The endoplasmic reticulum unfolded protein response in neurodegenerative disorders and its potential therapeutic significance. Front Mol Neurosci. 2017;10:187.

72. Rozpedek W, Markiewicz L, Diehl JA, Pytel D, Majsterek I. Unfolded protein response and PERK kinase as a new therapeutic target in the pathogenesis of Alzheimer's disease. Curr Med Chem. 2015;22:3169–84.

73. Singh R, Kaur N, Dhingra N, Kaur T. Protein misfolding, ER Stress and Chaperones: an approach to develop chaperone-based therapeutics for Alzheimer's disease. Int J Neurosci. 2021. https://doi.org/10.1080/00207454.2021.1968859.

74. L Tapella, T Soda, L Mapelli, V Bortolotto, H Bondi, FA Ruffinatti et al. Deletion of calcineurin from GFAP-expressing astrocytes impairs excitability of cerebellar and hippocampal neurons through astroglial Na+ /K+ ATPase. GLIA. 2019. https://doi.org/10.1002/glia.23737.

75. Ozcan U, Yilmaz E, Ozcan L, Furuhashi M, Vaillancourt E, Smith RO, et al. Chemical chaperones reduce ER stress and restore glucose homeostasis in a mouse model of type 2 diabetes. Science. 2006;313:1137–40.

76. Schmidt EK, Clavarino G, Ceppi M, Pierre P. SUnSET, a nonradioactive method to monitor protein synthesis. Nat Methods. 2009;6:275–7.

77. Koren SA, Hamm MJ, Meier SE, Weiss BE, Nation GK, Chishti EA, et al. Tau drives translational selectivity by interacting with ribosomal proteins. Acta Neuropathol. 2019;137:571–83.

78. Dalla Pozza E, Manfredi M, Brandi J, Buzzi A, Conte E, Pacchiana R, et al. Trichostatin A alters cytoskeleton and energy metabolism of pancreatic adenocarcinoma cells: an in depth proteomic study. J Cell Biochem. 2018;119:2696–707.

79. Manfredi M, Robotti E, Bearman G, France F, Barberis E, Shor P, et al. Direct analysis in real time mass spectrometry for the nondestructive investigation of conservation treatments of cultural heritage. J Anal Methods Chem. 2016;2016:6853591.

80. Manfredi M, Martinotti S, Gosetti F, Ranzato E, Marengo E. The secretome signature of malignant mesothelioma cell lines. J Proteom. 2016;145:3–10.

81. Manfredi M, Brandi J, Di Carlo C, Vita Vanella V, Barberis E, Marengo E, et al. Mining cancer biology through bioinformatic analysis of proteomic data. Expert Rev Proteom. 2019;16:733–47.

AUTHOR CONTRIBUTIONS

Conceptualization and data interpretation AAGe, DL and LT; methodology, GD, ER, MMa, MC, EDG, AAGr and MG; software, MG and MMa; validation, MMo, BP, ET, VVV, DG, ALF, EB, SV, GD and ER; formal analysis, MMo, GD, ER, MMa, DL and LT; investigation, GD, ER, VVV, AAGr, MMo, DL and LT; resources, AAGr, MC, MMa, MG and EDG; data curation, VVV, MMo, GD and LT; writing—original draft preparation, MMo, GD, LT and DL; writing—review and editing, GD, LT, DL, AAGr, AAGe; supervision, LT, DL and AAGe; project administration, LT, AAGe and DL; funding acquisition, MMa, AAGe, and DL. All authors have read and agreed to the published version of the manuscript.

COMPETING INTERESTS

The authors declare no competing interests.

ADDITIONAL INFORMATION

Chapter 6

Title

Investigation of the interplay between endoplasmic reticulum-mitochondria distances and mitochondrial Ca^{2+} uptake: a role in Alzheimer's disease astrocytes cellular dysfunction. (UNPUBLISHED)

Giulia Dematteis[1], Laura Tapella[1], Claudio Casali[2], Maria Talmon[1], Elisa Tonelli[1], Adele Ariotti[1], Emanuela Pessolano[1], Justyna Malecka[1], Gabriela Chrostek[1], Carla Distasi[1], Mariagrazia Grilli[1], Graham Ladds[4], Federica Pollastro[1], Luigia Fresu[3], Tito Cali[5], Marisa Brini[6], M. Biggiogera[2], A.A. Genazzani[1], Riccardo Miggiano[1], Dmitry Lim[1]

Affiliations

[1] Department of Pharmaceutical Sciences, Università del Piemonte Orientale "Amedeo Avogadro", Via Bovio 6, 28100, Novara, Italy;
[2] Laboratory of Cell Biology and Neurobiology, Department of Biology and Biotechnology, University of Pavia, Pavia, Italy,
[3] Department of Health Sciences, School of Medicine, University of Piemonte Orientale, Via Solaroli 17, 28100 Novara, Italy,
[4] Department of Pharmacology, University of Cambridge, Tennis Court Road, Cambridge, CB2 1PD, United Kingdom
[5] Department of Biomedical Sciences, Neuroscience Center (PNC), Neurodegeneration Study Center (CESNE), University of Padua, Padova, Italy
[6] Department of Biology, University of Padua, Padova, Italy,

ABSTRACT

Correct Ca2+ transfer from the endoplasmic reticulum (ER) to mitochondria (Mit) at MERCs (Mit-ER contact sites) is crucial for mitochondrial bioenergetics and proteostasis. MERCS alterations were found in many pathologies including Alzheimer's disease (AD). Recently, we have demonstrated that in immortalized AD astrocytes (3Tg-iAstro), ATP-induced cytosolic Ca^{2+} signals were enhanced while Ca^{2+} transients in mitochondrial matrix (MM) were lower compared with WT-iAstro cells. Surprisingly, ER-Mit interaction was increased at a distance of 8-10nm. These results were at odds, since, canonically, the increased ER-Mit interaction determines increased ER-Mit Ca^{2+} transfer. Although it has been hypothesized that 10-20 nm distance is required for ER-mitochondrial Ca^{2+} transfer, the optimal distance and the mechanisms of its regulation were unknown.

Employing artificial ER-mitochondrial linkers (EMLs) spanning a range from 5 to 30 nm, we show that 20nm-EML significantly increases, while shorter (5-10nm) EMLs strongly inhibited the ATP-induced Ca^{2+} transient in mitochondrial matrix, explaining the reduction of MM Ca^{2+} transients in AD astrocytes.

Mechanistically, 20nm-EML promoted localization of IP3R at MERCS and formation of IP3R-Grp75-VDAC1 complex. Using a newly designed split-GFP-based contact site sensor for 20 nm distance (20nm-SPLICS) we show that 20nm-MERCS are present in different cell lines including astrocytes and HeLa cells. Moreover, 20nm-MERCS are dynamically regulated throuth GPCR/Gαs→cAMP→EPAC signaling axis. During such a rearrangement, IP3-mediated ER-mitochondrial transfer significantly increased, suggesting a cross-talk between Gαs and Gαq/11.

Functionally, 10nm-EML expressed in WT astrocytes impaired tubule formation in an in vitro model of angiogenesis, replicating the effect of AD astrocytes. Instead, expression of 20nm-EML in AD astrocytes rescued the impaired tubulogenesis.

All in all, data provide a proof that ~20nm is the optimal distance for ER-MIT Ca2+ transfer. Furthermore, our results suggest that the shortening of the ER-mitochondrial distance may be the cause of astroglial dysfunction in AD while the optimization of the distance for Ca^{2+} transfer may be beneficial.

INTRODUCTION

Mitochondria-endoplasmic reticulum (ER) contact sites (MERCS), composed by the juxtaposed ER and outer mitochondrial membrane (OMM), represent multifunctional platforms hosting and organizing such important cellular processes as phospholipid and steroid biogenesis, mitochondrial bioenergetics, apoptosis, autophagy, unfolded protein response (UPR) and ribosomal protein synthesis[1,2]. The ER membrane and OMM at MERCS are hold together by so called tethering proteins. A prototypical ER mitochondrial tether in yeasts is represented by the ERMES complex (ER-mitochondria encounter structure) composed of four proteins, namely Mmm1, Mdm10, Mdm12 and Mdm34 [3]. In mammals, a prototypical ER-mitochondrial tether is represented by mitofusin 2 (MFN2) and its shorter splice variant ERMIT2 (ER mitofusin 2 tether) [4]. Other tethering proteins, implicated in MERCS organization include following pairs of proteins VAPB/PTPIP51, FIS1/BAP31, SYNJ2BP/RRBP1, Miro/VPS13D and others [5].

Mitochondrial Ca^{2+} signals are required to drive mitochondrial bioenergetics as the activity of several enzymes, such as pyruvate dehydrogenase, isocitrate dehydrogenase, α-ketoglutarate dehydrogenase and F0/F1 ATP synthase, directly or indirectly depend on Ca^{2+}-binding [6]. Mitochondria uptake Ca^{2+} through a low affinity mitochondrial Ca^{2+} uniporter complex composed of MCU (mitochondrial Ca^{2+} uniporter), EMRE (essential mitochondrial uptake regulator) and MICU1-3 (mitochondrial Ca^{2+} uptake) proteins [7]. Close apposition of the ER membrane and OMM warrants direct transfer of Ca^{2+} through a complex composed of inositol-1,4,5-trisphsophate receptors (IP3Rs) and porine/voltage-dependent cation channel 1 (VDAC1). A number of proteins have been implicated in stabilization and modulation of the IP3R-VDAC1 interaction. Glucose-regulated protein 75 (Grp75) has been shown to

interact with both IP3R and VDAC1 [8]. Other proteins, such as non-opioid sigma receptor 1 (SIGRMA1R), DJ-1, inositol-requiring enzyme 1 (IRE1), B-cell lymphoma 2 (Bcl2) and others, modulate localization and activity of IP3R at the OMM-opposed ER membrane (called also mitochondria-associated ER membrane, MAM) [9].

The transversal distance between ER and OMM at MERCS spans a range from <5 nm up to 80 nm. It is thought that a specific distance is required for the specific MERCS-associated process. For example, it is postulated that phospholipid biogenesis occurs at a distance ≤5 nm, while autophagosome formation requires a 40-50 nm distance between ER and OMM. We and others suggested that the optimal distance for ER-MIT Ca^{2+} transfer lays in the range of ~10-25 nm, and is defined by the size of the Ca^{2+} transfer protein complex composed of the IP3R, VDAC1 and associated proteins [10–12]. However, it is still not known if ER-mitochondrial Ca2+ transfer operates with the same efficiency in a range of ER-OMM distances or an optimal distance exists for the assembly of IP3R-VDAC1 complex to optimise Ca^{2+} flux. Furthermore, it was shown that ER-mitochondrial interaction and, presumably, Ca^{2+} transfer, undergo remodelling during mitochondrial dynamics or ER rearrangement [13]. However, it is not known if fast rearrangement of ER-mitochondrial Ca^{2+} transfer exists to modulate ER and/or mitochondrial Ca2+ signalling events. In this contribution we shown that 20 nm ER-OMM distance optimizes ER-MIT Ca^{2+} transfer allowing enrichment of MERCS with IP3R-Grp75-VDAC1 Ca^{2+} transferring complexes.

Further, we uncover a novel rout of signalling through which MERCS are rapidly set at 20nm through GPCR/Gαs→cAMP→EPAC→MERCS signalling. Interestingly, this rout is separated from GPCR/Gαq/11→IP3→IP3R-mediated Ca2+ release from the ER. However,

when co-stimulated, simultaneous Ca2+ release from the ER and increase of 20nm MERCS lead to enhanced Ca^{2+} transient in the mitochondrial matrix.

RESULTS

Generation of the extended palette of ER-MIT linkers

To investigate if there is an optimal distance between ER membrane and OMM for Ca2+ transfer, we employed synthetic ER-mitochondrial linkers (EMLs) designed to maintain the distance between membranes at 5-6nm (denominated as 5nm-EML), 10-12nm (10nm-EML), 15nm, 20nm and 30nm (15nm-EML, 20nm-EML and 30nm-EML, respectively). 5nm-EML and 10nm-EML (a kind gift from Georgy Hajnoczky, Jefferson University) were published elsewhere [14] [12]. 15, 20 and 30nm-EMLs were designed de novo (Fig. 1B). EMLs are composed of monomeric red fluorescent protein flanked by rigid α-helical spacer of a defined length [15]. At N- and C-terminal ends of the construct, sequences targeting the OMM and the ER membrane, were, respectively attached. (Fig. 1B). 5nm, 10nm and 20nm-EMLs were validated by electron microscopy, and their ability to impose the defined distance has been confirmed (Fig. 1C-D). Moreover, all linkers significantly increased the length of interaction between the two organelles (Fig. 1D – Interface extension). Importantly, none of EMLs affected neither cell viability up to 72 h post-transfection in HeLa cells nor protein levels of proteins implicated in mitochondrial dynamics such as dynamin-related protein (DRP), p-DRP, mitofusin 1 (MFN1) and MFN2 (Fig. 1E-F). After that, the effect of EMLs expression in HeLa cells on ATP induced ER-MIT Ca^{2+} transfer was assessed.

20nm between ER and OMM is the optimal distance ER-MIT Ca2+ transfer.

Mitochondrial calcium uptake was accessed, using a genetically encoded calcium indicator (GECI), 4mtD3cpv targeted to the mitochondrial matrix [16]. 48 h after co-transfection of EMLs with 4mtD3cpv, cells were stimulated with a purinergic agonist ATP and ATP-evoked Ca^{2+} signals in the mitochondrial

matrix $[Ca^{2+}]m$ were recorded. The amplitude of ATP-induced $[Ca^{2+}]m$ in 5- and 10-EML-expressing cells was significantly reduced compared with control ER-RFP-expressing cells (p=0.0002). 15nm-EML had no effect (p=0.4601), while 20nm-EML strongly enhanced ATP-evoked $[Ca^{2+}]m$ transient (p<0,0001). Overexpression of 30nm-EML resulted in a drastic reduction of ATP-evoked $[Ca^{2+}]m$ transient (p<0,0001) (Fig. 2A). These results confirm previous observations and predictions that at too short (5nm-EML) and too long (30nm-EML) ER-OMM distance Ca^{2+} transfer is inefficient [10] [14]. However, surprisingly, 10nm-EML exerted negative effect, while 15nm-EML was inefficient in changing ER-MIT Ca^{2+} transfer compared with control cells in spite of strong increase of the interface length between the membranes. Instead, our data suggest that 20nm is the optimal distance between ER and MIT for Ca^{2+} transfer.

Potentially, overexpression of EMLs could affect ER Ca^{2+} capacity and/or the efficiency of Ca^{2+} release from the ER. To investigate if there were alteration in ER Ca^{2+} handling and release upon EMLs overexpression, we, first assessed ATP-induced IP3R-mediatd cytosolic Ca^{2+} dynamics $[Ca^{2+}]c$ using Fura-2 probe. As shown in Fig. 2B, there were no differences in ATP-evoked $[Ca^{2+}]c$ transient upon overexpression of either EMLs apart from 10nm-EML, whose overexpression resulted in an enhanced $[Ca^{2+}]_C$. Resting steady state luminal ER Ca^{2+} levels ($[Ca^{2+}]_L$) and the ER releasable Ca^{2+} pool ($\Delta[Ca^{2+}]_L$) were evaluated using a ratiometric genetically encoded green fluorescent protein (GFP)-aequorin fusion protein (GAP3) low affinity Ca^{2+} sensor targeted to the ER lumen [17]. The GAP3-transduced HeLa cells were stimulated with a cocktail, containing ATP (100 μM) and tert-butyl hydroquinone (tBHQ, 100 μM) in a Ca^{2+}-free KRB solution supplemented with 500 μM EGTA, to induce rapid and complete ER depletion. No significant differences in $[Ca^{2+}]_L$ and

$\Delta[Ca^{2+}]_L$ were observed upon EMLs overexpression, with an exception of 20nm-EML which resulted in a modest by significant reduction of the steady-state $[Ca^{2+}]_L$ compared with control cells expressing ER-RFP. Nevertheless, the $\Delta[Ca^{2+}]_L$ in 20nm-EML-expressing HeLa was not different from control (Fig. 2C). These results suggest that the changes of ATP-evoked $[Ca^{2+}]m$ transients in EMLs-expressing cells were not due to differences in ER Ca^{2+} content and/or Ca^{2+} release capacity.

To check if, in 20nm-EML-expressing cells, Ca^{2+} flow follows IP3R→VDAC1→mitochondrial inter-membrane space (MIMS)→MCU→matrix rout, we employed recently developed ratiometric GECI targeted to cristae lumen of mitochondrial intermembrane space (MIMS) exploiting a targeting sequence from Reactive Oxygen Species Modulator 1 protein (denominated as ROMO-GemGeCO) [18]. Fig. 2D shows that ROMO-GemGeCO detect a significant decrease of MIMS Ca^{2+} signals upon ATP stimulation in 5nm-EML and 10nm-EML-expressing cells (p<0,0001). Expression of 15nm-EML did not have any effect, while 20nm-EML significantly potentiated Ca^{2+} transients in MIMS (p<0,0001). Lastly, 30nm-EML resulted in strong inhibition of MIMS Ca2+ transient (p<0,0001).

IP3R, Grp75 and VDAC1 are enriched in 20nm MERCS

It is postulated that IP3R-VDAC1 complex is responsible for direct Ca^{2+} transfer between ER and MIT [19] [20]. Therefore, we used a proximity ligation assay (PLA)[21] and immunolabelling of IP3Rs to investigate if the increase of Ca^{2+} transfer in 20nm-EML-expressing cells was due to major formation of IP3R-VDAC1 complexes at 20nm MERCS. As shown on Fig. 3A, in control ER-RFP-expressing cells, PLA signal shows diffuse dotty pattern corresponding to juxtaposed (≤40nm) IP3R and VDAC1 proteins, indicating

putative IP3R-VDAC1-interacting sites. Overexpression of 5nm-EML completely suppressed PLA signal (p= 0.0056), suggesting that at this distance juxtaposition of IP3R and VDAC1 is prevented. Overexpression of 10nm-EML resulted in a significant increase of PLA signal suggesting a juxtaposition of IP3R and VDAC1 (p<0.0001). However, a higher magnification examination shows only partial co-localization of PLA signal with 10nm-EML. Considering a reduced ATP-induced $[Ca^{2+}]m$ transient (Fig. 2A), this result indicates that, although juxtaposed, IP3R and VDAC1 do not form functional Ca2+-transferring complexes. Contrarily, overexpression of 20nm-EML resulted in a drastic increase of PLA signal (p<0.0001) with a complete co-localization between PLA signal and 20nm-EML, suggesting an enrichment of 20nm MERCS with IP3R-VDAC complexes.

Immunocytochemical analysis, using anti-pan-IP3R antibody, confirms enrichment of IP3R in 20nm MERCS showing a complete co-localization of IP3R signal with 20nm-EML (Pearson Coefficient=0.9368; ER-RFP vs. 20nm-EM: p<0.0001). Confirming PLA data, 10nm-EML resulted in a re-localization of IP3R, but with poor co-localization with 10nm-EML (Fig. 2B).

 Western blot analysis of total lysates showed that the enrichment of IP3R in 20nm MERCS was not due to increased expression of IP3Rs, but rather due to its re-localization to 20nm MERCS. VDAC1 and Grp75 proteins, implicated in the formation of the Ca2+-transferring complex, were either unchanged in whole cell lysate of 20nm-EML expressing Hela (Fig. 4A).

To strengthen the IP3R re-localization hypothesis, MERCS were isolated from ER-RFP and 20nm-EML-expressing cells using an established protocol [22], and abundance of IP3R, VDAC1 and Grp75 was assessed. IP3R protein was significantly increased in 20nm MERCS (p=0,0002), while VDAC1 and

Grp75 were not different from control cells (Fig. 4B). However, when IP3R was immunoprecipitated from whole cell lysate of HeLa-IP3R1-GFP [23] cells using anti-GFP resin, its amount was significantly higher in cells expressing 20nm-EML as compared with ER-RFP or with 5nm-EML-expressing cells. Importantly, Grp75 protein amount was also significantly increased (p=0,00905) in IP3R-immunoprecipitates from cells expressing 20nm-EML (Fig. 4C).

Collectively, these data suggest that IP3R is localized specifically at 20nm ER-OMM distance MERCS where it interacts with MERCS-located VDAC1 and Grp75.

20nm MERCS are physiologically present in cells.

The data, obtained using overexpression of artificial ER-OMM tethers, suggest that 20nm distance specifically promotes Ca2+ transfer between ER and mitochondria. This poses the question of 20nm MERCS are present in physiological conditions, and if yes, of what is their physiological role. To address these questions, we took advantage of a recently designed split-GFP contact site sensors (SPLICS) [24], which we adapted to reconstitute bright GFP fluorescence specifically at 20nm between ER and OMM (Fig. 5A). Fig. 5A shows the scheme of 20nm-SPLICS design and activation. Briefly, N-terminal GFP fragment containing 1-10 β-barrels (denominated as $GFP_{\beta1-10}$) was fused with a rigid α-helical spacer and a sequence targeted to the OMM, while N-terminal part containing the last 11th β-barrel (denominated as $GFP_{\beta11}$) was fused with an α-helical spacer and a targeting sequence to the ER membrane. To construct 20nm-SPLICS, α-helical spacers, identical to those used in 20nm-EML, were used. Transfection of 20nm-SPLICS results in appearance of bright fluorescent dots distributed throughout the cell and enriched in sites of a higher

mitochondrial density (Fig. 5B). Co-expression of 20nm-SPLICS probe with 20nm-EML resulted in a drastic increase of SPLICS signal and its complete co-localization 20nm-EML (Fig. 5C). Immunodecoration of IP3Rs shows close juxtaposition of 20nm-SPLICS with a fraction of IP3Rs, although, expectedly, SPLICS-free IP3Rs were also detected.

The next question was what the percentage of 20nm MERCS of all MERCS in the cell is. We therefore used TEM images of control HeLa cells to quantify the physiological abundance of MERCS in range of 18-22nm. Fig. 1C shows that 18-22nm MERCS account for ~18% of all MERCS ranging from 5 to 80nm, although this percentage is likely to differ between cell types and conditions [10].

20nm MERCS are dynamically regulated through Gαs→cAMP→EPAC axis.

ER-mitochondrial contacts are dynamic structures and are shown to undergo remodelling following mitochondrial dynamics, in response to stimuli and in pathological conditions [11,24]. However, the mechanisms of MERCS remodelling remain unexplored, and it is not known if MERCS dynamics are involved in regulation of ER-MIT Ca^{2+} flux. To assess a possible involvement of 20nm-MERCS in mitochondrial calcium signalling we capitalized on our previous finding that the activation of a Gαs-coupled G-protein coupled receptor (GPCR) hTAS2R46 with its natural agonist absinthin, results in a potentiation of histamine-induced mitochondrial Ca^{2+} uptake in airway smooth muscle cells ASM [25]. To investigate if this effect may involve 20nm MERCS remodelling to enhance ER-mitochondria Ca^{2+} transfer, we co-expressed hTAS2R46 together with 20nm-SPLICS in Hela cells (Fig. 6A). The changes in the intensity of GFP signal was monitored in live time-lapse imaging upon

stimulation with absinthin and/or histamine. As shown in Fig. 6A (light blue), stimulation with absinthin along produced a rapid (~2.5 sec) transient increase of 20nm-SPLICS fluorescence which returned to background in ~20-40 sec. Such transient was not observed in either of control conditions (in the absence of hTAS2R46 or in hTAS2R46-expressing cells stimulated with vehicle or histamine alone). Interestingly, when the cells were transfected with 8-10nm SPLICS (SPLICS-Short [24]), a decrease of SPLICS fluorescence was observed upon stimulation with absinthin (Fig. 6A graph in blue). This suggests that upon stimulation with absinthin, MERCS undergo a rapid remodelling towards 20nm ER-OMM distance. To investigate this remodelling enhances Ca^{2+} flow through IP3R-VDAC1 complex, we repeated the experiment with HeLa cells transduced with ROMO-GemGeCO Ca^{2+} probe to follow Ca^{2+} dynamics in the MIMS compartment. As shown in Fig. 6C, co-stimulation with absithin significantly potentiated histamine-induced Ca^{2+} transient in the cristae lumen (p=0,0002).

Assessment of 20nm SPLICS dynamics in primary ASM cells, endogenously expressing hTAS2R46 [25], corroborated the finding and confirmed that rapid 20nm MERCS remodelling is a physiological phenomenon (Fig.6D).

To investigate the mechanism of 20nm MERCS remodelling we checked if it could be mediated by a previously described hTAS2R46→Gαs→cAMP→EPAC axis [25]. Fig.6B shows that rapid increase of 20nm-SPLICS fluorescence was completely abolished by specific inhibitors of hTAS2R46 (3HDC, 10 µM) [26] and EPAC1 (ESI-09, 10 µM), but was insensitive to a PKA inhibitor H89 (10 µM).

To further investigate if EPAC-dependent 20nm MERCS remodelling could be instigated upon activation of other Gαs-coupled receptors, we co-expressed

20nm-SPLICS in HeLa cells together with either β1- or β2 adrenergic receptors (ARβ1 and ARβ2, respectively). Upon stimulation with an adrenergic stimulator isoproterenol, a rapid increase of 20nm-SPLICS was observed similar to that induced by absinthin in hTAS2R46-expressing cells (Fig.6E).

EMLs expression modulates astrocytes calcium signaling and cellular function.

We and others have described altered calcium signalling in AD cells. In particular we demonstrated, in AD immortalized astrocytes (Tg iAstro, here referred as Tg), reduced mitochondrial calcium uptake, and increased interaction between ER and MIT at 8-10 nm [27]. To investigate the role of ER-OMM distances in astrocytes, and in particular in AD, we expressed 10nm-EML in WT astrocytes (WT 10nm-EML), and 20nm-EML in Tg (Tg 20nm-EML). As shown in Fig. 7A, we monitored mitochondrial calcium uptake with 4mtD3cpv [16]. 48 h after co-transfection of EMLs with 4mtD3cpv, cells were stimulated with a purinergic agonist ATP and ATP-evoked Ca^{2+} signals in the mitochondrial matrix $[Ca^{2+}]m$ were recorded. ATP-induced $[Ca^{2+}]m$ increases in WT iAstro expressing 10nm-EML was significantly reduced compared to ER-RFP-expressing WT cells (p<0,0001). On the other hand, Tg iAstro expressing 20nm-EML displayed a significative increase in mitochondrial calcium uptake, compared to ER-RFP-expressing Tg cells (p<0,0001), completely rescuing the defect described in AD astrocytes (Fig. 7B).

Previously we also described reduced protein synthesis rate and impaired ability of Tg iAstro to support Pericytes/Editorial cells tubulogenesis [28]. Moreover, we already demonstrated that WT 10nm-EML completely recapitulate Tg iAstro dysfunction. Indeed, we investigated the effect of the

expression of 20nm-EML on Tg iAstro dysfunction. We accessed protein synthesis rate, via the SUnSET method, we found a significative increase of protein synthesis in Tg 20-EML, compared to Tg ER-RFP (p < 0,001), restoring normal protein synthesis rate (3Tg-20nm EML vs WT ER-RFP ns p=0,8541). We also assessed the effect of 3Tg-iAstro cells on a three-cell pericyte/EC/astrocyte 3D co-culture. When WT-iAstro or 3Tg-iAstro cells were added as a component of pericyte/EC/astrocyte 3D co-culture, WT-iAstro, but not 3Tg-iAstro, supported formation of vessel-like tubules by pericyte and EC. Strikingly, the effect of 3Tg-iAstro was reproduced by co-culture with 10nm-EML-overexpressing WT-iAstro cells (n= 3 independent experiments, p < 0.001). On the other hand, as presented in the figure, the Tg astrocytes expressing 20nm EML, rescue the ability to support tubulogenesis, reaching the level of WT astrocytes (n=3; 3Tg 20nm-EML vs 3Tg ER-RFP p<0,001; 3Tg-20nm EML vs WT ER-RFP ns p=0,3) (Fig. 7C). These results underline how, normalizing mitochondrial calcium signalling, acting on ER-OMM distances, may be an effective strategy for rescuing AD related astrocytes disfunction.

DISCUSSION

MERCS are dynamic structures with a transversal distance between ER and OMM ranging from <5 to ≥80 nm. For Ca^{2+} transfer, a range from ~10 to ~25 nm was hypothesized. However, it was not known if this broad range equally warrants an efficient Ca^{2+} flux or there could be a narrow range of distances with a maximal ER-mitochondrial Ca2+ transfer and if it could be dynamically regulated.

Here we show that the optimal distance for Ca^{2+} transfer is about 20 nm between ER and OMM. At 20nm-MERCS there is a spontaneous assembly of IP3R-VDAC1. Furthermore, we show that MERCS transversal distance undergoes a fast remodelling through GPCR/Gαs→cAMP→EPAC signalling cascade leading to facilitation of the concomitant Gαq agonist-induced Ca^{2+} transfer through IP3R-VDAC1 complex.

20nm is the optimal distance between ER and OMM for Ca2+ transfer: role of IP3R-Grp75-VDAC1 complex.

Since the discovery of the closed opposition between ER and mitochondrial membranes to warrant a low affinity mitochondrial Ca^{2+} uptake[19,20], several attempts have been made over the last three decades to determine the ER-mitochondria distance for the Ca^{2+} transfer. Such a distance should not be less than 10-12 nm which is the size of the cytosolic part of the Ca^{2+}-releasing channel IP3R [29], but it should also not be too wide due to a quick dissipation of $[Ca^{2+}]$ gradient following the lows of diffusion [10,12]. The distance of 10-15 nm has been considered to design ER-mitochondrial to quantify $[Ca^{2+}]$ in the ER-OMM cleft during IP3-mediated Ca^{2+} release [12]. Based on the analysis of TEM images, a distance between 10 and 15 nm has been considered as an average distance between two organelles and has been considered adequate for Ca^{2+} transfer. Our results compellingly suggest that mitochondrial Ca2+ uptake is strongly inhibited at the distances up to 15 nm, while ~20 nm strongly potentiate mitochondrial Ca^{2+} uptake compared to control and to 15 nm distance.

Given that the 10-12 nm steric hindrance of the IP3R at the cytosolic side of the ER membrane [29] and considering 3-4.5 nm height of the VDAC1 barrel, which is completely embedded into the lipid bilayer, there is a space of about

8-10 nm between IP3R and VDAC1 which is likely to be occupied by tethering and/or regulatory protein(s). At the current state of the art, the best candidate to fill this space is a known IP3R-VDAC1 interactor Grp75 (HSPA9) [8]. Other proteins which have been shown to interact with IP3R, VDAC1 or IP3R-VDAC1 complex or proteins, known to activate IP3R, include DJ-1, CIB1, CaBP1, Gβγ [9]. In silico modelling shows that all these proteins are small proteins unable to fill 8-10 nm gap. Instead modelling of an Hsp70 from E. coli (DnaK) suggest that a dimer of Hsp70 fits the 8-10 nm space between IP3R and VDAC1 in ~20 nm intermembrane space. Support for Grp75 and a IP3R-VDAC1 interactor comes from the results of immunoprecipitation experiments, suggesting that at 20nm-MERCS IP3R-Grp75 interaction is increased.

EPAC-dependent fast remodelling of 20nm-MERCS

Another key result of our work is the discovery of the fast remodelling of MERCS through GPCR/Gαs→cAMP→EPAC signalling which dynamically augments the amounts of 20nm-MERCS. Comparison of the dynamics with 20nm-SPLICS and 8-10nm-SPLICS [24] suggest that the increase of 20nm-MERCS occurs at the expensed of shorter contact sites, i.e., the average ER-OMM distance becomes wider. Strikingly, the temporal profile of 20nm-MERCS remodelling almost parallels that of the dynamics of Ca^{2+} transient through IP3Rs, i.e., fast rise of the 20nm-MERCS interaction which is followed by slower decay lasting about 30-50 sec. EPAC-dependent 20nm-MERCS remodelling occurs independently of the Ca^{2+} release. However, when co-stimulated, Gαs→cAMP→EPAC-MERCS and Gαq→IP3→IP3R→Ca^{2+} routs significantly potentiate Ca^{2+} transients in the mitochondrial matrix [25] (Fig. 6F). Importantly, 20nm-MERCS remodelling occurs downstream of all Gαs-coupled GPCRs tested, including hTAS2R46, AR-β1 and AR-β2, suggesting

broad translational and therapeutic potential of this phenomenon which links EPAC to mitochondrial Ca^{2+} signalling and bioenergetics. To the best of our knowledge, this is the first report on fast and signalling-dependent MERCS remodelling. There is a continuously growing interest to EPAC as a therapeutic target in heart diseases and cancer [30], which are the most frequent causes of disability and death. We believe that the newly discovered EPAC-dependent MERCS remodelling may find applications in drug development and therapy of these and other diseases.

Modulating ER-Mit distances is a valuable approach to restore AD astrocytes functionalities.
Once demonstrated that 20nm-EML is able to increase MIT Ca^{2+} uptake in Hela cells, we shown that the expression of this linker is also able to rescue mitochondrial calcium uptake deficit, in Tg-iAstro[27,31], while the expression of 10nm-EML in WT-iAstro strongly reduce calcium uptake in the Mit, recapitulating AD astrocytes behaviour (Fig.7A). These results demonstrate causal role of shortening the distance between ER and Mit for the impairment of mitochondrial calcium uptake. moreover, we also demonstrated that 20nm-EML expressed in Tg-iAstro can restore protein synthesis rate and tubulogenesis support, when added as a component of pericyte/EC/astrocyte 3D co-culture (Fig.7B-C). All in all, these results point out the modulation of ER-Mit distances as a valuable strategy to address AD related astrocytic cellular dysfunction, that are strongly associated with early phases of the disease[32,33].

MATERIALS AND METHODS

DNA constructs

- ### *Plasmids*

NAME	PROVENIENCE	REFERENCE
4mtD3cpv	Addgene #36324	[34]
ROMO-GemGeCO	Kind gift from Wolfgang Graier, Medical University of Graz, Austria	[18]
ER-GAP3	Addgene #78118	[17]
hTAS2R46	GenScript plasmid #OHu30358	NA
ARβ1	Addgene #14698	[35]
ARβ2	Addgene # 14697	[35]
pDsRed-Mito	Clontech plasmid # 632421	[36]

Table 1. Plasmids used in this contribution. Name, provenience and reference are here reported.

- ### *ER-mitochondrial linkers*

5nm-EML and 10nm-EML were a kind gift from Georgy Hajnoczky, Jefferson University, USA).

15nm-EML amino acid sequence is:

MAIQLRSLFPLALPGLLALLGWWWFFSRKKDPTRSANMEKERKRRE
EDEQRRRKEEEERRMKLEMEAKRKQEEEERKKREDDEKRIQAERNS

DPPVATLASSEDVIKEFMRFKVRMEGSVNGHEFEIEGEGEGRPYEGT
QTAKLKVTKGGPLPFAWDILSPQFQYGSKAYVKHPADIPDYLKLSFP
EGFKWERVMNFEDGGVVTVTQDSSLQDGEFIYKVKLRGTNFPSDGP
VMQKKTMGWEASTERMYPEDGALKGEIKMRLKLKDGGHYDAEVK
TTYMAKKPVQLPGAYKTDIKLDITSHNEDYTIVEQYERAEGRHSTGA
SGLRSRAQASNSMEKERKRREEDEQRRRKEEEERRMKLEMEAKRKQ
EEEERKKREDDEKRIQAESRAQASNSRVMVYIGIAIFLFVGLFMK.

20nm-EML amino acid sequence is:

MAIQLRSLFPLALPGLLALLGWWWFFSRKKDPTRSANKQQEEEAERL
RRIQEEMEKERKRREEDEQRRRKEEEERRMKLEMEAKRKQEEEERK
KREDDEKRIQAERNSDPPVATLASSEDVIKEFMRFKVRMEGSVNGHE
FEIEGEGEGRPYEGTQTAKLKVTKGGPLPFAWDILSPQFQYGSKAYV
KHPADIPDYLKLSFPEGFKWERVMNFEDGGVVTVTQDSSLQDGEFIY
KVKLRGTNFPSDGPVMQKKTMGWEASTERMYPEDGALKGEIKMRL
KLKDGGHYDAEVKTTYMAKKPVQLPGAYKTDIKLDITSHNEDYTIV
EQYERAEGRHSTGASGLRSRAQASNSKQQEEEAERLRRIQEEMEKER
KRREEDEQRRRKEEEERRMKLEMEAKRKQEEEERKKREDDEKRIQA
ESRAQASNSRVMVYIGIAIFLFVGLFMK;

30nm-EML amino acid sequence:

MAIQLRSLFPLALPGLLALLGWWWFFSRKKDPTRSANKQQEEEAERL
RRIQEEMEKERKRREEDEQRRRKEEEERRMKLEMEAKRKQEEEERK
KREDDEKRIQAEKQQEEEAERLRRIQEEMEKERKRREEDEQRRRKEE
EERRMKLEMEAKRKQEEEERKKREDDEKRIQAERNSDPPVATLASSE
DVIKEFMRFKVRMEGSVNGHEFEIEGEGEGRPYEGTQTAKLKVTKGG
PLPFAWDILSPQFQYGSKAYVKHPADIPDYLKLSFPEGFKWERVMNF
EDGGVVTVTQDSSLQDGEFIYKVKLRGTNFPSDGPVMQKKTMGWEA

STERMYPEDGALKGEIKMRLKLKDGGHYDAEVKTTYMAKKPVQLP
GAYKTDIKLDITSHNEDYTIVEQYERAEGRHSTGASGLRSRAQASNSK
QQEEEAERLRRIQEEMEKERKRREEDEQRRRKEEEERRMKLEMEAK
RKQEEEERKKREDDEKRIQAESRAQASNSRVMVYIGIAIFLFVGLFMK

Linkers are composed of targeting sequences of Tom20 (OMM targeting sequence) and UBC6 ER localization sequence (blue); flexible linkers (green), rigid α-helical spacers (yellow), and mRFP1 sequence (https://www.fpbase.org/protein/mrfp1/). EMLs were synthetized by GenScript (https://www.genscript.com/).

Split-GFP contact site sensors (SPLICS)

Generation of SPLICS-Short (8-10nm-SPLICS) was described elsewhere (doi: 10.1038/s41418-017-0033-z; doi: 10.1038/s41467-020-19892-6; doi: 10.1038/s41596-021-00614-1).

20nm-SPLICS-GFP$_{\beta1-10}$ sequence is:

MAIQLRSLFPLALPGLLALLGWWWFFSRKKDPTRSANKQQEEEAERL
RRIQEEMEKERKRREEDEQRRRKEEEERRMKLEMEAKRKQEEEERK
KREDDEKRIQAERNSDPPVATLMSKGEELFTGVVPILVELDGDVNGH
KFSVRGEGEGDATIGKLTLKFICTTGKLPVPWPTLVTTLTYGVQCFSR
YPDHMKRHDFFKSAMPEGYVQERTISFKDDGKYKTRAVVKFEGDTL
VNRIELKGTDFKEDGNILGHKLEYNFNSHNVYITADKQKNGIKANFT
VRHNVEDGSVQLADHYQQNTPIGDGPVLLPDNHYLSTQTVLSKDPN
EKGT.

20nm-SPLICS-GFP$_{\beta11}$ is:

MRDHMVLHEYVNAAGITGGDGGSGGGSKLKQQEEEAERLRRIQEEM
EKERKRREEDEQRRRKEEEERRMKLEMEAKRKQEEEERKKREDDEK
RIQAESRAQASNSRVMVYIGIAIFLFVGLFMK.

Linkers are composed of targeting sequences of Tom20 (OMM targeting sequence) and UBC6 ER localization sequence (blue); flexible linkers (red), rigid α-helical spacers (yellow), and GFP sequence (green). EMLs were synthetized by GenScript (https://www.genscript.com/).

Cell lines. Hela cells, human immortalized pericytes (CL 05008-CLTH) and endothelial cells EA.hy926 (CRL-2922™) were maintained in complete culture media containing Dulbecco's modified Eagle's medium (DMEM; Sigma-Aldrich, Cat. D5671) supplemented with 10% fetal bovine serum (Gibco, Cat. 10270) (FBS), 2 mM L-glutamine (Sigma-Aldrich), and 1% penicillin/streptomycin solution (Sigma-Aldrich).

Human primary lung ASM cells were obtained from ATCC (Cat. PCS-130-010). ASM cells were maintained in Vascular Cell Basal Medium (ATCC, at. PCS-100-030) supplemented with 5% heat-inactivated fetal bovine serum (FBS), 5% l-glutamine, 0.5% antibiotic-antimycotic (all Thermo Fisher), 5 ng/ml of basic fibroblasts growth factor and 5 ng/ml epidermal growth factor (ImmunoTools), 50 μg/ml of ascorbic acid, 10 ng/ml of insulin (Sigma-Aldrich).

Immortalized hippocampal astrocytes from WT and 3xTg-AD mice. Generation of immortalized astrocytes from hippocampi of WT and 3xTg-AD mice (WT- and 3Tg-iAstro cells) was described elsewhere[31]. iAstro lines were maintained in complete culture media containing Dulbecco's modified Eagle's medium (DMEM; Sigma-Aldrich, Cat. D5671) supplemented with 10% fetal

bovine serum (Gibco, Cat. 10270) (FBS), 2 mM L-glutamine (Sigma-Aldrich), and 1% penicillin/streptomycin solution (Sigma-Aldrich).

Cell transfection. 3×10^4 cells/well were resuspended in 250 µl of complete DMEM and 250 µl of transfection mix, and plated onto 13 mm glass coverslips in 24 well plates. For the transfection mix Lipofectamine 2000 (Thermo Fisher Scientific, Cat. 11668-019) and plasmid, in ratio 1:1, were mixed in Optimem (Gibco, Cat. 11058-021); after 3 h, transfection medium was replaced with complete medium. After 24 or 48 h, cells were used for experiments. A 10 nm ER-mitochondrial linker, which fixes the ER-mitochondrial distance at 10-12 nm, a modification of a 5 nm ER-mitochondrial linker [14], was a kind gift from Drs György Csordás and György Hajnóczky (Thomas Jefferson University). Generation of SPLIt-GFP Contact Sites sensor (SPLICS) was described elsewhere [13,24]

Cell viability assay: Crystal violet is a viability assay that discriminates between alive and dead cells in culture by employing a blue/violet dye exclusively binding to DNA and proteins in well-adherent, viable cells. HeLa and Huh-7 were seeded, respectively at a density of 7.5×103 and 15×103 cell/well, and transfected with 5nm-EML, 20nm-EML and ER-RFP on 96 wells plates. 48h post-transfection, media was removed, and cells were fixed in methanol at 4°C. After incubation for 10-20 minutes with 50 µl/well of crystal violet 0.1%, the dye was carefully removed, and each well was washed with phosphate buffered saline solution (PBS). Then, plates were allowed to dry for 12h, and crystal violet was solubilized in 50 µl/well of acetic acid at 30%. Lastly, absorbance at 595 nm was measured.

Transmission electron microscopy: for transmission electron microscopy (TEM) analysis, following trypsinization 1×10^6 cells were centrifuged at 900

rpm for 5 min and then fixed with 2.5% glutaraldehyde in culture medium, for 2 h at room temperature. The pellet was then rinsed in PBS, post-fixed in 1% aqueous OsO4 for 2 h at room temperature and rinsed in H_2O. Cells were pre-embedded in 2% agarose in water, dehydrated in a graded acetone scale and then embedded in epoxy resin (Electron Microscopy Sciences, EM-bed812). Ultrathin sections (60–80 nm) were cut on a Reichert OM-U3 ultramicrotome, collected on nickel grids and then stained with uranyl acetate and lead citrate. The specimens were observed with a JEM 1200 EX II (JEOL, Peabody, MA, USA) electron microscope operating at 100 kV and equipped with a MegaView G2 CCD camera (Olympus OSIS, Tokyo, Japan). Images were analysed with Fiji ImageJ 1.52p software.

Western Blot. 48h post transfection, cells were lysed with lysis buffer (50mM Tris-HCl (pH 7.4), sodium dodecyl sulphate (SDS) 0.5%, 5mM EDTA, complemented with protease inhibitors cocktail (PIC, Millipore, Cat. 539133) and phosphatase inhibitor cocktail (Thermo Fisher Scientific, Cat. 78428) and collected in a 1.5 ml tube. Lysates were quantified with QuantiPro BCA Assay Kit (Sigma, Cat. SLBF3463). 20 - 40 µg (according to the relative abundance of the protein of interest) of proteins were mixed with the right amount of Laemmli Sample Buffer 4X (Bio-Rad), and boiled. Then samples were loaded on a 6-12% polyacrylamide-sodium dodecyl sulphate gel for SDS-PAGE. Proteins were transferred onto nitrocellulose membrane, using Mini Transfer Packs or Midi Transfer Packs, with Trans-Blot® Turbo ™ (Bio-Rad) according to manufacturer's instructions (Bio-Rad). The membranes were blocked in 5% skim milk (Sigma, Cat. 70166) for 45' at room temperature. Subsequently membranes were incubated with indicated primary antibody, overnight at 4°C. Primary antibodies used are listed in Table 1, anti- β-Actin was used to normalize protein loading.

Primary antibody protein/modification target	Animal specificity	Dilution	Catalog n°	Supplier
Anti-IP$_3$R1	Rabbit	1:500	AB108517	Abcam
Anti-Grp75	Rabbit	1:500	14887-1-AP	Proteintech
Anti-VDAC1	Mouse	1:1000	AB14734	Abcam
Anti-Mfn1	Rabbit	1:200	SC-50330	Santa Cruz Biotechnology
Anti-Mfn2	Rabbit	1:100	SC-515647	Santa Cruz Biotechnology
Anti-Drp1	Rabbit	1:1000	AB-83896	Immunological Sciences
Anti-p-Drp1 (Ser637)	Rabbit	1:500	ABP-0812	Immunological Sciences
Anti-β-actin	Mouse	1:2000	A1978	Sigma Aldrich

Table2. Complete list of primary antibodies employed for western blot analysis.

Goat anti-mouse IgG (H+L) horseradish peroxidase-conjugated secondary antibody (Bio-Rad, 1:5000; Cat. 170-6516,) and Goat anti-rabbit Igg (H+L) horseradish peroxidase-conjugated secondary antibody (Bio-Rad, 1:5000; Cat. 170-6515,) were used as secondary antibodies. Detection was carried out with SuperSignal™ West Pico/femto PLUS Chemiluminescent Substrate (Thermo Scientific), based on the chemiluminescence of luminol and developed using ChemiDoc™ Imaging System (Bio-Rad).

Time-lapse ratiometric fluorescent imaging: Imaging of Fura-2, GAP3, 4mtD3cpv, ROMO-GemGeCO and MICU-GemGeCO Ca2+ probes was

performed using an epifluorescent Leica DMI6000B microscope equipped with an S Fluor 40×/1.3 objective, a Polychrome V monochromator (Till Photonics, Munich, Germany), a Photometrics DV2 dual imager (Teledyne Photometrics, Tucson, US). For imaging of mitochondria, an internal lens with a 1.6 optical increment was used. Images were acquired by a Hamamatsu cooled CCD camera (Hamamatsu Photonics, Hamamatsu City, Japan) and registered using MetaFluor software (Molecular Devices, Sunnyvale, CA, USA). Microsoft excel and GraphPad Prism were used for offline analysis and figure preparation.

Mitochondria Ca2+ imaging: mitochondrial Ca2+ dynamics was monitored with 4mtD3cpv-plasmids (referred to as D3-plasmid), a genetically encoded Ca2+ indicator belonging to the class of cameleons, in which Ca2+-responsive elements, such as calmodulin, alter the efficiency of fluorescence resonance energy transfer (FRET) between two fluorescent proteins[16]. 48h post transfection, expression of mitD3 was checked and mitochondrial matrix calcium dynamics were monitored. Coverslips were washed with KRB solution (125 mM NaCl, 5 mM KCl, 1 mM Na3PO4, 1 mM MgSO4, 5.5 mM glucose, 20 mM HEPES, pH 7.4) and transferred to a suitable imaging the acquisition chamber and mounted on the stage of the microscope. Samples were illuminated at 420nm and simultaneously acquired at 475nm (donor, ECFP) and 530nm (acceptor, circularly permuted (cp) Venus). CpVenus/ECFP ratio was calculated online using MetaFluor software. After acquisition of a basal Ca2+ levels (first 30s of acquisition), and the cells were stimulated subsequently with 100 μM ATP. Imaging was performed using a Leica epifluorescence microscope equipped with a S Fluor 40×/1.3 objective. Regions of interest (ROIs) were defined around individual mitochondria to measure changes in fluorescence intensity representing Ca2+ transients.

Fura-2 Ca2+ imaging: cells were plated onto 24 mm round coverslips (3x104 cell/coverslip), and loaded with 2.5 μM Fura-2/AM (Cat. No. F1201, Life Technologies, Milan, Italy) in the presence of 0.005% Pluronic F-127 (Cat. No. P6867, Life Technologies) and 10 μM sulfinpyrazone (Cat. S9509, Sigma) in KRB solution. After loading (30 min in the dark) cells were washed once with KRB solution and allowed to de-esterify for 30 min. After this, the coverslips were mounted in an acquisition chamber and placed on the stage of the microscope and cells were alternately excited at 340 and 380 nm ; the fluorescent signal was collected through a bandpass 510/20 nm filter. The cells were stimulated with 100 μM ATP, to detect cytosolic Ca2+. Baseline values are expressed as mean±SEM of 340/380 Fura-2 ratio values (referred to as Fura ratio). For comparison of Ca2+ dynamics, measured as an amplitude of Ca2+ increase from the baseline level, Fura-2 ratio values were normalized using formula (Fi-F0)/F0 (referred to as Normalized (Norm.) Fura Ratio).

Endoplasmic reticulum Ca2+ imaging. ER Ca2+ dynamics was monitored with ER-GAP3, a genetically encoded Ca2+ sensor, targeted to the ER lumen (referred to as GAP3) [17]. 48h post transfection, expression of GAP3 was checked and ER calcium dynamics were monitored. Coverslips were mounted in a chamber in KRB solution and placed on the stage of the microscope. Cells were alternately excited at 405 and 470 nm, and the fluorescent signal acquired using 510/20 nm bandpass filter. After recording basal signal for 30 s, KRB solution was removed and replaced with a Ca2+-free solution (KRB + 500 μM EGTA). After allowing the signal to stabilize for additional 30 s, cells were stimulated with 100 μM ATP and 50 μM Tert-butylhydroquinone (tBHQ), and the response was recorded for 300 s.

Mitochondrial inter membrane space Ca2+ imaging: Ca2+ dynamics in the space between the two mitochondrial membrane (MIMS) was monitored with ROMO-GemGeCO (referred to as ROMO), a genetically encoded Ca2+ indicator localized to the cristae lumen space[18]. 48h post transfection, expression of ROMO was checked and mitochondrial matrix calcium dynamics were monitored. Coverslips were washed with KRB solution and transferred to the acquisition chamber and mounted on the stage of the microscope. Samples were illuminated at 420 nm using and simultaneously acquired at 475 nm and 530 nm. 530/475 nm ratio was calculated online using MetaFluor software. After acquisition of a basal Ca2+ levels (first 30s of acquisition), and the cells were stimulated subsequently with 100 μM ATP. Regions of interest (ROIs) were defined around individual mitochondria to measure changes in fluorescence intensity representing Ca2+ transients.

Pharmacological treatment. Drugs used in this work are reported and described in Table 2.

Drug name	Solvent	Worck concentration	Catalog n°	Supplier
Absintin	DMSO	10μM	n.d.	Kindly gift of prof. F. Pollasto
ESI09	DMSO	10μM	SML0814	Sigma Aldrich
H89	DMSO	10μM	B1427	Sigma Aldrich

3HDC	DMSO	10μM	n.d.	Kindly gift of prof. F. Pollasto
Isoproterenol	H2O	100μM	420355	Sigma Aldrich

Table3. Complete list of compounds employed in this work.

Immunofluorescence. Cells, transfect or not according to the experimental design, were grown on 13 mm glass coverslips, were fixed with 4% formaldehyde, permeabilized (7 min in 0.1% Triton X-100 in phosphate-buffered saline (PBS)), blocked in 1% gelatine, and immunoprobed with an appropriate primary antibody (diluted in PBS supplemented with 1% gelatine) over night at 4°C. After 3 times washing in PBS, an Alexa-conjugated secondary antibody (1:300 in PBS supplemented with 1% gelatine) was applied for 1 h at room temperature (RT). The following primary antibodies were used: anti-IP3R (rabbit, 1:500, Abcam, Cat. AB108517), anti-Flag (rabbit, 1:500, Millipore, Cat. F7425), anti-Htas46 (rabbit, 1:500, Thermo Fisher, Cat. OSR00173W). Secondary antibodies were as follows: Alexa Fluor 488 anti-mouse IgG, Alexa Fluor 555 anti-rabbit IgG (all secondary antibodies were from Molecular Probes, Life Technologies, Monza, Italy). Nuclei were counter-stained with 4′,6-diamidino-2-phenylindole (DAPI). Images were acquired by Zeiss 710 confocal laser scanning microscope equipped with EC Plan-Neofluar 40×/1.30 Oil DIC M27 objective and Zen software or with a Leica SP8 LSCM equipped with a white light laser, and HCX PL APO 40X/1.25-075 OIL CL objective and LAS X software.

Proximity ligation assay (PLA). 17500 cells/well were plated in 8 wells chamber (IBIDI, Cat: 80806) and transfected with ER-RFP, 5nm-EML, 10nm-eml and 20nm-eml. After 40h PLA was performed according to datasheet and Paper[21]. Briefly, Cells were fixed in 4% paraformaldehyde, and incubated with

191

primary antibodies anti-IP3R (1:500) and anti-VDAC (1:100) for 16h at 4°C. Duolink PLA probe incubation, according to the primary antibody species, was carried on for 1h at 37°C, and then the development of the signal was obtained by Duolink green fluorescence detection reagent by ligation and amplification reactions. Duolink in situ mounting media with Dapi was used to stain nuclei and mount. Images were acquired by Zeiss 710 laser scanning confocal microscope (LSCM) equipped with EC Plan-Neofluar 40×/1.30 Oil DIC M27 objective and Zen software. Images were acquired under non-saturating conditions and analysed with Fiji ImageJ 1.52p software. Fluorescence was measured for the entire cell area (CTCF) = Integrated Density — (Area of selected cell X Mean background fluorescence).

Generation of stable lines expressing ER-RFP and 20nm-EML. To perform isolation of MERCS enriched cellular fraction, stable line expressing ER-RFP and 20nm-EML, were generated. The details of generation of production of lentiviral vectors expressing ER-RFP and 20nm-EML is described elsewhere [37]. 24 hours after plating (10E4 cell/well in 24 well plate), Hela cells were infected with lentiviral particles expressing ER-RFP and 20nm-EML at MOI from 5 to 20. The dilution of virus that gave more than 50% of infected cells, as was detected by fluorescence of reporter proteins, were further processed. Upon reaching confluence, the cells were expanded, and ER-RFP and 20nm-EML expressing cells were enriched using fluorescence-activated cell sorting (S3e Cell Sorter, Bio-Rad, Segrate, Milano). Sorted cells were expanded and frozen until needed.

MERCS enriched fraction isolation. Hela stably expressing ER-RFP and 20nm-EML were plated at concentration of 0.5 x10^6 cells/dish in 10 cm Petri dishes (50 dishes per line). 48h later cells the cells were washed twice with

PBS, detached with trypsin, and then collected in 50ml centrifuge tube. Cells were pelleted, and the pellets were processes according to the protocol described elsewhere[22], using an Eppendorf CR30NX ultracentrifuge equipped with a R25ST rotor.

Immunoprecipitation (IP): Cell lysates in Co-IP buffer containing 50 mM Tris HCl, 75 mM NaCl, 0,5%NP-40 plus protease and phosphatase inhibitors were quantified by BCA and 1,5 mg of proteins in each sample were subjected to IP with or without anti-GFP. Briefly, sepharose beads (sc-2003; Santa-Crutz) were incubated with or without anti-GFP antibodies 1,5 h at 4°C, Anti-GFP-beads were incubated with cell lysates o/n at 4°C and LMSB elution was performed. Wash buffer containing 50mM trisHCl, 150mM NaCl and Tween20 0,5% was used for washes. WB analysis of IP samples was done loading ½ of total IP samples.

Pericytes/EC/astrocyte co-culture. For tubulogenesis assay, a Matrigel synthetic extracellular matrix (Corning, Cat. 356234) was used. 96 well plates were coated with 50 µl of Matrigel, gelatinized at 37°C for 30 min. Pericytes, EA.hy926 and WT-iAstro or 3Tg-iAstro cells, in ratio 1:1:1 were resuspended in 100 µl of complete DMEM and plate on the matrix at the density of 1×10^4 cells/well, and incubated for 8 h. Phase contrast images were acquired with a Zeiss 710 confocal laser scanning microscope.

SUnSET for assessment of protein synthesis. Global protein synthesis rate was assessed using the Surface Sensing of Translation (SUnSET) method, as previously published [38]. Briefly, cells were incubated with 4 µM puromycin dihydrochloride (Sigma, Cat. P8833) supplemented in normal medium at 37 °C with 5% CO_2 for 1 h. Subsequently, cell lysates were lysate for western blot analysis [27,39].

BIBBLIOGRAPY

(1) Barazzuol, L.; Giamogante, F.; Calì, T. Mitochondria Associated Membranes (MAMs): Architecture and Physiopathological Role. *Cell Calcium* **2021**, *94*, 102343. https://doi.org/10.1016/j.ceca.2020.102343.

(2) Aoyama-Ishiwatari, S.; Hirabayashi, Y. Endoplasmic Reticulum-Mitochondria Contact Sites-Emerging Intracellular Signaling Hubs. *Front. Cell Dev. Biol.* **2021**, *9*, 653828. https://doi.org/10.3389/fcell.2021.653828.

(3) Kornmann, B.; Currie, E.; Collins, S. R.; Schuldiner, M.; Nunnari, J.; Weissman, J. S.; Walter, P. An ER-Mitochondria Tethering Complex Revealed by a Synthetic Biology Screen. *Science* **2009**, *325* (5939), 477–481. https://doi.org/10.1126/science.1175088.

(4) Naón, D.; Hernández-Alvarez, M. I.; Shinjo, S.; Wieczor, M.; Ivanova, S.; Martins de Brito, O.; Quintana, A.; Hidalgo, J.; Palacín, M.; Aparicio, P.; Castellanos, J.; Lores, L.; Sebastián, D.; Fernández-Veledo, S.; Vendrell, J.; Joven, J.; Orozco, M.; Zorzano, A.; Scorrano, L. Splice Variants of Mitofusin 2 Shape the Endoplasmic Reticulum and Tether It to Mitochondria. *Science* **2023**, *380* (6651), eadh9351. https://doi.org/10.1126/science.adh9351.

(5) Herrera-Cruz, M. S.; Simmen, T. Over Six Decades of Discovery and Characterization of the Architecture at Mitochondria-Associated Membranes (MAMs). *Adv. Exp. Med. Biol.* **2017**, *997*, 13–31. https://doi.org/10.1007/978-981-10-4567-7_2.

(6) Rossi, A.; Pizzo, P.; Filadi, R. Calcium, Mitochondria and Cell Metabolism: A Functional Triangle in Bioenergetics. *Biochim. Biophys. Acta BBA - Mol. Cell Res.* **2019**, *1866* (7), 1068–1078. https://doi.org/10.1016/j.bbamcr.2018.10.016.

(7) Feno, S.; Rizzuto, R.; Raffaello, A.; Vecellio Reane, D. The Molecular Complexity of the Mitochondrial Calcium Uniporter. *Cell Calcium* **2021**, *93*, 102322. https://doi.org/10.1016/j.ceca.2020.102322.

(8) Szabadkai, G.; Bianchi, K.; Várnai, P.; De Stefani, D.; Wieckowski, M. R.; Cavagna, D.; Nagy, A. I.; Balla, T.; Rizzuto, R. Chaperone-Mediated Coupling of Endoplasmic Reticulum and Mitochondrial Ca2+ Channels. *J. Cell Biol.* **2006**, *175* (6), 901–911. https://doi.org/10.1083/jcb.200608073.

(9) Prole, D. L.; Taylor, C. W. Inositol 1,4,5-Trisphosphate Receptors and Their Protein Partners as Signalling Hubs. *J. Physiol.* **2016**, *594* (11), 2849–2866. https://doi.org/10.1113/JP271139.

(10) Giacomello, M.; Pellegrini, L. The Coming of Age of the Mitochondria–ER Contact: A Matter of Thickness. *Cell Death Differ.* **2016**, *23* (9), 1417–1427. https://doi.org/10.1038/cdd.2016.52.

(11) Lim, D.; Dematteis, G.; Tapella, L.; Genazzani, A. A.; Calì, T.; Brini, M.; Verkhratsky, A. Ca2+ Handling at the Mitochondria-ER Contact Sites in Neurodegeneration. *Cell Calcium* **2021**, *98*, 102453. https://doi.org/10.1016/j.ceca.2021.102453.

(12) Csordás, G.; Várnai, P.; Golenár, T.; Roy, S.; Purkins, G.; Schneider, T. G.; Balla, T.; Hajnóczky, G. Imaging Interorganelle Contacts and Local Calcium Dynamics at the ER-Mitochondrial Interface. *Mol. Cell* **2010**, *39* (1), 121–132. https://doi.org/10.1016/j.molcel.2010.06.029.

(13) Vallese, F.; Catoni, C.; Cieri, D.; Barazzuol, L.; Ramirez, O.; Calore, V.; Bonora, M.; Giamogante, F.; Pinton, P.; Brini, M.; Calì, T. An Expanded Palette of Improved SPLICS Reporters Detects Multiple Organelle Contacts in Vitro and in Vivo. *Nat. Commun.* **2020**, *11* (1), 6069. https://doi.org/10.1038/s41467-020-19892-6.

(14) Csordás, G.; Renken, C.; Várnai, P.; Walter, L.; Weaver, D.; Buttle, K. F.; Balla, T.; Mannella, C. A.; Hajnóczky, G. Structural and Functional Features and Significance of the Physical Linkage between ER and Mitochondria. *J. Cell Biol.* **2006**, *174* (7), 915–921. https://doi.org/10.1083/jcb.200604016.

(15) Barnes, C. A.; Shen, Y.; Ying, J.; Takagi, Y.; Torchia, D. A.; Sellers, J. R.; Bax, A. Remarkable Rigidity of the Single α-Helical Domain of Myosin-VI As Revealed by NMR Spectroscopy. *J. Am. Chem. Soc.* **2019**, *141* (22), 9004–9017. https://doi.org/10.1021/jacs.9b03116.

(16) Miyawaki, A.; Llopis, J.; Heim, R.; McCaffery, J. M.; Adams, J. A.; Ikura, M.; Tsien, R. Y. Fluorescent Indicators for Ca2+ based on Green Fluorescent Proteins and Calmodulin. *Nature* **1997**, *388* (6645), 882–887. https://doi.org/10.1038/42264.

(17) Alonso, M. T.; Rojo-Ruiz, J.; Navas-Navarro, P.; Rodríguez-Prados, M.; García-Sancho, J. Measuring Ca 2+ inside Intracellular Organelles with Luminescent and Fluorescent Aequorin-Based Sensors. *Biochim. Biophys. Acta BBA - Mol. Cell Res.* **2017**, *1864* (6), 894–899. https://doi.org/10.1016/j.bbamcr.2016.12.003.

(18) Waldeck-Weiermair, M.; Gottschalk, B.; Madreiter-Sokolowski, C. T.; Ramadani-Muja, J.; Ziomek, G.; Klec, C.; Burgstaller, S.; Bischof, H.; Depaoli, M. R.; Eroglu, E.; Malli, R.; Graier, W. F. Development and

Application of Sub-Mitochondrial Targeted Ca2 + Biosensors. *Front. Cell. Neurosci.* **2019**, *13*, 449. https://doi.org/10.3389/fncel.2019.00449.

(19) Rizzuto, R.; Brini, M.; Murgia, M.; Pozzan, T. Microdomains with High Ca2+ Close to IP3-Sensitive Channels That Are Sensed by Neighboring Mitochondria. *Science* **1993**, *262* (5134), 744–747. https://doi.org/10.1126/science.8235595.

(20) Rizzuto, R.; Pinton, P.; Carrington, W.; Fay, F. S.; Fogarty, K. E.; Lifshitz, L. M.; Tuft, R. A.; Pozzan, T. Close Contacts with the Endoplasmic Reticulum as Determinants of Mitochondrial Ca2+ Responses. *Science* **1998**, *280* (5370), 1763–1766. https://doi.org/10.1126/science.280.5370.1763.

(21) Alam, M. S. Proximity Ligation Assay (PLA)Proximity Ligation Assay (PLA). In *Immunohistochemistry and Immunocytochemistry: Methods and Protocols*; Del Valle, L., Ed.; Methods in Molecular Biology; Springer US: New York, NY, 2022; pp 191–201. https://doi.org/10.1007/978-1-0716-1948-3_13.

(22) Wieckowski, M. R.; Giorgi, C.; Lebiedzinska, M.; Duszynski, J.; Pinton, P. Isolation of Mitochondria-Associated Membranes and Mitochondria from Animal Tissues and Cells. *Nat. Protoc.* **2009**, *4* (11), 1582–1590. https://doi.org/10.1038/nprot.2009.151.

(23) Thillaiappan, N. B.; Chavda, A. P.; Tovey, S. C.; Prole, D. L.; Taylor, C. W. Ca2+ Signals Initiate at Immobile IP3 Receptors Adjacent to ER-Plasma Membrane Junctions. *Nat. Commun.* **2017**, *8* (1), 1505. https://doi.org/10.1038/s41467-017-01644-8.

(24) Cieri, D.; Vicario, M.; Giacomello, M.; Vallese, F.; Filadi, R.; Wagner, T.; Pozzan, T.; Pizzo, P.; Scorrano, L.; Brini, M.; Calì, T. SPLICS: A Split Green Fluorescent Protein-Based Contact Site Sensor for Narrow and Wide Heterotypic Organelle Juxtaposition. *Cell Death Differ.* **2018**, *25* (6), 1131–1145. https://doi.org/10.1038/s41418-017-0033-z.

(25) Talmon, M.; Rossi, S.; Lim, D.; Pollastro, F.; Palattella, G.; Ruffinatti, F. A.; Marotta, P.; Boldorini, R.; Genazzani, A. A.; Fresu, L. G. Absinthin, an Agonist of the Bitter Taste Receptor hTAS2R46, Uncovers an ER-to-Mitochondria Ca2+–Shuttling Event. *J. Biol. Chem.* **2019**, *294* (33), 12472–12482. https://doi.org/10.1074/jbc.RA119.007763.

(26) Brockhoff, A.; Behrens, M.; Roudnitzky, N.; Appendino, G.; Avonto, C.; Meyerhof, W. Receptor Agonism and Antagonism of Dietary Bitter Compounds. *J. Neurosci.* **2011**, *31* (41), 14775–14782. https://doi.org/10.1523/JNEUROSCI.2923-11.2011.

(27) Dematteis, G.; Vydmantaitė, G.; Ruffinatti, F. A.; Chahin, M.; Farruggio, S.; Barberis, E.; Ferrari, E.; Marengo, E.; Distasi, C.; Morkūnienė, R.; Genazzani, A. A.; Grilli, M.; Grossini, E.; Corazzari, M.; Manfredi, M.;

Lim, D.; Jekabsone, A.; Tapella, L. Proteomic Analysis Links Alterations of Bioenergetics, Mitochondria-ER Interactions and Proteostasis in Hippocampal Astrocytes from 3xTg-AD Mice. *Cell Death Dis.* **2020**, *11* (8), 645. https://doi.org/10.1038/s41419-020-02911-1.

(28) Tapella, L.; Dematteis, G.; Moro, M.; Pistolato, B.; Tonelli, E.; Vanella, V. V.; Giustina, D.; Forgia, A. L.; Restelli, E.; Barberis, E.; Villani, S.; Grosso, E. D.; Grilli, M.; Manfredi, M.; Corazzari, M.; Grolla, A. A.; Genazzani, A. A.; Lim, D. Protein Synthesis Inhibition and Loss of Homeostatic Functions in Astrocytes from an Alzheimer's Disease Mouse Model: A Role for ER-Mitochondria Interaction. bioRxiv March 27, 2022, p 2022.03.24.485644. https://doi.org/10.1101/2022.03.24.485644.

(29) Serysheva, I. I. Toward a High-Resolution Structure of IP₃R Channel. *Cell Calcium* **2014**, *56* (3), 125–132. https://doi.org/10.1016/j.ceca.2014.08.002.

(30) Wang, P.; Liu, Z.; Chen, H.; Ye, N.; Cheng, X.; Zhou, J. Exchange Proteins Directly Activated by cAMP (EPACs): Emerging Therapeutic Targets. *Bioorg. Med. Chem. Lett.* **2017**, *27* (8), 1633–1639. https://doi.org/10.1016/j.bmcl.2017.02.065.

(31) Rocchio, F.; Tapella, L.; Manfredi, M.; Chisari, M.; Ronco, F.; Ruffinatti, F. A.; Conte, E.; Canonico, P. L.; Sortino, M. A.; Grilli, M.; Marengo, E.; Genazzani, A. A.; Lim, D. Gene Expression, Proteome and Calcium Signaling Alterations in Immortalized Hippocampal Astrocytes from an Alzheimer's Disease Mouse Model. *Cell Death Dis.* **2019**, *10* (1), 1–18. https://doi.org/10.1038/s41419-018-1264-8.

(32) Lim, D.; Rodríguez-Arellano, J. J.; Parpura, V.; Zorec, R.; Zeidán-Chuliá, F.; Genazzani, A. A.; Verkhratsky, A. Calcium Signalling Toolkits in Astrocytes and Spatio-Temporal Progression of Alzheimer's Disease. *Curr. Alzheimer Res.* **2016**, *13* (4), 359–369. https://doi.org/10.2174/1567205013666151116130104.

(33) Preman, P.; Alfonso-Triguero, M.; Alberdi, E.; Verkhratsky, A.; Arranz, A. M. Astrocytes in Alzheimer's Disease: Pathological Significance and Molecular Pathways. *Cells* **2021**, *10* (3), 540. https://doi.org/10.3390/cells10030540.

(34) Palmer, A. E.; Giacomello, M.; Kortemme, T.; Hires, S. A.; Lev-Ram, V.; Baker, D.; Tsien, R. Y. Ca2+ Indicators Based on Computationally Redesigned Calmodulin-Peptide Pairs. *Chem. Biol.* **2006**, *13* (5), 521–530. https://doi.org/10.1016/j.chembiol.2006.03.007.

(35) Tang, Y.; Hu, L. A.; Miller, W. E.; Ringstad, N.; Hall, R. A.; Pitcher, J. A.; DeCamilli, P.; Lefkowitz, R. J. Identification of the Endophilins (SH3p4/P8/P13) as Novel Binding Partners for the Beta1-Adrenergic

Receptor. *Proc. Natl. Acad. Sci. U. S. A.* **1999**, *96* (22), 12559–12564. https://doi.org/10.1073/pnas.96.22.12559.

(36) Matz, M. V.; Fradkov, A. F.; Labas, Y. A.; Savitsky, A. P.; Zaraisky, A. G.; Markelov, M. L.; Lukyanov, S. A. Fluorescent Proteins from Nonbioluminescent Anthozoa Species. *Nat. Biotechnol.* **1999**, *17* (10), 969–973. https://doi.org/10.1038/13657.

(37) Lim, D.; Bertoli, A.; Sorgato, M. C.; Moccia, F. Generation and Usage of Aequorin Lentiviral Vectors for Ca(2+) Measurement in Sub-Cellular Compartments of Hard-to-Transfect Cells. *Cell Calcium* **2016**, *59* (5), 228–239. https://doi.org/10.1016/j.ceca.2016.03.001.

(38) Goodman, C. A.; Hornberger, T. A. Measuring Protein Synthesis With SUnSET: A Valid Alternative to Traditional Techniques? *Exerc. Sport Sci. Rev.* **2013**, *41* (2), 107–115. https://doi.org/10.1097/JES.0b013e3182798a95.

(39) Dematteis G.; Restelli E.; Chiesa R.; Aronica E.; Genazzani A. A.; Lim D.; Tapella L. Calcineurin Controls Expression of EAAT1/GLAST in Mouse and Human Cultured Astrocytes through Dynamic Regulation of Protein Synthesis and Degradation. *Int. J. Mol. Sci.* **2020**, *21*, 2213. https://doi.org/10.3390/ijms21062213.
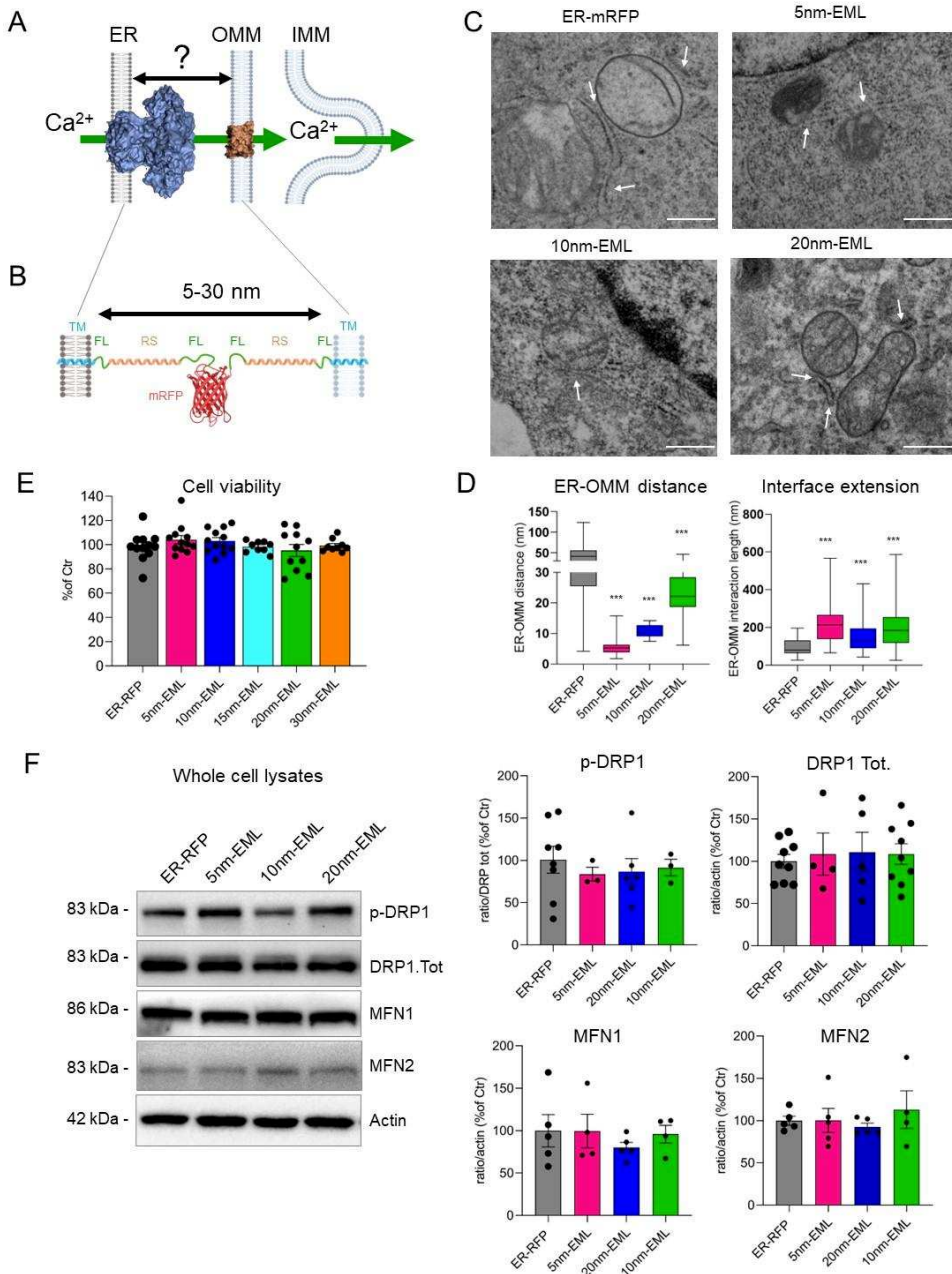
Figure1. design and characterization of ER-Mitochondria linkers (EMLs) pallet. (B) Schematic representation of EMLs structure, in light blue ER and Mit

targeting sequences, are reported, flanked by a flexible region (FL here reported in green), followed by the spacer regions, that via fine modulation of its length can spam the distance from 5 to 30nm (RS in orange); in the middle alle the EMLs present a mRFP in other to visualize their localization and expression. (C) Representative images of cells expressing ER-RFP, 5nm-EML, 10nm-EML and 20nm-EML acquired via electron microscopy; MERCs are indicated with arrows, scale bar = 500nm (D) box plot of ER-OMM distances (ER-RFP: n=162, mean= 43.08nm; 5nm-EML: n=45, mean=5.563nm; 10nm-EML: n=47, mean=10.69nm; 20nm-EML: n=119, mean=21.27nm) and ER-OMM length of interaction (ER-RFP: n=162, mean= 57.18;nm 5nm-EML: n=45, mean=233nm; 10nm-EML: n=47, mean=156nm; 20nm-EML: n=119, mean=200.99nm), measured on electron microscopy images. (E) quantification of cell viability assay in cells expressing our palette of EMLs, data are expressed as % of control (ER-RFP) (ER-RFP: n=12, mean= 98; 5nm-EML: n=12, mean=104; 10nm-EML: n=12, mean=103; 15nm-EML: n=9, mean=99; 20nm-EML: n=12, mean=95.23; 30nm-EML: n=10, mean=99.2). (F) Representative blots and corresponding quantification of the integrated density of protein bands. Protein levels of MFN1 (n=5-6; ER-RFP: mean= 100; 5nm-EML: mean=99; 10nm-EML: mean=95; 20nm-EML: mean=98) and MFN2 (n=5-6; ER-RFP: mean= 100; nm 5nm-EML: mean=101; 10nm-EML: mean=92; 20nm-EML: mean=113), well described ER-Mit tethers, and DRP (n=6; ER-RFP: mean= 100; nm 5nm-EML: mean=99; 10nm-EML: mean=95; 20nm-EML: mean=98) and its phosphorylated form (p-DRP) (n=4-8; ER-RFP: mean= 100; nm 5nm-EML: mean=108; 10nm-EML: mean=110; 20nm-EML: mean=108.9), have been accessed in whole cell lysates 48h upon expression of EMLs. Data are normalized on actin levels and expressed as % of control. Data are reported as mean ± SEM from 3 to 6 independent experiments. *, $p < 0.05$, **, $p < 0.01$ and ***, $p < 0.001$ by one-way ANOVA, Sidak's multiple comparison.
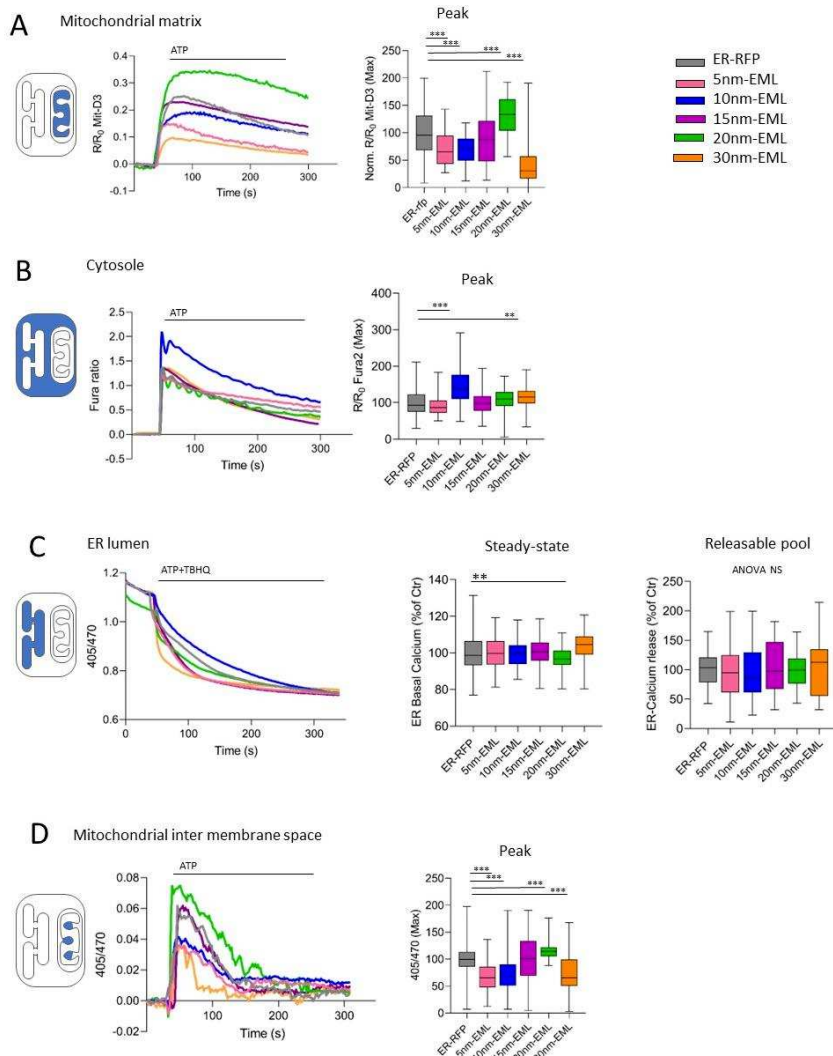
Figure2. 20nm is the optimal distance for efficient ER-Mit Ca^{2+} transfer.
(A) Representative curves of mitochondrial matrix Ca^{2+} uptake, upon ATP
100μM stimulation, and box plot of the peak of the response, in Hela cells
expressing EMLs   (ER-RFP: n=132, mean=100; 5nm-EML: n=88,
mean=69.49; 10nm-EML: n=92, mean=70.59; 15nm-EML: n=110,
mean=92.7; 20nm-EML: n=104, mean=130.4; 30nm-EML: n=150,
mean=42.94). (B) Representative curves of cytosolic Ca^{2+} uptake, upon ATP
100μM stimulation, and box plot of the peak of the response, in Hela cells
expressing EMLs   (ER-RFP: n=492, mean=100; 5nm-EML: n=168, mean=92.12;

10nm-EML: n=200, mean=143.8; 15nm-EML: n=135, mean=110.7; 20nm-EML: n=437, mean=99.59; 30nm-EML: n=130, mean=116.8). (C) Representative curves of ER Ca^{2+} release, upon ATP 100µM + TBHQ 50 µM stimulation, and box plot of ER basal Ca^{2+} levels (ER-RFP: n=157, mean=100; 5nm-EML: n=154, mean=99.06; 10nm-EML: n=118, mean=99.52; 15nm-EML: n=119, mean=101,6; 20nm-EML: n=155, mean=92.59; 30nm-EML: n=140, mean=101.8) and of the delta of the response (basal-minimum) (ER-RFP: n=157, mean=100; 5nm-EML: n=154, mean=94.06; 10nm-EML: n=118, mean=95.08; 15nm-EML: n=119, mean=104,6; 20nm-EML: n=155, mean=98.59; 30nm-EML: n=140, mean=105.8), in Hela cells expressing EMLs. (D) Representative curves of mitochondrial inter membrane space (MIMS) Ca^{2+} uptake, upon ATP 100µM stimulation, and box plot of the peak of the response, in Hela cells expressing EMLs (ER-RFP: n=212, mean=100; 5nm-EML: n=162, mean=67.55; 10nm-EML: n=131, mean=71.7; 15nm-EML: n=95, mean=100.7; 20nm-EML: n=128, mean=115; 30nm-EML: n=98, mean=74.3). Data are expressed as % of control. Data are reported as mean ± SD from 3 to 6 independent coverslip. *, $p < 0.05$, **, $p < 0.01$ and ***, $p < 0.001$ by one-way ANOVA, Sidak's multiple comparison.
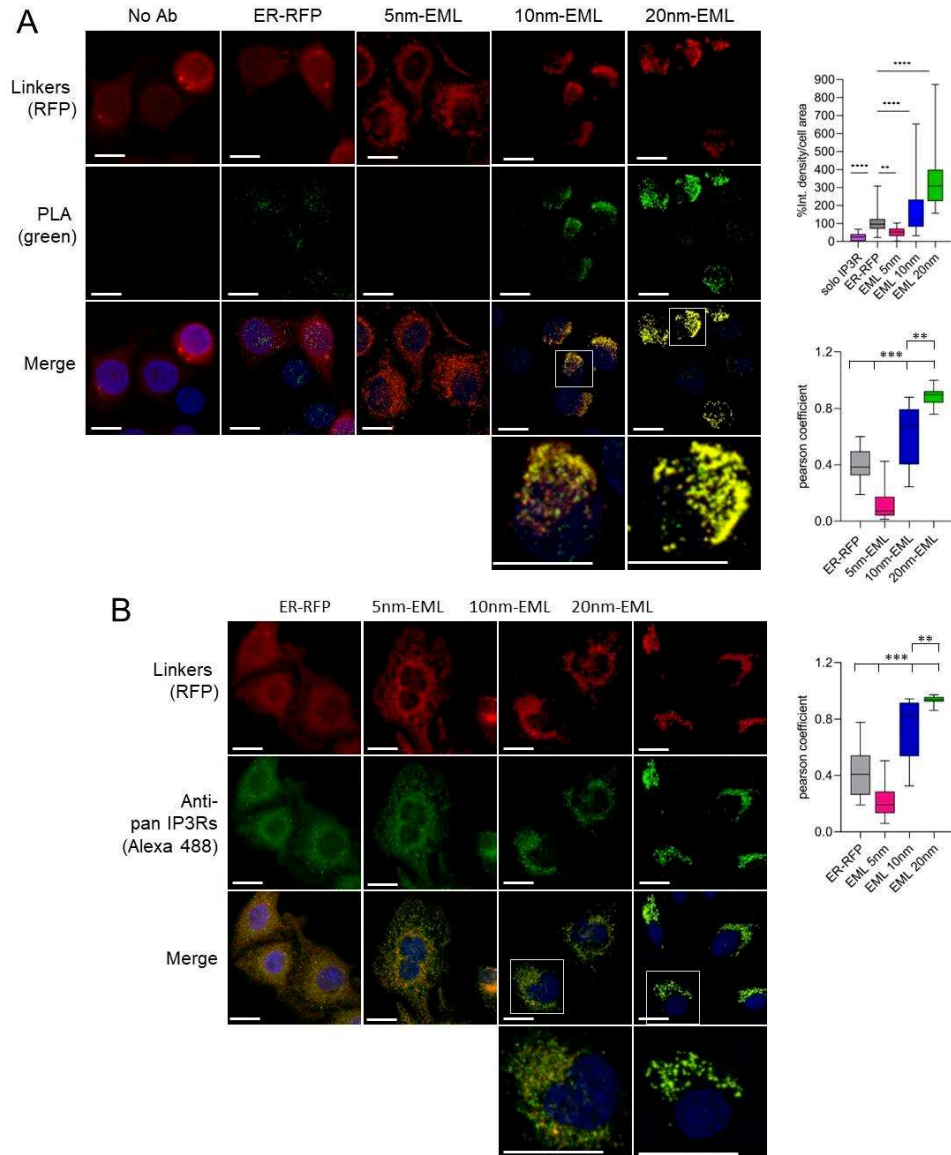
Figure3. EMLs expression modulates IP3R-VDAC1 complexes formation and IP3R localization. (A) representative images of Proximity Ligation Assay (PLA) for IP3R and VDAC1 performed in Hela cells expressing ER-RFP, 5nm-EML, 10nm-EML and 20nm-EML, assay in absence of IP3R antibody have been performed as control of the experiment (No Ab). Intensity of PLA (green) signal has been quantified and expressed as % of integrated density of ER-RFP and normalized on cell area (No Ab: n=73, mean=22.92; ER-RFP: n=106, mean=100; 5nm-EML: n=63, mean=52.23; 10nm-EML: n=54, mean=181.5; 20nm-EML: n=61, mean=336.5). The colocalization

between EMLs signal (red) and PLA one (green) has been evaluated via Pearson-s coefficient measurement (ER-RFP: n=32, mean=0.399; 5nm-EML: n=32, mean=0.112; 10nm-EML: n=30, mean=0,619; 20nm-EML: n=34, mean=0.884). (B) representative images of immunocytochemistry of IP3Rs (green) in Hela cells expressing ER-RFP, 5nm-EML, 10nm-EML and 20nm-EML. The colocalization between EMLs signal (red) and IP3Rs one (green) has been evaluated via Pearson-s coefficient measurement (ER-RFP: n=14, mean=0.433; 5nm-EML: n=10, mean=0.225; 10nm-EML: n=10, mean=0,743; 20nm-EML: n=18, mean=0.937). Data are reported as mean ± SD from 3 to 6 independent coverslips. *, $p < 0.05$, **, $p < 0.01$, ***, $p < 0.001$ and ****, $p<0.0001$ by one-way ANOVA, Sidak's multiple comparison. Scale bar = 20μm.
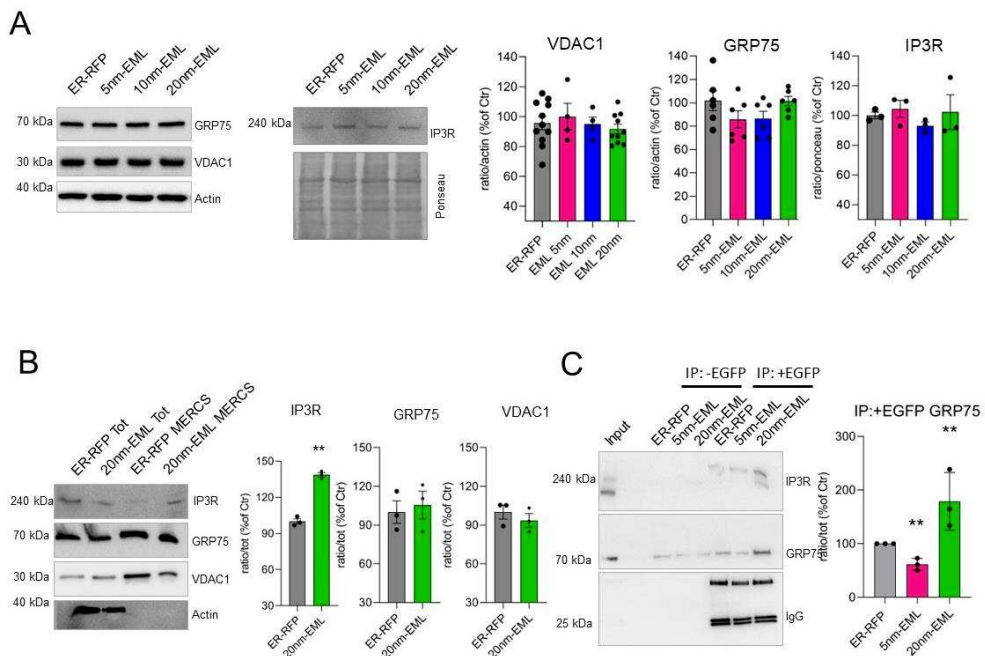

Figure4. IP3R is enriched in 20nm MERCs. (A) Representative blots and corresponding quantification of the integrated density of protein bands. Protein levels of GRP75 (n=6; ER-RFP: mean= 100; nm 5nm-EML: mean=85; 10nm-EML: mean=86; 20nm-EML: mean=101) VDAC1 (n=4-11; ER-RFP: mean= 100; nm 5nm-EML: mean=95; 10nm-EML: mean=96; 20nm-EML: mean=94), and IP3R (n=3; ER-RFP: mean= 100; nm 5nm-EML: mean=104; 10nm-EML: mean=95; 20nm-EML: mean=102) have been accessed in whole cell lysates 48h upon expression of EMLs. Data are normalized on actin levels of ponceux staining and expressed as % of control.

(B) Representative blots and corresponding quantification of the integrated density of protein bands. Protein levels of GRP75 (n=3; ER-RFP: mean= 100; 20nm-EML: mean=105.6) VDAC1 (n=3; ER-RFP: mean= 100; 20nm-EML: mean=93.2), and IP3R (n=3; ER-RFP: mean= 100; 20nm-EML: mean=138.7) have been accessed MERCs cell fraction, obtained from stable Hela cell lines expressing ER-RFP and 20nm-EML. Data are normalized on the corresponding protein level in the total lysate (Tot) and expressed as % of control. (C) Immunoprecipitation of IP3R-EGFP representative blots and quantification. Immunoprecipitation of GRP75 with IP3R has been accessed in ER-RFP, 5nm-EML or 20nm-EML expressing cells, 48h upon transfection (n=3; ER-RFP: mean= 100; nm 5nm-EML: mean=61.28; 20nm-EML: mean=178.9). Data are normalized on the input protein level and expressed as % of control. Data are reported as mean ± SEM from 3 to 6 independent experiments. *, $p < 0.05$, **, $p < 0.01$, ***, $p < 0.001$ and ****, $p<0.0001$ by one-way ANOVA, Sidak's multiple comparison.
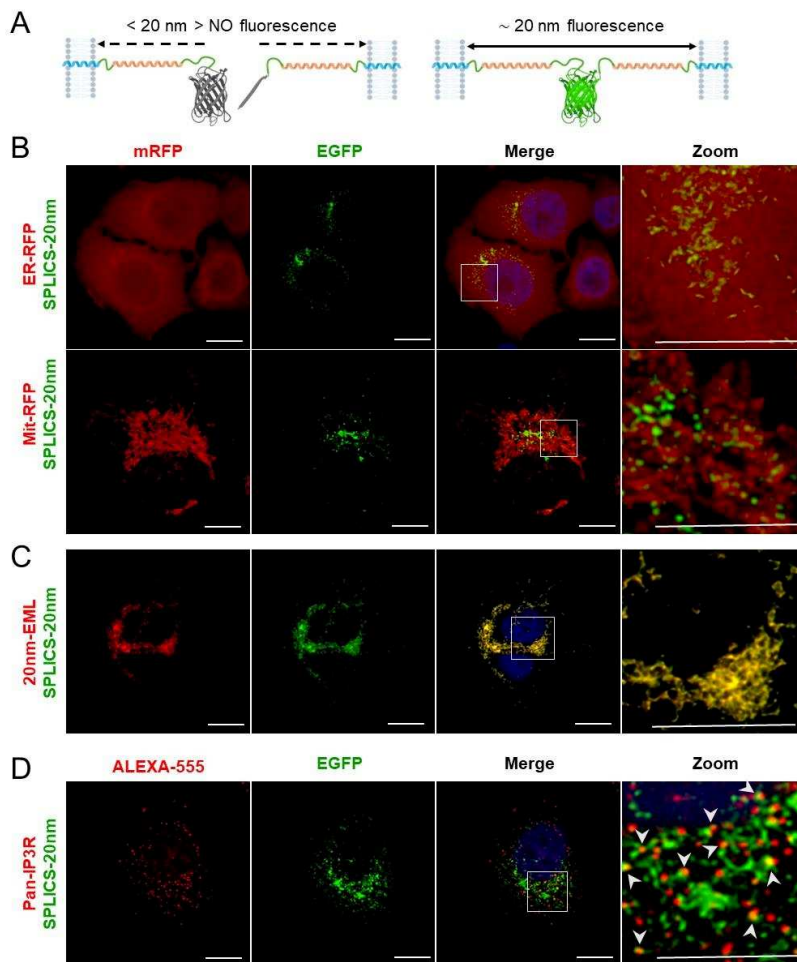
Figure5. characterization of 20nm- Split GFP Contact Sites sensor (SPLICS-20nm). (A) Schematic representation of the structure and of how the sensor works. The sensor is composed by two components, targeted to the two organelles (ER and Mit). In light blue ER and Mit targeting sequences, are reported, flanked by a flexible region (FL here reported in green), followed by the spacer regions (RS in orange) that fix the reconstitution of the GFP signal at 20nm. The RS is flanked by 1-10 GFP or 11GFP, that can reconstitute the GFP signal only when the two components are exactly at 20nm of distance. (B) SPLICS-20nm localization at MERCs has been validated via the co-expression of ER-RFP and Mit-RFP plasmids. (C) SPLIC-20nm ability to reconstruct the GFP signal at 20nm has been confirmed via co-expression of 20nm-EML. (D) representative images of immunocytochemistry for IP3R, in SPLICS-20nm expressing cells. Scale bar = 10μm.

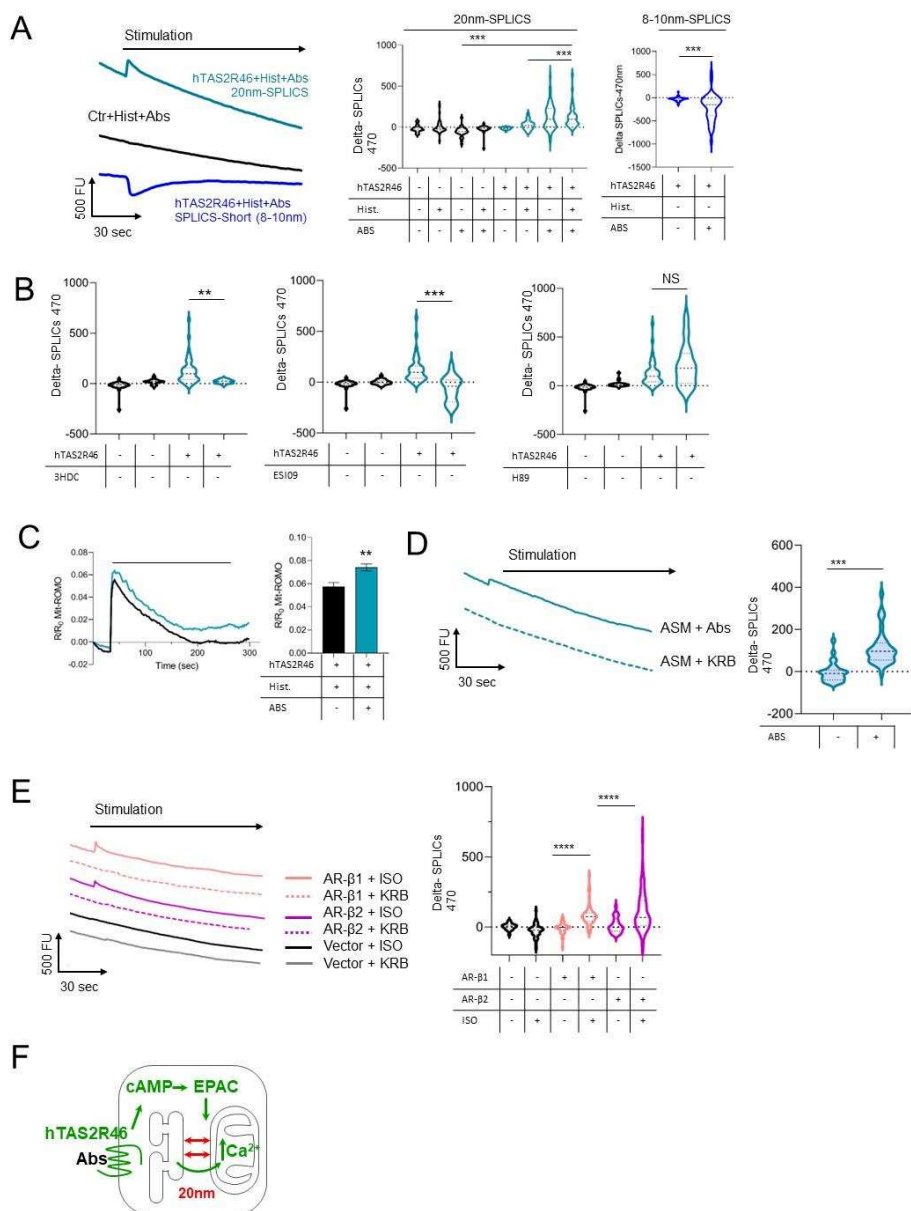**Figure6. 20nm MERCS are dynamically regulated through Gαs→cAMP→EPAC axis.** (A) Representative curves of SPLCS signal (GFP), in Hela cells overexpressing hTAS2R46, and expressing SPLICS-20nm (Light blue) or SPLICS-Short (Blue); in black is reported a representative curve of Hela cells not expressing hTAS2R46. Violin plot of delta of the GFP signal from SPLICS-20nm, upon stimulation with vehicle

(KRB) (-hTAS2R46: n=43, mean=-18.80; +hTAS2R46: n=38, mean=-14.67), absintin (ABS) (-hTAS2R46: n=39, mean=-34.4; + hTAS2R46: n=50, mean=127.5), histamine (Hist) (-hTAS2R46: n=54, mean=-14.4; + hTAS2R46: n=66, mean=-2.34) and both histamine and absintin (-hTAS2R46: n=32, mean=-20.4; +hTAS2R46: n=43, mean=124.2). Violin plot of delta of the GFP signal from SPLICS-short (in blue) upon stimulation with vehicle (n=48, mean=-30.5) or ABS (n=45, mean=-213.1), of Hela cells overexpressing hTAS2R46. (B) Violin plot of ABS induced SPLICS-20nm response in presence of hTAS2R46 inhibitor (3HDC 10µM) (-3HDC: n=43, mean=124.2; +3HDC: n=34, mean=12.08); EPAC inhibitor (ESI09 10µM) (-ESI09: n=44, mean=124; +ESI09: n=32, mean=-60.5) and PKA inhibitor (H89 10µM) (-H89: n=43, mean=124.2; +H89: n=40, mean=209.2). (C) representative curves and histograms of Ca^{2+} dynamics in the MIMS, in cells overexpressing hTAS2R46, stimulated with histamine +/- ABS (-ABS (in black): n=132, mean=0.057; +ABS (in light blue): n=153, mean=0.074). (D) representative curves and violin plot of SPLICS-20nm dynamics in ASM cells in response stimulated with or without ABS (-ABS: n=37, mean=-3,7; +ABS: n=35, mean=111.9). (E) SPLICS-20nm signal has been monitored along stimulation with or without isoproterenol (ISO 100µM) in Hela cells transfected with vector plasmid (in black) (-ISO: n=46, mean=3.15; +ISO: n=62, mean=-14.5), or plasmid encoding for AR-β1 (in pink) (-ISO: n=48, mean=-7.2; +ISO: n=70, mean=81.7) or AR-β2 (in purple) (-ISO: n=45, mean=8.92; +ISO: n=82, mean=112,8). Here are reported representative curves and violin plot of the delta of the response. (F) Schematic representation of the here demonstrated pathway. Data are reported as mean ± SD from 3 to 6 independent coverslips. *, $p < 0.05$, **, $p < 0.01$, ***, $p < 0.001$ and ****, $p<0.0001$ by one-way ANOVA, Sidak's multiple comparison. Scale bar = 20µm.
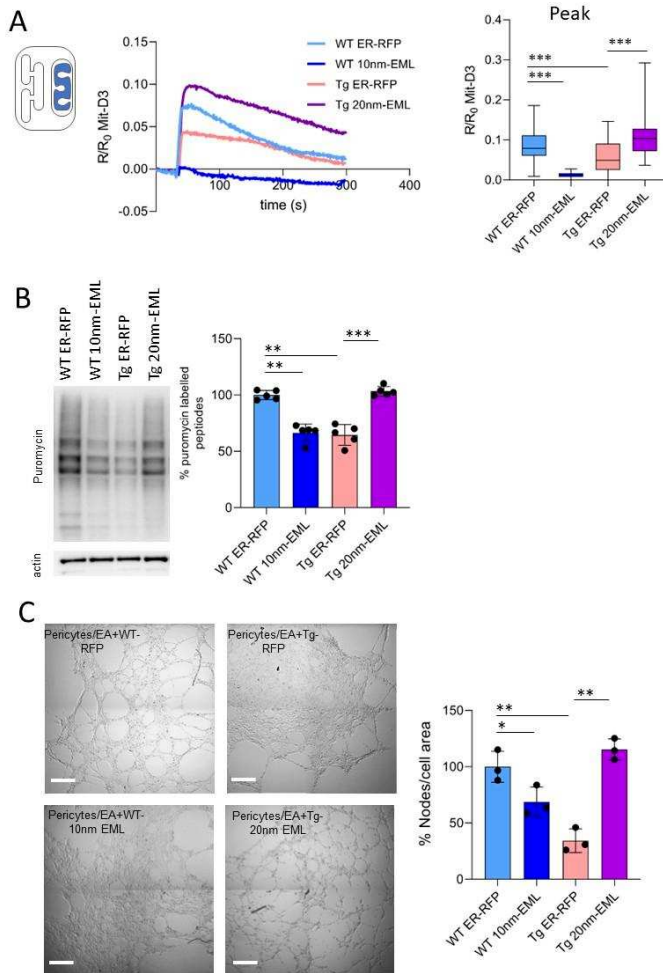
Figure7. EMLs expression impacts on astrocytes function. (A) Representative curves of mitochondrial matrix Ca^{2+} uptake, upon ATP 100μM stimulation, and box plot of the peak of the response, in iAstro cells expressing EMLs (WT ER-RFP: n=58, mean=0.083; WT 10nm-EML: n=52, mean=0.010; Tg ER-RFP: n=59, mean=0.058; Tg 20nm-EML: n=64, mean=0.119). Data are reported as mean ± SD from 4 independent coverslips. ***, $p < 0.001$ by one-way ANOVA, Sidak's multiple comparison. (B) representative WB with anti-puromycin antibody and actin on lysates of iAstro cells treated with 4 μM puromycin (n=5 WT ER-RFP: mean=100; WT 10nm-EML: mean=66.41; Tg ER-RFP: mean=64.60; Tg 20nm-EML: mean=103.4); data are expressed as mean ± SD of 5 independent experiments; ***, $p<0.001$ by one-way ANOVA, Sidak's multiple comparison. Data are normalized on actin levels and

expressed as % of control. (C) Co-culture of pericytes and endothelial cells (EC) with either WT-iAstro ER-RFP (P/EC/WT ER-RFP) or Tg-iAstro ER-RFP (P/EC/Tg ER-RFP) or WT-iAstro expressing 10nm-EML (P/EC/WT EML-10nm) or Tg-iAstro expressing 20nm-EML (P/EC/Tg 20nm-EML) cells on a layer of Matrigel (n=3; WT ER-RFP: mean=100; WT 10nm-EML: mean=68.11; Tg ER-RFP: mean=34.5; Tg 20nm-EML: mean=115.3), scale bar = 500µm. Images were acquired by Zeiss 710 confocal laser scanning microscope, scale bar = 500µm. Data are expressed as mean ± SEM of 3 independent experiments;*, $p < 0.05$, **, $p < 0.01$, ***, $p < 0.001$ by one-way ANOVA, Sidak's multiple comparison.

Chapter 7

DISCUSSION

Calcium (Ca2+) is a pleiotropic intracellular messenger regulating many cellular processes including mitochondrial (Mit) bioenergetics and proteostasis, both altered in Alzheimer's disease (AD). In my PhD project I have studied the cause-effect relationships between calcium dishonesties and cellular dysfunction in astrocytes.

In this context I demonstrated that, the regulation of astrocytic calcium homeostasis is linked to many of the pathological features of AD astrocytes. This dysfunction includes bioenergetic deficit, profound deregulation of cellular proteostasis, including both protein synthesis and degradation, alteration of cellular secretome, and defect of homeostatic support to other cells. In particular, emerged a defect of protein degradation mechanisms related to both autophagic and proteasomal degradation, with strong downregulation of constitutive proteasome components, with consequent increased expression of the component of immune proteasome.

Among all these alterations, I focused my efforts on the alteration of mitochondrial calcium homeostasis, in particular on the discrepancy between deficient mitochondrial calcium uptake and increased interaction between ER and mitochondria, which in principle should augment the juxtaposition of the two membrane e consequently promote ER-mitochondrial calcium transfer. To solve this issue, I undertaken a comprehensive study of the correlation between ER-mitochondria distances and efficiency of calcium transfer. To do this I designed a palette of ER-mitochondria linkers (EMLs), and I discovery that ER-mitochondria calcium transfer is strongly inhibited at the distances of 5 to

10nm, and is strongly potentiated at 20nm, explaining why upon increased ER-mitochondria interaction at 8-10nm, in AD astrocytes, results in reduced mitochondrial calcium uptake.

Then I focused my interest on the characterization of assembly of ER-mitochondria calcium transfer units, composed of IP3R-GRP75-VDAC1, and described an enhanced presence of functional complexes at the distance of 20 nm.

In the third year of my PhD, I characterized a fluorescence reporter for measuring distances between ER and mitochondria at 20nm (SPLICS-20nm). I demonstrated that 20nm distances are dynamically modulated through GPCR→Gαs→cAMP→EPAC axis. The fast dynamics of the report (GFP signal), resembles the GPCR mediated ER-mitochondria calcium transfer. To the best of our knowledge this is the first report of fast dynamic cAMP-mediated response.

To demonstrate the translational potential of modulation of ER-mitochondrial distances I expressed 20nm-EML in AD hippocampal astrocytes, rescuing cell, and non-cell, autonomous AD related dysfunction.

Another aspect of my PhD thesis is the investigation of Calcineurin role in both physiology of astrocytes and AD related astrocytes dysfunction.

In this context, I found that, in astrocytes, both eIF2α-mediated protein synthesis and proteasomal degradation are under control of calcineurin, a Ca2+/calmodulin-activated phosphatase: astrocyte-specific calcineurin deletion disrupts eIF2α-mediated protein synthesis in vitro and, in vivo. This result indicates that, in physiological conditions CaN regulates cellular proteostasis. On the other hand, in and AD mice model, the deletion of

astroglial CaN, at 10 months of age, displayed a protective effect, reducing memory impairment and well described AD hallmarks, aβ plaques deposition and tau hyper-phosphorylation. These results indicate that CaN, under pathological conditions can drive and regulate pathology progression. In a wider prospective, our findings points out astroglial cells as crucial regulators of CNS pathology.

Taken together I've investigated two important aspects of calcium signaling dysfunction in AD astrocytes. Namely, the deregulation of ER-mitochondria calcium transfer in relation to ER-mitochondria interaction; and dysfunction of calcineurin signaling in AD astrocytes.

My results demonstrated that both ER-mitochondria interaction and calcineurin represents promising therapeutic targets to mitigate AD related astroglial pathophysiology, given the importance of astrocytes for brain functions further studies are warranted to elucidate mechanisms of these dysfunctions.

Chapter 8

LIST OF PUBBLICATIONS

1. Tapella, L.; **Dematteis, G.*;** Moro, M.; Pistolato, B.; Tonelli, E.; Vanella, V.V.; Giustina, D.; Forgia, A.L.; Restelli, E.; Barberis, E.; et al. Protein Synthesis Inhibition and Loss of Homeostatic Functions in Astrocytes from an Alzheimer's Disease Mouse Model: A Role for ER-Mitochondria Interaction. 2022, 2022.03.24.485644.

2. Tapella, L.; **Dematteis, G.*;** Ruffinatti, F.A.; Ponzoni, L.; Fiordaliso, F.; Corbelli, A.; Albanese, E.; Pistolato, B.; Pagano, J.; Barberis, E.; et al. Deletion of Calcineurin from Astrocytes Reproduces Proteome Signature of Alzheimer's Disease and Epilepsy and Predisposes to Seizures. Cell Calcium 2021, 100, 102480, doi:10.1016/j.ceca.2021.102480.

3. **Dematteis, G.;** Restelli, E.; Vanella, V.V.; Manfredi, M.; Marengo, E.; Corazzari, M.; Genazzani, A.A.; Chiesa, R.; Lim, D.; Tapella, L. Calcineurin Controls Cellular Prion Protein Expression in Mouse Astrocytes. Cells 2022, 11, 609, doi:10.3390/cells11040609.

4. Gong, C.; Bonfili, L.; Zheng, Y.; Cecarini, V.; Cuccioloni, M.; Angeletti, M.; **Dematteis, G.;** Tapella, L.; Genazzani, A.A.; Lim, D.; et al. Immortalized Alzheimer's Disease Astrocytes: Characterization of Their Proteolytic Systems. Mol. Neurobiol. 2023, doi:10.1007/s12035-023-03231-z.

5. Villani, S.; **Dematteis, G**.; Tapella, L.; Gagliardi, M.; Lim, D.; Corazzari, M.; Aprile, S.; Del Grosso, E. Quantification of the Chemical Chaperone 4-Phenylbutyric Acid (4-PBA) in Cell Culture Media via LC-HRMS: Applications in Fields of Neurodegeneration and Cancer. Pharm. Basel Switz. 2023, 16, 298, doi:10.3390/ph16020298.

6. Tapella, L.; **Dematteis, G.;** Genazzani, A.A.; De Paola, M.; Lim, D. Immortalized Hippocampal Astrocytes from 3xTg-AD Mice, a New Model to Study Disease-Related Astrocytic Dysfunction: A Comparative Review. Neural Regen. Res. 2023, 18, 1672–1678, doi:10.4103/1673-5374.363192.

7. Lim, D.; Tapella, L.; **Dematteis, G**.; Genazzani, A.A.; Corazzari, M.; Verkhratsky, A. The Endoplasmic Reticulum Stress and Unfolded Protein Response in Alzheimer's Disease: A Calcium Dyshomeostasis Perspective. Ageing Res. Rev. 2023, 87, 101914, doi:10.1016/j.arr.2023.101914.

8. Lim, D.; Tapella, L.; **Dematteis, G.;** Talmon, M.; Genazzani, A.A. Calcineurin Signalling in Astrocytes: From Pathology to Physiology and Control of Neuronal Functions. Neurochem. Res. 2022, doi:10.1007/s11064-022-03744-4.

9. Lim, D.; **Dematteis, G**.; Tapella, L.; Genazzani, A.A.; Calì, T.; Brini, M.; Verkhratsky, A. Ca2+ Handling at the Mitochondria-ER Contact Sites in Neurodegeneration. Cell Calcium 2021, 98, 102453, doi:10.1016/j.ceca.2021.102453.

CONGRESS AND POSTERS

- **Giulia Dematteis**, Elena Restelli, Roberto Chiesa, Eleonora Aronica, Armando A Genazzani, Dmitry Lim and Laura Tapella: "Calcineurin Controls Expression of EAAT1/GLAST in Mouse and Human Cultured Astrocytes through Dynamic Regulation of Protein Synthesis and Degradation"; at XL SIF seminar, 10-13 March 2021. **(Poster presentation)**

- **Giulia Dematteis**, Marcello Manfredi, Teresa Soda, Egidio D'Angelo, Armando Genazzani, Laura Tapella, Dmitry Lim: "Astroglial

calcineurin - a novel regulator of CNS proteostasis: between physiology and pathology"; at the workshop of glial cell-neurons crosstalk, Turin, 1-2 October 2020. **(Poster presentation)**

- **Giulia Dematteis**, Gabrielė Vydmantaitė, Federico Alessandro Ruffinatti, Malak Chahin, Serena Farruggio, Elettra Barberis, Eleonora Ferrari, Emilio Marengo, Carla Distasi, Ramunė Morkūnienė, Armando A Genazzani, Mariagrazia Grilli, Elena Grossini, Marco Corazzari, Marcello Manfredi, Dmitry Lim, Aistė Jekabsone, Laura Tapella. "Proteomic analysis links alterations of bioenergetics, mitochondria-er interactions and proteostasis in hippocampal astrocytes from 3xTg-AD"; at the congress Glial biology in medicine; virtual conference, 25-26 October 2021. **(Poster presentation)**

- **Giulia Dematteis,** Armando Genazzani, Tito Calì, Marisa Brini, Federica Zulliani, Laura Tapella, Dmitry Lim. "Minding the gap: modulation of ER mitochondria Ca^{2+} transfer by manipulation of inter-organellar interaction"; at the junior European Calcium Society online meeting: Calcium research across kingdoms, 23-24 November 2021. **(Poster presentation)**

- **Giulia Dematteis,** Laura Tapella, Marianna Moro, Beatrice Pistolato, Elisa Tonelli, Ambra Grolla, Riccardo Miggiano, Armando A Genazzani, Dmitry Lim. "Mind the gap: a role for ER-mitochondria interaction in Alzheimer's disease astrocytes cellular dysfunction", at the SINS PhD meeting, Brescia, 11 June 2022 **(Oral communication)**

- **Giulia Dematteis**, Laura Tapella, Pietro La Vitola, Susanna Leva, Elisa Tonelli, Marco Raddi, Marta Delconti, Letizia Dacomo, Mariagrazia Grilli, Gianluigi Forloni, Armando A Genazzani, Claudia Balducci, Dmitry Lim. "Genetic deletion of calcineurin B1 in

astrocytes reduces amyloid burden, neuroinflammation and improves memory in acute and chronic mouse models of Alzheimer's disease", at SIFnational congress, Roma, 15-19 November 2022 **(Oral communication)**

- **Giulia Dematteis**, Laura Tapella, Marianna Moro, Beatrice Pistolato, Elisa Tonelli, Aiste' Jekabsone, Ambra A Grolla, Mariagrazia Grilli, Marcello Manfredi, Marco Corazzari, Armando A Genazzani, Dmitry Lim. "Protein synthesis inhibition and loss of homeostatic functions in astrocytes from an Alzheimer's disease mouse model: a role for ER-mitochondria interaction", at More than Neuron 2022 conference, Turin, 15-17 December 2022. **(Poster presentation)**

- **Giulia Dematteis**, Laura Tapella, Riccardo Miggiano, Marisa Brini, Tito Calì, Armando A Genazzani, Dmitry Lim. "Investigation of the interplay between endoplasmic reticulum-mitochondria distances and mitochondrial Ca2+ uptake", at Workshop of the European Calcium Society on Mitochondrial Ca2+ Signaling in Health and Disease, Padova, 7-9 September 2023. **(Oral communication)**

- **Giulia Dematteis**, F.Cavaliere, L. Tapella, M. Grilli, A. Genazzani, D. Lim "Role of mitochondria-ER interaction in astrocyte cellular disfunction associated with neurodegeneration", at SINS national congress, Turin, 15-17 September. **(Poster presentation)**

Chapter 9

CURRICULUM VITAE

Giulia Dematteis

Personal data

Date of birth:	06/03/1995
Address:	Cascina Rocco 19, borgo d'Ale, 13040 (VC).
Phone number:	+ 39 3405586075
Email	Giulia.dematteis@uniupo.it

Education

October 2019	Master's degree in chemistry and pharmaceutical technology, at Università del Piemonte Orientale, with graduation mark of 110/110 cum lode, and a thesis entitled "Control of sodium and potassium homeostasis by astroglial calcineurin: from neuronal excitability to memory formation". Supervisor: Dmitry Lim.
Since November 2020	PhD in Drug Innovation, at "Università del Piemonte Orientale", with a project entitled "Ca2+ related mechanisms of cellular dysfunction in neurodegeneration". Supervisor: Dmitry Lim
12 November 2022	Theoretical courses for animal care (36 CFU), at Istituto Zooprofilattico Sperimentale della Lombardia e dell'Emilia Romagna

Fellowships and Contracts

July-August 2018	Free Mover fellowship for an internship at the Neuroscience department of Amsterdam University, Supervisor: Eleonora Aronica
January-October 2020	Post graduated fellowship in the pharmacological Laboratory, led by Prof. Genazzani. Supervisor: Dmitry Lim..

November 2020 - October 2023	PhD fellowship at the Department of pharmacology of Università del Piemonte Orientale. Supervisor: Dmitry Lim.
March-July 2021	Contract as tutor of physiology, at the Department of pharmacology of Università del Piemonte Orientale. Supervisor: Carla Distasi
March-July 2022	Contract as tutor of physiology, at the Department of pharmacology of Università del Piemonte Orientale. Supervisor: Carla Distasi
July September 2022	Short Term Fellowship, financed by EMBO foundation, at Achucarro Basque Canter for Neuroscience, with a project entitled "Role of mitochondria-ER interaction in cellular disfunction of Parkinson's disease astrocytes". Supervisor: Fabio Cavaliere.
March-July 2023	Contract as tutor of physiology, at the Department of pharmacology of Università del Piemonte Orientale. Supervisor: Carla Distasi
Since November 2023	Research fellow (assegno di ricerca) at the Department of pharmacology of Università del Piemonte Orientale, entitled "generation and functional characterization of neuronal models of ataxia telengectasia pathology". Supervisor: Dmity Lim.

Conferences and congress	
1-2 October 2020	Poster presentation at the workshop of glial cell-neurons crosstalk, in Turin, of a poster entitled "Astroglial calcineurin - a novel regulator of CNS proteostasis: between physiology and pathology".
10-13 March 2021	Poster presentation at XL SIF seminar, of a poster entitled "Astroglial calcineurin - a novel regulator of CNS proteostasis: between physiology and pathology"
23-24 October 2021	poster presentation at the 2nd junior European Calcium Society online meeting, with a poster entitled "Minding the gap: modulation of ER mitochondria Ca2+ transfer by manipulation of inter-organellar interaction".
11 June 2022	Oral communication at the SINS PhD meeting, in Brescia, with presentation entitled "Mind the gap: a role for ER-mitochondria interaction, in Alzheimer's disease astrocytes cellular dysfunction".
15-22 November 2022	Oral communication at the SIF national congress, in Roma, with a presentation entitled "Genetic deletion of calcineurin B1

	in astrocytes reduces amyloid burden, neuroinflammation and improves memory in acute and chronic mouse models of Alzheimer's disease".
15-17 December 2022	Poster presentation at More than Neuron congress, in Torino, with poster entitled "Protein synthesis inhibition and loss of homeostatic functions in astrocytes from an Alzheimer's disease mouse model: a role for ER-mitochondria interaction".
26 March - 1 April 2023	Student member at the international Astrocytes School, in Bertinoro, with a talk entitled "The role of ER-mitochondria interaction in Alzheimer's disease astrocytes cellular dysfunction".
7-9 September 2023	Oral communication at Workshop of the European Calcium Society on Mitochondrial Ca2+ Signalling in Health and Disease, with a presentation entitled "Investigation of the interplay between endoplasmic reticulum-mitochondria distances and mitochondrial Ca2+ uptake".
15-17 September 2023	Poster presentation at the SINS national congress, in Turin, with a poster entitled "Role of mitochondria-ER interaction in astrocyte cellular disfunction associated with neurodegeneration".

Awards

11 June 2022	Best oral communication at SINS PhD meeting.
19 November 2022	Best oral communication at SIF national Congress.
9 September 2023	Best oral communication at Workshop of the European Calcium Society on Mitochondrial Ca2+ Signaling in Health and Disease.
17 September 2023	Best poster presentation at 2023 SINS national congress.

Scientific Interest

	Alteration in endoplasmic reticulum-mitochondria (ER-Mit) interaction has been reported in different pathological condition, including Alzheimer disease (AD) models. One of the most important processes that takes place at the ER-Mit site is the ER to mitochondria Ca2+ transfer. However, the mechanisms and alteration of calcium transfer in different diseases conditions are far from understanding.

In one of our publications, we have reported that the ER-Mit interaction is affected in an astrocytic cellular model of AD, and we identified alterations in intracellular Ca2+ handling, reduced protein synthesis and ATP production.

To directly evaluate the effects of shortening ER-Mit distances on Ca2+ handling, we overexpressed in Hela cells, linkers that fix the ER-Mit distance at 6nm and 10nm. We observed a reduction of mitochondrial Ca2+ uptake both in the mitochondrial matrix and in the lumen of the cristae of the mitochondria, while ER [Ca2+] was not affected. We also reported reduced protein synthesis and metabolic activity, recapitulating alterations identified in AD astrocytes. Moreover, we designed a linker that fixes the ER-Mit distances at 20nm (20nm EML), the one supposed to promotes ER-Mit calcium transfer. We found that the expression of the 20nm EML promotes ER to mitochondria calcium transfer, increasing the basal calcium concentration in the lumen of the cristae, and ATP-induced calcium pick in the mitochondrial matrix. These data correlates with an increased amount of calcium transfer units formed by IP3R and VDAC1, evaluated via proximity ligation assay. Cells expressing 20nmEML also display increased cellular metabolic activity, rescuing the alterations described in AD astrocytes.

Indeed, our results suggest a causal role for the increased ER-Mit interaction in AD related astroglial dysfunction, indicating that normalizing calcium transfer between ER-Mit could represent a valuable strategy for AD treatment.

Publications

1. Tapella, L.; **Dematteis, G.*;** Moro, M.; Pistolato, B.; Tonelli, E.; Vanella, V.V.; Giustina, D.; Forgia, A.L.; Restelli, E.; Barberis, E.; et al. Protein Synthesis Inhibition and Loss of Homeostatic Functions in Astrocytes from an Alzheimer's Disease Mouse Model: A Role for ER-Mitochondria Interaction. 2022, 2022.03.24.485644.

2. Tapella, L.; **Dematteis, G.*;** Ruffinatti, F.A.; Ponzoni, L.; Fiordaliso, F.; Corbelli, A.; Albanese, E.; Pistolato, B.; Pagano, J.; Barberis, E.; et al. Deletion of Calcineurin from Astrocytes Reproduces Proteome Signature of Alzheimer's Disease and Epilepsy and Predisposes to Seizures. Cell Calcium 2021, 100, 102480, doi:10.1016/j.ceca.2021.102480.

3. **Dematteis, G.;** Vydmantaitė, G.; Ruffinatti, F.A.; Chahin, M.; Farruggio, S.; Barberis, E.; Ferrari, E.; Marengo, E.; Distasi, C.; Morkūnienė, R.; et al. Proteomic Analysis Links Alterations of Bioenergetics, Mitochondria-ER

Interactions and Proteostasis in Hippocampal Astrocytes from 3xTg-AD Mice. Cell Death Dis. 2020, 11, 645, doi:10.1038/s41419-020-02911-1.

4. **Dematteis, G.;** Restelli, E.; Vanella, V.V.; Manfredi, M.; Marengo, E.; Corazzari, M.; Genazzani, A.A.; Chiesa, R.; Lim, D.; Tapella, L. Calcineurin Controls Cellular Prion Protein Expression in Mouse Astrocytes. Cells 2022, 11, 609, doi:10.3390/cells11040609.

5. **Dematteis, G**.; Restelli, E.; Chiesa, R.; Aronica, E.; Genazzani, A.A.; Lim, D.; Tapella, L. Calcineurin Controls Expression of EAAT1/GLAST in Mouse and Human Cultured Astrocytes through Dynamic Regulation of Protein Synthesis and Degradation. Int. J. Mol. Sci. 2020, 21, doi:10.3390/ijms21062213.

6. Gong, C.; Bonfili, L.; Zheng, Y.; Cecarini, V.; Cuccioloni, M.; Angeletti, M.; **Dematteis, G.;** Tapella, L.; Genazzani, A.A.; Lim, D.; et al. Immortalized Alzheimer's Disease Astrocytes: Characterization of Their Proteolytic Systems. Mol. Neurobiol. 2023, doi:10.1007/s12035-023-03231-z.

7. Villani, S.; **Dematteis, G.;** Tapella, L.; Gagliardi, M.; Lim, D.; Corazzari, M.; Aprile, S.; Del Grosso, E. Quantification of the Chemical Chaperone 4-Phenylbutyric Acid (4-PBA) in Cell Culture Media via LC-HRMS: Applications in Fields of Neurodegeneration and Cancer. Pharm. Basel Switz. 2023, 16, 298, doi:10.3390/ph16020298.

8. Tapella, L.; Soda, T.; Mapelli, L.; Bortolotto, V.; Bondi, H.; Ruffinatti, F.A.; **Dematteis, G.;** Stevano, A.; Dionisi, M.; Ummarino, S.; et al. Deletion of Calcineurin from GFAP-Expressing Astrocytes Impairs Excitability of Cerebellar and Hippocampal Neurons through Astroglial Na+ /K+ ATPase. Glia 2020, 68, 543–560, doi:10.1002/glia.23737.

9. Tapella, L.; **Dematteis, G.;** Genazzani, A.A.; De Paola, M.; Lim, D. Immortalized Hippocampal Astrocytes from 3xTg-AD Mice, a New Model to Study Disease-Related Astrocytic Dysfunction: A Comparative Review. Neural Regen. Res. 2023, 18, 1672–1678, doi:10.4103/1673-5374.363192.

10. Lim, D.; Tapella, L.; **Dematteis, G.;** Genazzani, A.A.; Corazzari, M.; Verkhratsky, A. The Endoplasmic Reticulum Stress and Unfolded Protein Response in Alzheimer's Disease: A Calcium Dyshomeostasis Perspective. Ageing Res. Rev. 2023, 87, 101914, doi:10.1016/j.arr.2023.101914.

11. Lim, D.; Tapella, L.; **Dematteis, G.;** Talmon, M.; Genazzani, A.A. Calcineurin Signalling in Astrocytes: From Pathology to Physiology and Control of Neuronal Functions. Neurochem. Res. 2022, doi:10.1007/s11064-022-03744-4.

12. Lim, D.; **Dematteis, G.;** Tapella, L.; Genazzani, A.A.; Calì, T.; Brini, M.; Verkhratsky, A. Ca2+ Handling at the Mitochondria-ER Contact Sites in Neurodegeneration. Cell Calcium 2021, 98, 102453, doi:10.1016/j.ceca.2021.102453.